Forschungszentrum Jülich
in der Helmholtz-Gemeinschaft

Effect of geometry and composition of Cr steels on oxide scale properties relevant for interconnector applications in Solid Oxide Fuel Cells (SOFCs)

Paweł Huczkowski, Willem J. Quadakkers

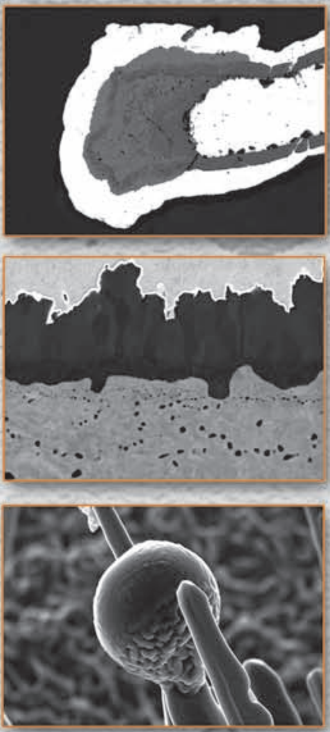

Energietechnik
Energy Technology

Schriften des Forschungszentrums Jülich
Reihe Energietechnik / Energy Technology Band / Volume 65

Forschungszentrum Jülich GmbH
Institut für Energieforschung (IEF)
Werkstoffstruktur und Eigenschaften (IEF-2)

Effect of geometry and composition of Cr steels on oxide scale properties relevant for interconnector applications in Solid Oxide Fuel Cells (SOFCs)

Paweł Huczkowski*, Willem J. Quadakkers

*Dissertation

Schriften des Forschungszentrums Jülich
Reihe Energietechnik / Energy Technology Band / Volume 65

ISSN 1433-5522 ISBN 978-3-89336-484-8

Bibliographic information published by the Deutsche Nationalbibliothek.
The Deutsche Nationalbibliothek lists this publication in the Deutsche
Nationalbibliografie; detailed bibliographic data are available in the
Internet at http://dnb.d-nb.de.

Publisher and Distributor:	Forschungszentrum Jülich GmbH Zentralbibliothek, Verlag D-52425 Jülich Telefon (02461) 61-5368 · Telefax (02461) 61-6103 e-mail: zb-publikation@fz-juelich.de Internet: http://www.fz-juelich.de/zb
Cover Design:	Grafische Medien, Forschungszentrum Jülich GmbH
Printer:	Grafische Medien, Forschungszentrum Jülich GmbH

Schriften des Forschungszentrums Jülich
Reihe Energietechnik / Energy Technology Band / Volume 65

D 82 (Diss., Aachen, RWTH, 2005)

ISSN 1433-5522
ISBN 978-3-89336-484-8

The complete volume is freely available on the Internet on the Jülicher Open Access Server (JUWEL)
at http://www.fz-juelich.de/zb/juwel

Abstract

A number of high-Cr ferritic steels have been investigated as possible construction materials (interconnectors) for Solid Oxide Fuel Cells (SOFCs). The mentioned materials have the advantage of a higher electronic conductivity, lower cost and easier fabrication than so far used lanthanum chromite-based ceramics. A large number of ferritic steels are commercially available in a wide range of compositions, however it seems that none of them can fulfil all requirements for the SOFC interconnector application. Therefore the main emphasis was put to the investigation of the high temperature properties of recently introduced high chromium ferritic steels especially designed for SOFC applications.

The scale formation mechanisms were investigated during oxidation times ranging from a few minutes up to 6000 hours. For scale characterization a number of conventional analysis techniques such as optical metallography, scanning electron microscopy and X-ray diffraction were used in combination with two-stage oxidation studies using ^{18}O-tracer. It was found that the growth rates of the scales were not only governed by the main scale forming alloying elements Cr and Mn, but to a substantial extent by minor additions of Si and Al. At the test temperatures of 800°C and 900°C these latter elements affect the scale formation although they are not directly incorporated in the surface scales.

SOFC market requirements lead in many cases to the demand for a reduction of the fuel cell size and/or weight and thus of the interconnector thickness. Therefore, the main emphasis was made to investigate changes in the oxidation behaviour in the case of thin components. It was found that with decreasing sample thickness the lifetime of the mentioned steels decreases due to breakaway phenomena. This effect is caused by faster exhaustion of the chromium reservoir from the bulk alloy in case of thinner components. The observed lifetime limits can be predicted with reasonable accuracy by a theoretical model, using oxide growth rate parameters, initial alloy Cr content and critical Cr content required for protective chromia scale formation. In the calculation of the Cr-reservoir exhaustion it has, however, to be taken into account, that during air exposure the oxidation rates increase with decreasing specimen thickness. The possible explanation of this effect is discussed on the basis of scale formation mechanisms involving microcrack formation in the surface oxide scale and depletion of major and minor alloying additions in the bulk alloy.

The electrical conductivity of the interconnect is a crucial property for SOFC application whereby the conductivity of the chromium based oxide scale which forms during high temperature service has to be taken into account in the overall conductivity value. Therefore experimental data concerning the electrical conductivity of the surface oxide scales formed in the temperature range 600-800°C on the investigated ferritic steels have been determined. The data are correlated with oxide scale morphologies and scale formation mechanisms and the results are compared with those obtained for two “pure chromia” forming materials.

Zusammenfassung

Es wurden eine Reihe ferritischer, hochlegierter Cr-Stähle als mögliche Konstruktionswerkstoffe für Interkonnektoren in Festoxid-Brennstoffzellen (SOFCs) entwickelt. Diese Stähle sind preiswert, einfacher herzustellen und besitzen eine höhere elektrische Leitfähigkeit als das bisher verwendete, keramische Lanthanchromit. Es sind viele ferritische Stähle mit einer großen Bandbreite von Zusammensetzungen verfügbar, jedoch erfüllt keiner von ihnen die Anforderungen eines Brennstoffzellen-Interkonnektors vollständig. Deswegen wurde der Schwerpunkt der vorliegenden Arbeit auf die Untersuchung der Eigenschaften der aktuell für SOFC Anwendungen entwickelten, ferritischen, hochlegierten Cr-Stähle gelegt.

Das Oxidationsverhalten wurde zwischen einigen Minuten und 6000 h Oxidationsdauer untersucht. Zahlreiche Analysemethoden, wie die optische Mikroskopie, die Elektronenmikroskopie (REM) mit Energiedispersiver Röntgenanalyse (EDX), die Röntgenfeinstrukturanalyse (XRD), die Sekundärneutralteilchen-Massenspektrometrie (SNMS) und die Raman Spektroskopie (RS) wurden für die Charakterisierung der Oxidationsprodukte verwendet. Die Oxidationsrate zeigte sich nicht nur von den deckschichtbildenden Elementen Cr und Mn abhängig, sondern auch von den Legierungszusätzen Si und Al. Bei Versuchstemperaturen von 800 und 900°C beeinflussen diese geringen Legierungszusätze die Oxidschichtbildung, obwohl sie nicht direkt in die Oxidschicht eingebaut werden.

Der Brennstoffzellenmarkt fordert in vielen Fällen eine geringere Größe und/oder geringeres Gewicht der Brennstoffzellen und damit eine Verringerung der Dicke der Interkonnektorenbleche. Deswegen ist es besonders wichtig die Veränderung des Oxidationsverhaltens bei besonders dünnen Komponenten zu untersuchen. Es fällt auf, dass die Lebensdauer der untersuchten Stähle, aufgrund von breakaway (Eisenoxidbildung), mit abnehmender Probendicke abnimmt. Dies geschieht, da das bei dünneren Komponenten geringere Chromreservoir der Probe schneller verarmt. Die Lebensdauer kann durch ein theoretisches Modell mit guter Näherung vorhergesagt werden. In das Modell fließen die Wachstumsparameter der Oxidschicht, der Ausgangschromgehalt der Legierung und der kritische Chromgehalt (unter dem sich keine schützende Chromoxidschicht mehr bilden kann) ein. In die Berechnung der Chromverarmung wird einbezogen, dass die Oxidationsrate in Luft mit abnehmender Probendicke zunimmt. Als mögliche Erklärung dieses Effekts werden Oxidschichtbildungsmechanismen, wie Mikrorissbildung in der Oberfläche der Oxidschicht und Verarmung der Legierungselemente und – zusätze diskutiert.

Die elektrische Leitfähigkeit eines Interkonnektors ist ein ausschlaggebender Faktor bei Brennstoffzellenanwendungen. Hierbei muss mit der Leitfähigkeit der Oxidschicht gerechnet werden, die sich bei den hohen Betriebstemperaturen bildet. Deswegen wurden Daten über die Leitfähigkeit an der Oberfläche der Oxidschicht bei Temperaturen zwischen 600-800°C ermittelt. Diese Daten wurden in Zusammenhang mit der Morphologie der Oxidschicht und deren Bildungsmechanismus gebracht und mit den Werten von zwei rein-chromoxid-bildenenden Werkstoffen verglichen.

1. Introduction

For decades the energy situation in the world has become more and more critical. Conventional energy sources are not sufficient to meet the constantly expanded needs of humanity so exploration of new energy sources seems to be a huge task for the future. One possibility for the alternatives to conventional energy conversion systems is fuel cell development.

One of the most promising fuel cell systems seems to be solid oxide fuel cells (SOFC) because they can use fossil fuels as well as pure hydrogen. SOFC development requires the united work of broad groups of different engineering branches. One of the tasks is to invent the most suitable materials for all SOFC components (anode, cathode, electrolyte and interconnect). Based on the SOFC requirements, steels seem to be promising construction materials for one of the components - the interconnector plate.

Development of the particular steel is a relatively complicated task because the material needs to fulfil several requirements, which sometimes can be even contrary. Based on the requirements in respect to oxidation resistance, thermal expansion coefficient and electrical conductivity of the surface oxide scale, Cr-based alloys and high Cr- steels seem to be the most promising metallic interconnector materials. A large number of ferritic steels are commercially available in a wide range of compositions, however it seems that none of them can fulfil all requirements for the SOFC interconnector. Therefore, new Cr-based alloys have recently been developed especially for SOFC applications. Mentioned materials seem to be sufficiently good for most of the envisaged SOFC applications, however it is still necessary to improve their composition to design a steel, which possesses excellent properties during operation in SOFC relevant atmospheres.

2. Aim of the studies

Planar Solid Oxide Fuel Cells (SOFC's) operating in the temperature range between 700°C - 800°C allow the use of metallic materials instead of lanthanum chromite-based ceramics as construction materials for SOFC interconnects [Stöver-1]]. Metallic materials have the advantage of a higher electronic conductivity, lower cost and easier fabrication than ceramics [Quadakkers-1]. Based on the requirements in respect to oxidation resistance and thermal expansion coefficient, high chromium ferritic steels seem to be promising interconnect materials [Tietz-1].

In the present studies recently developed SOFC interconnect materials as well as other commonly used high-Cr commercial steels were investigated with respect to their oxidation behaviour in the temperature range required for SOFC application (700°C - 900°C). SOFC market requirements (e.g., in the automotive industry) lead in many cases to the demand for a reduction of the fuel cell size and/or weight and thus of the interconnector thickness. Therefore, the main emphasis was made to investigate changes in the oxidation behaviour in the case of thin components. It is shown that for chromia forming ferritic steel components the oxidation limited life is primarily governed by the reservoir of the scale forming alloying elements (mainly Cr and Mn), rather than by their absolute concentration in the steel. The scale formation mechanisms in the case of the most promising materials were investigated during oxidation times ranging from a few minutes up to 6000 hours and the influence of minor alloy additions in the steels was also elaborated. For a better understanding of the mechanisms of oxidation for high-Cr ferritic steels, several "pure" model alloys were prepared and incorporated into the test program.

The electrical conductivity of the interconnect is a crucial property for SOFC application whereby the conductivity of the chromia based oxide scale formed on the metallic surface during stack operation has to be taken into account in the overall conductivity value. A wide program of conductivity tests for different chromium steels as well as different conducting pastes was performed in the temperature range 600°C - 800°C.

3. Literature review

3.1 Fuel cells

A fuel cell is a device that converts chemical energy directly into electricity during an electrochemical process [Stambouli-1]. The operating principles of fuel cells are similar to those of batteries however in contrast to batteries – where the chemical energy is stored in substances inside the battery – fuel cells are just converting systems, the reagents have to be supplied continuously to the fuel cell in order to obtain electricity [Cappadonia-1, Stambouli-2]. All the fuel cells operate without combusting fuel and thus they are very attractive from both energy and environmental standpoints [Song-1]. Although the principal operation of a fuel cell has been known since the last century, the necessary technology for producing fuel cell systems of high efficiency and acceptable costs at an industrial level has only been developed in the last few decades [Cappadonia-1].

3.1.1 Historical overview

The history of fuel cells starts in 1893 when Sir William Grove constructed first cell using porous platinum electrodes and sulphuric acid (H_2SO_4) as the electrolyte bath [Grove-1, Chau-1]. In the 20th century the first important work on the fuel cells field was done by Dr. Francis T. Bacon. Dr. Bacon developed porous nickel electrodes and built the first high pressure, medium temperature alkaline fuel cell system in the kilowatt-range [Cappadonia-1]. The concept of Bacon, after adaptation by Pratt and Whitney, was used as an on-board power system for the Apollo missions in the 1960s. Besides, it is important to note that the work of Bacon stimulated the start of the current interest in fuel cell technology for sustainable stationary and mobile power generation [Acres-1]. From the 1980s the fuel cell research started to develop as a wide range of different technological concepts in many countries around the world [Stambouli-1].

3.1.2 Principle of operation

The primary components of each fuel cell are an ion conducting electrolyte, a cathode and an anode, as shown schematically in figure 3.1. All fuel cells have the same basic operating principles [Song-1]. In the simplest example, a fuel such as hydrogen is brought into the anode compartment and the oxidant (typically oxygen) into the cathode compartment. Direct chemical combustion is prevented by the electrolyte that separates the fuel from the oxidant.

Accordingly, half-cell reaction occurs at the anode and cathode, producing ions that can traverse the electrolyte, and water as a by-product. The flow of ionic charges through the electrolyte is balanced by the flow of electrons through an outside circuit and electrical power is obtained [Haile-1].

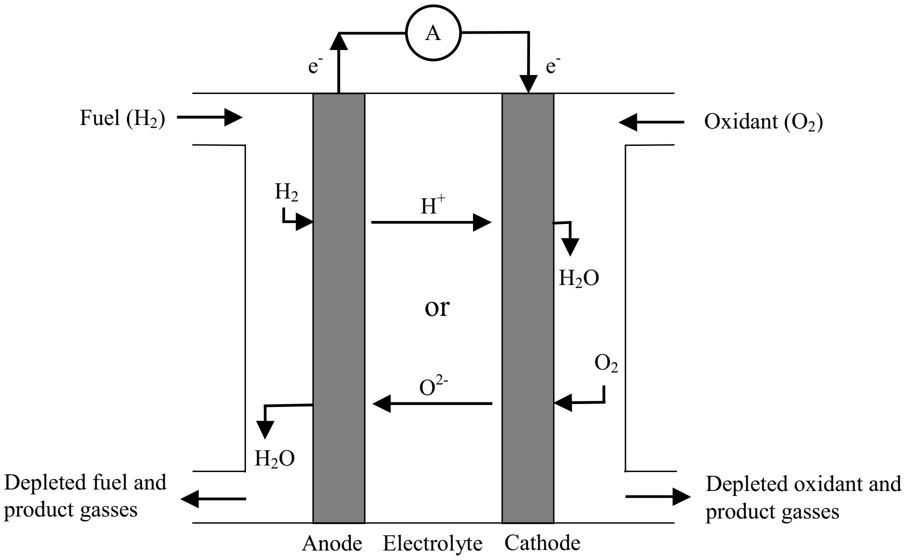

Figure 3.1: Typical fuel cell configuration

The nature of the electrolyte, liquid or solid, determines the operating temperature of the fuel cell [Stambouli-2]. The ideal fuel cell electrolyte should be high ionically conductive, impermeable for gases, electronically resistant and chemically stable under a wide range of conditions. Additionally, the electrolyte should exhibit sufficient mechanical and chemical integrity to prevent cracks and pore formation during manufacturing or long-term operation. The perfect electrode must be porous, electronically and ionically conducting, electrochemically active and have a high surface area [Haile-1].

3.1.3 Types of fuel cells

At the present status of fuel cell technology, there are six classified types: alkaline fuel cells (AFC), phosphoric acid fuel cells (PAFC), molten carbonate fuel cells (MCFC), proton exchange membrane fuel cells (PEMFC), solid oxide fuel cells (SOFC) and direct methanol fuel cells (DMFC) [Chau-1, Acres-1]. This classification is made on the basis of chemical characterization of the electrolyte used as an ionic conductor in the cell (DMFC is an exception where the name characterise the fuel used during cell operation). Typical characteristics of different fuel cells systems are summarized in Tables 3.1 and 3.2 [Haile-1, Song-1, Stambouli-1, 2, Chau-1, Acres-1, Cappadonia-1, Jiang-1, Dillon-1, Larminie-1, Carrette-1].

Type of FC	Electrolyte type	Mobile ion	Operating temperature [°C]	Efficiency [%]
AFC	Potassium hydroxide	OH^-	50 - 250	50 - 55
PAFC	Phosphoric acid	H^+	150 - 250	40 - 50
DMFC	Sulphuric acid or polymer	H^+	60 - 200	40 - 55
PEMFC	Polymer	H^+	50 - 125	40 - 50
MCFC	Lithium / potassium carbonate mixture	CO_3^{2-}	600 - 700	50 - 60
SOFC	Stabilized zirconia	O^{2-}	700 - 1000	45 - 60

Table 3.1: Typical characteristics of fuel cell systems. Part 1

Type of FC	Principle reactions [A-anode, C-cathode]	By-product formation	Fuel	Oxidant
AFC	A: $H_2 + 2OH^- \rightarrow 2H_2O + 2e^-$ C: $1/2O_2 + 2e^- + 2H_2O \rightarrow OH^-$	H_2O (Anode)	H_2	O_2 / Air
PAFC	A: $H_2 \rightarrow 2H^+ + 2e^-$ C: $1/2O_2 + 2e^- + 2H^+ \rightarrow H_2O$	H_2O (Cathode)	H_2	O_2 / Air
DMFC	A: $CH_3OH + H_2 \rightarrow CO_2 + 6H^+ + 6e^-$ C: $3/2O_2 + 6H^+ + 6e^- \rightarrow 3H_2O$	H_2O (Cathode) CO_2 (Anode)	Liquid methanol	O_2 / Air
PEMFC	A: $H_2 \rightarrow 2H^+ + 2e^-$ C: $1/2O_2 + 2e^- + 2H^+ \rightarrow H_2O$	H_2O (Cathode)	H_2	O_2 / Air
MCFC	A: $H_2 + CO_3^{2-} \rightarrow H_2O + CO_2 + 2e^-$ C: $1/2O_2 + CO_2 + 2e^- \rightarrow CO_3^{2-}$	H_2O, CO_2 (Anode)	Hydrocarbons, H_2, CO	CO_2 / O_2 / Air
SOFC	A: $H_2 + O^{2-} \rightarrow H_2O + 2e^-$ C: $1/2O_2 + 2e^- \rightarrow O^{2-}$	H_2O (Anode)	Hydrocarbons, H_2, CO	O_2 / Air

Table 3.2: Typical characteristics of fuel cell systems. Part 2

Detailed characterisation of the systems mentioned above can be found in comprehensive references [Larminie-1] and [Carrette-1].

Among all fuel cells types solid electrolyte systems seem to have an advantage because they do not contain dangerous corrosive liquids. Thus, many developers prefer polymer electrolyte and solid oxide fuel cells to alkali, phosphoric acid or molten carbonate fuel cells [Haile-1].

3.1.4 Solid oxide fuel cells

The main features of the SOFC are an all solid-state construction and high temperature operation. The combination of these features leads to a number of unique characteristics and advantages for this type of fuel cell, including flexibility in cell and stack design, manufacturing processes and power plant sizes [Minh-1]. Additionally, SOFC provide a major advantage over other fuel cell systems in that they can use fossil fuels as well as pure hydrogen [Lu-1].

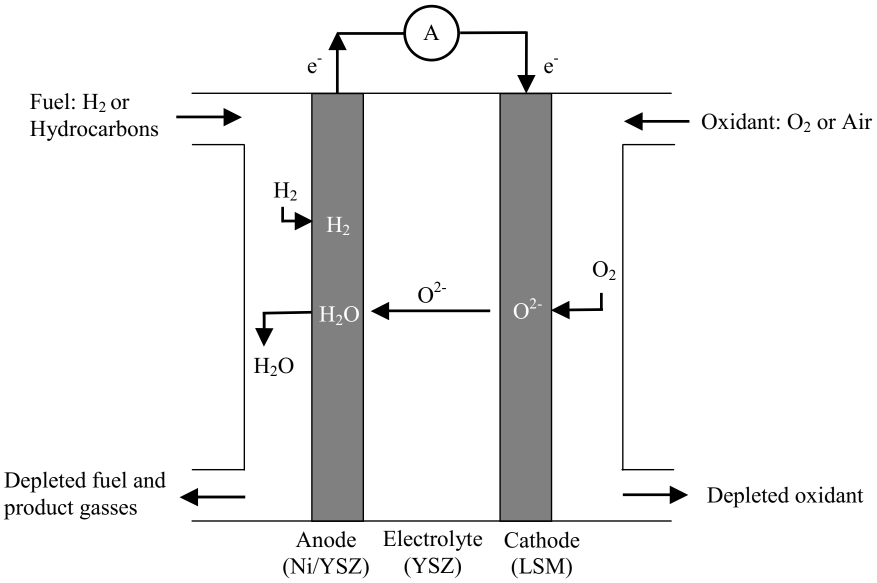

Figure 3.2: Typical SOFC cell configuration [Stambouli-1]

The history of SOFC started in 1930s when Baur and Preis [Baur-1, Singhal-1, McEvoy-1] applied zirconia stabilized with 15 wt% yttria as an electrolyte in the first cell on a laboratory scale. The authors used an idea of Nernst who was the first to describe zirconia (ZrO_2) as an oxygen ion conductor [Nernst-1, Larminie-1]. A typical SOFC configuration is shown in Figure 3.2 and Tables 3.1 and 3.2 summarise the characteristics of the SOFC system.

SOFC components

Every SOFC cell consists of four main parts: electrolyte, anode, cathode, and interconnect. Specific combinations of properties required for SOFC components necessitates the use of specifically designed materials and force the development of new advanced SOFC materials.

Zirconia doped with 8-10 mole % yttria (YSZ) is the most effective electrolyte for the high temperature SOFC although several others have been investigated including Bi_2O_3, CeO_2 and Ta_2O_5 [Steele-1]. Zirconia is highly stable in both the reducing and oxidizing environments. The ability to conduct O^{2-} ions is brought about by the fluorite crystal structure of zirconia in which some of the Zr^{4+} ions are replaced Y^{3+} ions. When this ion exchange occurs, a number of oxide-ion sites become vacant because of three O^{2-} ions replacing of four O^{2-} ions. Oxide ion transport occurs between vacancies located at tetrahedral sites in the perovskite lattice [Larmine-1, Skinner-1].

Among the SOFC components, the porous anode serves to provide electrochemical reaction sites for oxidation of the fuel, allows the fuel and byproducts to be delivered and removed from the surface sites, and to provide a path for electrons to be transported from the electrolyte/anode reaction sites to the interconnect in the SOFC stack. Porous Ni/YSZ cement is currently the most common anode material because of the acceptable thermodynamic stability and desirable electrochemical properties [Zhu-1].

The most important properties of SOFC cathodes are their catalytic activity for oxygen reduction and their compatibility with the electrolyte. The lanthanum manganite-based materials are the most common perovskites that are used with YSZ electrolytes at 1000°C because of their superior chemical stability. For lower cell operation temperatures composite cathodes made from LSM / YSZ are used [Haanappel-1], moreover Sr- / Co-doped lanthanum ferrites has been widely investigated [Singhal-1].

The last component of every SOFC stack is an interconnector plate. The main function of the interconnector is to act as a current collector and provide the electrical connection between the various single cells. The most important properties required for the interconnector material are therefore, high electronic conductivity, thermal stability in the anode and cathode side gases at high service temperature (650 – 1000°C), and the thermal expansion coefficient (CTE) similar to that of the ceramic, electro-active components. Ceramic materials on the basis of La-chromite have been shown to possess the property combination required for interconnectors. In recent years, especially for planar SOFC design (compare: Cell configuration and stack design, section 3.1.4) where the interconnect additionally has to supply the mechanical support for the thin ceramic parts and it is the gas-proof separation between fuel gas and oxidant, metals have gained more and more attention as possible replacements for the La-chromite because they offer a number of advantages over ceramics materials. They are easier, and therefore cheaper to fabricate than ceramics, they are less brittle, easier to machine, end they can be joined with a number of standard welding and brazing techniques. Additionally, they possess higher electrical and thermal conductivities than most ceramics [Quadakkers-1]. Detailed discussion about suitable metallic materials for SOFC application is elaborated in paragraph 3.3 and electrical conductivity considerations are introduced in paragraph 3.5.

Cell configuration and stack design

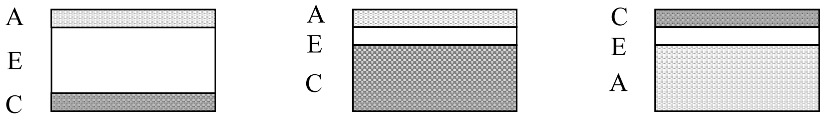

Electrolyte-supported Cathode-supported Anode-supported

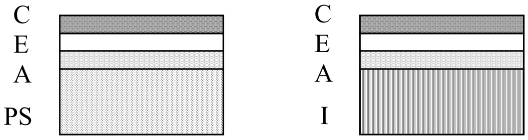

Porous substrate-supported Interconnect-supported

Figure 3.3: SOFC single cell configuration [Minh-1]
A - anode, C - cathode, E - electrolyte, PS - porous substrate, I - interconnect

The configurations in SOFC single cell can be classified into two categories: self-supporting (one of the cell components, often the thickest one, acts as the cell structural support) and external-supporting (cell is configured as thin layers on the interconnect or a porous substrate) [Minh-1]. The various cell configurations for SOFCs are schematically shown in Figure 3.3

Each single SOFC cell (anode, electrolyte, cathode) is connected to the next single cell via the interconnect plate. The group of connected cells is the so called SOFC stack. At present, two main designs of the stack have been proposed and developed: tubular and planar design [Singhal-2] (Figure 3.4). In the tubular design, the cell is configured as a tube, and stacks consisting of a bundle of single cell tubes. In the most common tubular design (i.e. Siemens Westinghouse design [Singhal-3, George-1]), the tube is made of the cathode material (cathode-supported) and closed at one end. Electrolyte and anode layers are formed on the outside of the tube. In the planar design (i.e. Research Centre Jülich [Tietz-1, Buchkremer-1]) the cell is configured as flat plates, which are connected in electrical series. All types of cell configurations (self-supporting or external-supporting) have been considered for the planar design [Minh-1].

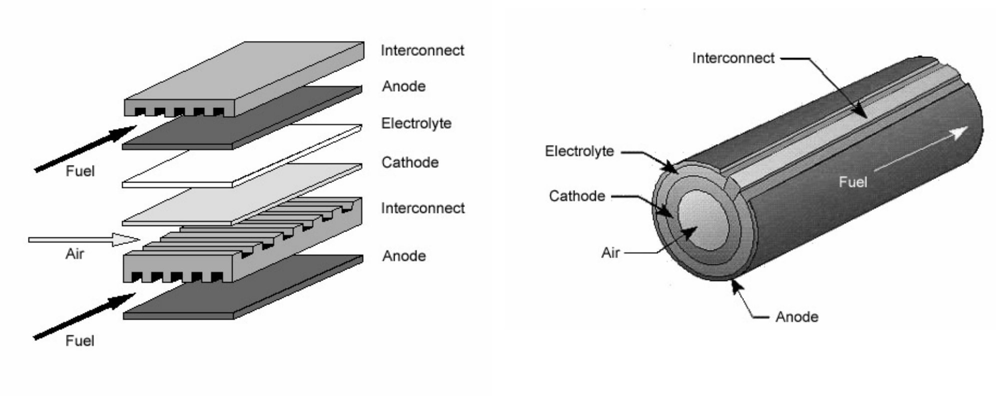

Figure 3.4: Solid Oxide Fuel Cell - planar and tubular design [Singhal-1, 2]

3.1.5 SOFC stack development at Research Centre Jülich

At Research Centre Jülich (FZJ) several generations of SOFC stacks have been designed and tested since the mid-nineties (more than 180 stacks and short stacks), all based on the concept of anode-supported cells. Research Centre Jülich is currently testing the 6th and 7th generation of stack design for SOFC. These stack designs are based on the planar, anode supported type cells and metallic interconnect plates made of the ferritic steel developed in Jülich (Figure 3.5). SOFC activities are concentrated on stacks suitable for practical stationary and mobile application. The aim is to design all components for high performance, low degradation, optimal industrialised processing, low weight, high flexibility and low cost. Integration of these results is expected to move stack lifetime well above 20 000 hours [Steinberger-1].

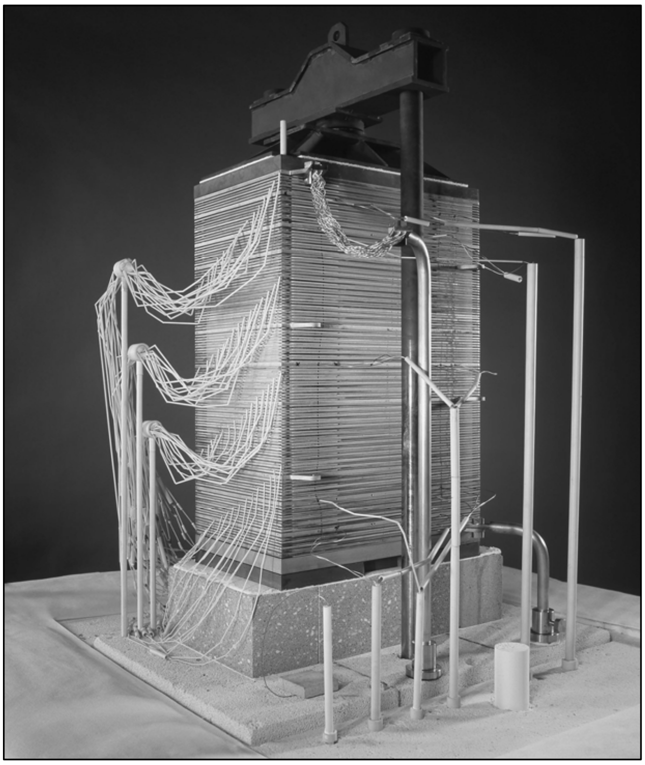

Figure 3.5: The 60-cell stack operated at FZJ from April 2004. 13.3 kW_{el} power production with hydrogen fuel, 11.9 kW_{el} with methane [Steinberger-1]

3.2 Basics of oxidation

3.2.1 Thermodynamics considerations

One of the most important questions in corrosion science is whether or not a reaction between a material and surrounding gas can occur. This question can be answered by the second law of thermodynamics. In most cases during high temperature exposure temperature and pressure are constant, so the second law is most conveniently written in terms of the Gibbs free energy (G') [Birks-1].

$$G' = H' - TS' \qquad (3.1)$$

where H' is the enthalpy and S' the entropy of the system. Under these conditions the second thermodynamics law states:

$\Delta G' < 0$ spontaneous reaction expected

$\Delta G' = 0$ equilibrium

$\Delta G' > 0$ thermodynamically impossible process

For a chemical reaction [Kofstad-1], e.g.:

$$M + O_2 = MO_2 \tag{3.2}$$

$\Delta G'$ is expressed as:

$$\Delta G' = \Delta G^\circ + RT \ln\left(\frac{a_{MO_2}}{a_M a_{O_2}}\right) \tag{3.3}$$

where ΔG° is the free energy change when all species are present in their standard states, R is a gas constant, T is a temperature and a is the thermodynamic activity which describes the deviation from the standard state for a given species.

Activity for a given species may be expressed as:

$$a_i = \frac{p_i}{p_i^\circ} \tag{3.4}$$

where p_i is either the vapour pressure over a condensed species or the partial pressure of a gaseous species and p_i° is the same quantity corresponding to the standard state of i. It is then possible to modify equation 3.3 replacing a_{O_2} by the oxygen partial pressure p_{O_2}:

$$\Delta G' = \Delta G^\circ + RT \ln\left(\frac{a_{MO_2}}{a_M p_{O_2}}\right) \tag{3.5}$$

For the special case of equilibrium ($\Delta G' = 0$), equation 3.5 reduces to:

$$\Delta G^\circ = -RT \ln\left(\frac{a_{MO_2}}{a_M p_{O_2}}\right) \tag{3.6}$$

If the activities of M and MO_2 are taken as unity, equation 3.6 may be used to express the oxygen partial pressure at which the metal and oxide coexist, i.e. the dissociation pressure of the oxide.

$$\Delta G^\circ = -RT \ln p_{O_2} \tag{3.7}$$

or:

$$p_{O_2} = \exp\left(-\Delta G^\circ / RT\right) \tag{3.8}$$

The value of dissociation pressure can be derived from the Ellingham/Richardson diagram (Figure 3.6), i.e. a plot of standard free energies for the formation of oxides as a function of temperature. Stabilities of the oxides can be directly compared on the diagram – the lower the position of the line on the diagram (lower dissociation pressure) the more thermodynamically stable is the oxide. The dissociation pressure increases with increasing temperature and from the viewpoint of thermodynamics the tendency of metals to oxidise decreases with increasing temperature.

Important information for designing industrial alloys can be obtained from the Ellingham/Richardson diagram. It is clearly visible that the oxides of iron, nickel and cobalt which are the basis for the majority of engineering alloys, are significantly less stable than the oxides of some of the solutes (e.g. Cr, Al, Si etc.) in these alloys. When one of these solute elements is added to iron, nickel or cobalt in a reasonable concentration, the base alloy is protected due to formation of a stable oxide on the surface. This is the basis of protection for most of the engineering alloys [Khanna-1].

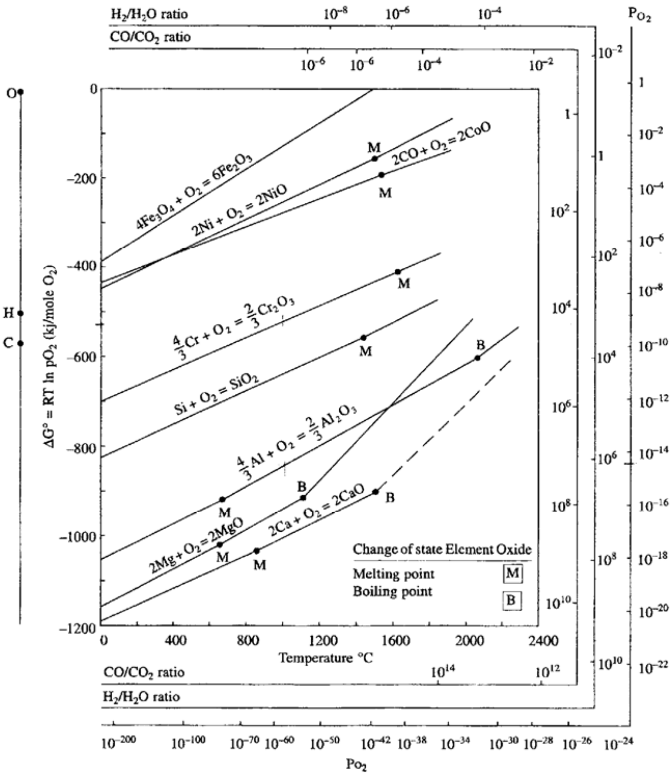

Figure 3.6: Standard free energy of formation of selected oxides as a function of temperature (Ellingham/Richardson Diagram) [Khanna-1]

3.2.2 Kinetics of oxidation

During high temperature exposure under thermodynamically favourable conditions (compare section 3.2.1) corrosion products start to form at the interface between two reactants. When dense films or scales are formed, the reactants, i.e. the metal and the oxidant, are separated, and the reaction may proceed only through the solid state diffusion of the reactants through the scale. Diffusion and transport of electrical charges in solids take place because of the occurrence of imperfections or defects in solids [Kofstad-1]. It is necessary to take into consideration that oxides have an ionic nature with stoichiometric or nonstoichiometric compositions, however an exact stoichiometric composition in inorganic compounds is in principle an exception [Kofstad-2]. Nonstoichiometric ionic compounds are classified as semiconductors and may show negative or positive behaviour and thus different kinds of defects in the lattice. The classification refers to the fact that electrical charge is transferred by negative carriers (N-type semiconductors) or positive carriers (P-type semiconductors). Ionic and electronic transport processes through the oxide are accompanied by ionising phase boundary reactions and the formation of new oxide at a site whose position depends upon whether cations or anions are transported through the oxide layer [Birks-1].

The basis for understanding high temperature oxidation of metals has been explained by Carl Wagner [Wagner-1]. In the classical Wagner's theory, lattice diffusion of ions or electrons across the scale is the rate controlling process. It is assumed that thermodynamic equilibria are established between the oxide and the oxygen gas at the oxide/oxygen interface and between the metal and the oxide at the metal/oxide interface (Figure 3.7). A gradient in the partial pressure (activity) of oxygen exist across the scale from the partial pressure of oxygen in the ambient atmosphere at the outer oxide surface to the partial pressure of oxygen at the metal/oxide interface. The latter partial pressure is the dissociation pressure of the oxide in equilibrium with the metal [Kofstad-1].

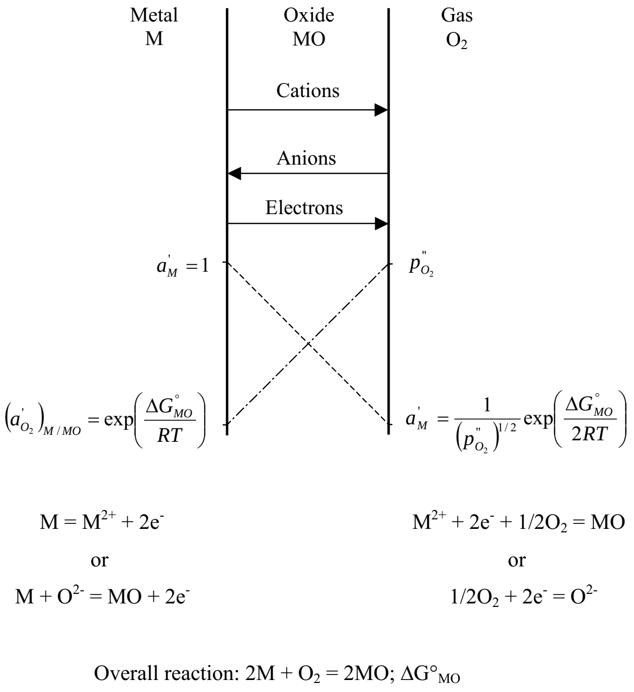

Figure 3.7: Diagram of scale formation according to Wagner's model [Birks-1]

Assuming that ionic transport across the growing oxide layer controls the rate of scaling and that thermodynamic equilibrium is established at each interface the outward cation flux, $j_{M^{2+}}$, is equal and opposite to the inward flux of cation defects. According to Fick's first law of diffusion:

$$J_{M^{2+}} = -J_{V_M} = D_{V_M} \frac{C''_{V_M} - C'_{V_M}}{x} \tag{3.9}$$

where x is the oxide thickness, D_{V_M} is the diffusion coefficient for cation vacancies, and C''_{V_M} and C'_{V_M} are the vacancy concentrations at the scale-gas and scale-metal interfaces respectively.

Since there is thermodynamic equilibrium at each interface, the value ($C''_{V_M} - C'_{V_M}$) is constant:

$$j_{V_M} = const. \frac{dx}{dt} = D_{V_M} \frac{C''_{V_M} - C'_{V_M}}{x} \tag{3.10}$$

so, $$\frac{dx}{dt} = \frac{k'}{x} \tag{3.11}$$

Integrating and noting that $x = 0$ at $t = 0$

$$x^2 = 2k't \tag{3.12}$$

The expression 3.12 is the common parabolic rate law [Birks-1].

It is shown in equation 3.12 that according to Wagner's theory the growth of the oxide scale is parabolic with time. Nevertheless, it is necessary to point out that this theory assumed highly idealistic conditions. During oxidation of different metals of alloys it is, in many cases, possible to observe deviations from parabolic oxidation kinetics into linear, logarithmic or combinations of two different kinetic laws. This behaviour is strictly connected with the rate determining step of the reaction and can also depend upon a number of factors, i.e. temperature, oxygen pressure, surface preparation and pre-treatment of the metal. For example the growth rate of alumina scales on reactive element containing, high temperature alloys has often been found to show a large deviation from classical parabolic kinetics; generally scale growth rates near to sub-parabolic (near-cubic) time dependence are observed. This has been explained in most cases by assuming that oxygen grain-boundary diffusion is the dominating scale growth process (compare also paragraph 3.4.1).

For engineering design, kinetics of oxidation are very important as they give an estimate of the design life of the metal to be used as a particular component at a specific temperature and environment [Khanna-1].

3.3 High temperature alloys for SOFC interconnect applications

3.3.1 Requirements for SOFC interconnectors

The most important requirements for SOFC interconnectors can be specified as follows [Quadakkers-1, Haile-1]:

- High electronic conductivity
- Excellent impermeability
- Chemical stability under both oxidising and reducing conditions
- Good mechanical properties
- Thermo-mechanical compatibility with other cell components (CTE)

Ceramics, perovskite type materials on the basis of La-chromite have been shown to possess the property combination required for interconnector materials, especially in the case of SOFC tubular design [Minh-2, Steele-1]. However, as introduced in paragraph 3.1.4, metallic, high temperature alloys can also withstand most of the requirements and therefore are being considered as construction materials for the SOFC interconnectors especially in the case of planar design [Stöver-1]. Metals additionally offer a number of advantages over La-chromite based ceramics especially when considering their lower cost and ease of fabrication [Quadakkers-1]. The last feature is of a great importance in designing fuel cells for mobile (e.g. automotive) applications. SOFC market requirements force the reduction of the fuel cell size and thus the interconnector thickness [Lamp-1, Zizelman-1, Friedrich-1]. Production of thin ceramic sheets is of course much more difficult (and in some cases even impossible) so metallic materials should have a large advantage for such an application over ceramic based interconnects.

Several groups of metallic materials were considered as possible interconnector materials for SOFC applications. At first, noble metals were investigated [Kofstad-3], but because of their high cost and limited availability this solution has been abandoned for commercial applications.

The main attention, therefore were paid to conventional high temperature alloys [England-1]. The most important ability of such an alloy is the formation of slow, thermally grown, protective oxide scales. For temperatures up to 1200°C the best choice would be MCrAl alloys (where M - Ni, Co or Fe) because of excellent oxidation protection of the alumina scale [Quadakkers-2]. In respect to a low CTE the best material to choose from this group of alloys would be FeCrAl [Lai-1]. Unfortunately, excellent oxidation protection of alumina formers is accompanied by very low, insufficient electrical conductivity of the surface scale (Al_2O_3) [Kofstad-3]. This is also the case for alumina forming intermetallics on the basis of NiAl, which were also investigated as possible interconnector materials because of their superior oxidation resistance and low CTE [Yamamoto-1].

Nickel-, cobalt- or iron based silica forming alloys could be potentially used as interconnects. However, formation and long term stability of protective silica requires quite large amounts of silicon additions to the mentioned alloys. This leads to substantial embrittlement, thus making the alloy unsuitable as construction material. Besides, silica has a very low electronic conductivity, leading to similar problems in SOFC application as alumina forming alloys [Quadakkers-1].

The most promising metallic materials for SOFC interconnectors are chromia forming alloys [Kofstad-3, Quadakkers-1]. In respect to their reasonable oxidation protection, satisfactory CTE and relatively high electronic conductivity chromia formers seem to be most suitable as interconnectors for SOFC application.

3.3.2 Chromia formers for SOFC applications

The most of the commercial chromia forming alloys is based on the systems NiCr, NiFeCr or FeCr. Ni-base alloys were investigated as SOFC interconnectors [Matsuzaki-1, England-1,2], however in respect to their substantially high thermal expansion coefficient Ni-base alloys are probably less promising for SOFC interconnects. Application of such a material would require a special cell design to overcome the stresses generated between interconnect and other cell components during thermal cycling [Quadakkers-1].

Chromia forming alloys based on the system FeCr are the most promising materials for SOFC application. These kinds of materials could be divided into two main groups: chromium base alloys and iron base ferritic steels [Tietz-1].

Typical alloy/steel compositions contain several elements, which are necessary for optimal behaviour during high temperature service. The main groups of these components are:

- Base material (for the FeCr systems Fe or Cr) – the component that is in majority and determines the thermo-mechanical properties of the alloy.
- Oxide forming elements (for the FeCr systems mainly Cr) – the elements that according to thermodynamics and kinetics form slowly growing, protective oxide scales (Cr_2O_3) [Wood-1].
- Reactive elements (RE) – elements like Zr, Hf, Y, La, Ce that reduce the growth rate of the oxide scale (Figure 3.8) and provide better adhesion at the scale/alloy interface [Quadakkers-3].
- Minor alloying elements (i.e. Ti, Mn) – incorporated into the scale and/or as an internal oxidation zone, can improve different alloy properties [Quadakkers-1].

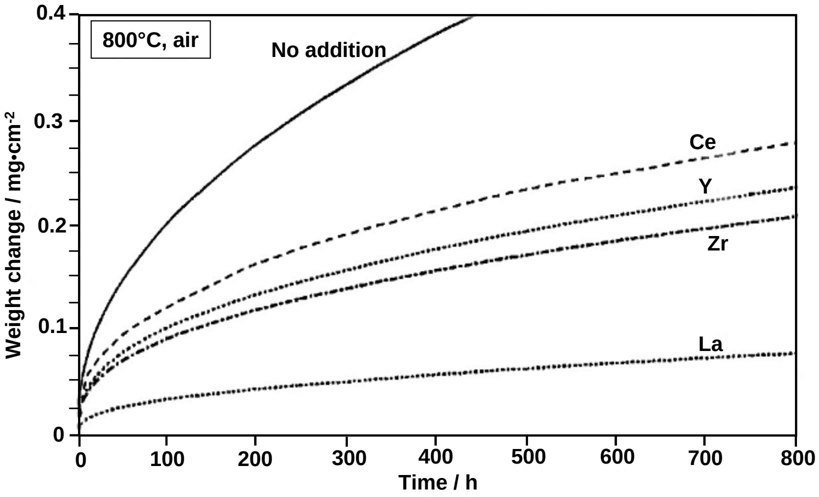

Figure 3.8: Weight change data of wrought Fe-24Cr alloys containing additions of Y, Ce, Zr, or La during oxidation at 800°C in air [Quadakkers-3]

Addition of the reactive elements to the alloy/steel could be carried out through two different alloying methods. Elements could be added into the alloy/steel in the form of pure elements (conventional method) or as oxide dispersions in the material matrix [Quadakkers-3]. The latter alloying method leads to the formation of so-called oxide dispersion strengthened materials (ODS) [Greiner-1, Köck-1]. The main advantage of ODS materials is improved mechanical properties compared to conventionally melted alloys/steels. The main disadvantage is the relatively high price of the material because of the complicated manufacturing process [Tietz-1].

Cr-based alloys for SOFC application

During high temperature exposure pure chromium forms a protective chromia scale. Unfortunately, during air/oxygen exposure the oxide scale formed on pure chromium is not ideally flat [Quadakkers-1]. It was shown by several authors that outward chromium diffusion is a dominant transport mechanism [Graham-1, Cotell-1] and therefore in many cases voids and cavities are formed leading to poor scale adherence and scale spallation. During low oxygen partial pressure exposure (Ar-H_2-H_2O) oxide scales exhibit far better adherence to the metallic substrate than those formed in air or oxygen [Hänsel-1]. This effect could be explained by a similar mechanism as proposed by Rahmel and Tobolski [Ramhel-1] for porous iron oxide scales. Incorporation of water vapour or hydrogen into the scale can cause a rapid re-oxidation of the exposed metal by a dissociation mechanism involving a "H_2/H_2O-bridger" within the voids. In this way crack/pore healing occurs, thus preventing growth of the voids at the metal/scale interface [Quadakkers-1].

Poor oxide scale adherence formed on pure chromium can be improved by the addition of reactive elements especially in the form of oxides (ODS alloys, see section 3.3.2) making alloys more suitable for SOFC application. A good example of an alloy with such an addition is Cr5Fe1Y_2O_3 material developed and produced by Plansee [Greiner-1, Köck-1]. Addition of yttrium oxide into the chromium suppresses scale growth by outward chromium transport, improves scale adherence and reduces oxide scale growth (Figure 3.9). Additionally, oxide dispersion reactive elements substantially improve the mechanical properties of chromium (improvement in ductility). The addition of iron is necessary to adjust the thermal expansion coefficient to as close as possible to that of the ceramic electrolyte material in the case of SOFC application [Greiner-1, Köck-1].

Another Cr-ODS alloy has also been recently reported. The addition of MgO dispersions to chromium appears to increase ductility, however no further data on other mechanical properties of such an alloy have been reported [Brady-1].

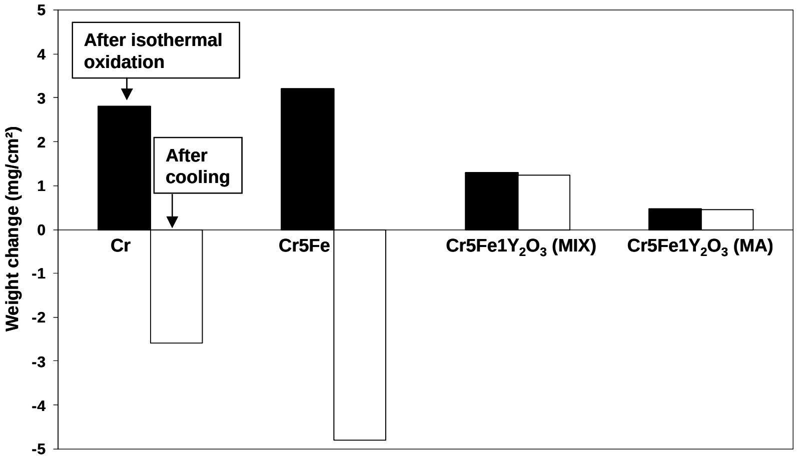

Figure 3.9: Weight change data of various Cr base alloys after exposure at 1000°C in Ar/O_2 showing improvement of scale growth and adherence in case of Cr-ODS alloys [Quadakkers-3]. MIX - elemental mixing, MA - mechanical alloying

One of the most important problems for the application of Cr base alloys for SOFC interconnects is vaporisation of chromium. In air/oxygen exposure chromia tends to form volatile oxides (CrO_3) and/or hydroxides $CrO_2(OH)_2$ [Quadakkers-4, Ebbinghaus-1]. It was reported by several authors [Badwal-1, Batawi-1, Günther-1, Das-1, Hilpert-1] that in the case of SOFC applications volatile chromium species could cause serious cell degradation by poisoning the cathode. Several protection methods have been proposed to minimize evaporation of Cr-species, such as coating of the interconnector with La-chromite [Gindorf-1], or-manganite [Batawi-2], metallic layers [Quadakkers-5], oxide layers [Quadakkers-5] or aluminium surface enrichment to promote alumina surface scale formation on interconnector areas, where electrical conductivity is not a major issue [Quadakkers-5, 6].

Commercial ferritic steels as SOFC interconnectors

Commercially available ferritic steels contain between 7 and 28 wt. % of chromium. In the case of low chromium steels (< 5 wt. %) formation of chromium oxide and/or Fe/Cr-spinel is observed during exposures in air in the temperature range 700 – 1000°C. With increasing Cr content in the steel the oxide scale becomes richer in spinel and when the Cr content exceeds 17-20 wt. %, formation of an exclusive Cr_2O_3 layer is observed (Figure 3.10). It is also necessary to take into account that the Fe-Cr system contains a closed field of a terminal fcc solid solution of Cr in γFe (figure 3.11), which is referred to in the literature as austenite. It means that at temperatures higher than 851°C austenite phase will form if the Cr concentration is smaller than ~ 12 at. % resulting in changes in oxidation resistance as well as thermal expansion coefficients.

The addition of minor alloying elements into the steel also has a great influence on the oxidation behaviour. Manganese, frequently used as a minor addition in the range of a few tenths of a percent, incorporates into the scale forming an exclusive Cr/Mn-spinel layer (figure 3.12). Ti, Si and/or Al also frequently appear as minor alloying additions and often precipitate as internal oxidation zones beneath the external chromia scale, however, Ti can also be dissolved into the chromia, especially at low oxygen partial pressures [Naoumidis-1]. Addition of Al and/or Si by more than 1 wt. % can cause external alumina/silica scale formation instead of internal precipitation.

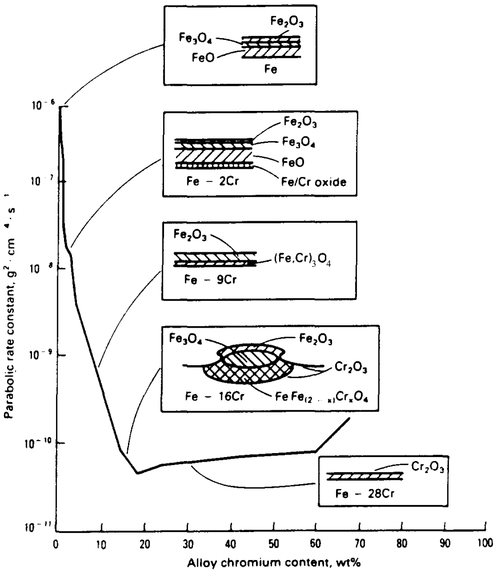

Figure 3.10: Oxidation rate and scale formation of Fe-Cr alloys at 1000°C in 0.13 bar oxygen [Wright-1]

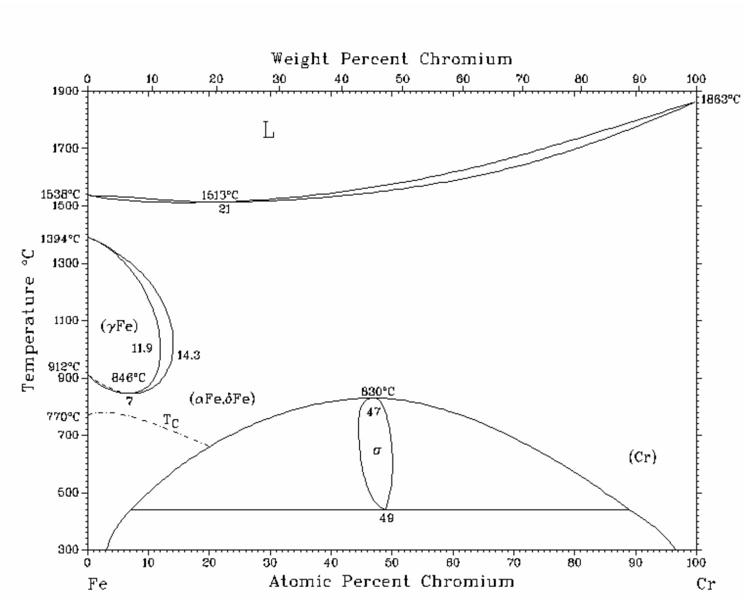

Figure 3.11: Fe-Cr phase diagram [Massalski-1]

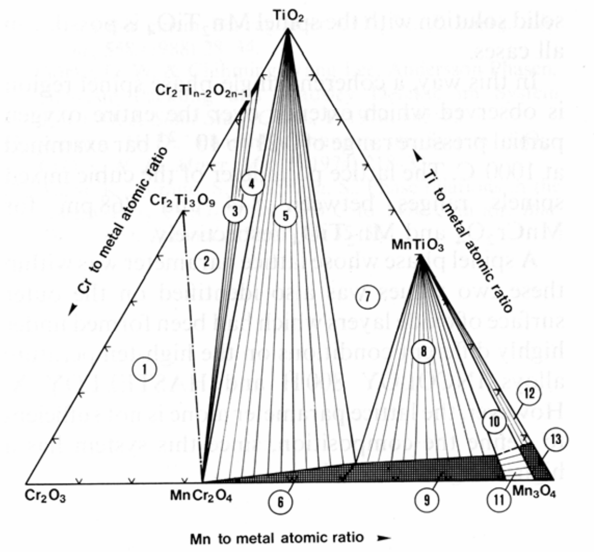

Figure 3.12: Phase equilibria in the quasi-ternary system Cr_2O_3-Mn_3O_4-TiO_2 after annealing at 1000°C in air. White: three-phase regions, radiate-shaded: two-phase regions, dark: one-phase regions [Naoumidis-1]

A change of the test atmosphere from air to the simulated anode side gas (H_2/H_2O) has similar effects for high-Cr steels as described for Cr based alloys [Quadakkers-1]. The morphology of the chromia- and spinel-rich surface layers is slightly modified [Horita-1] and the adherence of the scale is improved [Malkow-1].

The important problem associated with most commercially available ferritic steels in SOFC application is that slight changes in alloy composition, service temperature or design-related parameters can dramatically change the oxidation properties. Additionally, a change from one oxide scale type into another can occur during long-term service due to depletion of the scale forming elements Al, Si, Mn, Ti in the alloy matrix because of their low concentrations [Quadakkers-1]. Therefore, it was necessary to design steels with a special combination of properties for SOFC interconnect applications.

Ferritic steels designed for SOFC application

In recent years, a number of ferritic steels especially for SOFC applications operated in the temperature range 600°C – 800°C have been designed. Quadakkers et al. studied the suitability for interconnector application of model steels with Cr contents of 16-25 % and evaluated the effect of various RE additions to achieve an optimum combination of low scale rate and excellent scale adherence as shown in figure 3.13 [Quadakkers-7, Piron-1-3]. As a result of these studies the semi-commercial JS-3 steel [Piron-3] and the commercial ferritic steel Crofer 22 APU [Hojda-1] were introduced to the market. Crofer 22 APU produced by ThyssenKrupp VDM [Hojda-1] contains ~23 wt. % Cr to obtain a large “Cr-reservoir” for protective chromia scale formation. As a reactive element La was chosen because this element appeared to be most beneficial, mainly because, contrary to other commonly used RE’s, it does not form intermetallic compounds with iron [Quadakkers-1]. Small amounts of Mn and Ti were added to obtain external spinel formation, which is expected to decrease the formation of volatile Cr-species [Piron-1, 3, Gindorf-2] (compare section 3.3.2, Cr-base alloys for SOFC application). Minor Ti additions were added to obtain fine internal oxide precipitates of titania which lead to strengthening of the near-surface region, thus reducing the tendency for occurrence of surface wrinkling caused by relaxation of oxidation-related stresses during thermal cycling [Quadakkers-1].

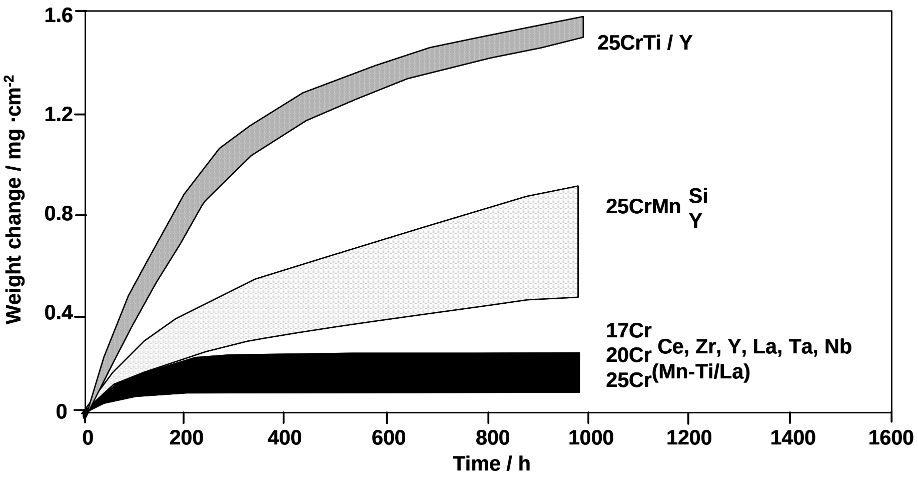

Figure 3.13: Oxidation of model high-Cr steels at 800°C in air [Piron-2]

Ferritic steels for SOFC interconnectors were also designed by Hitachi Metals [Uehara-1, Horita-2, 3]. Steel ZMG232 produced by Hitachi Metals contain high amounts of Cr (~23 wt.%) with Zr as a reactive element and also forms a double protective oxide scale with Cr, Mn-spinel on the top (addition of Mn into the steel).

Further reading for the development of steels, which are especially designed for SOFC application, are described in references [Ghosh-1, Kung-1, Krumpelt-1], however no detailed information of the steel compositions were given.

Recently high-Cr ferritic steels produced by powder metallurgical techniques (ODS alloys) have been reported. Honnegger et al. [Honnegger-1] developed a ferritic material for SOFC application with approximately 20 % Cr. Another example of such material are IT-alloys recently designed by Plansee Aktiengesellschaft [Glatz-1] with systematic variations of minor alloying additions. The latter materials seem to possess better properties in comparison to commercially available, ingot-metallurgical ferritic steels but on the other hand, the relatively high price of these ODS-steels could be a big disadvantage over a traditional method of melting.

Protective coatings for metallic SOFC interconnectors

In evaluating the growth rates and electronic properties of the surface scale of metallic interconnectors, it has to be borne in mind that parts of the interconnectors are in direct contact with the electrodes or with the contact materials.

Most studies concerning compatibility of metallic interconnectors with electrodes or contact materials relate to the cathode side of the cell. Here, in most designs the interconnector is in direct contact with La-based perovskites. Due to the interaction between the interconnector and the perovskite two important processes can occur: change of the oxide composition on the interconnector surface and change in the alloy composition in the surface near region, mainly due to Cr transport into the perovskite [Quadakkers-1].

To prevent interactions between the interconnector and cathode, several authors proposed contact layers containing large amounts of spinel-forming elements such Co or Ni. The dense, Cr-free spinel layer, formed by interdiffusion of manganese, which outwardly diffuses through the chromia scale on the ferritic steels, acts as a barrier against vapour phase transport of volatile chromium oxides and hydroxides [Larrying-1, Piron-3, Zahid-1].

It was also reported that Sr, frequently, present as a dopant in La-manganites, - chromites and - cobaltites, is easily transported from the cathode or contact layer in the direction of the Cr-rich or Cr-based interconnector surface. This effect leads to the formation of compounds of the type $SrCrO_4$ and/or $Sr_3Cr_2O_8$ in the chromia layer and was claimed to be beneficial for the electrical conductivity of the scale [Quadakkers-1].

On the anode side of the cell, the interconnector is in direct contact with a Ni-ZrO_2-cement or Ni-based contacting material. In the case of a ferritic steel, interdiffusion between interconnector and the spot-welded nickel wire mesh will lead to Ni transport into the steel, resulting in local austenite formation and thus the related changes in oxidation resistance as well as thermal expansion coefficient. Vice versa, transport of Fe, Cr and other steel constituents into the wire mesh converts the latter into an alloy, which will form surface oxide layers in the anode-side environment [Quadakkers-1].

3.4 Oxidation kinetics and lifetime prediction of the ferritic steels

As introduced in section 3.2.2, kinetics of oxidation are one of the key features for the material during high temperature service. Kinetics of the protective oxide scale formation limit the time in which a material can be used for its particular application – the lifetime of the material. When, for the various reasons, the protective oxide scale can no longer be formed, a non-protective, fast growing oxide starts to form and this process destroys the high temperature resistance of the material. The above-described phenomenon is known in corrosion science as “breakaway”. Calculations of the material lifetime – prediction of the beginning of breakaway oxidation have been widely studied in recent years especially for the case of alumina forming ferritic steels [Quadakkers-8, 9, Gurrappa-1, Nichols-1].

3.4.1 Lifetime prediction of the alumina forming ferritic steels

Ferritic steels of the type Fe-20Cr-5Al (in wt.%) are among the most oxidation resistant metallic materials because the alumina surface scales which form during high temperature exposure show small growth rates and have excellent thermodynamic stability [Quadakkers-9]. The growth rates of alumina scales on RE-containing, high temperature alloys have often been found to show a large deviation from classical parabolic kinetics [Quadakkers-2] (compare section 3.2.2). This has been explained in most cases by assuming that oxygen grain boundary diffusion is the dominating scale-growth process, in combination with an oxide grain size increasing in the growth direction and perhaps also with time [Liu-1, Hindam-1].

For alumina forming ferritic steels, it was shown that the oxidation limited lifetime of thin components is primarily governed by the Al reservoir in the component [Quadakkers-8, 9]. If growth and re-healing of the oxide scale leads to a decrease in the Al-concentration below a critical level, breakaway oxidation occurs (figure 3.14). Due to the very high oxide growth rates accompanied by this effect, the time at which breakaway occurs, represents the lifetime limit of the component [Gurrappa-1, Nichols-1].

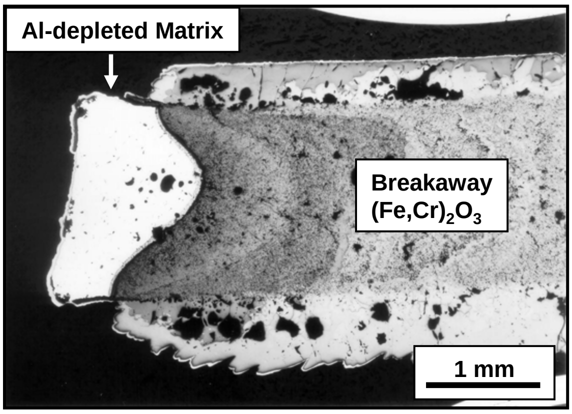

Figure 3.14: Metallographic cross-section showing typical breakaway oxidation on FeCrAl-alloys [Naumenko-1]

Recently, a model was developed which allows the prediction of the time to breakaway oxidation for alumina forming FeCrAl-based alloys as a function of temperature, component thickness and alloy Al content [Quadakkers-8, 9]. In reference [Quadakkers-9], the assumptions and limitations of the model were extensively discussed. Two important simplifying assumptions establish that [Gurrappa-1]:

- Aluminium depletion in the alloy due to scale formation does not result in a clear gradient beneath the scale, but the Al concentration profile in the bulk alloy can be considered to remain ideally flat.
- If scale spallation occures, it leads to spalling over the whole specimen/component surface and reoxidation proceeds as on a fresh surface.

It is now possible to calculate the time to breakaway (t_B) for a flat specimen of thickness d and infinite length and width knowing the initial alloy Al content (C_0), the remaining Al content at time $t(C_t)$, the alloy density (ρ), the oxidation rate constant (k), the oxidation rate exponent (n) and assuming that the surface oxide consists completely of Al_2O_3 (i.e. the Al/O weight ratio is equal to 1.124) [Gurappa-1]:

$$t_B = \left[4.4 \cdot 10^{-3} \cdot (C_0 - C_B) \cdot \frac{\rho \cdot d}{k} \right]^{\frac{1}{n}} \qquad (3.13)$$

In the case of a rectangular specimen of length L, width b and thickness d (all values in cm) equation (3.13) changes to:

$$t_B = \left[4.4 \cdot 10^{-3} \cdot (C_0 - C_B) \cdot \frac{\rho \cdot d}{k \cdot (1 + d/L + d/b)} \right]^{\frac{1}{n}} \qquad (3.14)$$

in which the specimen thickness d is replaced by the factor:

$$\frac{d}{(1 + d/L + d/b)} \qquad (3.15)$$

for considering the total surface area and volume of the specimen. It is of course also possible to make a similar calculation for different specimen shapes taking the correct volume to surface ratios of various types of specimen geometries such a bars or wires into account [Gurrappa-1, Nichols-1].

As explained in references [Quadakkers 8, 9, Gurrappa-1], the alumina scales on the FeCrAl-based alloys become prone to spallation after long term exposure. Assuming that this spallation starts after the oxide thickness reaches a critical thickness x^*, corresponding to a critical weight change Δm^*, the following expression was derived in reference [Quadakkers-9] for the time to breakaway for a flat specimen of infinite size (compare equation 3.13):

$$t_B = 4.4 \cdot 10^{-3} \cdot (C_0 - C_B) \cdot \rho \cdot d \cdot (k)^{-\frac{1}{n}} \cdot (\Delta m^*)^{\frac{1}{n} - 1} \qquad (3.16)$$

Figure 3.15 shows a typical calculation of the lifetime for FeCrAl-alloy base on the equations presented above. The lifetime prediction seems to be in reasonable agreement with the experimental data, showing that, for a given alloy, the Al reservoir decreases with decreasing component thickness, the lifetime will decrease with decreasing component thickness. The above presented calculation is very important from the practical point of view because it gives possible guidelines for lifetime extension of alumina forming FeCrAl-alloys.

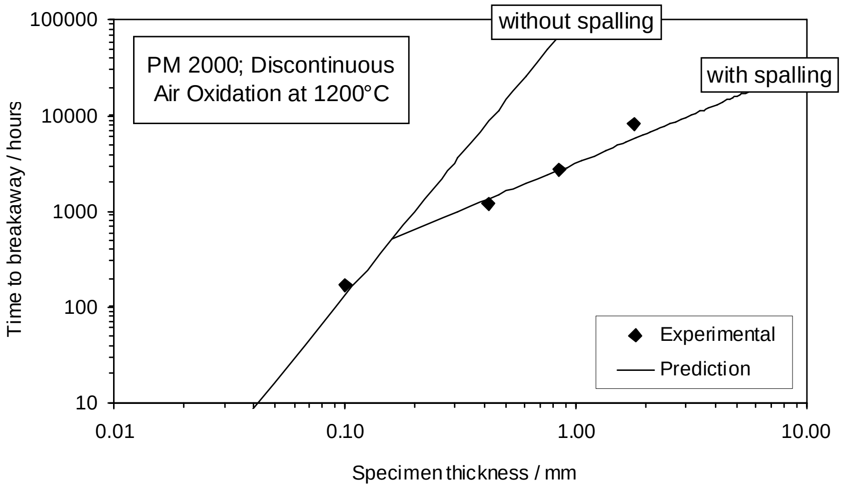

Figure 3.15: Calculated lifetime for FeCrAl-ODS alloy compared with experimental results [Quadakkers-10]

3.4.2 Lifetime limits of chromia forming ferritic steels

Classical Wagner oxidation theory [Kofstad-1] (compare section 3.2.2) predicts that scale growth will obey a parabolic time dependence if oxidation is controlled by diffusion of metal and/or oxygen ions through the oxide lattice:

$$x^2 = k \cdot t \tag{3.17}$$

in which x is the scale thickness, t the time and k the parabolic oxidation rate constant. Expressed as oxygen uptake per unit area (Δm), equation 3.17 is mostly written in the following form:

$$(\Delta m)^2 = K_p \cdot t \tag{3.18}$$

For Cr, Cr-alloys and especially Cr-based ODS-alloys, equation 3.18 is rarely obeyed [Hänsel-1, Rahmel-1, Gil-1] because the assumptions made to describe scale growth by equation 3.18 are mostly not fulfilled [Bongartz-1]. Chromia scale growth proceeds in this case via rapid diffusion paths, such as oxide grain boundaries [Cotell-1, Sabioni-1].

Literature kinetics data in the case of Fe-based chromia forming ferritic steels are contradictory and depend on the exposure atmosphere, temperature, oxidation time and initial chromium content. Extended studied carried out by Wood et al. [Wood-1-4] shows that most of the common growth relations were observed dependent upon of specific alloy type and conditions that were used. However, in order to attempt some form of generalisation, the schematic weight change/time diagram may be used [Wood-1] (Figure 3.16). Under mild conditions, a thin protective film is built up at a declining rate according to the curve OAD. When the atmosphere is somewhat more severe, however, after an initial protective period OA (sometimes referred to as an induction period), there is a sudden increase in rate AB (breakaway). This stage is often followed by a further reduction in rate BC (self-healing) but in some cases where the oxide stays non-protective BE may followed instead [Wood-1].

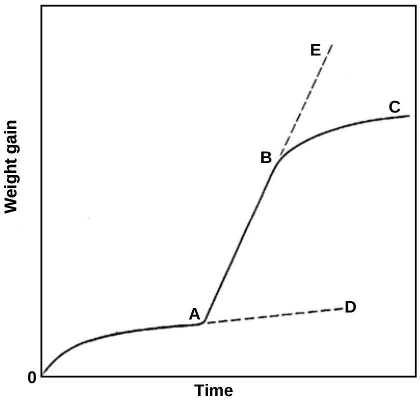

Figure 3.16: Typical growth curves for the oxidation of iron-chromium alloys and stainless steels [Wood-1]

Whittle [Whittle-1] claimed that during the period of oxidation immediately following the nucleation stages, at temperatures in the range of 800°C – 1200°C (oxidation atmosphere: flowing oxygen at 1 atm pressure), virtually pure chromium oxide is formed on Fe-Cr alloys containing greater than about 13 % Cr. Chromia scales formed in this case grew approximately according to a parabolic rate law. In the case of alloys with Cr contents between 13 – 25 wt.% at the higher temperatures (i.e. 1200°C), oxidation rates showed (after an induction period during which Cr_2O_3 is formed) a rapid increase, and a thick stratified scale containing mainly iron oxide replaced the protective scale (breakaway oxidation, compare section 3.4) [Whittle-2].

Two main theories have been proposed to account for breakaway [Whittle-2]. Firstly, a “chemical” mechanism is considered possible [Bandel-1, Edström-1, Menzies-1] where the initial chromium oxide layer is attacked from within by the chromium-depleted alloy and transformed into iron-containing oxides, which then grow rapidly – the chromium concentration at the alloy/oxide interface must be reduced below that necessary for thermodynamic stability of this oxide in contact with the alloy [Whitlle-2].

The second mechanism involves mechanical separation and cracking of the chromium rich oxide from the surface of the alloy [Wood-3, 4], thus exposing fresh, chromium depleted alloy to the hot oxidizing gases. The disruption of the protective scale may be due to one or more factors: ferrite to austenite phase changes in the underlying alloy [Smeltzer-1], grain growth of the alloy [Decroix-1], recrystallization of the oxide [Caplan-1, 2, Yearian-1, 2], void formation at the alloy/oxide interface [Caplan-1, 2] and stress development during scale growth [Wood-3, 4, McCullough-1]. If mechanical rupture of the protective oxide scale occurs, then the exposed chromium depleted alloy can either [Whittle-2]:

- Re-form a Cr_2O_3 scale if the surface chromium concentration of the exposed underlying alloy is greater than that for the formation of Cr_2O_3 at the ambient oxygen pressure.
- Form less protective oxides, such as spinel, allowing rapid scaling to ensure.

From the overview presented above it is clearly visible that the lifetime of the chromia forming alloys depends on the chromium reservoir [Otsuka-1], similar to aluminium in the case of FeCrAl-alloys (compare section 3.4.1). However, practically no literature data has been found regarding the lifetime prediction of chromia forming ferritic steels.

3.5 Electrical conductivity of chromia

For SOFC application not only the electrical conductivity of the interconnector material itself is of great importance, but also that of the chromia-based scales which form on the surface parts of the interconnector which are in direct contact with the electrode materials or, depending on the stack design, with the contacting materials [Quadakkers-1].

3.5.1 Electrical conductivity - introduction

When an electric field E, is applied across a crystal, a force is exerted on the charged particles. If an ion or a defect has a charge q_i, the force, F_i, is given by [Kofstad-2]:

$$F_i = q_i \cdot E \qquad (3.19)$$

This force causes directional transport of the charged particles in addition to their random thermal motion. The resulting current density is given by:

$$I_i = \sigma_i \cdot E \qquad (3.20)$$

where σ_i is the conductivity of particles of type i. Equation 3.20 is an expression of Ohm's law.

If a crystal contains different types of charge carriers, the total current density I, is given by:

$$I_i = \sigma \cdot E \qquad (3.21)$$

where σ represents the total electrical conductivity.

The electrical conductivity is given by the sum of the conductivity due to electrons and holes. In the case of nonstoichiometric oxides two main behaviours of the electrical conductivity could be described: intrinsic and extrinsic.

In the intrinsic region of nonstoichiometric oxides, either electrons or holes will predominate, and the oxygen pressure dependence of the electronic conductivity will be determined by that of the concentration of the predominating electronic charge carrier. In this case n=p and the electrical conductivity is independent of the oxygen pressure.

In the extrinsic region it will often be necessary to consider the conductivity of both electrons and holes, and the electronic conductivity may change from n- to p-type conductivity with a change in oxygen pressure [Kofstad-2].

The temperature dependence of the electrical conductivity is shown in equation 3.22:

$$\sigma T = f \exp\left(\frac{-E_a}{RT}\right) \qquad (3.22)$$

where f is pre-exponential constant, E_a is activation energy, R is universal gas constant, and T is temperature [Kofstad-2]. Thus, in evaluating the activation energy associated with the diffusion coefficient from conductivity measurements, it is necessary to plot $\ln(\sigma T)$ vs. $1/T$ [Kofsted-2] (compare figures 3.17, 3.18 and 7.3).

Practically, electrical conductivity can be calculated using the following equation:

$$R = \rho \cdot \frac{L}{A} \tag{3.23}$$

where R is an electrical resistance (in Ω), L is the length of the specimen (in cm) and A is the surface area of the specimen (in cm^2). ρ (in $\Omega \cdot cm$) is an electrical specific resistance of the material and it is inversely proportional to the electrical conductivity.

$$\rho = \frac{1}{\sigma} \tag{3.24}$$

In the case of thermally grown oxide scales the data for electrical properties presented in the literature are often shown as area specific resistance or contact resistance (ASR, in $\Omega \cdot cm^2$) illustrated by equation (3.25):

$$ASR = R \cdot A = \rho \cdot L \tag{3.25}$$

which can be easy transferred to electrical conductivity σ if the thickness of the oxide scale (L) is known:

$$\sigma = \frac{L}{ASR} \tag{3.26}$$

3.5.2 Electrical conductivity of bulk chromium oxide

The electrical conductivity of chromium oxide may be divided into two main temperature regimes:

- High temperature region (>1000°C) [Park-1, Holt-1, 2] in which intrinsic behaviour is observed and the electrical conductivity is claimed to be independent of the oxygen partial pressure.

- Lower temperatures (<1000°C) [Holt-1-4] in which the concentration of electronic defects due to intrinsic electronic equilibrium becomes so small that chromia changes into an extrinsic electronic conductor, the electronic conductivity being dominated by the presence of impurities or dopants.

Figure 3.17 presents a literature overview of the electrical conductivity of bulk chromia (the most common way of plotting as log (σT) vs. 1/T has been chosen), showing large discrepancies in the conductivity data for lower temperatures (< 1000°C).

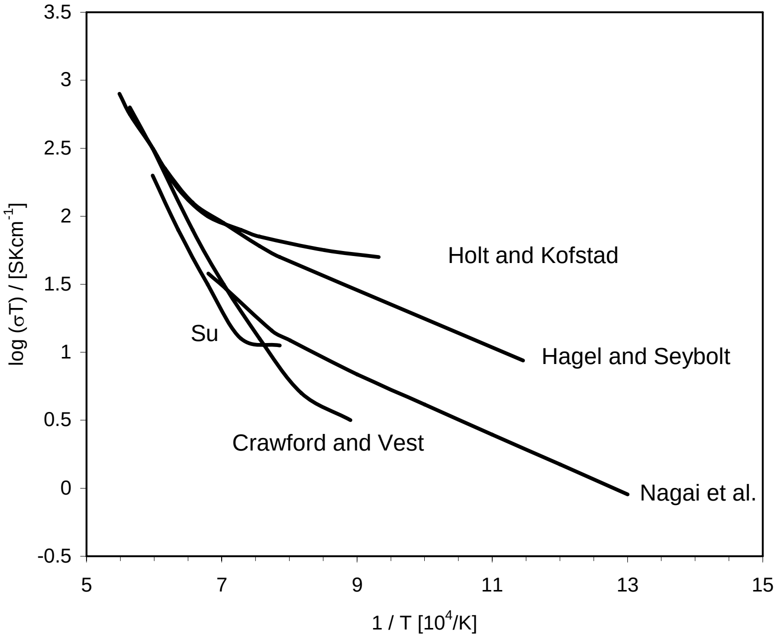

Figure 3.17: Literature data for the electrical conductivity of chromia [Holt-1, 2, Su-1, Crawford-1, Hagel-1, Nagai-1]

Several authors investigated the doping effect of chromia as shown in the figure 3.18. Below 1000°C, Mg doped chromia was found to be a p-type conductor, whereby the electronic conductivity only marginally depends on oxygen partial pressure [Holt-2]. In H_2/H_2O mixtures the conductivity is affected by dissolved protons [Holt-2, 3]. In the temperature range 400-1000°C Ti doped chromia is an n-type conductor at low oxygen partial pressure and a p-type conductor at near atmospheric oxygen partial pressure. No effect of hydrogen on conductivity was detected in TiO_2 doped chromia [Holt-4]. Nagai et al. [Nagai-1-3] found doping by Y_2O_3 and La_2O_3 to increase the electronic conductivity of chromia (Figure 3.18). It decreases with increasing oxygen partial pressure, although this effect is not very pronounced, especially at high temperatures. The strongest increase of the conductivity was observed for doping by NiO (Figure 3.18), whereby in this case no oxygen partial pressure dependence was found. Also doping by CeO_2 or Fe_2O_3 increased the conductivity, however the effect was much smaller than that observed for NiO-doping [Quadakkers-1].

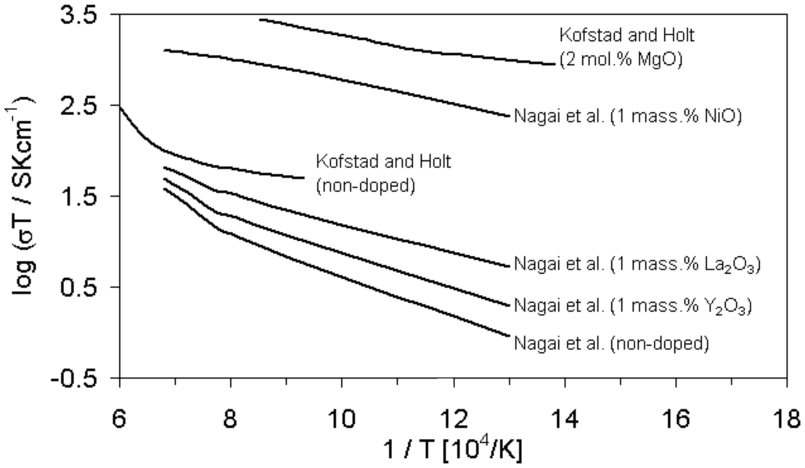

Figure 3.18: Literature data for the electrical conductivity of chromia [Holt-1-4, Nagai-1-3]

3.5.3 Electrical conductivity of thermally grown chromia

Several authors investigated the electrical conductivity of thermally grown chromia scales on metallic materials, with and without surface oxide coatings [Chen-1, Tietz-2, Piron-1, 2, Huang-1, 2, Larring-1, 2, Zhu-1, 2, Yang-1, 2, Horita-2, 3]. Piron et al. [Piron-2] investigated the contact resistance at 800°C of several FeCrMn(Ti/La) model alloys and compared the results with commercially available high Cr-steels as show in figure 3.19. The contact resistances of model high Cr-steels with Mn, Ti and La additions are lower than commercially available ferritic steels. This is probably caused by the doping effect of the chromia which is of significant importance when considering the electronic conductivities of the oxide scales formed on commercial metallic materials because their surface oxides do not frequently consist of pure chromia but they may be doped with major and/or minor alloying elements as well as impurities. Besides, the surface scales on the mentioned materials are in many cases not single-phase but may contain additional oxides, e.g. of the spinel type, adjacent to the chromia [Quadakkers-1]. In the case of the commercial 18%Cr alloy (1.4742) the alumina layer that formed explains the very high ASR of the oxide scale.

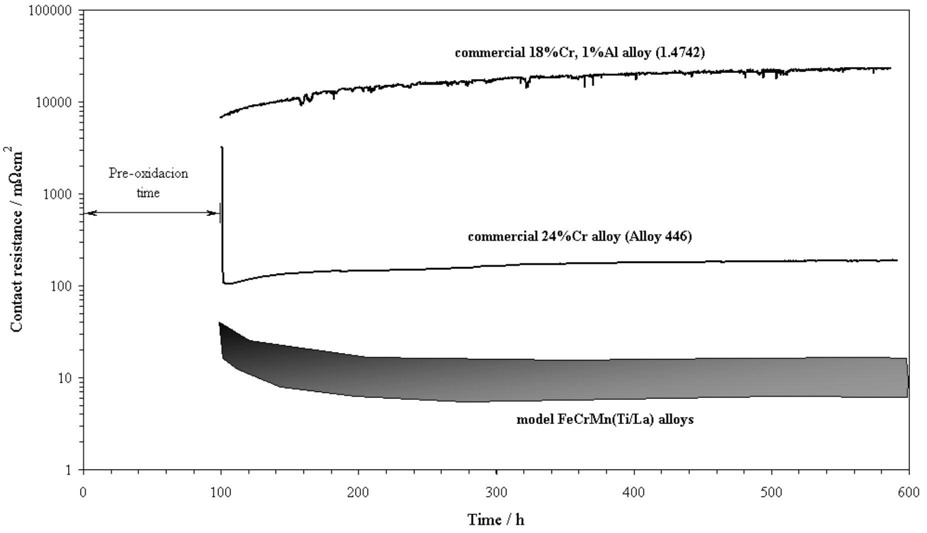

Figure 3.19: Contact resistance of various steels during isothermal exposure at 800°C in air [Piron-2]

Huang et al. [Huang-1, 2] studied the effect of various reactive-element coatings on the oxidation behaviour of commercial chromia forming, iron based alloys and found that in some cases the use of a coating can reduce the contact resistance of the oxide scale. Larring et al. [Larring-1] investigated the effect of water vapour and presence of a Ce-coating on the electronic conductivity of the oxide scale formed on Cr-ODS alloys. They found that the measured conductivity after oxidation increased with increasing water vapour partial pressure and decreasing temperature used in the oxidation. It was also shown that the use of an LSM+LSC coating can be beneficial for obtaining high electrical conductivity values [Larring-2].

3.6 Summary of the literature review

Fuel cells are one of the most promising candidates to partially replace conventional power generation systems because they are very attractive from both energy and environmental standpoints.

High temperature alloys seem to be good candidates for SOFC interconnectors because of their low cost and ease of fabrication compared to ceramic materials.

Specially designed, Fe-based chromia forming ferritic steels can fulfil most of the SOFC interconnector requirements, however, further work is necessary to fully understand and subsequently optimise the behaviour of the mentioned materials under SOFC operating conditions.

In many cases SOFC market requirements (i.e. automotive industry) force the reduction of the fuel cell size and thus the interconnector thickness. Therefore, it is necessary to investigate the behaviour of thin interconnector components during high temperature service.

A model, which allows the prediction of the time to breakaway oxidation as a function of component thickness for alumina forming FeCrAl-based alloys has been widely studied in recent years. It is advisable to elaborate a similar model for the Cr-forming ferritic steels.

The literature data for electrical conductivity of chromia are ambiguous especially in the case of lower temperatures (< 1000°C), therefore further studies would be necessary to understand the electronic properties of the chromium oxide actually formed on ferritic steels.

4. Experimental

4.1 Materials

For the oxidation experiments several high chromium ferritic steels were used as listed in table 4.1. The first main group of these materials was commercial and semi-commercial steels with Cr contents between 16 – 25 wt.%. The second main group of the materials was model high Cr steels. Additionally pure (99.96 wt.%) chromium and a Cr-ODS alloy (Cr, 5Fe, $1Y_2O_3$) [Greiner-1, Köck-1] were incorporated into the test program. The detailed chemical compositions analyzed by Inductively Coupled Plasma Atomic Emission Spectroscopy (ICP-AES) for each of the studied steels is listed in Table 10.1 and 10.2 in the Appendix.

4.2 Specimen preparation

For most of the oxidation experiments, samples of 20x10 mm or 10x10 mm were cut from the delivered plates and ground to 1200 grit surface finish using SiC grinding paper. In the case of very “surface-sensitive” analytical techniques (SNMS, compare section 4.3.4) specimens were polished to 1 μm surface finish using a diamond polishing paste. Depending on the requirements of the experimental set-up, in some of the specimens a 2 mm hole close to the specimen edge was drilled. In order to determine a thickness dependence behaviour of the investigated materials (compare section 6) a couple of specimens with a different initial thickness were used. For some of the materials, plates with a different initial thickness already existed (i.e. Crofer 22 APU) however in some cases it was necessary to grind thick components to the required levels. For most of the “thickness dependence” experiments thick (2-1 mm) medium (~0.5 mm) and thin (0.3-0.1 mm) specimens were prepared. In the case of experiments where component thickness was not a priority feature (compare section 5) samples with ~ 2 mm thickness were used. Before oxidation all specimens were degreased using ethanol in an ultrasonic cleaner.

Steel	Melting variation	Batch name	Composition (wt. %)							
			Fe	Cr	Mn	Ti	La	Si	Al	Others
JS-3	-	JEX	Bal.	23.3	0.4	0.047	0.089	0.009	0.005	
JS-3	-	JEW	Bal.	22.9	0.4	0.046	0.087	≤0.01	≤0.01	
Crofer 22 APU	Crofer A1)	JDA	Bal.	22.5	0.42	0.05	0.075	0.1	0.12	
Crofer 22 APU	Crofer A1)	JMB	Bal.	23.1	0.4	0.08	0.074	0.073	0.12	
Crofer 22 APU	Crofer A1)	JMC	Bal.	22.6	0.4	0.072	0.07	0.056	0.12	
Crofer 22 APU	Crofer A1)	JMD	Bal.	23.0	0.4	0.076	0.077	0.067	0.12	
Crofer 22 APU	Crofer B1)	JZF	Bal.	22.2	0.46	0.055	0.07	0.026	0.022	
Crofer 22 APU	Crofer B1)	JZN	Bal.	22.2	0.47	0.066	0.072	0.028	0.021	
Crofer 22 APU	Crofer B1)	KCB	Bal.	22.2	0.45	0.065	0.096	0.014	0.011	
ZMG232	-	HXT	Bal.	22.1	0.48	-	<0.01	0.36	0.19	Zr: 0.13
Alloy 446	-	HNK	Bal.	24.9	0.5	<0.005	<0.01	<0.01	-	
1.4509	-	HLH	Bal.	18	0.38	0.12	-	0.7	0.03	
1.4016	-	HMM	Bal.	16.3	0.19	<0.01	-	0.25	<0.02	
1.4016-C3	-	HMP	Bal.	16.2	0.29	<0.01	-	0.41	<0.02	
Model steel FeCrLa	-	HCE	Bal.	25.2	-	1)	0.42	-	1)	
Model steel FeCrMnY	-	HCH	Bal.	25.4	1.55	-	-	-	-	
Pure Cr	-	CSX	-	Bal.	-	-	-	-	-	
Fe5Cr1Y_2O_3 (ODS)	-	DCU	4.9	Bal.	-	-	-	-	-	
Fe5Cr1Y_2O_3 (ODS)	-	DCV	4.8	Bal.	-	-	-	-	-	
Model steel (JS-3 base)	-	JLV	Bal.	23.3	0.38	0.049	0.06	0.12	≤0.01	
Model steel (JS-3 base)	-	JLT	Bal.	23.4	0.36	0.048	0.11	≤0.01	0.14	

1) Compare paragraph 5.3.5

Table 4.1: List of steels used for oxidation experiments

4.3 Experimental procedures for oxidation testing

The experimental work was concentrated on the conditions which simulated the cathode side of the fuel cell, therefore, most of the experiments were performed in laboratory air.

Cyclic oxidation studies were chosen to simulate the behaviour of the steels for mobile (automotive) application. Non-continuous operation in such a case is a standard operation condition.

The standard temperature for SOFC operation is known to be about 800°C [Piron-2, Singhal-4], however higher temperatures are also applied [Minh-1]. Therefore 800°C as well as 900°C was chosen for long-term cyclic oxidation studies to simulate the standard and border conditions for SOFC operation. Moreover, during exposures at higher temperature (i.e. 900°C) it is possible to investigate the catastrophic oxidation behaviour after relatively short times, which can be used for the prediction of the oxidation behaviour at lower temperatures (i.e. 800°C).

At first, several “SOFC applicable” high-Cr ferritic steels were chosen as listed in Table 4.1 (classical and specially designed for SOFC interconnections). The steels were investigated during cyclic long-term oxidation experiments and the most promising materials were chosen for further investigations – short term and long term exposures to determine the oxide growth mechanism (compare sections 4.3.1 – 4.3.5 and 5).

The second group of oxidation experiments lead to determine the lifetime of selected materials with a different initial thickness. For these experiments cyclic long term exposures were also chosen, as most typical for standard stack operation (compare sections 4.3.1, 4.3.5 and 6).

The last part of the experiments was concentrated on the evaluation of the electrical conductivity of the thermally grown chromia oxide scales and other chromium containing oxides (compare sections 4.3.6 and 7).

4.3.1 Cyclic long-term oxidation studies

Cyclic oxidation tests (each cycle consisted of 2 h heating and 15 min cooling) were carried out at 800°C and 900°C in laboratory air. For the oxidation experiments vertical furnaces with mobile specimen holders were used as shown in figure 4.1. During each cooling step air was blown on to the specimens (see figure 4.1 c) to minimize the cooling time. Mass change measurements were conducted every 36 hours and the specimens were visually inspected for the occurrence of breakaway oxidation.

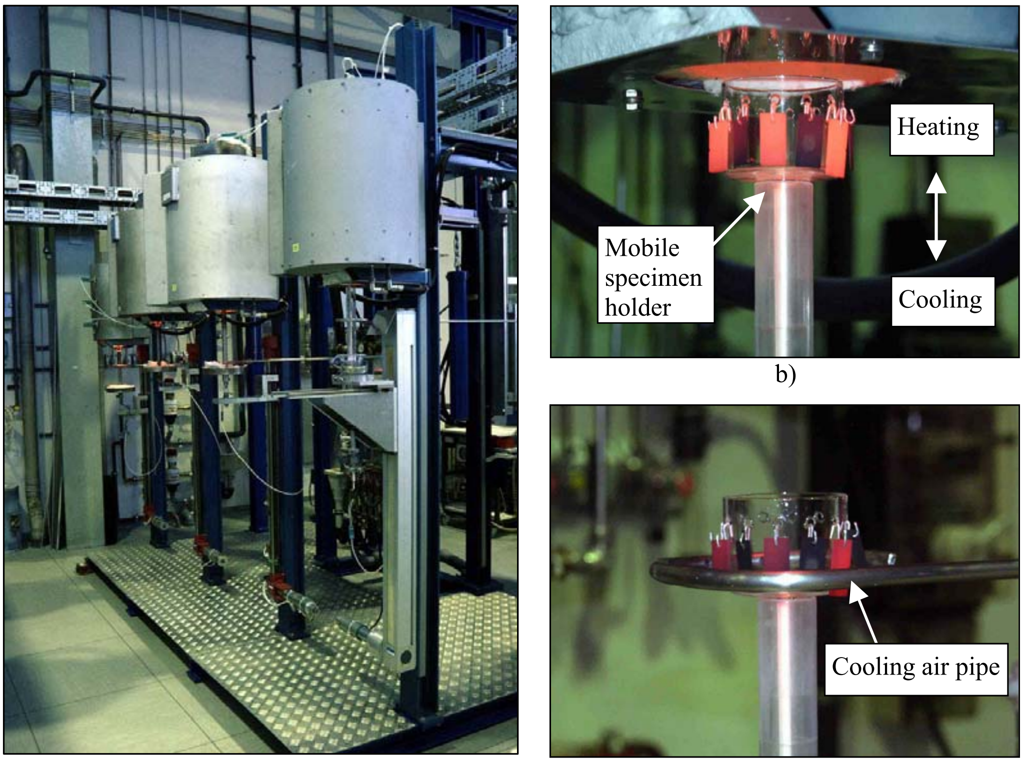

a) b) c)

Figure 4.1: Experimental set up for the cyclic long-term exposures
a) vertical furnaces for cyclic exposures
b) specimens arrangement - start of the cooling step
c) cooling of the specimens

4.3.2 Thermogravimetry (TG)

In order to perform short-term isothermal oxidation studies with full monitoring of the weight change behavior of the specimen, thermogravimetry (TG) techniques were used. For these experiments a SETARAM® microbalance was used. The heating/cooling rates were 90°C/min, the flow rate of the gas was 2 l/h. All experiments were performed during 72 or 100 h oxidation tests in synthetic air and wet air (synthetic air + 7 wt % H_2O).

4.3.3 Discontinuous long-term oxidation studies

Discontinues long-term oxidation tests were carried out at 800°C in laboratory air for 1000/6000 hours. Mass change measurements were carried out every 250 hours (cooling to room temperature) and the specimens were visually inspected for the occurrence of breakaway oxidation.

4.3.4 Isothermal oxidation studies for SNMS investigations

Short term, isothermal experiments (ranging from 1 min to 100 h) were carried out at 800°C in laboratory air whereby the main emphasis was oxide scale formation mechanisms during the early stages of oxidation. For these studies, samples of 10x10x2 mm were cut and subsequently polished to a 1 μm surface finish. After single-stage and two-stage oxidation exposures (the latter using ^{18}O-tracer) the specimens were investigated by Secondary Neutral Mass Spectrometry (SNMS, compare sections 5.3.2 and 7.2).

4.3.5 Short-term isothermal / cyclic oxidation studies

In order to compare short-term isothermal / cyclic oxidation behaviour selected steels were oxidized during isothermal and parallel cyclic 100 h oxidation tests in laboratory air. Thick (2 mm) as well as thin (0.3 mm) specimens were used to determine the importance of cycles and thickness on oxidation behaviour. For cyclic oxidation testing each cycle consisted of 2 h heating and 15 min cooling (compare sections 4.3.1 and 6.1.3).

4.3.6 Contact resistance experiments

The contact resistances of the oxide scales were measured using a conventional four point method. For these studies, specimens of 10x10x2 mm were ground to 1200 grit surface finish and then pre-oxidised for 100 h at 800°C in air. Subsequently, a layer of Pt or Au-paste was applied to both oxidized surfaces. For the electrical connection a Pt-mesh was used. An alumina cover and a 35 g weight were applied to the top of each specimen to force better connection to the platinum mesh. The contact resistance was monitored in-situ at a constant current (100 mA /cm^2) during 300/1000 h exposure at 800°C in air and subsequently during step-wise cooling to 750°C, 700°C, 650°C and 600°C whereby each temperature stage was run for 10 h. Experimental set-up and typical conductivity/temperature curves are shown in figures 4.2 and 4.3, respectively.

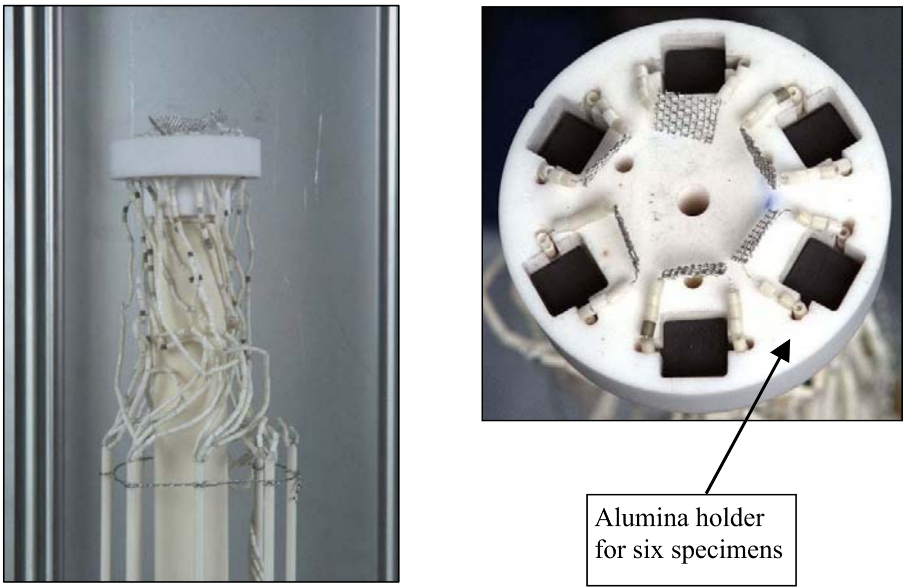

a) b)

Figure 4.2: Experimental set up for the conductivity tests

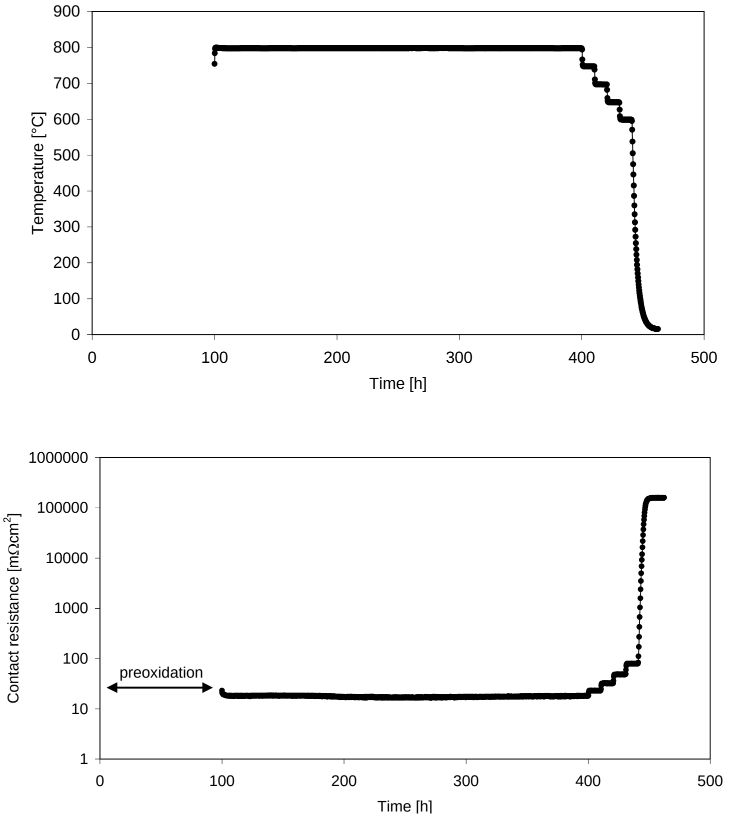

Figure 4.3: Typical course of contact resistance/temperature curves during conductivity experiments

4.4 Microstructural analysis

The oxide scales formed during the different types of oxidation testing were studied using a variety of techniques commonly used in material science. These included light optical microscopy, scanning electron microscopy (SEM) with energy dispersive X-ray analysis (EDX), X-ray diffraction (XRD), secondary neutral mass spectrometry (SNMS), transmission electron microscopy (TEM) and Raman spectroscopy (RS Dilor HR 800 equipped with a He-Ne laser, =632.8 nm). The application of the above methods for the study of thermally grown oxide scales has been described elsewhere [Khanna-1]. Procedures used for quantification of the SNMS profiles of oxide scales are given in reference [Pfeifer-1]. Before mounting for metallographic cross section analyses, the specimens were sputtered with a thin gold layer and subsequently electroplated with nickel. This coating provided protection of the surface oxide layer during grinding and polishing and it ensured better optical contrast between oxide and mounting material.

4.5 Noble metal coatings

In order to determine the platinum effect on oxidation behaviour selected materials were oxidized during two-stage exposure where after the first step, one side of the sample was sputtered with platinum. Specimens with platinum layers were oxidized during the second step using ^{18}O-tracer gas. In the final stage specimens were investigated by Secondary Neutral Mass Spectrometry (SNMS, compare section 7.2). Platinum coatings were manufactured using Radio Frequency (RF) Magnetron Sputtering in a commercial device (Classic 500 by Pfeifer Vacuum). The MS – sputtering facility was a coaxial magnetron with a 51 mm diameter target. The target was made of Pt supplied by MaTeck GmbH.

Results and discussion

5. Growth mechanisms of oxide scales on ferritic steels for SOFC application

5.1 Cyclic long-term oxidation behaviour of thick components

Based on previous investigations [Piron-2], a number of high chromium ferritic steels as SOFC interconnector candidates were selected for long-term (cyclic) oxidation studies. The initial Cr concentration in these materials varied between 16 and 23 wt. % (Table 4.1). In the following studies thick specimens were investigated (initial thickness between 1-2 mm). For the oxidation experiments the temperatures of 800 and 900°C were chosen (see section 4.3).

5.1.1 Cyclic oxidation behaviour at 800°C

Figure 5.1 shows the oxidation behaviour of the selected ferritic steels during cyclic oxidation at 800°C in air. All investigated materials show relatively small weight changes, however the best oxidation protection seems to have been steel JS-3. Metallographic cross-sections of the investigated materials are presented in figure 5.2. Steels JS-3, Crofer 22 APU (A and B, compare section 5.3.5), ZMG232 and 1.4509 show excellent adhesion of the oxide scale to the metallic substrate and a well-developed internal oxidation zone. In the case of Alloy 446 and the two steels 1.4016 and 1.4016-3C, gaps between oxide scale and metallic substrate were observed, however no indication of oxide scale spallation was found.

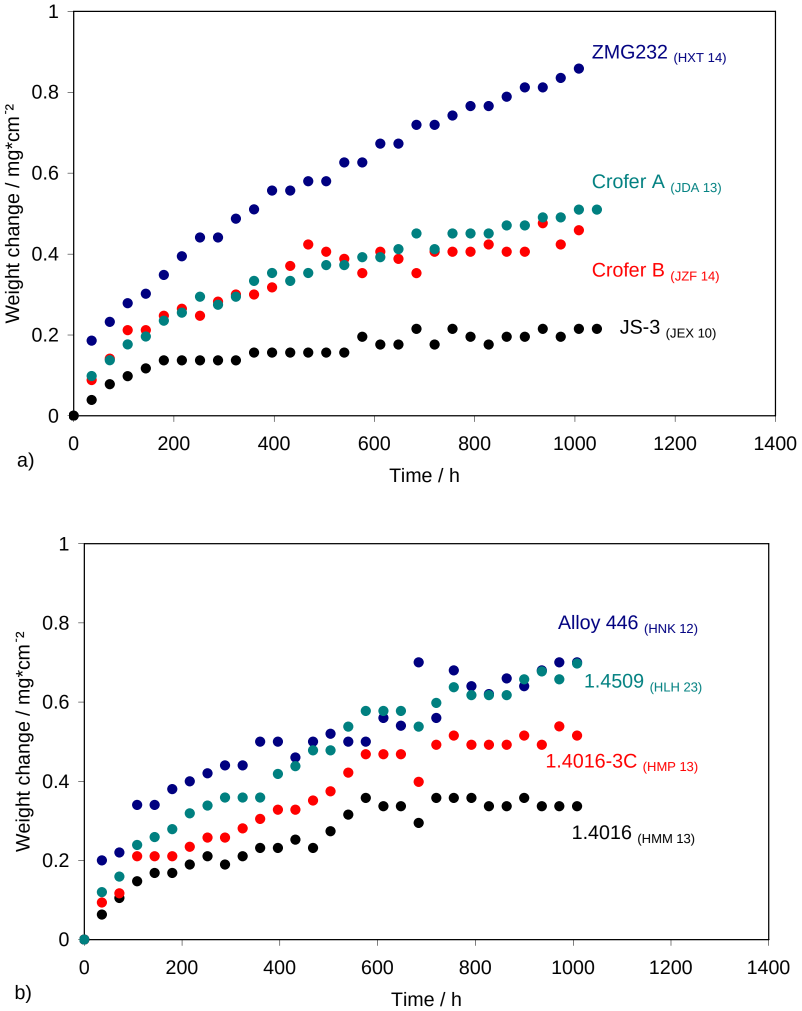

Figure 5.1: Weight change of different ferritic steels (thick specimens, initial thickness between 1-2 mm) during cyclic oxidation at 800°C in air

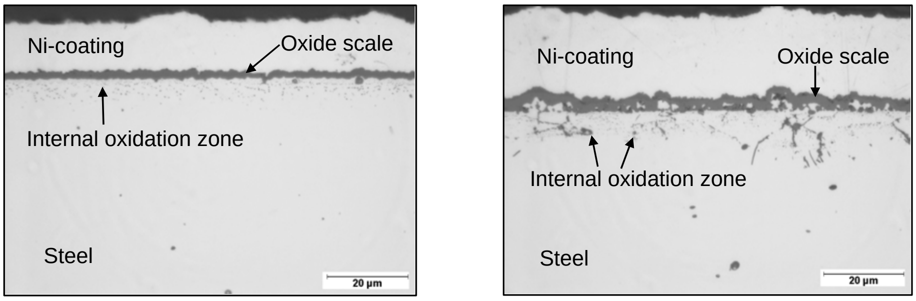

a) JS-3 (JEX 10) b) Crofer A (JDA 13)

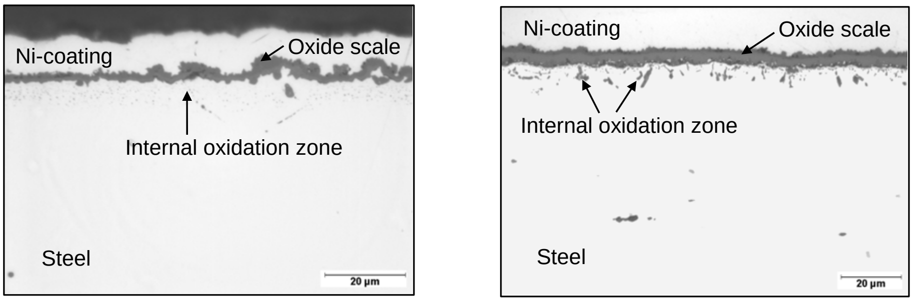

c) Crofer B (JZF 14) d) ZMG232 (HXT 14)

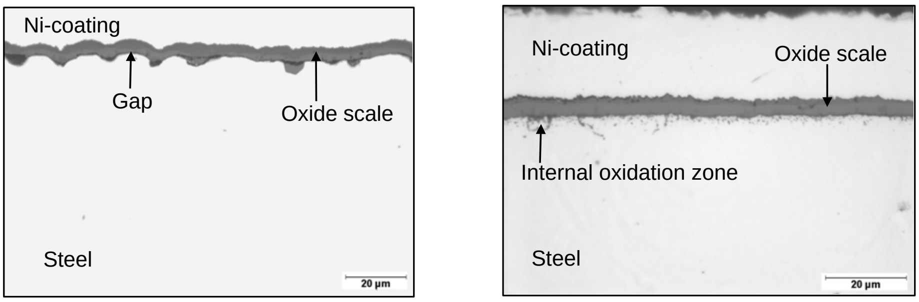

e) Alloy 446 (HNK 12) f) 1.4509 (HLH 23)

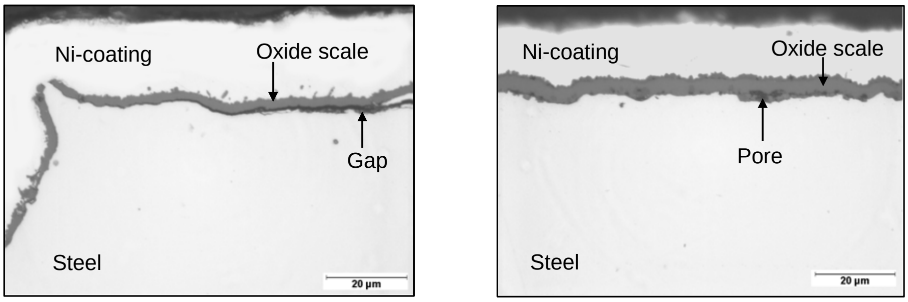

g) 1.4016 (HMM 13) h) 1.4016-C3 (HMP 13)

Figure 5.2: Metallographic cross-sections of various high-Cr steels after 1000 h cyclic oxidation at 800°C in air

5.1.2 Cyclic oxidation behaviour at 900°C

Figure 5.3 presents weight change results of the selected high chromium steels during cyclic oxidation at 900°C in air. In accordance with the 800°C oxidation test, steel JS-3 showed the lowest weight change data. The results presented in figure 5.3 b clearly indicate oxide scale spallation after relatively short times of a few hundred hours for steels 1.5409 and Alloy 446 or breakaway oxidation in case of the steels 1.4016 and 1.4016-3C.

Corresponding metallographic cross-sections of the studied materials are presented in figure 5.4. Steels JS-3, Crofer 22 APU and ZMG232 show good oxide scale adhesion to the metallic substrate and a well-developed internal oxidation zone. Steel JS-3 and Crofer B showed flat and relatively thin scales with TiO_2 as an internal oxide. Two other steels (Crofer A and ZMG232) show evidently thicker scales with Al_2O_3 as an internal oxidation zone and inclusions of SiO_2 at the oxide-metal interface (figure 5.4 b, d). The latter two steels also show characteristic metal inclusions within the oxide scale especially in places where large agglomerations of Al_2O_3 in the internal oxidation zone was formed.

Metallographic cross-sections of Alloy 446 and steel 1.4509 also presented in figure 5.4 show substantial spallation of the oxide scale from the metallic substrate, confirming the weight change results presented in figure 5.3. In the case of steels 1.4016 and 1.4016-3C, the protective Cr-rich oxide scale is totally destroyed within a few hours, forming Fe-rich oxide with thickness of about 100 µm.

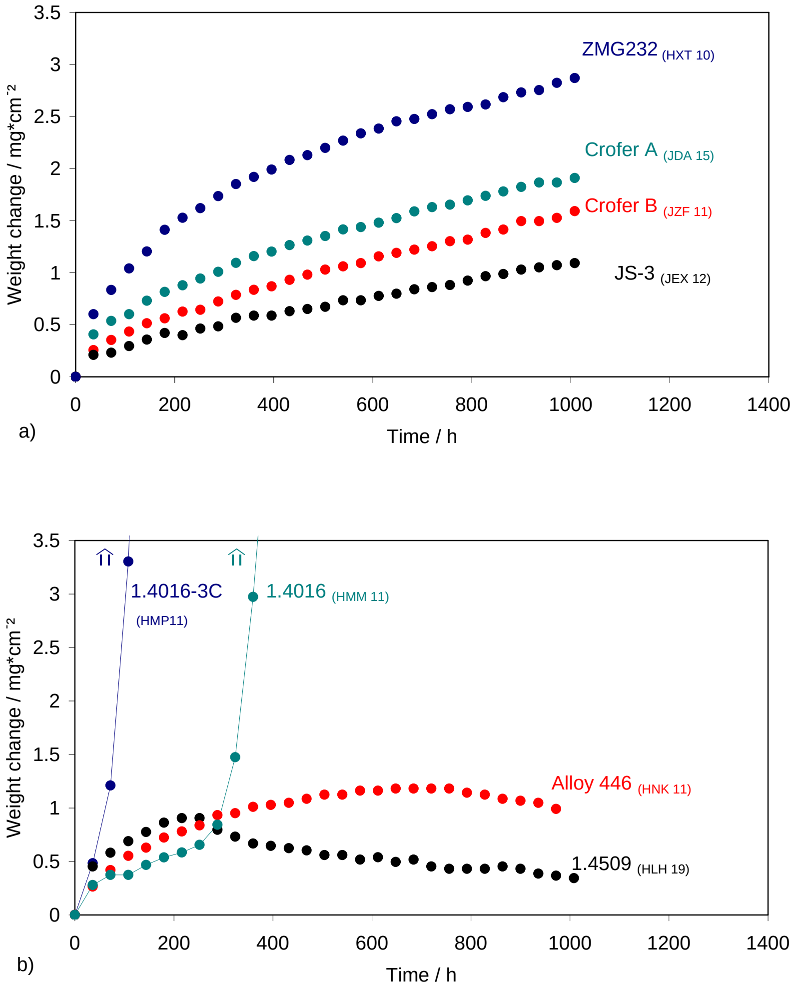

Figure 5.3: Weight change of different ferritic steels (thick specimens, initial thickness between 1-2 mm) during cyclic oxidation at 900°C in air

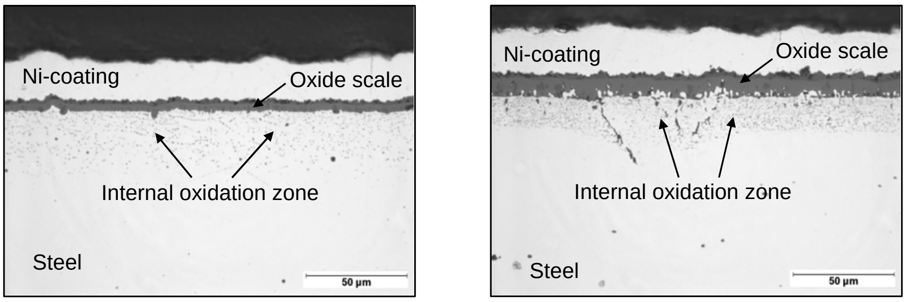

a) JS-3 (JEX 12) b) Crofer A (JDA 15)

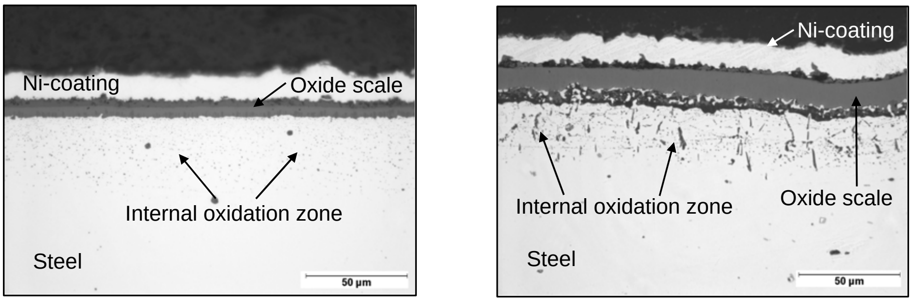

c) Crofer B (JZF 11) d) ZMG232 (HXT 10)

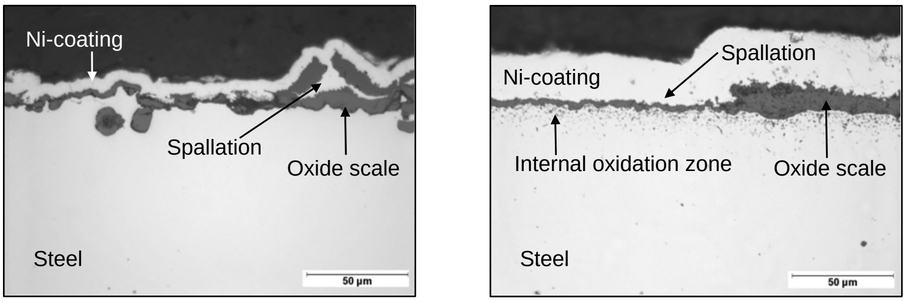

e) Alloy 446 (HNK 11) f) 1.4509 (HLH 19)

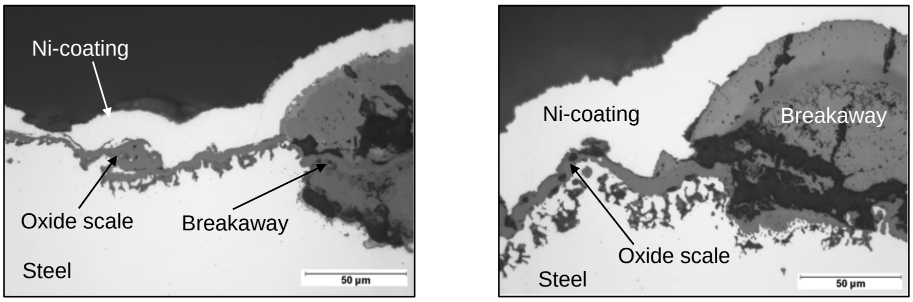

g) 1.4016 (HMM 11) h) 1.4016-C3 (HMP 11)

Figure 5.4: Metallographic cross-sections of various high-Cr steels after cyclic oxidation at 900°C in air (oxidation time 1000 h, HMM 11 and HMP 11 oxidation up to breakaway)

5.2 Selection of the steels for further investigations

The cyclic oxidation results revealed that the most promising steels in respect to oxidation behaviour are JS-3 / Crofer 22 APU type materials. At both studied temperatures, the steels showed the lowest oxidation rates without spallation of the oxide scale. In respect to results obtained so far the JS-3 / Crofer 22 APU type steels were selected for further, detailed investigations. For most of the oxidation tests only Crofer A was used because Crofer B was developed and delivered in the final stage of the laboratory studies as a result of investigations presented in the thesis (compare section 5.3.5).

5.3 Oxidation mechanism of JS-3 / Crofer 22 APU type steels

5.3.1 Long-term oxidation behaviour

A typical example of the differences in a oxidation rates of Crofer A and JS-3 is presented in Figure 5.5, showing that Crofer A exhibits a much higher oxidation rate than JS-3.

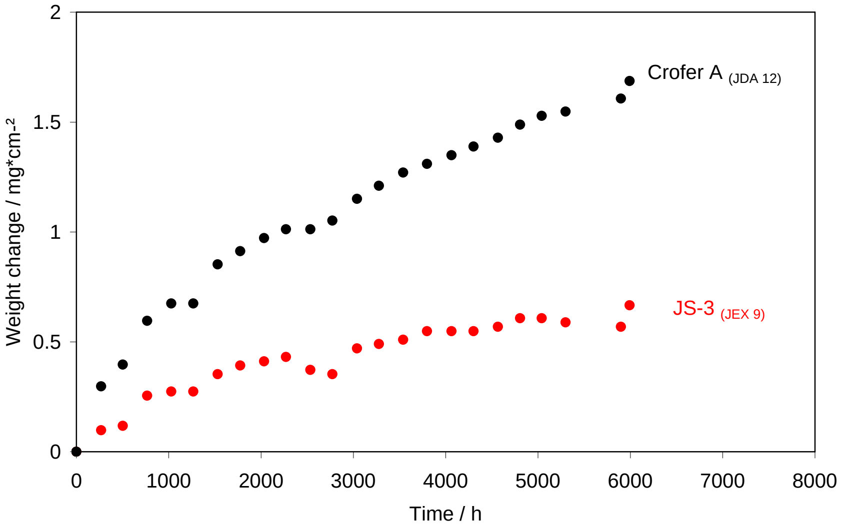

Figure 5.5: Mass change during discontinuous oxidation of steels JS-3 and Crofer A at 800°C in air

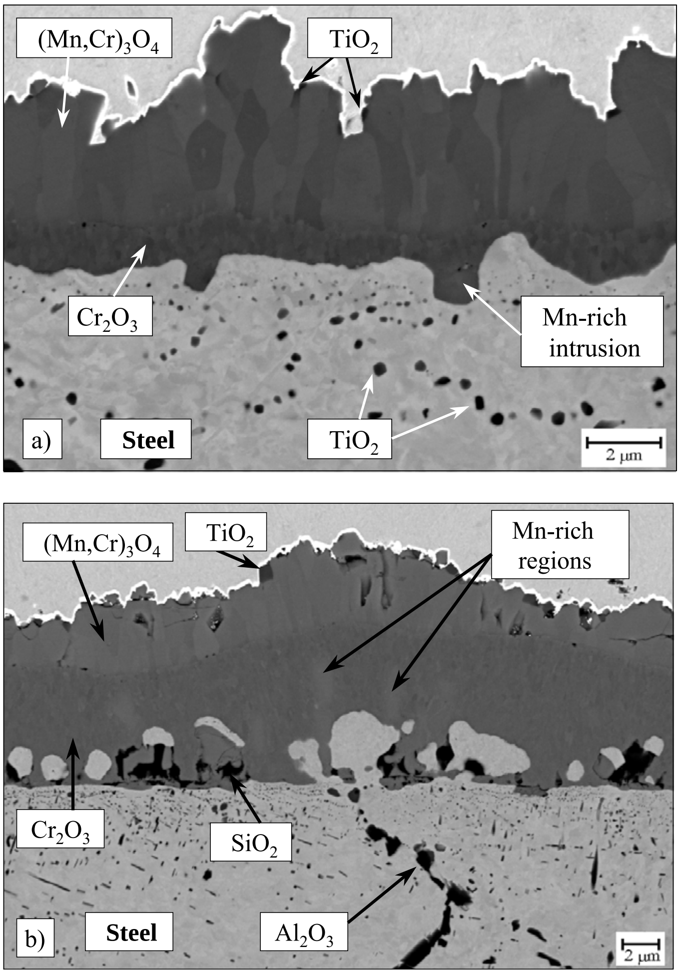

Figure: 5.6: Metallographic cross-sections (SEM images) of the two studied steels after 6000 h discontinuous oxidation at 800°C in air. a) Steel JS-3 $_{\text{(JEX 9)}}$, b) Steel Crofer A $_{\text{(JDA 12)}}$

Fig. 5.6 shows the differences in oxide scale morphologies of the two studied ferritic steels after 6000 h oxidation at 800°C in air. In both cases the scales consisted of an outer $(Mn,Cr)_3O_4$ layer and an inner Cr_2O_3 layer. The most apparent difference in the scale morphologies of the two steels is the presence of different types of internal oxidation. In the case of steel JS-3, precipitates of TiO_2 are found in the sub-scale zone in the alloy. In steel Crofer A the presence of the impurities of Si and Al led to internal oxide precipitates of silica and alumina instead of titanium oxide. The volume increase imparted by formation of these internal oxide precipitates results in the formation of metal protrusions into the oxide scale thereby causing an increase of the oxidation rate of the steel [Quadakkers-1]. The higher oxidation rate of steel Crofer A mainly relates to an enhanced growth of the inner chromia layer, leading to a clear difference of the $(Mn,Cr)_3O_4/Cr_2O_3$ ratio in the surface scale compared to that on steel JS-3. The higher growth rate of the chromia is very likely related to the formation of microcracks in the oxide layer leading to enhanced access of oxygen to the metal surface. The cracks will be formed due to the mentioned metal protrusions into the oxide scale (volume increase) related to the internal precipitates of silica and alumina. Minor amounts of titania were found near the scale / gas interface, especially in the case of steel Crofer A. In the scale on this steel, Mn-rich zones were found in the inner chromia based layer after the long exposure time of 6000 h (Figure 5.6), however, after this very long exposure time, indications for scale spalling were not found on either steel Crofer A or steel JS-3.

5.3.2 Early stages of oxidation of JS-3 and Crofer A

Figure 5.7 shows weight change data during isothermal oxidation (TG) of the studied materials at 800°C and 900°C in synthetic air. From the measured weight change data, k_p-values as a function of time were calculated (figure 5.8). Typical oxide scale morphology after this short oxidation time is presented in figure 5.9.

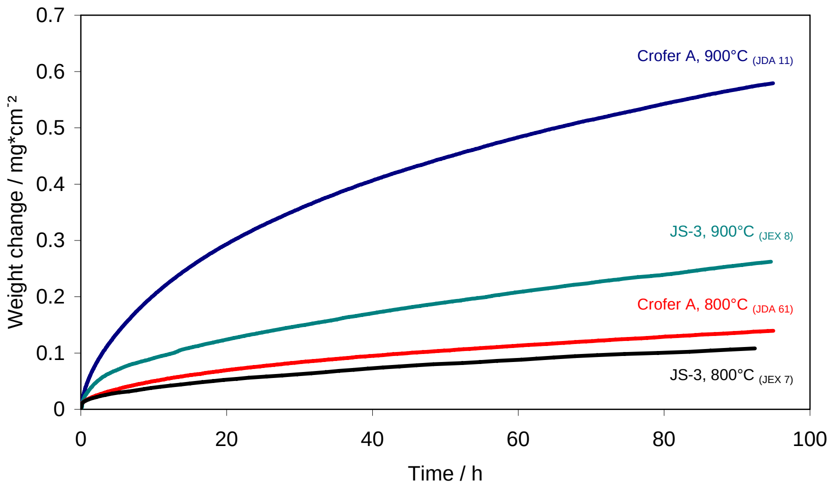

Figure 5.7: Weight change during isothermal oxidation (TG) of steels JS-3 and Crofer A at various temperatures in synthetic air. Partially [Piron-2].

The results clearly indicate that the oxidation rate of steel JS-3 is much lower than that of Crofer A at both studied temperatures. Moreover, the oxidation behaviour can be described with reasonable accuracy by a parabolic time dependence of the scaling rate for both studied materials.

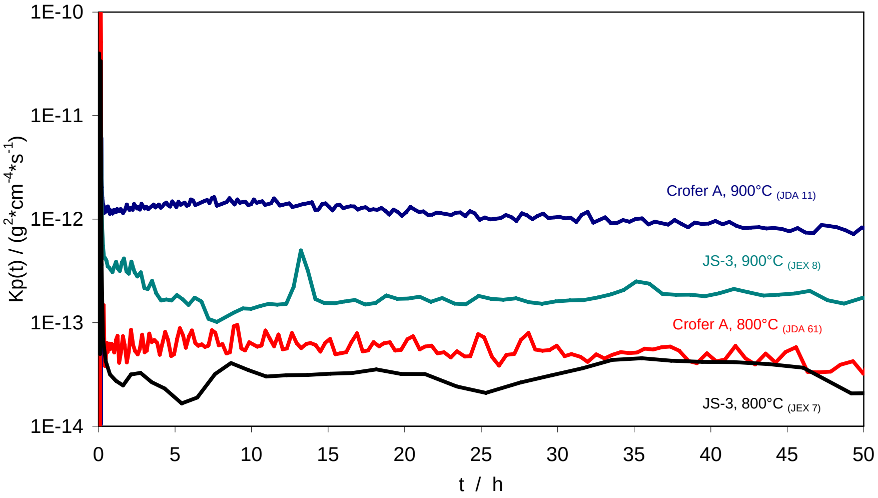

Figure 5.8: Measured k_p-values as function of time during isothermal oxidation (TG) of steels JS-3 and Crofer A at various temperatures in synthetic air.

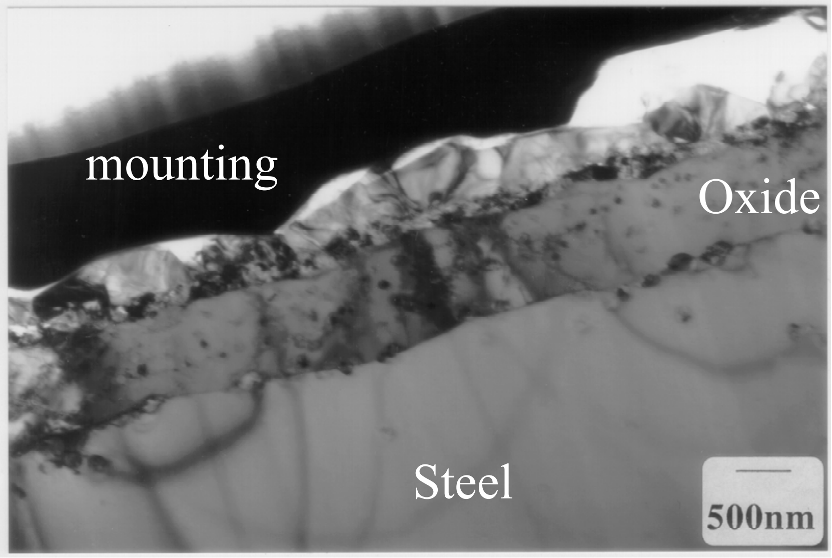

Figure 5.9: TEM image of steel JS-3 after 100 h oxidation at 800°C in synthetic air (TG)

To obtain more detailed information concerning differences in the oxidation mechanisms of the two steels, short time oxidation studies were carried out and the oxide scales subsequently analysed by SNMS. Figures. 5.10, 5.11 and 5.12 show quantified SNMS profiles for both steels after different exposure times. Both steels initially tended to form an Fe-rich oxide scale (Figures 5.10 a and 5.11 a). During prolonged exposure the surface scales became enriched in Cr and Mn until eventually the double layered oxide scale of spinel on top of chromia prevails in both studied cases. The results indicate, that, after this two-layered scale was established, the Fe content in the oxide layer on Crofer A is higher than that in the scale on steel JS-3.

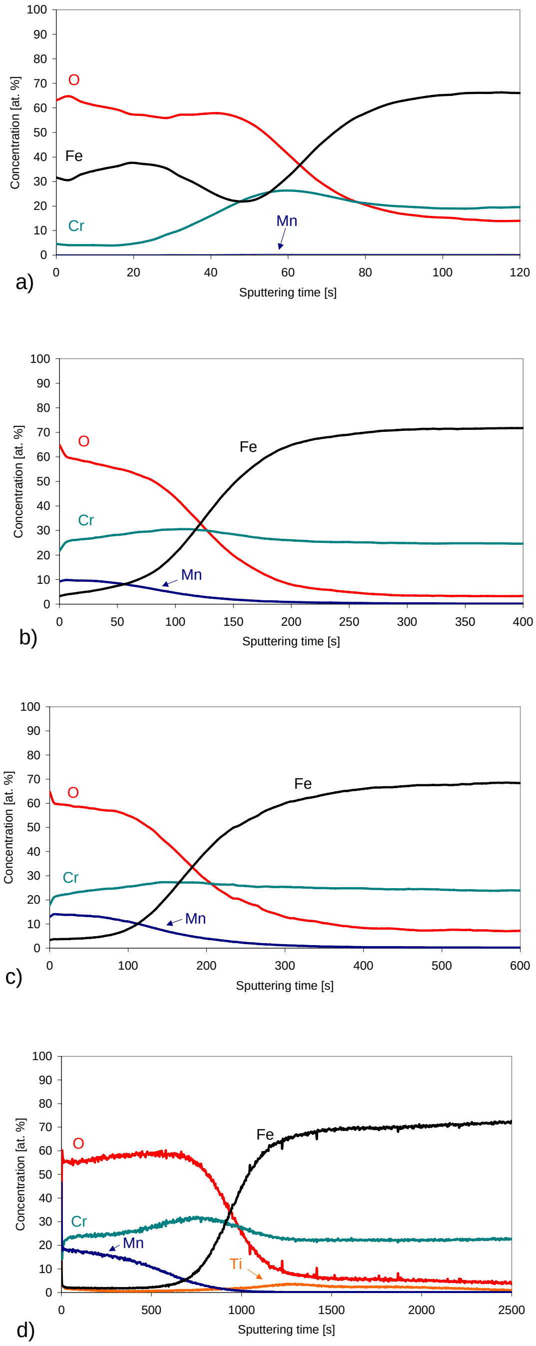

Figure 5.10: SNMS profiles of Steel JS-3 (main elements) after isothermal oxidation at 800°C in air; a) 1 min, b) 10 min, c) 1 h, d) 24 h

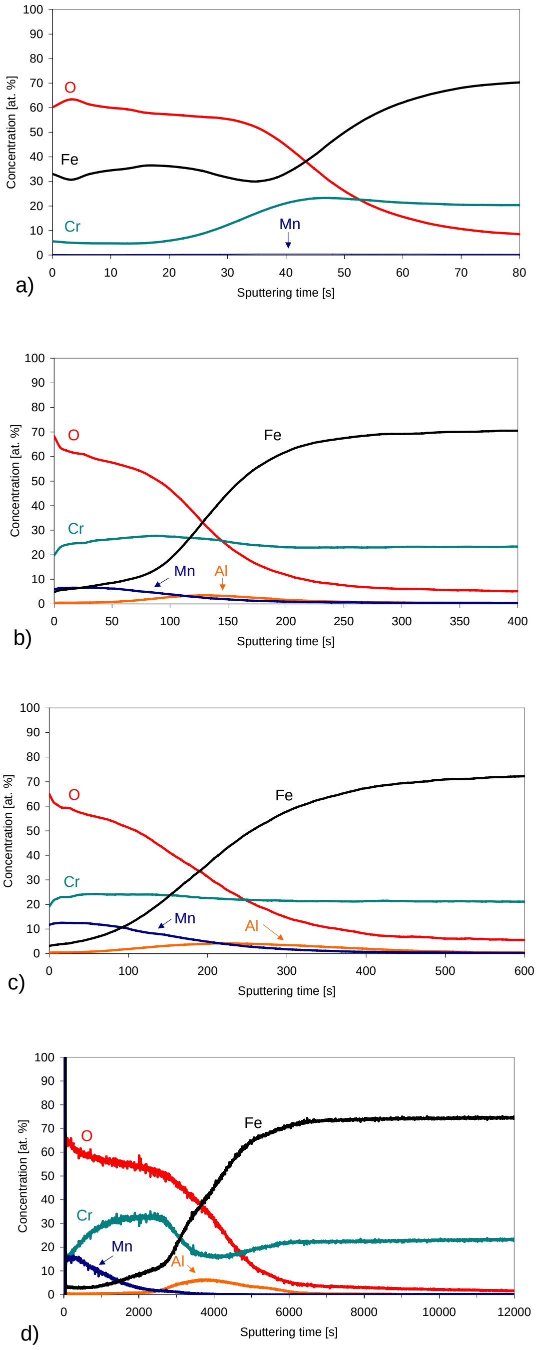

Figure 5.11: SNMS profiles of Steel Crofer A (main elements) after isothermal oxidation at 800°C in air. a) 1 min, b) 10 min, c) 1 h, d) 24 h

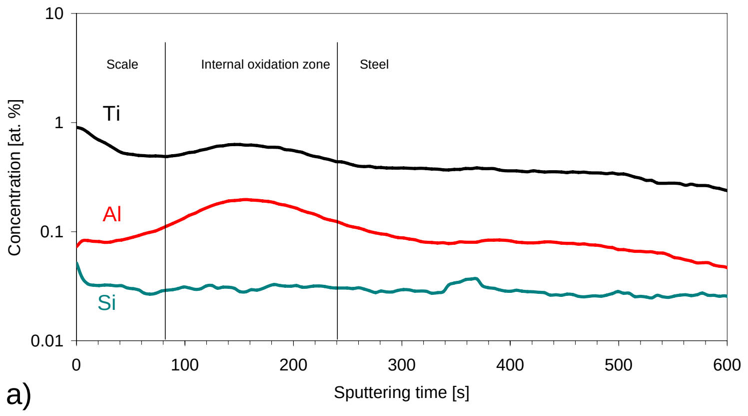

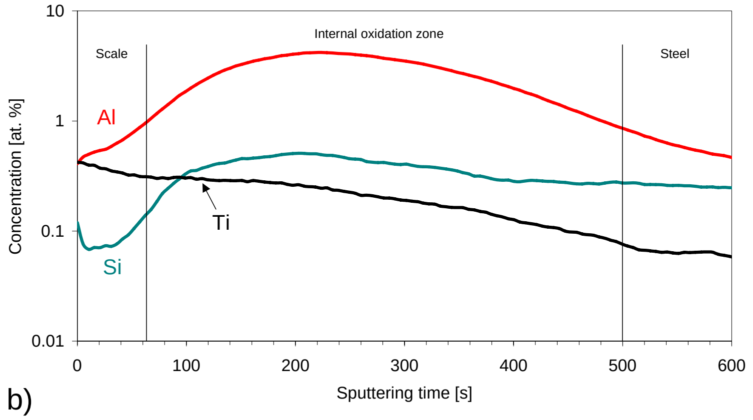

Figure 5.12: SNMS profiles of Ti, Al, Si for the studied materials after 1 h isothermal oxidation at 800°C in air. a) Steel JS-3, b) Steel Crofer A

Another clear difference between the depth profiles of the two materials is, that in the case of Crofer A a broad aluminium peak at the metal/oxide interface appears which relates to the Al_2O_3 containing internal oxidation zone described for the long term exposures (Figure. 5.12). In agreement with the results in Figures 5.10 and 5.12 the element which is mainly present in the internal oxide precipitates in the case of steel JS-3 is Ti (Fig. 5.12 a) although minor amounts of Al-oxide are found in the internal oxidation zone. Unlike Al, Ti is also present in the outer part of the scale. The tendency for Ti to become internally oxidised is more pronounced in steel JS-3 than in steel Crofer A, which is related to the higher Al content in the latter material. The higher thermodynamic stability of alumina compared to that of titania decreases the tendency for the Ti to oxidize internally. In steel Crofer A Si can also be found in the internal oxidation zone, especially in the vicinity of the scale/alloy interface.

Additionally, indications were found that very minor amounts of Si are present in the outermost part of the oxide layer (Fig. 5.12 b).

It is also necessary to take into account that in the case of both steels, after 24 h oxidation time the concentration of Mn in the SNMS profile is relatively high (figures 5.10 d and 5.11 d). This indicates that the externally growing oxide is probably a $CrMn_2O_4$ type spinel as was also shown by Malkow for Crofer 22 steel after oxidation at 800°C in Ar-$^{16}O_2$/$^{18}O_2$ [Malkow-1].

Figure 5.13 shows SNMS depth profiles of steel JS-3 after two-stage oxidation in Ar- 20% $^{16}O_2$ / Ar- 20% $^{18}O_2$ (total exposure time 1 and 25 h respectively). The profiles strongly indicate a major outward growth of the scale, likely governed by the formation of the external Cr/Mn spinel layer. By analysing the oxygen profiles it is possible to conclude that in the case of the profile in figure 5.13 a “mixed” scale growth still occurs (transient oxidation). It means that the Cr_2O_3 scale is formed accompanied by fast Mn outward diffusion [Malkow-1]. Figure 5.13 b shows the oxide scale after longer oxidation times. In this stage the Cr_2O_3 scale has already formed and formation of the Cr/Mn-spinel phase is a dominating process in that case.

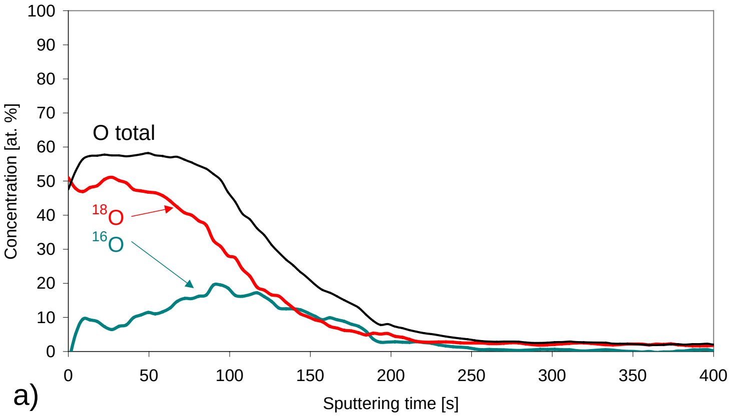

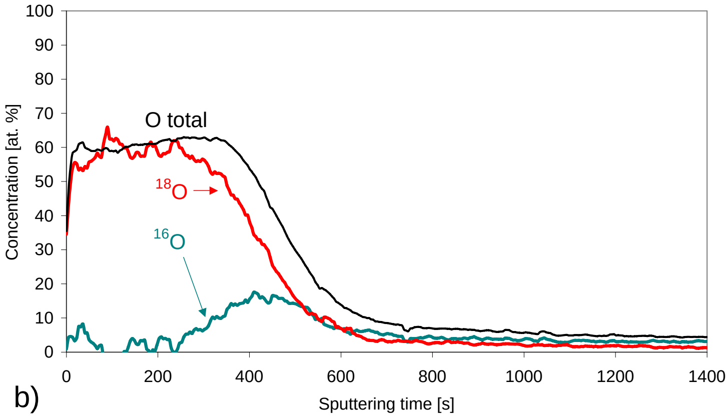

Figure 5.13: SNMS profiles of steel JS-3 after isothermal oxidation at 800°C Ar-O_2. (two-stage oxidation using $^{18}O_2$ in the second oxidation step)
a) 12 minutes Ar-$^{16}O_2$, 48 minutes Ar-$^{18}O_2$, b) 5 h Ar-$^{16}O_2$, 20 h Ar-$^{18}O_2$

5.3.3 Effect of minor alloying additions on oxidation behaviour of Crofer type steels

The steels Crofer 22 APU and JS-3 mainly differ in respect to Al and Si contents. Based on the results from paragraphs 5.3.1 and 5.3.2, further detailed studies in respect to the influence of Si and/or Al impurities for the oxidation behaviour of Crofer 22 APU were carried out. For these studies, several model alloys with various additions of Si or Al were prepared. As a base material the "pure" steel JS-3 was used.

Figure 5.14 presents weight change data for steels JS-3 and Crofer A compared with model, JS-3 based alloys with 0.1 wt. % Si or Al. It is clearly visible that the addition of Al results in a much higher growth rate of the oxide scale than in the case of Si addition.

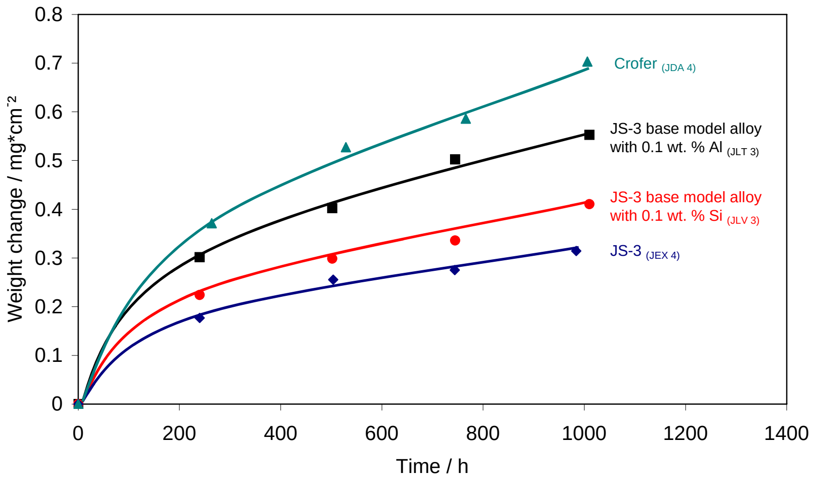

Figure 5.14: Mass change during discontinuous oxidation of steels JS-3, Crofer A and model alloys with various additions of Si/Al at 800°C in air (specimen thickness ~ 2 mm)

Figure 5.15 shows metallographic cross-section (SEM images) of the investigated steels after 1000 h oxidation at 800°C in air. Characteristic metal protrusions into the oxide scale observed in the case of Crofer A (compare figure 5.6) are also visible in both model steels; however, the effect is enhanced in the steel with the addition of Al.

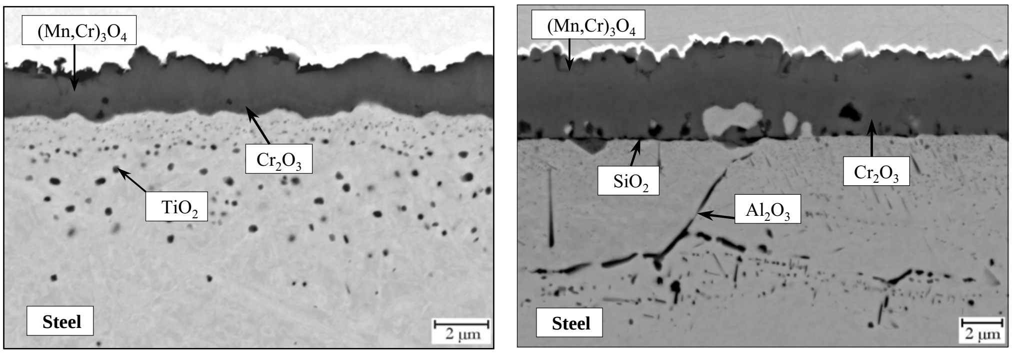

a) JS-3 $_{\text{(JEX 4)}}$ [Piron-2] b) Crofer A $_{\text{(JDA 4)}}$ [Piron-2]

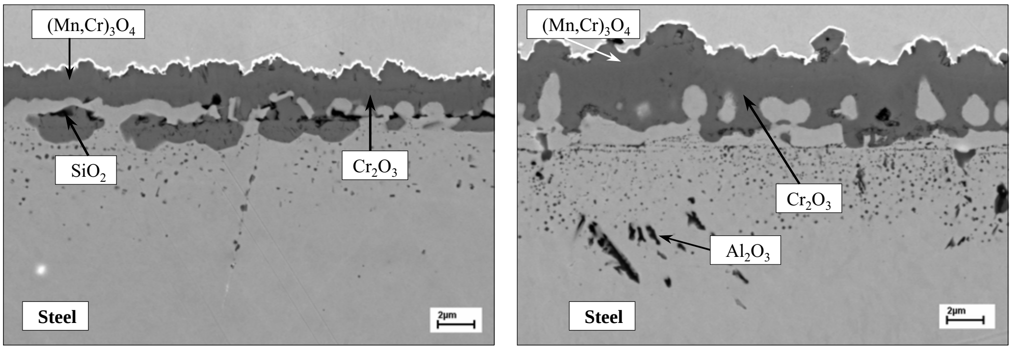

c) JS-3 + 0.1 wt. % Si $_{\text{(JLV 3)}}$ d) JS-3 + 0.1 wt. % Al $_{\text{(JLT 3)}}$

Figure 5.15: Metallographic cross-sections (SEM images) of steels JS-3, Crofer A and JS-3 base model alloys with 0.1 wt. % additions of Si or Al after 1000 h oxidation at 800°C in air (specimen thickness ~ 2 mm)

From previous studies it is known that internal corrosion processes such as internal oxidation [Young-1], carburization [Ahmed-1] or nitridation [Chang-1] result in a compressive stress in the near-surface metal matrix. At the prevailing high oxidation temperatures, these stresses trigger metal creep resulting in outward metal transport. In atmospheres in which the pO_2 does not allow external oxide formation, this results in the formation of metal "nodules" on the outer surface [Young-1]. If external scale formation prevails, as in the present case, the process leads to the formation of metal inclusions in the external oxide scale. A clear confirmation of this process can be derived from the location of the internal oxide precipitates. Due to the oxygen partial pressure gradient in the alloy beneath the scale, the extent of internal oxide precipitates should decrease starting from the scale/alloy interface in the direction of the bulk alloy. This is indeed the case, with the exception of the in-scale metallic inclusions (Fig. 5.15 b, c, d). The latter are a result of the fact that these inclusions form after a critical amount of internal oxide precipitates have formed. The surrounding alloy matrix is then depleted in the strong oxide forming elements, mainly Al and Si, and consequently no internal oxide formation is possible in the metallic inclusions. As the formation of metal inclusions will continuously occur, i.e. in parallel to the growth of the external chromia base scale, the oxide scale should, also during isothermal exposure, be subjected to damage and crack formation. This process is schematically illustrated in figure 5.16.

If cracks are formed in the scale as a result of metal inclusion formation, the metallic surface in the cracks will be directly exposed to the atmosphere. For a description of the re-oxidation processes of the metal in the cracked scale areas, we consider the scale formation measured by SNMS in the very early stages of the oxidation process for Crofer A. The results in figure 5.11 clearly reveal that the scale in the early stages of oxidation is quite rich in iron. Longer exposure times are needed to form the oxides, which are in equilibrium with the prevailing alloy composition, i.e. chromia near the scale/alloy interface and Cr/Mn-spinel at the interface with the gas. It is therefore likely, that the formation of Fe-rich oxide will also initially occur during the healing process of the formed micro cracks, especially because the alloy near the interface with the oxide will at that moment already be depleted in Cr and especially Mn. Longer times are needed to again form a Cr-rich oxide scale. The amount of Fe-rich oxide formed in the crack will depend on the Cr and Mn contents prevailing at the scale/alloy interface, the amount of Fe oxide increasing with decreasing Cr- and Mn content. The initially formed Fe-rich oxide will subsequently become incorporated into the healed Cr based scale. At low amounts of Fe-rich oxide, it will become dissolved in the chromia thus leading to a Fe-doped chromia scale, which results in higher growth rates compared to that of “pure” chromia.

Indications for Fe-dissolution in the chromia scale have already been indicated by other authors [Wood-4] and also found by our own SNMS depth profiles as well as EDX-analyses of specimens after long-term exposure. However, an unequivocal, quantitative value was difficult to derive, because the SNMS analyses were affected by the non-even oxide/alloy interfaces whereas the absolute accuracy of the EDX analyses was affected by its limited lateral and depth resolution.

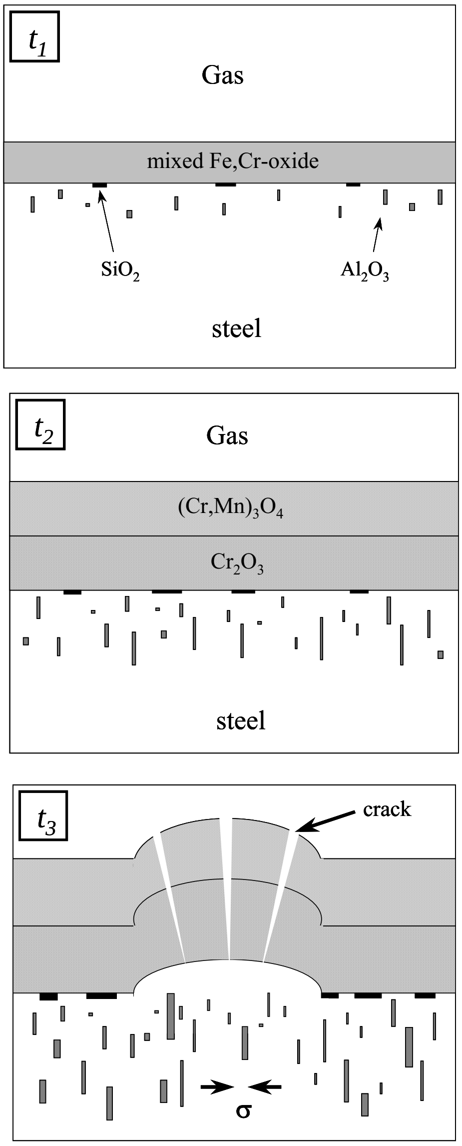

Figure 5.16: Proposed scale formation mechanism in case of steel Crofer A

Some experimental evidence for the significance of microcrack formation and healing in the overall oxidation process was found in oxide scales after long term exposure. Comparing images in figure 5.6 both steels JS-3 and Crofer A exhibit the well-known two-layered oxide morphology consisting of an outer spinel layer on top of an inner chromia scale, the latter being substantially thinner in steel JS-3. In steel Crofer A “bands” of Mn-rich oxide were found in the chromia scale arranged perpendicular to the scale/alloy interface. It is believed that these Mn-rich oxides, which were not found in steel JS-3, are formed as a result of "crack-healing". Bands of similar morphologies were frequently found in the chromia scale formed on thin specimens of steel JS-3, as illustrated for a 0.2 mm specimen after 900 h exposure at 900°C (Fig. 5.17). However, in this case the oxide bands are not rich in Mn but in Fe. They become clearly visible if the exposure times approached the time to breakaway oxidation. Apparently the limited reservoir of the protective-scale forming elements Cr and Mn have been so extensively depleted, that a crack healing by formation of Cr- and Cr/Mn-rich oxide could no longer proceed and Fe-rich oxide bands were formed.

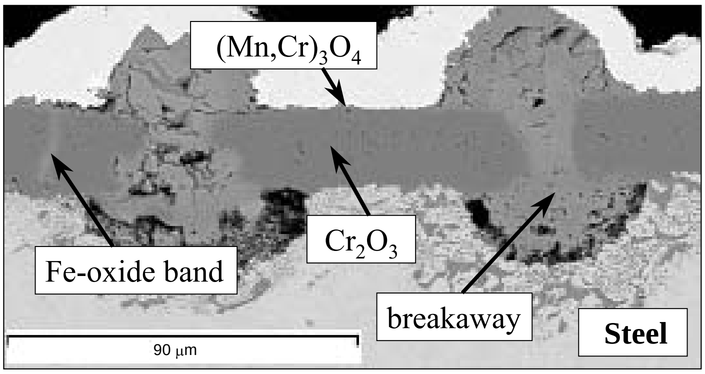

Fig. 5.17: Metallographic cross-section of 0.2 mm thick specimen of steel B after 900 h cyclic oxidation at 900°C in air (breakaway)

For steel JS-3 (Figure 5.15 a) the oxide scale is much less affected by the formation of an internal oxidation zone. The reason for that could be that there is less Ti in steel JS-3 (~ 0.05 wt. %) than Si and/or Al in Crofer A (~ 0.1 wt. %). Besides, the fine, spherical internal oxide precipitates of titania result in strengthening of the near-surface region, and thus reducing the tendency for the occurrence of surface wrinkling. The rod shaped precipitates found for silica and especially for alumina develop much more rapidly than the spherical ones [Joung-1] which causes a fast volume changes in Al_2O_3 precipitates and thus deformation of the surface oxide scale.

5.3.4 Effect of water vapour on the air oxidation behaviour of Crofer type steels

To simulate the real conditions of the SOFC stack, in most studied cases laboratory air was used for the oxidation experiments. It is, however, necessary to take into account, that the laboratory air contains some water vapour. Also, hydrogen can diffuse from the anode side through the metallic interconnect resulting in formation of water vapour at the cathode side. It was reported by several authors [Otsuka-1, Fujikawa-1, Garcia-1, Pint-1] that the addition of water vapour enhances the oxidation rate of iron based high-Cr steels. Therefore, isothermal oxidation studies (TG) were performed in two different controlled atmospheres, synthetic air (dry air) and synthetic air + 7 % H_2O (wet air).

Figure 5.18 shows weight change data for Crofer A (thick specimens of 2 mm thickness, compare section 6.1.3) during isothermal oxidation (TG) at 900°C in various atmospheres. It was found that at least for short oxidation times of 100 h there is hardly any difference in the oxidation rate between wet and dry air exposures. Metallographic cross-sections (SEM images) after 100 h isothermal oxidation at 900°C in the discussed atmospheres are presented in figure 5.19. The oxide scale thickness and the depth and shape of the internal oxidation zones are practically the same. The only minor difference between the oxides scales is that for dry air large crystals of $(Mn,Cr)_3O_4$ occur, while in wet air the spinel forms as a dense, compact layer.

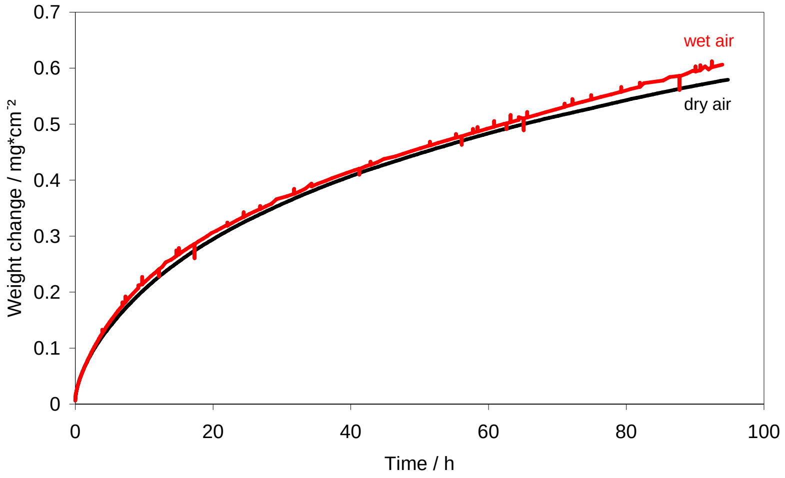

Figure 5.18: Mass change during isothermal oxidation of steel Crofer A at 900°C in various atmospheres (wet air: synthetic air + 7 % H_2O).

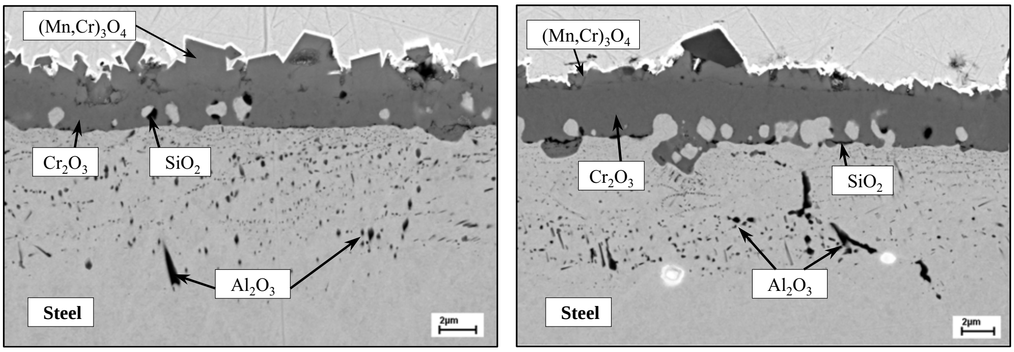

a) b)

Figure 5.19: Oxide scale morphology (SEM images) of steel Crofer A after 100 h isothermal oxidation at 900°C in various atmospheres; a) - dry air (synthetic air), b) - wet air (synthetic air + 7 % H_2O)

5.3.5 Optimisation of steel Crofer 22 APU (Crofer B)

In accordance with experimental results shown in sections 5.3.1 – 5.3.3 minor alloying additions of Si and/or Al play a very important role in the oxidation behaviour of Crofer 22 APU type materials. The mentioned elements accelerate the oxide growth rate of the steel, therefore making the material less useful for SOFC applications. Therefore, after the first commercial batch of Crofer 22 APU (with “high” concentrations of impurities of Si and Al) further batches were produced with reduced amounts of Si / Al making the steel compositions more similar to those of steel JS-3. To prevent nomenclature misunderstanding in the present studies, the first commercial batch of Crofer 22 APU (“high” concentration of impurities of Al and Si) is described as Crofer A, while further Crofer 22 APU batches (with reduced amounts of Si/Al) are described as Crofer B.

Figure 5.20 compares weight change data of steel JS-3, Crofer A and one of the newer batches of Crofer 22 APU (Crofer B) during air oxidation at 800°C. The data shows that the oxidation rate of Crofer B is substantially smaller than that of Crofer A, however it is still slightly higher than that of steel JS-3. Microstructural characterisation (figure 5.21) reveals the scale on Crofer B to be similar to that on steel JS-3 (Compare figure 5.15).

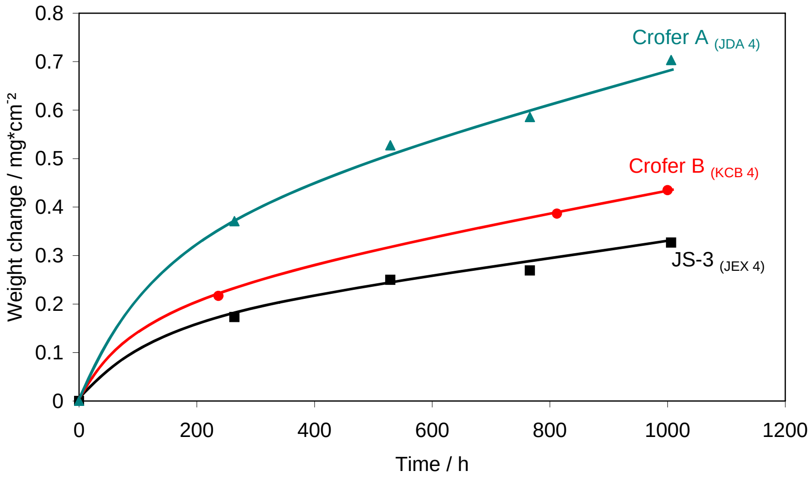

Figure 5.20: Mass change during discontinuous oxidation of steels JS-3, Crofer A and Crofer B at 800°C in air

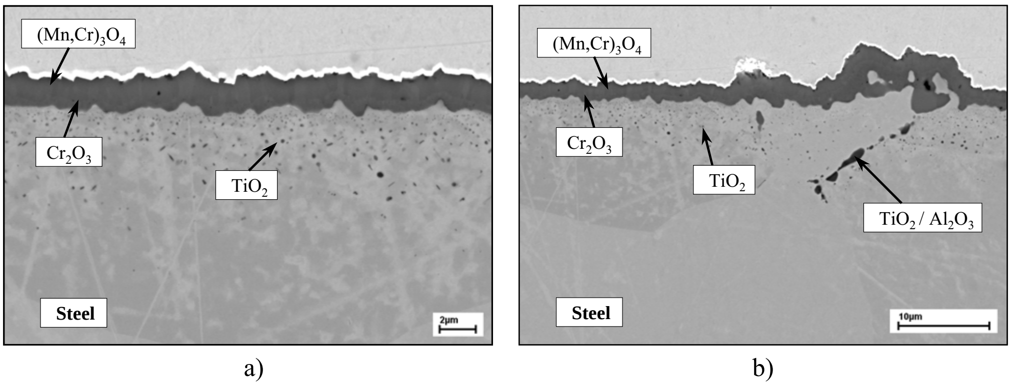

a) b)

Figure 5.21: Metallographic cross-sections (SEM images) of steel Crofer B after 1000 h oxidation at 800°C in air, showing differences in oxidation attack on different locations of the specimen (compare Figure 5.15 a, b).

The slightly higher overall weight change of Crofer B compared to steel JS-3 is related to local areas, in which the oxidation rates are slightly higher than on the rest of the specimen surface (figure 5.21 b). This effect is probably related to the amount and distribution of minor alloying additions and impurities. Reduction of Si and Al in Crofer B probably causes increases the amount of oxygen in the melt. This has a consequence that lanthanum reacts with oxygen forming La_2O_3 reducing the amount of “free” lanthanum in the steel. Insufficient La in the steel melt can lead to increasing oxidation rates as well as void formation at the interface between the oxide scale and the steel. This effect was actually found for one Crofer variant (Crofer C), which contained hardly any lanthanum (figure 5.22)

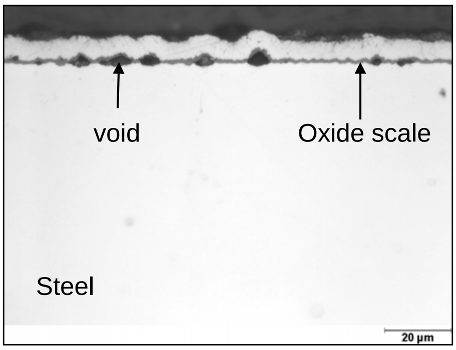

Figure 5.22: Metallographic cross-sections of steel Crofer C (hardly any La addition) after 250 h oxidation at 800°C in air, showing formation of voids at the scale/alloy interface due to the absence of reactive elements.

Another example of the interactions between minor alloying elements and impurities could be the formation of Ti-carbides / nitrides because of high amounts of carbon/nitrogen in the steel. This has a consequence that titanium could not be evenly distributed in the steel causing a change in size and quantity of the titania internal oxidation zone formed during oxidation (Figure 5.21 b). The enhanced oxidation as a result of in-scale nodule formation seems to be related to local, preferential formation of internal oxides on alloy grain boundaries.

5.4 Summary of differences in oxidation behaviour of high-Cr ferritic steels

Fe based high-Cr ferritic steels seem to be good candidate materials as interconnects for SOFC applications. After characterisation of several high-Cr ferritic steels (commercial and specially designed for SOFC interconnectors) the most promising results show the steels JS-3 / Crofer 22 APU. These steels possess the best oxidation protection and excellent adhesion of the oxide scale to the metallic substrate at both studied temperatures of 800°C and 900°C.

One of the most important factors in the case of possible SOFC applications of high-Cr ferritic steels is the concentration of scale forming elements in the alloy. In the present studies, ferritic steels with a Cr contents between 16 and 24 wt % were investigated. It was found that for a relatively low Cr content of 16 wt. % breakaway oxidation related to Cr depletion occurs after very short times when oxidised in air at 900°C. Therefore, higher chromium concentrations (i.e. ~ 24 wt. %) seem to be advisable to prevent fast destruction of the steel due to an insufficient Cr reservoir.

Detailed characterisation of steels JS-3 and Crofer 22 APU after different kinds of oxidation tests (long term exposures as well as short-term oxidation tests) showed outward growth of the scale, likely governed by the formation of the external Cr/Mn spinel layer if oxidised at 800°C and 900°C in air. The top spinel layer of $(Cr,Mn)_3O_4$ is known to reduce the formation of volatile Cr species [Piron-1, 3, Gindorf-2] reducing poisoning of the cathode in the SOFC's.

It was found that the presence of manufacturing related impurities (Si, Al) in steel Crofer A results in an evident changes in the oxide scale morphology compared to steel JS-3. The volume increase imparted by formation of internal oxide precipitates of Si and Al results in the formation of metal protrusions into the oxide scale. This caused an increase of the oxidation rate of the chromia because of oxide scale cracking and thus enhanced access of oxygen to the metal surface. The higher oxidation rate of the inner chromia layer, leads to a clear difference of the $(Mn,Cr)_3O_4/Cr_2O_3$ ratio in the surface scale compared to that on steel JS-3.

It was found that there is hardly any difference in the oxidation rate between wet and dry air at least in the first 100 hours of oxidation when oxidising thick specimens of steels JS-3 / Crofer A. (compare section 6.1.3, atmosphere effect)

Reduction of Si and Al contents in steel Crofer B substantially reduces the oxidation rate of the steel thus making the material more promising for SOFC applications.

6. Oxidation induced lifetime limits of chromia forming ferritic steels

6.1 Cyclic oxidation behaviour of components with different thicknesses

It this section components with different initial thicknesses were investigated. A number of commercial ferritic steels (paragraph 6.1.1) as well as model high-Cr alloys (paragraph 6.1.2) were used for the oxidation experiments. Detailed information about specimen preparation techniques and experimental procedures were given in section 4.

6.1.1 Cyclic oxidation behaviour of selected commercial steels

The most promising materials for SOFC interconnectors from the previous studies (compare section 5) were chosen and investigated during long-term cyclic oxidation at 800°C and 900°C in laboratory air. For the most extensive studies Crofer A was chosen because a number of plates with different initial thicknesses already existed (thickness range 2 mm – 0.1 mm). From the most other steels only one plate of each alloy prevailed and thus specimens of different thickness were made by grinding the thick specimens to the required levels.

Steel Crofer A

Figures 6.1 and 6.2 show weight change results during long-term oxidation tests at both studied temperatures (800°C and 900°C). In both cases there is clear difference in the oxidation rate between various component thicknesses (i.e. thinner specimens oxidise faster than thicker ones). At 900°C (figure 6.2) the effect is more pronounced than at 800°C and additionally breakaway oxidation phenomena can be found for the two thinnest specimens (i.e. 0.1 mm and 0.3 mm). Figures 6.3 and 6.4 show the measured parabolic k_p-values as a function of time presented for both temperatures. Most of the specimens show a near parabolic time dependence of the scaling rate. In the case of the specimen with an initial thickness of 0.1 mm oxidised at 900°C in air (figure 6.4) a steady increase of k_p during the oxidation process was observed. This effect is related to breakaway phenomenon occurring after a short oxidation time of about 100 h.

During post-experimental macroscopic observations of the thinnest specimens (Figure 6.5, 6.6 and 6.7) a strong mechanical deformation of the metallic substrate was found. This effect is related to a non-homogeneous stress distribution in the specimen during the oxidation process (compare sections 6.1.3 and 6.2).

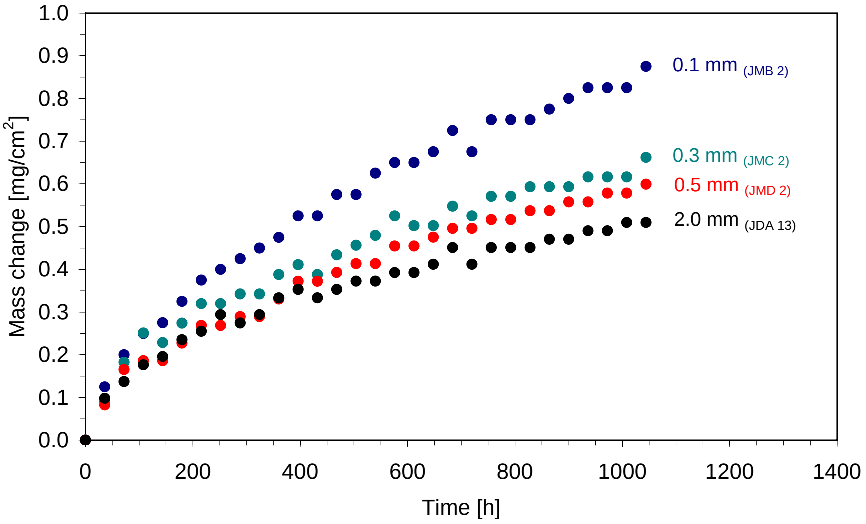

Figure 6.1: Weight change during cyclic oxidation of steel Crofer A at 800°C in air (specimens with different initial thicknesses)

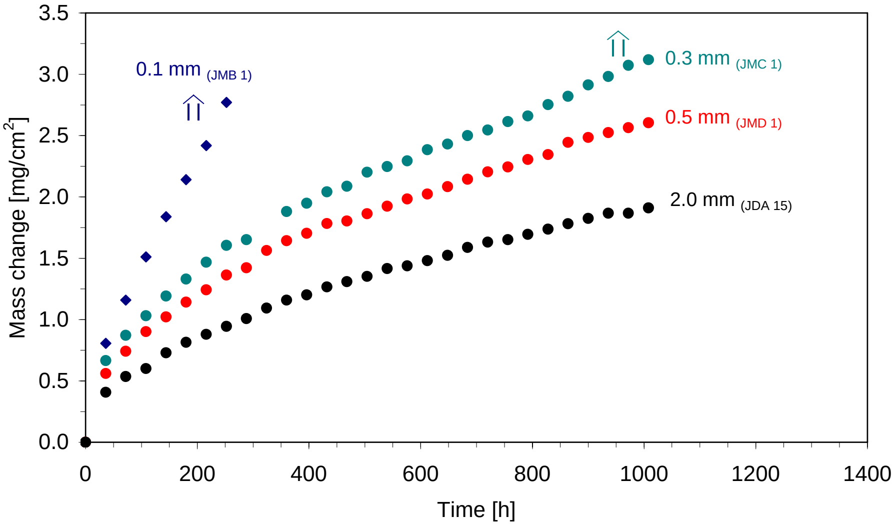

Figure 6.2: Weight change during cyclic oxidation of steel Crofer A at 900°C in air (specimens with different initial thicknesses)

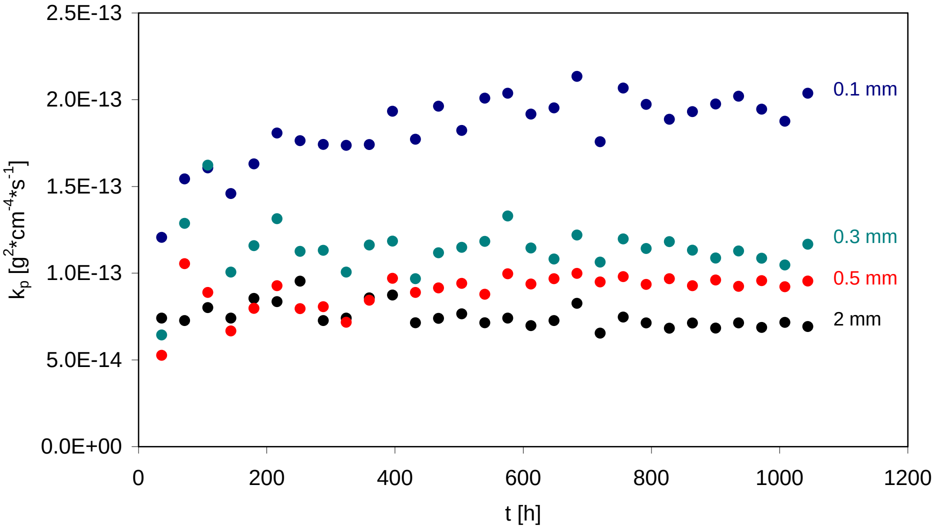

Figure 6.3: Measured parabolic k_p – values as a function of time during cyclic oxidation of steel Crofer A at 800°C in air (specimens with different initial thicknesses)

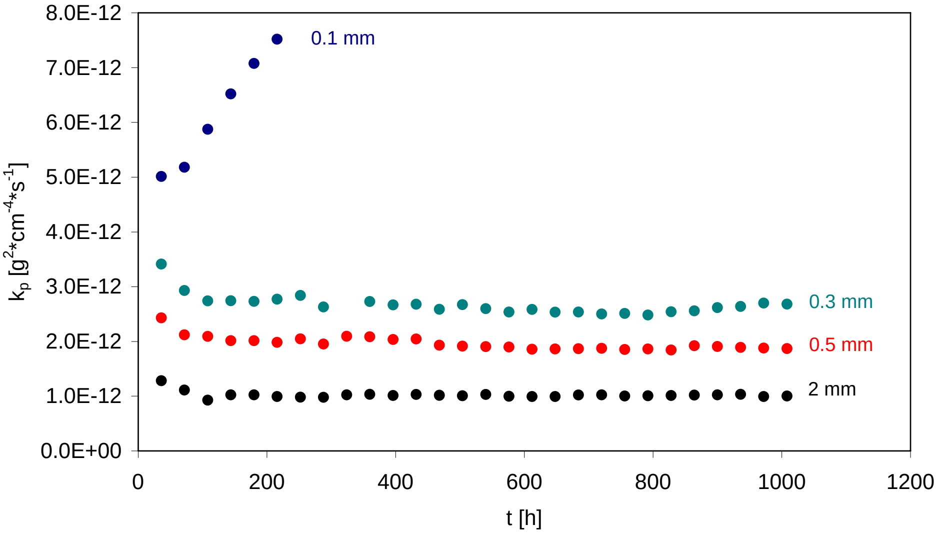

Figure 6.4: Measured parabolic k_p – values as a function of time during cyclic oxidation of steel Crofer A at 900°C in air (specimens with different initial thicknesses)

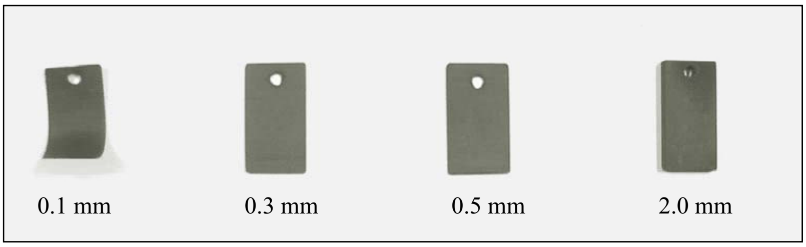

Figure 6.5: Macro images of specimens with different initial thicknesses (steel Crofer A) after 1000 h cyclic oxidation at 800°C in air

Figure 6.6: Macro image of specimen with 0.1 mm initial thickness (steel Crofer A) after 1000 h cyclic oxidation at 800°C in air showing deformation of the specimen after oxidation

Figure 6.7: Macro images of specimens with different initial thicknesses (steel Crofer A) after cyclic oxidation at 900°C in air showing breakaway and deformation of the specimens after oxidation

Figure 6.8 presents metallographic cross-sections and oxide scale morphologies (SEM images) of steel Crofer A for specimens with different initial thicknesses after 1000 h oxidation at 800°C in air (compare figure 6.1). In all studied cases a double-layered oxide scales are found (Cr/Mn-spinel and chromia). It was found that there is a clear difference in the thickness of the oxide scale between the 2 mm specimen (figure 6.8 a) and the specimen with an initial thickness of 0.1 mm (figure 6.8 d). SEM images clearly show that on the thin specimen the layer of Cr/Mn spinel is thinner than that on thick specimens. It can be found that the higher oxidation rate of the thin specimen compared to the thick one is determined by the formation of a thick Cr_2O_3 scale. It is also possible to observe that for the thick specimens the zone of internal oxidation is much more developed than that of the thin specimens (compare section 6.1.3). This effect is related to faster depletion of minor alloying elements and/or impurities (Ti, Si, Al) from the specimen with a smaller initial thickness due to its smaller reservoir [Ertl-1].

Oxide surface images presented in figure 6.8 b, c and e show a similar oxide scale morphologies for both specimens. Two different sizes of oxide crystals can be observed across the specimen surface for the thick as well as the thin specimen. Based on EDX analyses it was found that both observed structures are Cr/Mn spinel.

Figure 6.9 presents metallographic cross-sections and oxide scale morphologies (SEM images) of steel Crofer A for specimens with different initial thicknesses after 1000 h oxidation at 900°C in air (compare figure 6.2). In all studied cases double-layered oxide scales can be found (Cr/Mn-spinel and chromia). As in case of the 800°C experiment there is a clear difference in the oxide scale thickness when specimens of different thickness are compared. The growth rate of the chromia scale (thicker scale for the thinner specimens) determined the higher oxidation rate of thinner specimens (figure 6.9 a, c, e). It is also found that the morphology of the internal oxidation zone is much more developed in the case of the thicker specimens.

During observation of the oxide scale morphology for specimens with a different initial thickness (figure 6.9 b, d, f) it can be found that, different from the 800°C exposures, only one size of Cr/Mn crystal is present after oxidation in 900°C. It is probably related to the faster diffusion of Mn at higher temperatures and thus the faster growth rate of spinel across the whole specimen surface.

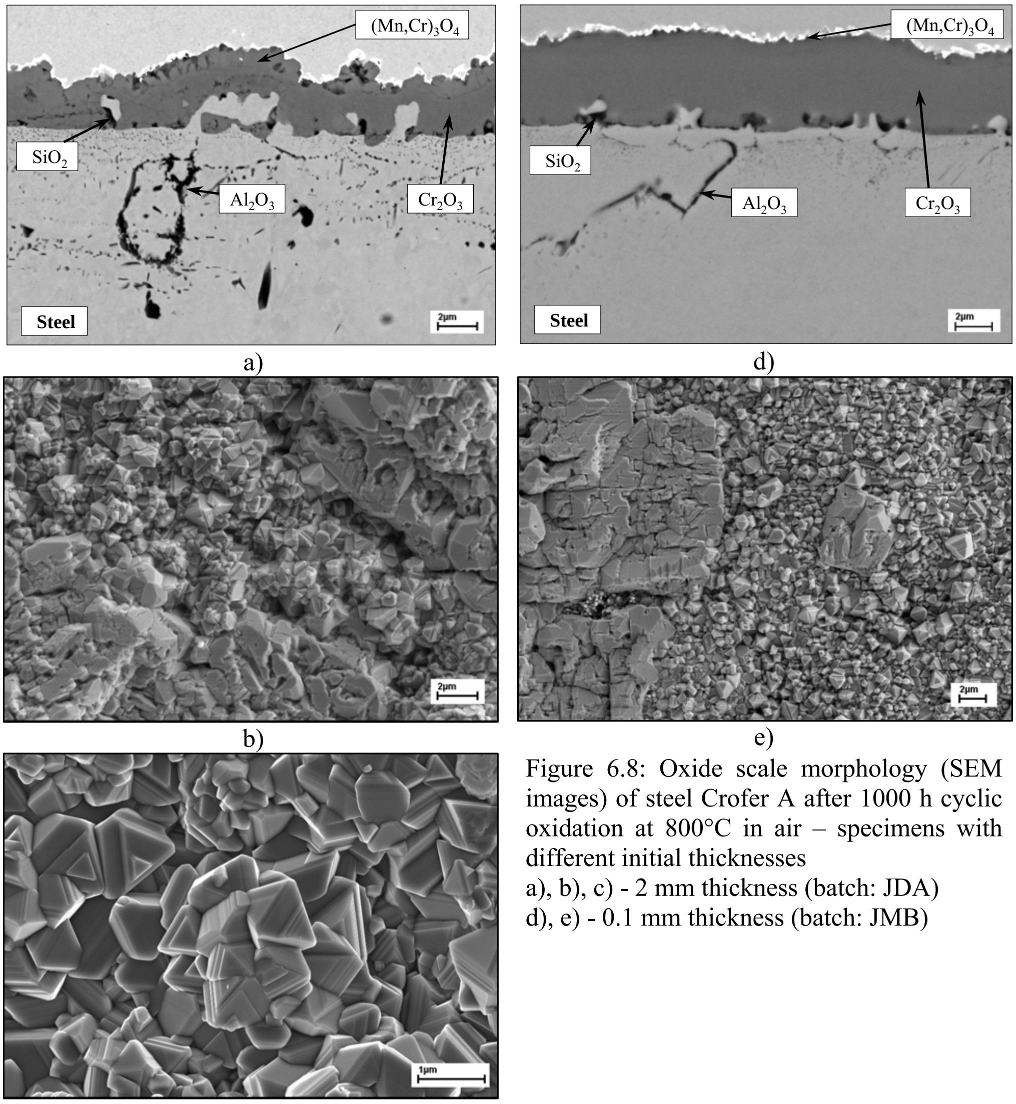

a) d)

b) e)

c)

Figure 6.8: Oxide scale morphology (SEM images) of steel Crofer A after 1000 h cyclic oxidation at 800°C in air – specimens with different initial thicknesses
a), b), c) - 2 mm thickness (batch: JDA)
d), e) - 0.1 mm thickness (batch: JMB)

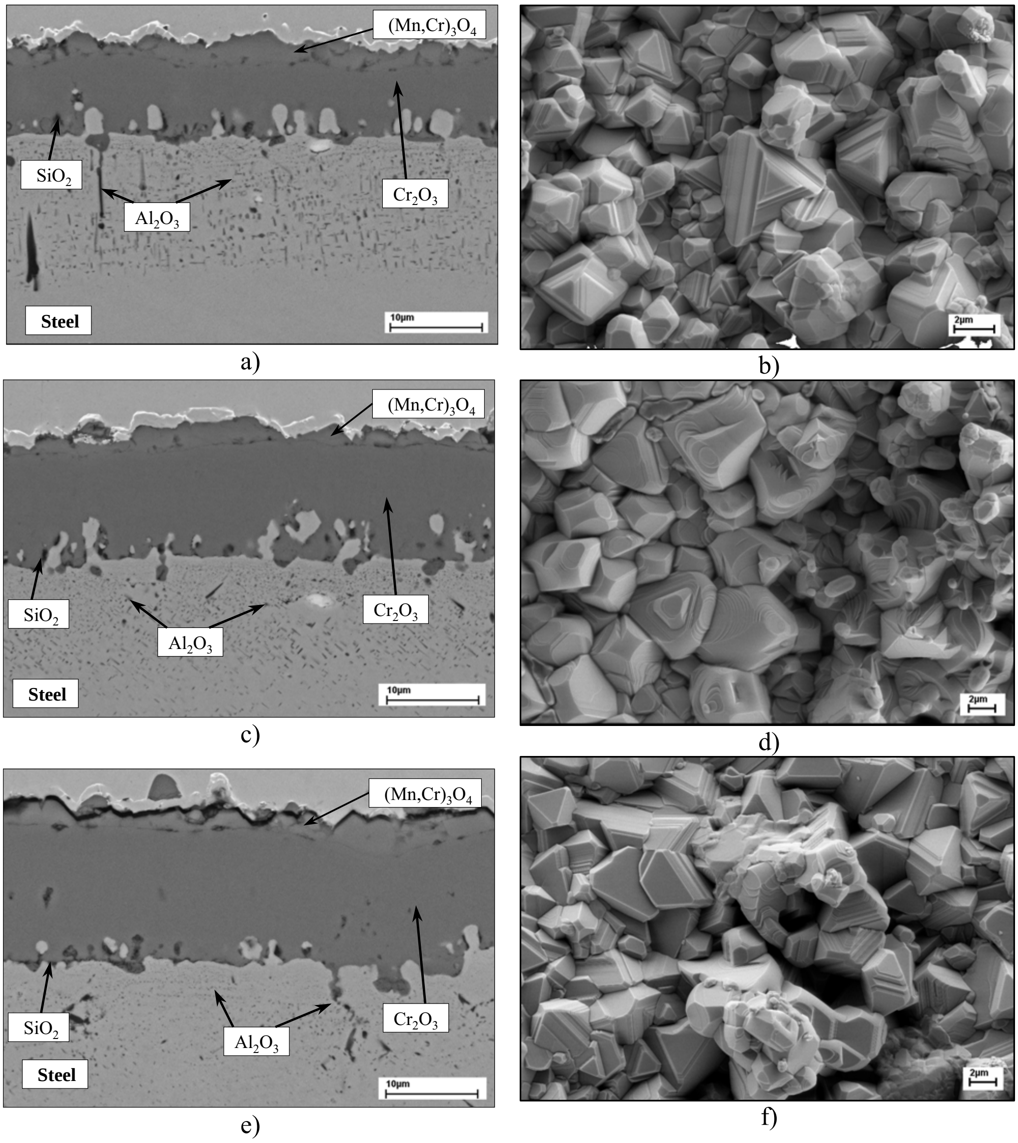

Figure 6.9: Oxide scale morphology (SEM images) of steel Crofer A after 1000 h cyclic oxidation at 900°C in air - specimens with different initial thicknesses; a), b) - 2 mm thickness, c), d) - 0.5 mm thickness, e), f) - 0.3 mm thickness

Figure 6.10 shows oxide scale morphology (SEM images) for a specimen with 0.1 mm thickness oxidised for 250 h at 900°C in air (until breakaway). It can be concluded that where no breakaway was found (figure 6.10 a, b) there is only a very thin film of Cr/Mn spinel on top of the thick chromia layer. In areas of breakaway (Figure 6.10 c, d) several cracks through the oxide scale are observed. The oxide scale in that case consisted of fast inward and outward grown Fe- oxide, which is surrounded by initially grown Cr-rich oxides (Cr_2O_3 and Cr/Mn spinel).

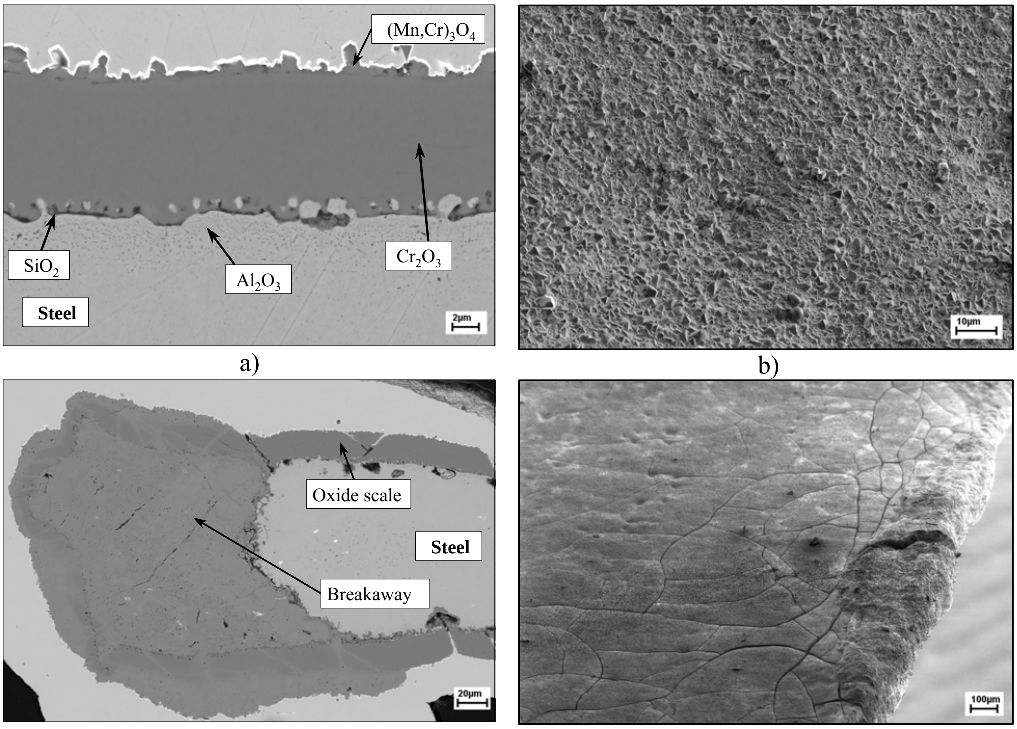

a) b)

c) d)

Figure 6.10: Oxide scale morphology (SEM images) of steel Crofer A after 252 h cyclic oxidation at 900°C in air (breakaway) - specimen thickness: 0.1 mm; a), b) - area without breakaway, c), d) - area with breakaway

Steel JS-3

Figures 6.11 and 6.12 show weight change results for the studied semi-commercial ferritic steel JS-3 during oxidation at 800°C and 900°C in air. Analogous to the results derived for steel Crofer A, there is a clear difference in the oxidation rates between specimens of different thickness. However, after longer oxidation times a deviation from the parabolic oxide growth rate were observed (compare section 6.2). In the case of the thinnest specimens oxidised at 900°C breakaway oxidation occurred after relatively short oxidation times, i.e. after shorter times than Crofer A.

Figure 6.13 shows metallographic cross-sections of specimens (SEM images) of steel JS-3 after 1000 h oxidation at 800°C in air with different thicknesses. In all studied cases, a double-layered oxide scale can be found (Cr/Mn-spinel and chromia). It was found that there is a clear difference in the oxide scale thickness on the various specimens (compare figure 6.11).

Figure 6.14 presents metallographic cross-sections (SEM images) of steel JS-3 after 1000 h oxidation at 900°C in air. In all studied cases, a double-layered oxide scale can be found. Also here, there is a clear difference in the thickness of the oxide scale between specimens with different thicknesses (compare figure 6.12). Additionally, a strong indication of oxide cracking during the oxidation and/or cooling was observed for the two thinner specimens (figure 6.14 b, c). Furthermore, if a cracked oxide scale is found, then the thickness of the Cr/Mn – spinel layer appears to be non-homogeneous in thickness (figure 6.14 c, compare sections 6.1.3 and 6.2).

Figure 6.15 shows a metallographic cross-section (SEM image) of steel JS-3 after 216 h oxidation at 900°C in air (breakaway). The specimen area without breakaway (figure 6.15 a) shows an oxide scale with a very thin Cr/Mn spinel layer on top of the thick inner chromia scale. The area with breakaway (figure 6.15 b) presents a relatively early stage of the catastrophic attack where Fe-rich oxide started to grow through the cracked Cr- rich oxide (compare section 6.2).

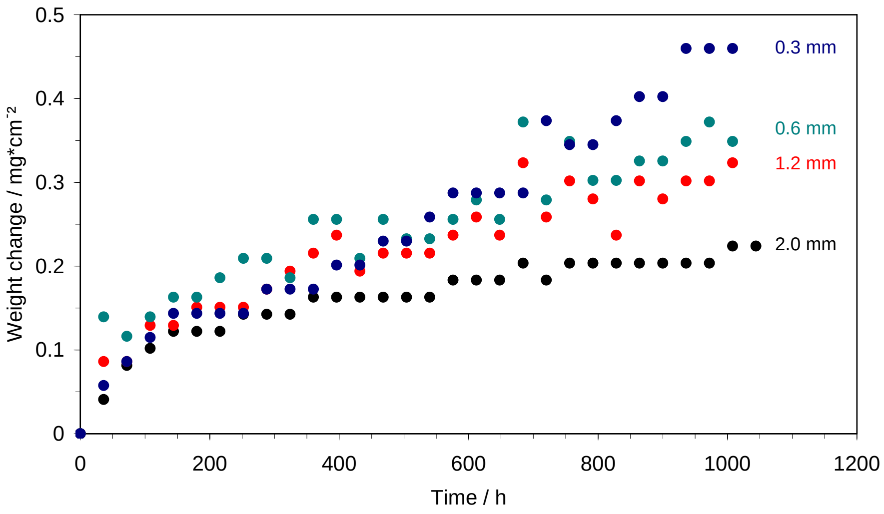

Figure 6.11: Weight change during cyclic oxidation of steel JS-3 (batch JEW) at 800°C in air (specimens with different initial thicknesses).

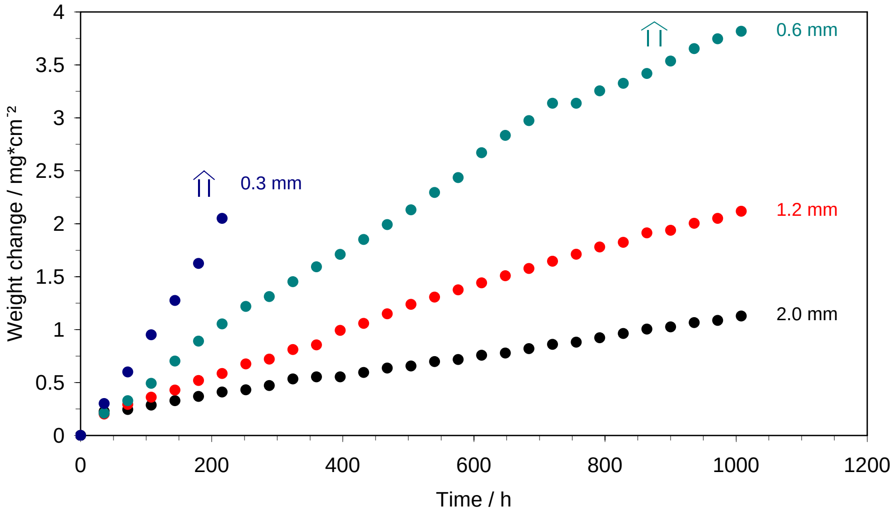

Figure 6.12: Weight change during cyclic oxidation of steel JS-3 (batch JEW) at 900°C in air (specimens with different initial thicknesses).

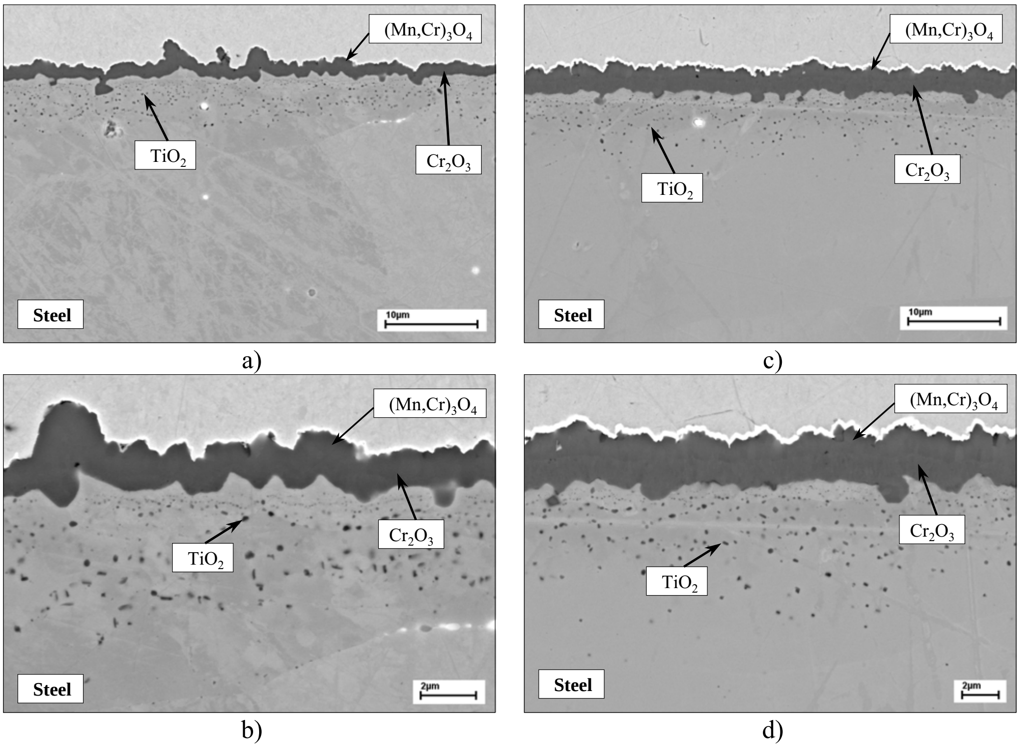

a) c)

b) d)

Figure 6.13: Oxide scale morphology (SEM images) of steel JS-3 (batch: JEW) after 1000 h cyclic oxidation at 800°C in air; a), b) - 2 mm thickness, c), d) - 0.3 mm thickness

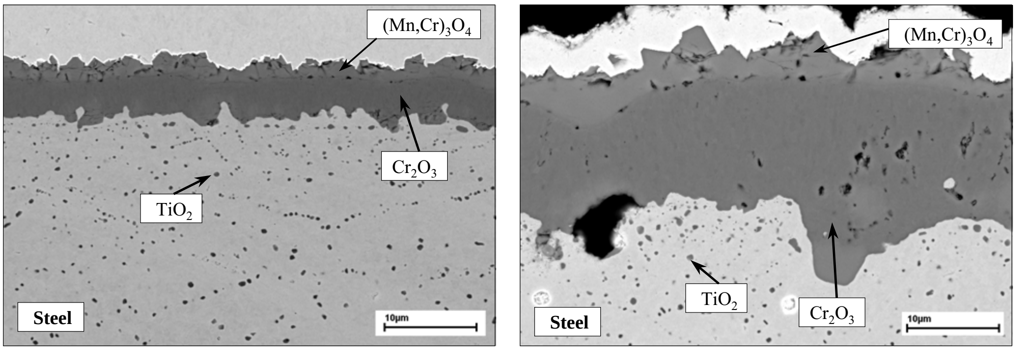

a)

c)

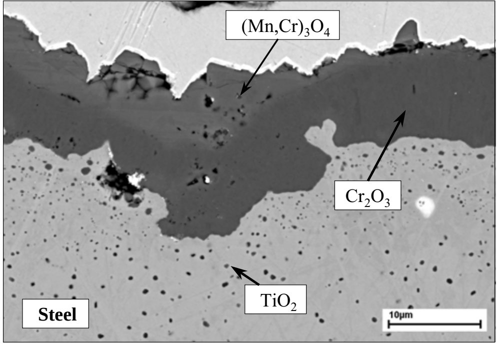

b)

Figure 6.14: Oxide scale morphology (SEM images) of steel JS-3 (batch: JEW) after 1000 h cyclic oxidation at 900°C in air - specimens with different thicknesses
a) - 2 mm thickness
b) - 1.2 mm thickness
c) - 0.6 mm thickness

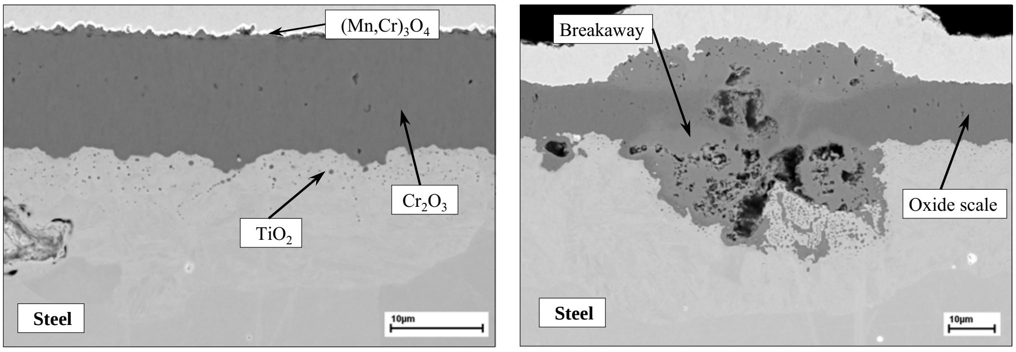

a)

b)

Figure 6.15: Oxide scale morphology (SEM images) of steel JS-3 (batch: JEW) after 216 h cyclic oxidation at 900°C in air (breakaway) - specimen thickness: 0.3 mm; a) - area without breakaway, b) - area with breakaway

Steel Crofer B

Figures 6.16 and 6.17 present weight change data for Crofer B after 1000 h cyclic oxidation at 800 and 900°C in air. During the 900°C experiment (figure 6.17) breakaway oxidation occurs in thin components. At both studied temperatures there is a clear difference between the oxidation rates in thick and thin specimens.

Figures 6.18 and 6.19 show metallographic cross-sections (SEM images) of samples with different specimen thicknesses at both studied temperatures. In all studied cases the well-known double-layered oxide scale can be found. At 800°C as well as at 900°C there is a clear difference in the oxide scale thickness between thick and thin components. The thin components studied at the 900°C (Figure 6.19 b) additionally show the indication of oxide cracking during the oxidation process and/or cooling (compare sections 6.1.3 and 6.2).

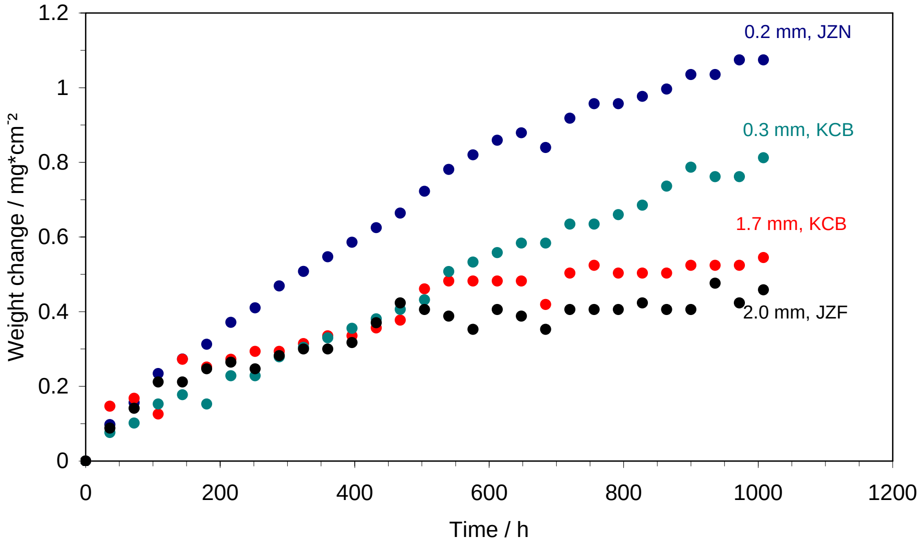

Figure 6.16: Weight change during cyclic oxidation of steel Crofer B at 800°C in air (specimens with different initial thicknesses).

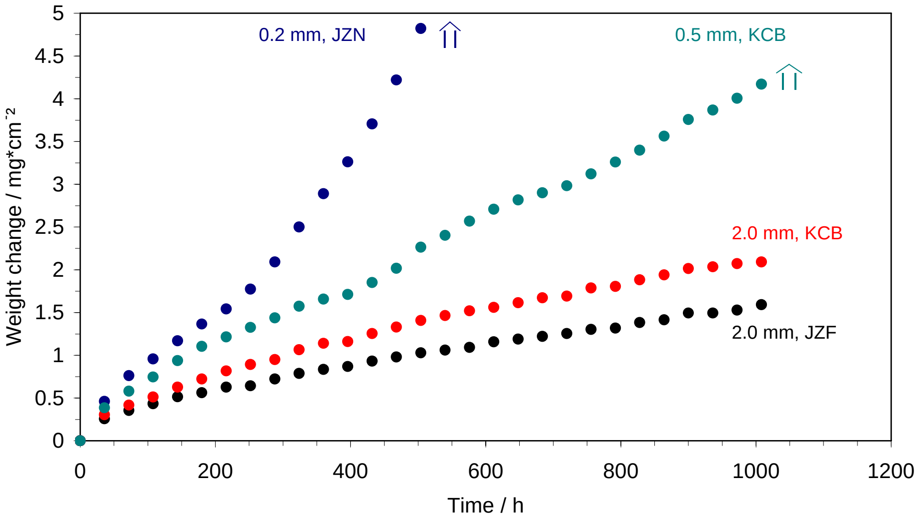

Figure 6.17: Weight change during cyclic oxidation of steel Crofer B at 900°C in air (specimens with different initial thicknesses).

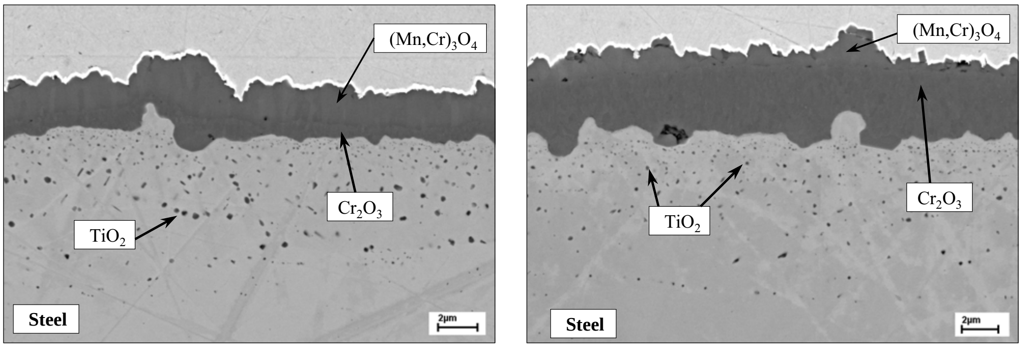

a) b)

Figure 6.18: Oxide scale morphology (SEM images) of steel Crofer B (batch: KCB) after 1000 h cyclic oxidation at 800°C in air; a) - 1.7 mm thickness, b) - 0.3 mm thickness

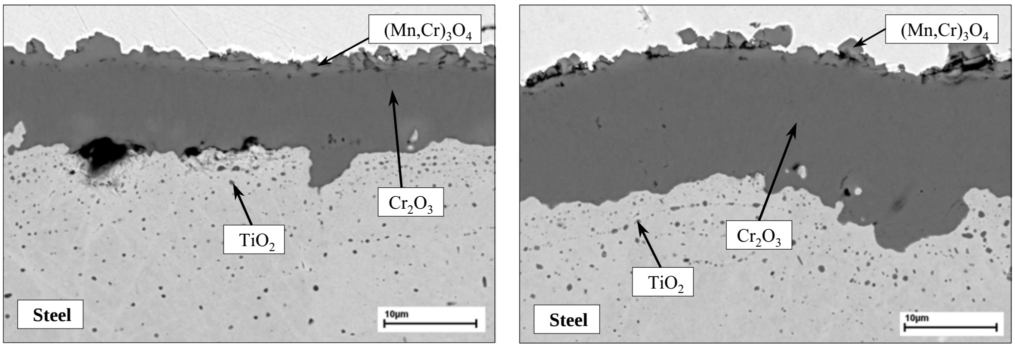

a) b)

Figure 6.19: Oxide scale morphology (SEM images) of steel Crofer B (batch: KCB) after 1000 h cyclic oxidation at 900°C in air: a) - 2.0 mm thickness, b) - 0.5 mm thickness

Steel ZMG232

Figures 6.20 and 6.21 present weight change data during cyclic oxidation of steel ZMG232 at both studied temperatures. Breakaway oxidation after 900°C exposure was found for the three thinnest specimens after various oxidation times. It was observed that at 800°C and 900°C, thinner specimens oxidised faster than the thicker ones.

Figures 6.22 and 6.23 show metallographic cross-sections (SEM images) of steel ZMG232 after oxidation at both studied temperatures (specimens with a different initial thickness). After exposure at 800°C the difference in oxide scale thickness is relatively small which is in good agreement with the data presented in figure 6.20 (small difference between oxidation rate of specimens). Cross-sections made on 900°C samples show a large difference in the oxide scale thickness between the two studied specimens. In all studied cases at 800°C as well as at 900°C, a near-continuous layer of silica can be found beneath the Cr-rich oxide scale.

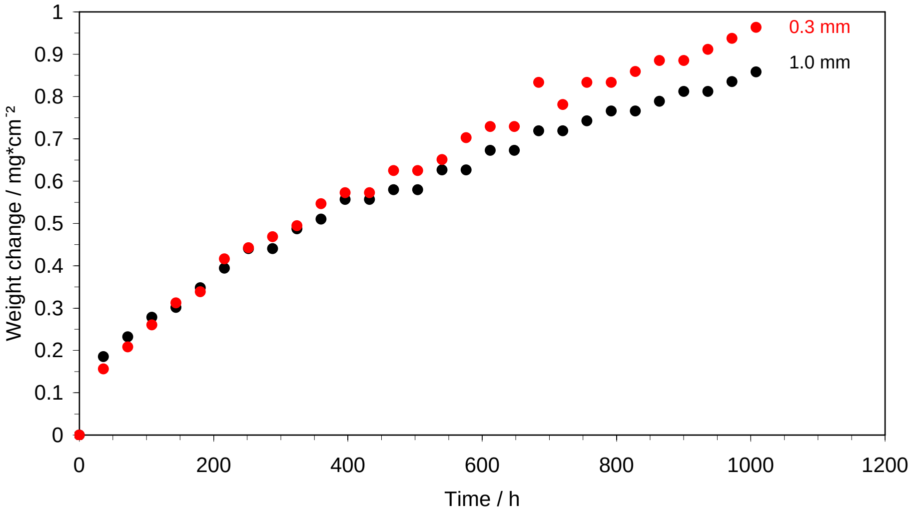

Figure 6.20: Weight change during cyclic oxidation of steel ZMG232 (batch HXT) at 800°C in air (specimens with different initial thicknesses).

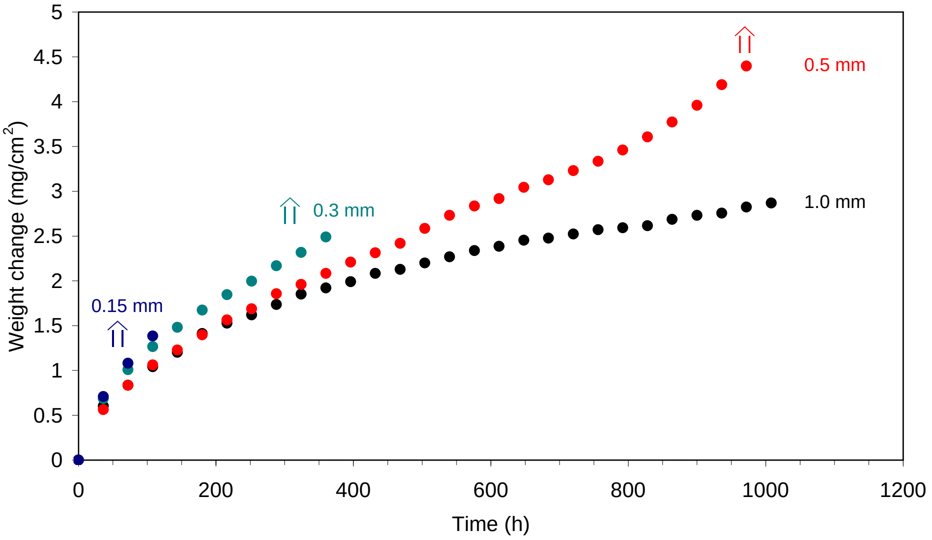

Figure 6.21: Weight change during cyclic oxidation of steel ZMG232 (batch HXT) at 900°C in air (specimens with different initial thicknesses).

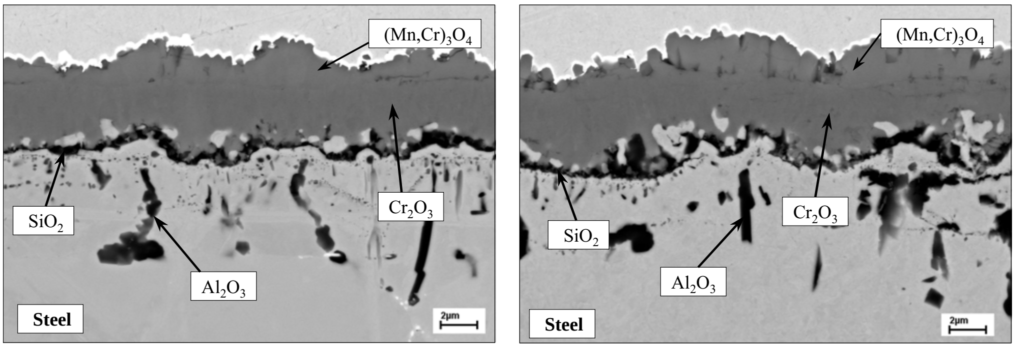

a) b)

Figure 6.22: Oxide scale morphology (SEM images) of steel ZMG232 (batch: HXT) after 1000 h cyclic oxidation at 800°C in air; a) - 1.0 mm thickness, b) - 0.3 mm thickness

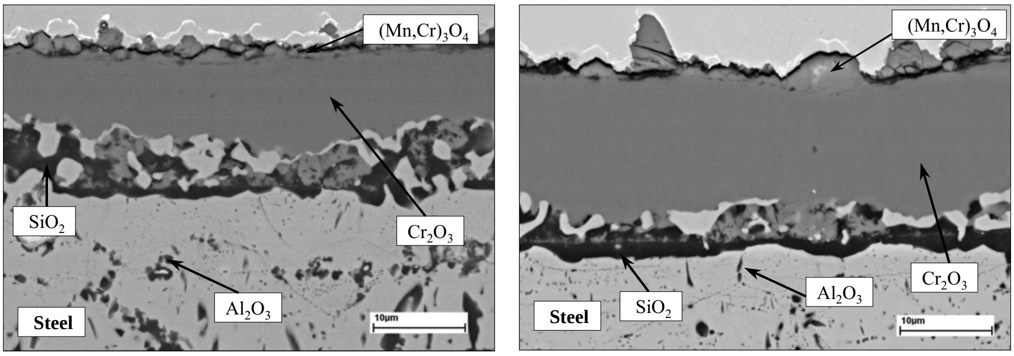

a) b)

Figure 6.23: Oxide scale morphology (SEM images) of steel ZMG232 (batch: HXT) after 1000 h cyclic oxidation at 900°C in air; a) - 1.0 mm thickness, b) - 0.5 mm thickness

6.1.2 Cyclic oxidation behaviour of selected model alloys

Results derived during cyclic oxidation of the selected commercial ferritic steels at 800 and 900°C in air (compare section 6.1.1) show a strong difference of the oxide scale thickness for thick and thin components. In all studied cases a double-layered oxide scale formed (Cr/Mn spinel and chromia), however there is a change between the thickness ratio of Cr/Mn spinel to Cr_2O_3 when comparing thick and thin specimens oxidised at the same temperature. To clarify the role of Mn in the oxide scale formation, a Mn-free model steel (Mn concentration ~ 0.01 wt %) as well as a model steel with a relatively high Mn content (~ 1.5 wt. %) were tested under the same experimental conditions as the steels in the previous section.

Model steel FeCrLa (Mn free steel, HCE)

Figures 6.24 and 6.25 show weight change data versus time for the specimens with different initial thicknesses at 800 and 900°C in air. The steel shows a strong dependence of oxidation rate for different component thicknesses during the 900°C oxidation test. The two thinnest specimens showed breakaway oxidation occur after various oxidation times. At 800°C (figure 6.24), the thinner specimen oxidised faster than the thick one, however the effect is less substantial than in the case of the 900°C.

Figures 6.26 and 6.27 present metallographic cross-sections (SEM images) of specimens with different thicknesses after oxidation at both studied temperatures. In this case, the oxide scale consisted of a thick, single layer of chromia. The results confirm the weight change data from figures 6.24 and 6.25 showing that at 800°C, the oxide scale thickness in the two studies are almost identical, however at 900°C the thin specimen shows a much thicker oxide scale than the thick specimen after the same oxidation time.

Figure 6.28 shows metallographic cross-sections of the thin specimen of model steel HCE oxidised at 900°C until breakaway. Such components studied during oxidation at 900°C show the indication of oxide cracking during oxidation and/or cooling (compare section 6.2).

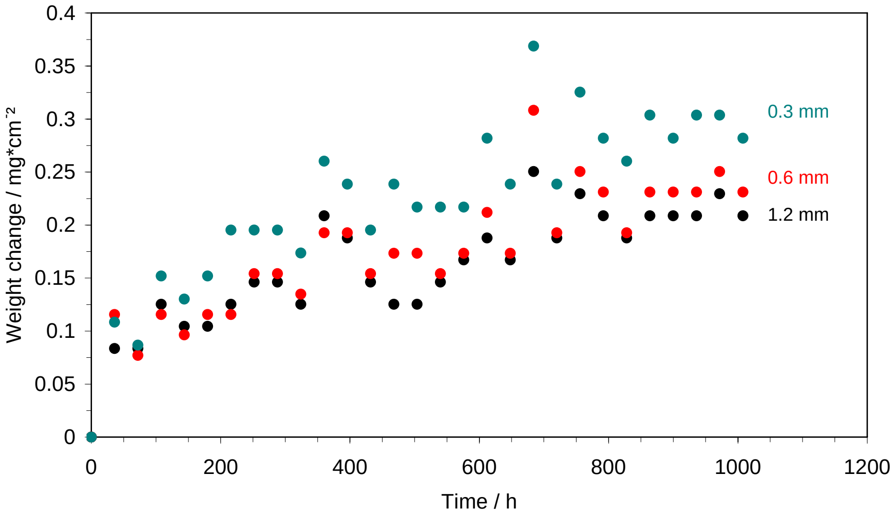

Figure 6.24: Weight change during cyclic oxidation of model alloy HCE at 800°C in air (specimens with different initial thicknesses).

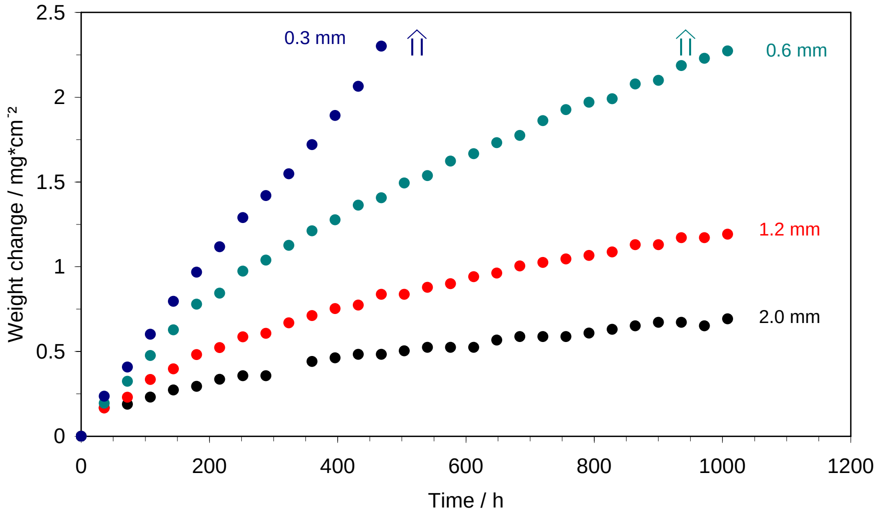

Figure 6.25: Weight change during cyclic oxidation of model alloy HCE at 900°C in air (specimens with different initial thicknesses).

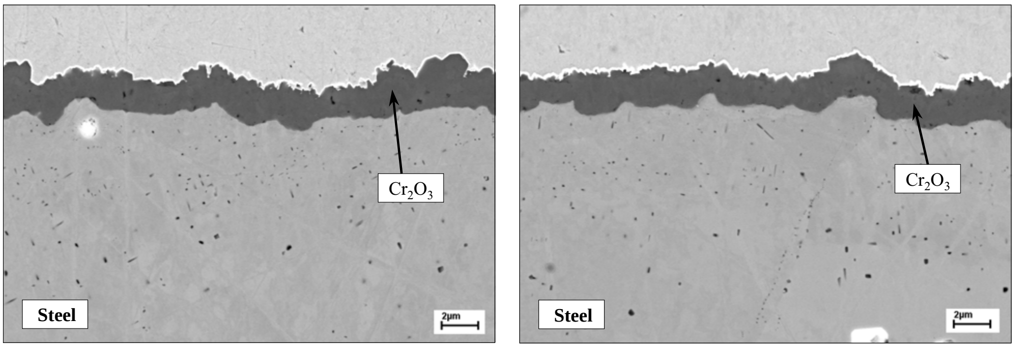

a) b)

Figure 6.26: Oxide scale morphology (SEM images) of model steel HCE after 1000 h cyclic oxidation at 800°C in air; a) – 1.2 mm thickness, b) – 0.3 mm thickness

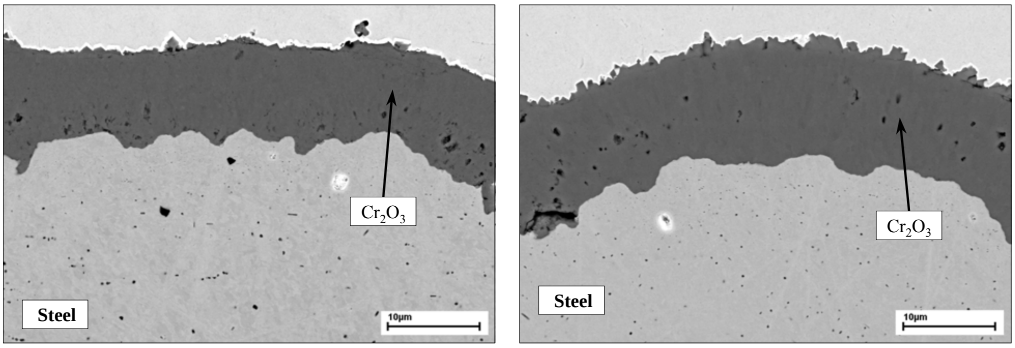

a) b)

Figure 6.27: Oxide scale morphology (SEM images) of model steel HCE after 1000 h cyclic oxidation at 900°C in air; a) – 2.0 mm thickness, b) – 0.6 mm thickness

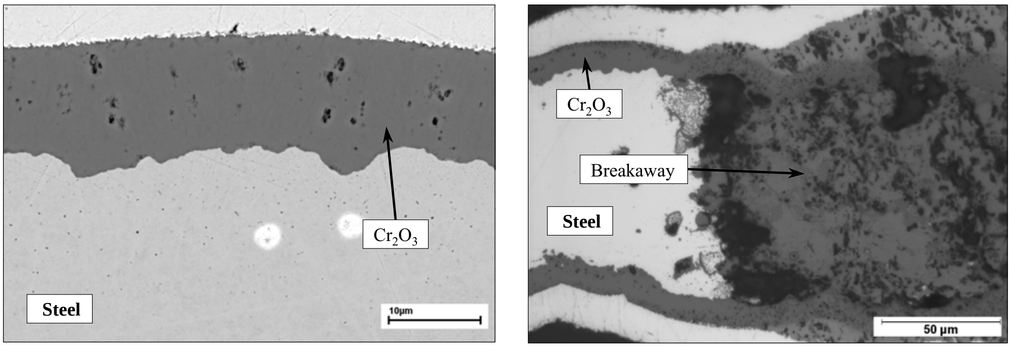

a) b)

Figure 6.28: Oxide scale morphology of model steel HCE after 468 h cyclic oxidation at 900°C in air; a) – area without breakaway (SEM image), b) – area with breakaway (metallography)

Model steel FeCrMnY (high Mn concentration, HCH)

Figures 6.29 and 6.30 show weight change data versus time for the model steel HCH for long-term oxidation at 800 and 900°C in air. At both studied temperatures, thick as well as thin specimens show similar weight change results. At 900°C, the weight change of the thin specimens is slightly lower than that of the thick one despite the fact that breakaway oxidation occurred in the thin specimen.

Figures 6.31 and 6.32 present metallographic cross-sections (SEM images) for steel HCH after long-term oxidation at 800 and 900°C in air. At 800°C, the oxide scale consisted of an outer layer of Cr/Mn spinel, chromia layer beneath and Mn-rich oxide at the scale alloy interface. There is no difference in oxide scale thickness between the two studied specimens. Cross-sections presented in figure 6.32 (900°C) show a double-layered oxide scales (Cr/Mn spinel and chromia) in both cases. In the case of the thin component, the oxide scale is thinner than that of the thick component. Besides, a clear difference exists in the Cr/Mn spinel – Cr_2O_3 ratio for samples with different initial thicknesses (compare section 6.1.3).

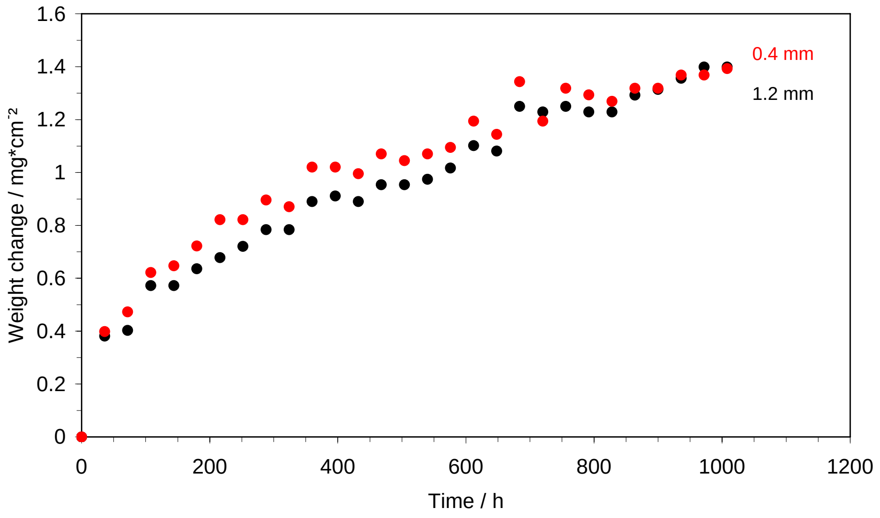

Figure 6.29: Weight change during cyclic oxidation of model alloy HCH at 800°C in air (specimens with different initial thicknesses).

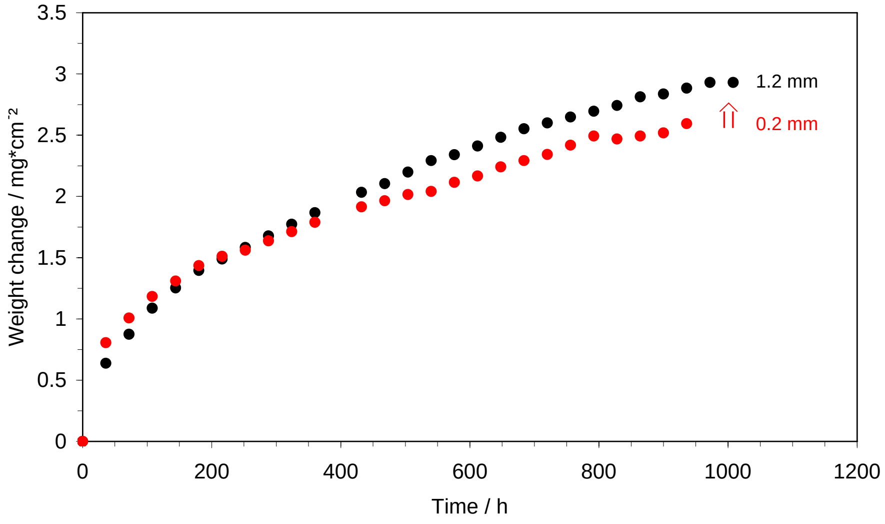

Figure 6.30: Weight change during cyclic oxidation of model alloy HCH at 900°C in air (specimens with different initial thicknesses).

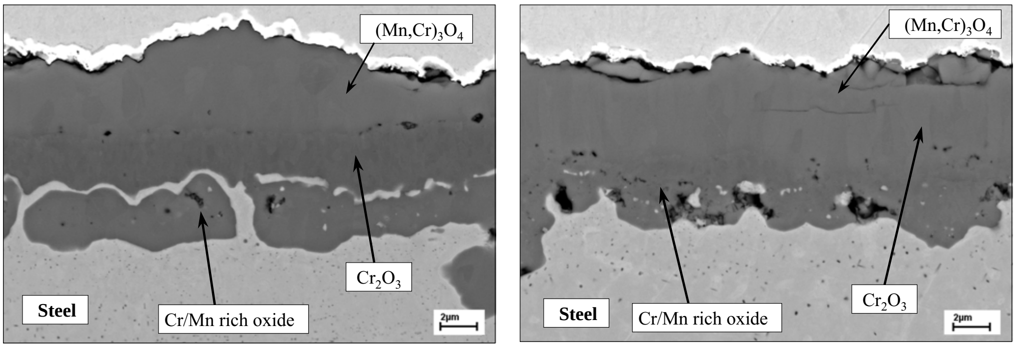

a) b)

Figure 6.31: Oxide scale morphology (SEM images) of model steel HCH after 1000 h cyclic oxidation at 800°C in air; a) – 1.2 mm thick, b) – 0.4 mm thick

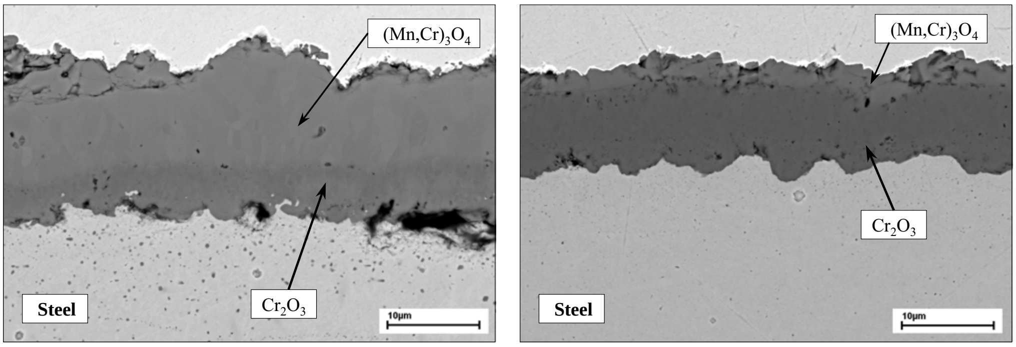

a) b)

Figure 6.32: Oxide scale morphology (SEM images) of model steel HCH after cyclic oxidation at 900°C in air; a) – 1.2 mm thick (oxidation time 1000 h), b) – 0.1 mm thick (oxidation time 900 h, breakaway)

6.1.3 Oxidation rate dependence on the specimen thickness – discussion

Summarising the long-term oxidation studies for the investigated steels it can be concluded that, with exception of steel HCH, there is a clear difference in the oxidation rate between specimens of different component thicknesses. In other words, the oxidation rate k_p is higher for thinner than for thicker components. In this section a detailed discussion about a possible explanations for this effect will be elaborated.

Depletion of chromium

A first possible explanation for this k_p dependence on specimen thickness might be that the continuing depletion of scale forming elements, mainly Cr, leads to a change in the composition of the surface scale and consequently to a change in the oxide growth rate. For Fe – xCr ferritic steels (x = 16 - 20 wt. %, i.e. even for Cr contents which provide protective scale formation) it was found by several authors that a lower initial concentration of chromium in the alloy leads to a slight increase in the parabolic oxidation rate (k_p) [Wright-1, Malkow-2]. Upon oxidizing specimens of different initial thickness, the Cr content remaining in the alloy after a given period of time will be higher in thicker than in thinner specimens, because the latter possess a smaller Cr reservoir. If the oxidation rate would strongly depend on the Cr content, a steady increase of k_p during the oxidation test should be observed, whereby the time dependence should depend on specimen thickness. However, the results presented in figures 6.3 and 6.4 for Crofer A specimens show that, especially at 900°C, no increase of k_p as a function of oxidation time was observed. It is of course necessary to point out that there is a difference between the oxidation behaviour of steels with initially variable amounts of chromium (compare figure 3.10) and steels where chromium is depleted due to oxidation.

Depletion of minor alloying elements

Minor alloying additions (in a range of a few hundreds to a few tenths of a percent) are known to play an extremely important role in the high temperature behaviour of high-Cr ferritic steels (compare section 3.3.2). For thick sheets, the reservoir of the mentioned elements (i.e. Mn, Ti, La, Y, etc.) in the steel is high enough and therefore they fulfil their task during the oxidation process. However, when the oxidised specimen is relatively thin the depletion of the mentioned elements can have a great influence on the oxidation behaviour in the later stages of oxidation.

Most of the iron based high-Cr ferritic steels for SOFC applications contain of a few tenths of a percent of Mn to create an outer Cr/Mn spinel layer preventing high evaporation of chromium and thus poisoning the cathode in SOFC's [Quadakkers-1]. During oxidation studies of the model steel HCH (high Mn content of ~ 1.5 wt. %) at 900°C in air (compare section 6.1.2) it was found that the thin component had a relatively thin oxide layer of Cr/Mn spinel when compared with the spinel thickness for the thick specimen (compare figure 6.32). EDX manganese depletion profiles performed for both specimens (figure 6.33) show a clear difference in the distribution of Mn after the oxidation process for the samples with different initial thicknesses. The data indicates that for the thin component of steel HCH (figure 6.33 b) manganese was totally depleted from the alloy during oxidation and therefore no more spinel could be formed during further oxidation. Likewise, the manganese profile for the thick specimen (figure 6.33 a) shows that there is still a large Mn reservoir in the steel and therefore further spinel formation is possible. To confirm this finding a theoretical calculation was performed taking into account the Mn concentration in the alloy for different component thicknesses and the theoretical spinel thicknesses, which can be formed from the prevailing reservoir of manganese.

Theoretically, the thickness of the spinel can be calculated using the formula:

$$d_{sp} = \frac{V_{sp}}{S_s} \qquad (6.1)$$

where: d_{sp} is spinel thickness (in μm) built on the specimen surface, V_{sp} is a spinel volume and S_s is the surface of the specimen.

Knowing the mass and volume of the specimen it is easy to calculate the mass of the Mn in the specimen from the steel composition. From the reaction of the formation of Cr/Mn spinel it is possible to calculate the mass of spinel formed from the mass of manganese. Knowing the mass of the spinel and its density (4.91 mg·cm^{-3} [Database]) V_{sp} can be calculated and used in equation 6.1. Calculated values for the maximum thickness of the Cr/Mn spinel for the FeCrMnY model steel (HCH) and Crofer A (JDA) are presented in Table 6.1.

Steel	Batch	Initial Mn concentration [wt. %]	Specimen thickness [mm]	Calculated maximum thickness of Cr/Mn spinel [µm]	Experimental data of thickness of Cr/Mn spinel after oxidation at 900°C in air [µm]
FeCrMnY	HCH	1.55	1.2	53	~ 10 (after 1000 h oxidation)
			0.1	4.7	~ 3 (after 900 h oxidation)
Crofer A	JDA	0.4	2	19	~ 3 (after 1000 h oxidation)
			0.1	1.22	~ 1 (after 250 h oxidation)

Table 6.1: Calculation of the theoretical maximum spinel thickness using equation 6.1

Analysing the calculated data shown in Table 6.1 one may conclude that for the thick specimen (1.2 mm) of model steel FeCrMnY (HCH) it is theoretically possible to form a ~ 53 µm of Cr/Mn spinel, however for 0.1 mm specimen, the theoretical maximum thickness of Cr/Mn spinel layer is only ~ 4.7 µm.

An analogous consideration is also valid for JS-3 / Crofer 22 APU type steels which contains only a relatively low Mn content (compared to model steel HCH). The Mn can be depleted very rapidly in the thin specimens (i.e. 0.1 mm). Figures 6.8, 6.10 and 6.15 present examples of very thin Cr/Mn spinel layers as a result of Mn depletion because of an insufficient Mn reservoir in thin components.

One of the possible explanations for the k_p-dependence on specimen thickness can be that after depletion of manganese in thin specimens, formation of a pure chromia scale is possible in the later stages of the oxidation. Changing from the formation of a double-layered oxide scales (Cr/Mn spinel and chromia) to a single layer of chromia could therefore be responsible for the change of the oxidation rate in thinner components. In other words, formation of Cr/Mn spinel suppresses faster chromia formation in thick components. That would explain the thicker layer of chromia for the thinnest specimens in long-term exposures.

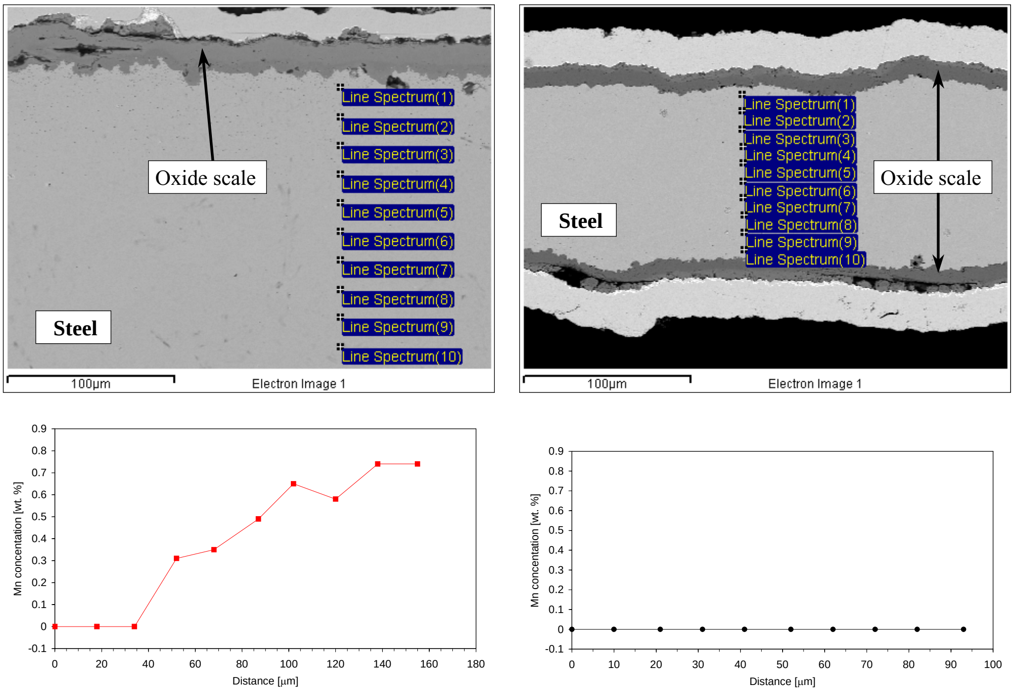

a) b)

Figure 6.33: Oxide scale morphology (SEM images) and corresponding Mn depletion profiles of high-Mn model steel HCH after cyclic oxidation at 900°C in air; a) – 1.2 mm thickness (oxidation time 1000 h), b) – 0.1 mm thickness (oxidation time 900 h, breakaway)

Confirmation for this hypothesis can be seen in the oxidation behaviour of selected model steels (paragraph 6.1.2) with different manganese contents. One of the steels where the thickness dependence of k_p was not observed is the high-Mn model steel FeCrMnY (HCH). In this case, especially during the 800°C exposure the manganese reservoir in thick as well as thin components was high enough to form a Cr/Mn spinel during the whole oxidation process. On the other hand, in steel HCE (model steel with trace impurity of Mn) a clear k_p-dependence as function of component thickness was observed at both studied temperatures. Depletion of Mn in such a case is extremely fast making chromia growth responsible for the oxidation process.

Another important aspect if considering depletion of minor alloying additions can be depletion of reactive elements (i.e. La, Y, etc.) in the alloy. Among other factors, addition of reactive elements into the steel slows down the oxidation rate during the high temperature exposure. If one assumes that, as for manganese, reactive elements are also depleted from the steel matrix (incorporation into the scale), then the oxidation rate could probably be hastened for the thinner specimens.

Internal oxidation

The minor alloying elements Si, Ti and/or Al might also play a role in the k_p dependence on specimen thickness. All these elements tend to internally oxidise, resulting in a “generation of volume” and thus stress formation in the bulk alloy (compare sections 5.3.1 and 5.3.3). The resulting plastic deformation of the substrate and its effect on scale formation will be more pronounced for a thin than for a thick specimen. On the other hand it was observed that in thin components depletion of silicon and especially aluminium took place which reduced the width of the internal oxidation zone in thinner components (compare figure 6.8)

Doping effect in the oxide scale

The explanation of the thickness dependent oxidation rate has to incorporate the fact that oxidation rates of the studied steels (especially Crofer A) are in certain periods of the exposure affected by in-scale microcrack formation (see section 5.3.3). This is the case even during isothermal exposure but is expected to become even more pronounced during thermal cycling.

If we consider the micro crack-formation and –healing mechanism mentioned in section 5.3.3 (figure 5.16) comparing two specimens of different thicknesses, then the Cr and Mn content at the scale/alloy interface at the base of a micro crack will, because of the differences in Cr- and Mn-reservoir, after a given oxidation time be smaller in the thinner than in the thicker specimen. Consequently, the oxide on the thinner specimen will tend to incorporate larger amounts of Fe than the oxide on the thicker specimen. The oxide on the thin specimen will tend to experience a stronger increase in growth rate by Fe incorporation than that on the thick specimen.

Oxide growth and thermally induced stresses

The change in oxidation rate with changing specimen thickness could also be related to stresses generated during the oxidation process. Growth stresses in the oxide [Schütze-1, Schütze-2] may lead to plastic deformation of the metallic substrate [Wilber-1]. Assuming the growth stresses in the oxide to be compressive, and thus the stresses in the bulk alloy to be tensile, the specimen would in the ideal case increase in length [Evans-1] (see also: Elongation effect, section 6.1.3). The length increase will depend on numerous factors such as the magnitude of the growth stress, the creep resistance of the alloy as well as the thickness of the oxide scale and the metallic substrate [Schütze-2]. However, in reality the oxide scale thickness will not be absolutely identical over the whole specimen. The stress generated in the metallic substrate will thus represent a stress state, which is non-homogeneous over the specimen thickness. This may result in a bending of the metallic substrate, as was, macroscopically observed of the thinnest specimen of 0.1 mm (compare figures 6.5, 6.6 and 6.7). The specimen bending will likely result in scale cracking leading to enhanced access of oxygen to the metal surface and thus to an increased oxidation rate.

An additional factor might be that during thermal cycling, relaxation of thermally induced stresses during cooling may, after re-heating to the oxidation temperature, lead to tensile cracking of the scale [Evans-1] resulting in paths for access of molecular oxygen and thus enhanced scale growth rates. The process is schematically shown in figure 6.34.

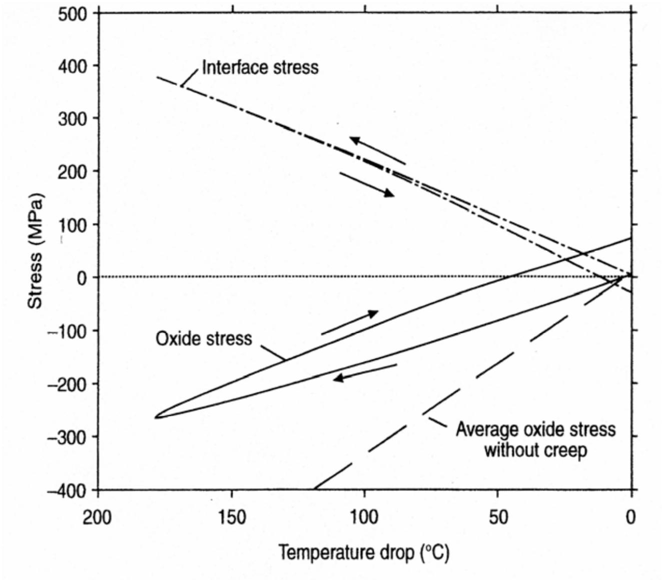

Figure 6.34: Schematic diagram of the stress formation during cooling of the specimen leading to a tensile cracking [Evans-2]

Figure 6.35 shows a typical example of such a behaviour for steel JS-3 oxidised for 1000 h at 900°C in air, showing deformation points and their influence on the formation of a double-layered oxide scale (inhomogeneity in Cr/Mn spinel thickness).

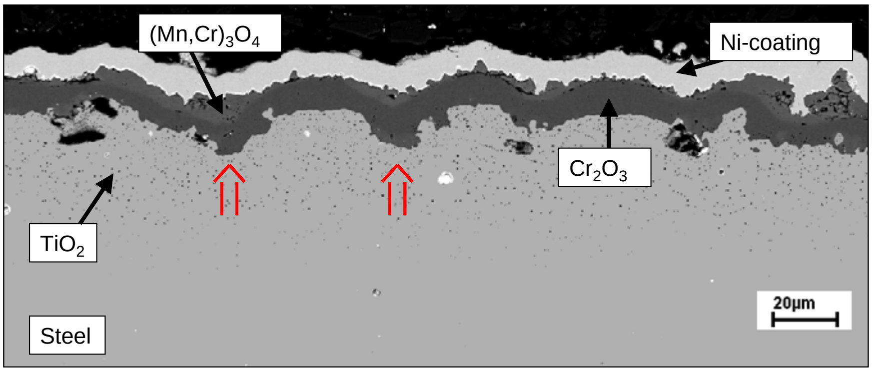

Figure 6.35: Oxide scale morphology (SEM images) of steel JS-3 after 1000 h cyclic oxidation at 900°C in air (specimen thickness: 1.2 mm)

Elongation effect

Investigation of specimens with a different initial thickness could lead to thinnest components increasing in length during oxidation as a result of oxide growth stresses. In such a case the area of the specimen before the oxidation would be different from that after high temperature exposure. This would finally change the specimen area used for weight change calculations showing higher weight changes because of smaller specimen areas used for calculations. Therefore, the dimensions of the selected specimens were investigated before and after oxidation tests. For the thinnest specimens this was sometimes not possible because of bending of the sample during oxidation. As a result a slight increase of specimens dimensions was found especially in the 900°C exposures (Table 6.2), however this effect is not strong enough the explain the k_p-dependence on the specimen thickness. Besides, the numerous metallographic cross-sections (see e.g. Figure 6.9) revealed that higher weight change are indeed mainly related to thicker oxide scale rather than larger effective specimens surface areas.

Material	Specimen thickness [mm]	Oxidation time [h]	Length of specimen before oxidation [mm]	Length of specimen after oxidation [mm]
Crofer A $_{\text{(JMB1)}}$	0.1	250	19.28	1)
Crofer A $_{\text{(JMC1)}}$	0.3	1000	19.52	20.71
Crofer A $_{\text{(JMD1)}}$	0.5	1000	20.10	21.08

1) Strong deformation – measurement impossible

Table 6.2: Elongation of Crofer A specimens after cyclic oxidation at 900°C in air

Thermal cycling effect

For the long term-oxidation studies in most cases cyclic or discontinuous oxidation tests were performed. Therefore, the change in oxidation rate with changing specimen thickness could also be related to the “cycling effect”. To prove this hypothesis cyclic as well as isothermal oxidation was performed for 100 h oxidation test at 900°C. Thick and thin specimens were used and for minimising external effects the same furnace was used for both types of experiments. Figure 6.36 shows weight changes for three different steels (JS-3, Crofer A and model steel HCE) after 100 h oxidation at 900°C in air in cyclic and isothermal oxidation conditions. The results clearly show that for thin as well as thick specimens there is almost no difference between these two kinds of exposures. The oxidation rate dependence on specimen thickness occurs in both studied cases (cyclic exposures – isothermal exposures).

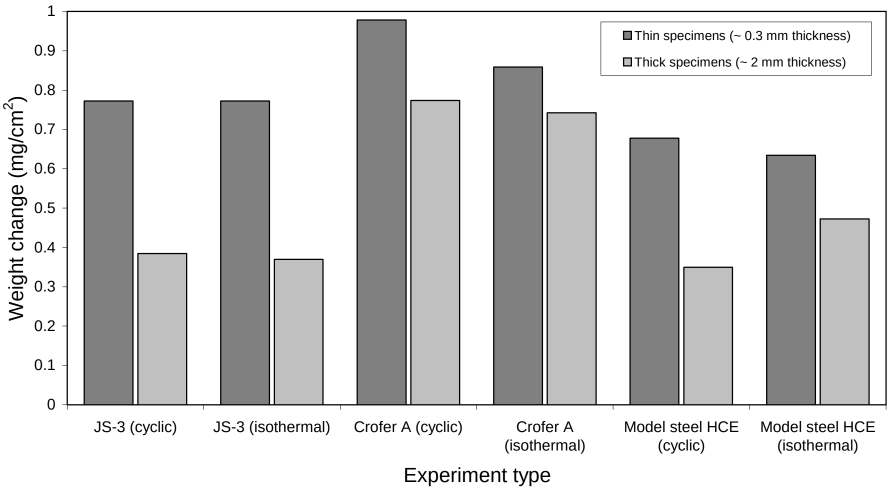

Figure 6.36: Weight change after 100 h oxidation of various steels at 900°C in air (components with different initial thicknesses, cyclic and isothermal oxidation)

Also the oxide scale morphology analysed after the oxidation tests (figure 6.37) show a large difference in the oxide scale thickness between thick and thin components but a similar morphology of the oxide scale for different oxidising atmospheres for the same specimen thickness. This finding leads to the conclusion that at least in the earlier stages of oxidation (e.g. < 100 h at 900°C) the “cycling effect” is not responsible for the k_p dependence on specimen thickness.

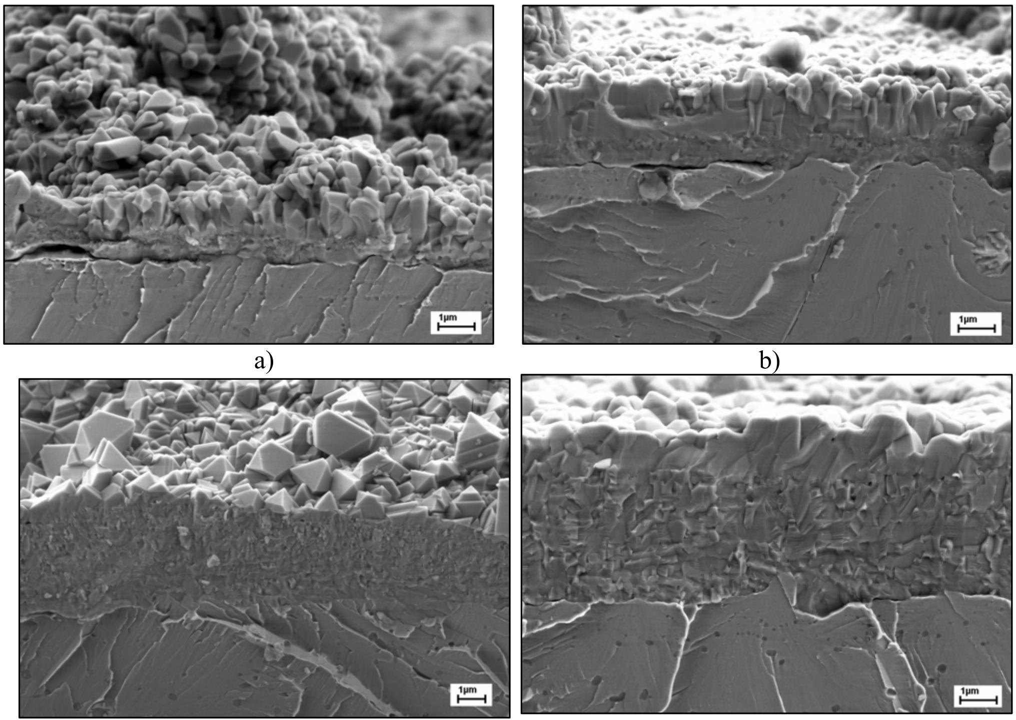

a) b)

c) d)

Figure 6.37: Oxide scale morphology (SEM cross fracture) of steel JS-3 (batch: JEW) after 100 h oxidation at 900°C in air; a) – 2 mm thickness (cyclic), b) – 2 mm thickness (isothermal), c) – 0.3 mm thickness (cyclic), d) – 0.3 mm thickness (isothermal)

Effect of water vapour during the air oxidation

Extensive oxidation studies performed in laboratory air show a strong thickness dependence on the oxidation rate. However, similar studies in the controlled atmosphere of dry synthetic air show far lower changes in the oxidation rate for different component thicknesses. Therefore, to fully understand this effect a number of experiments for specimens with different initial thicknesses were performed in controlled atmospheres of dry and wet air. For thin components, as opposed to the thick samples discussed in paragraph 5.3.4, there was a real difference in oxidation rate between the different oxidising atmospheres. The results presented in figure 6.38 show weight change data for the specimens with different component thicknesses in various controlled atmospheres. Analogous to the results presented in the literature [Otsuka-1, Fujikawa-1, Garcia-1, Pint-1] it was concluded that the addition of water vapour enhanced the oxidation rate of high-Cr ferritic steels. This effect is more pronounced for thin specimens when oxidised during a relatively short times of 100 h. Figure 6.39 presents differences in oxide scale morphology and thickness for samples of Crofer A with an initial thickness of 0.1 mm after 100 h oxidation in various atmospheres. This results show a clear difference between thicknesses of the chromia scale for different oxidising atmospheres. Figure 6.40 shows Cr depletion profiles for the specimens presented in figures 6.38 and 6.39, which show that in the wet air atmosphere the depletion of chromium is much faster than in dry air for thin components.

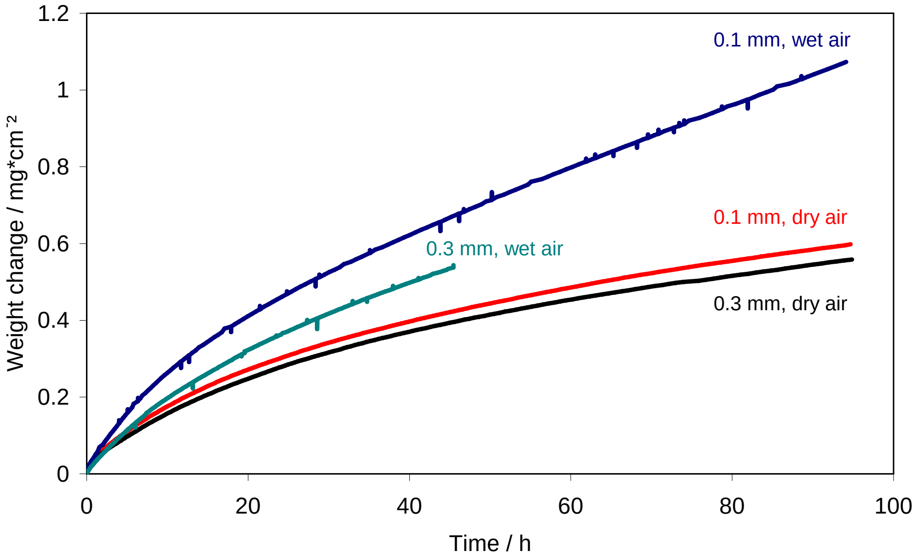

Figure 6.38: Mass change during isothermal oxidation of steel Crofer A at 900°C in various atmospheres for specimens with different initial component thicknesses (wet air: synthetic air + 7 % H_2O).

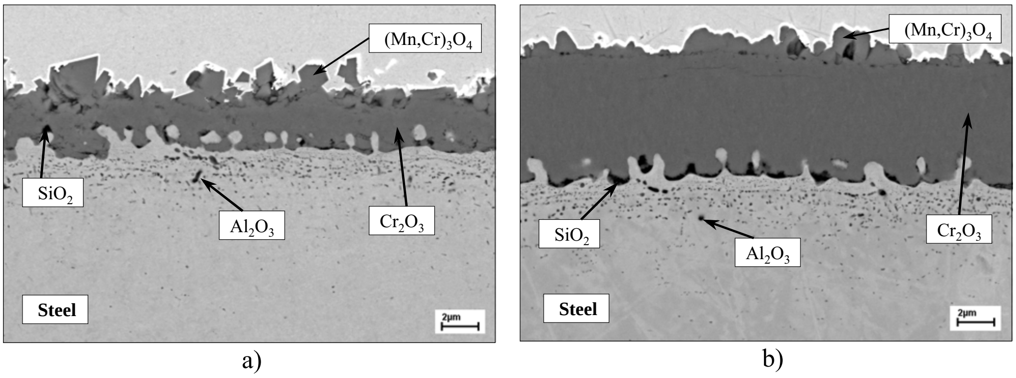

a) b)

Figure 6.39: Oxide scale morphology (SEM images) of steel Crofer A after 100 h isothermal oxidation (TG) at 900°C in air (specimen thickness: 0.1 mm); a) – dry air (synthetic air), b) – wet air (synthetic air + 7 % H_2O)

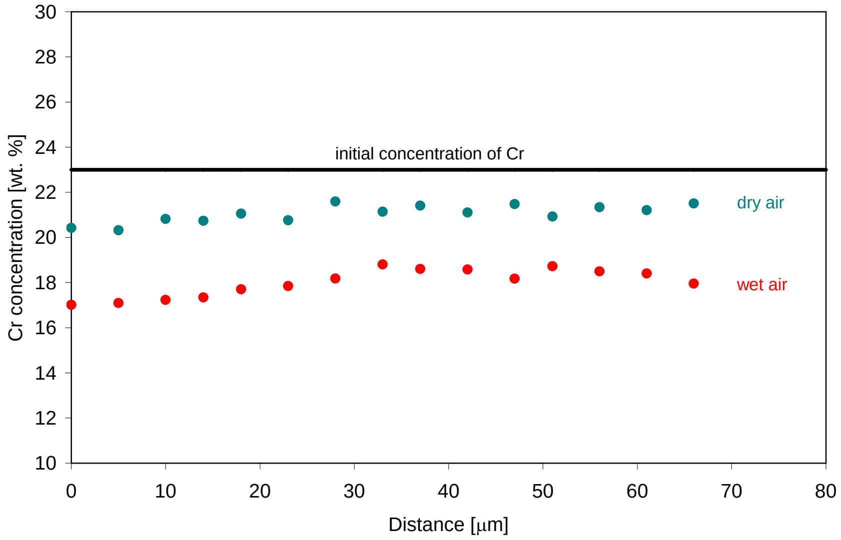

Figure 6.40: Measured Cr depletion profiles for specimens of Crofer A (specimen thickness: 0.1 mm) after 100 hours of isothermal oxidation at 900°C in various atmospheres (wet air – synthetic air with 7 % H_2O).

Effect of steel microstructure

The growth rate of the chromia scale could also be related to the microstructure of the steel. It is, for instance, well established that the transition to selective oxidation of chromium takes place at lower chromium contents for cold-worked alloys and for alloys with a small grain size. It is generally concluded that this is due to the more rapid diffusion of chromium along grain boundaries and short-circuit paths in the alloy [Kofstad-1].

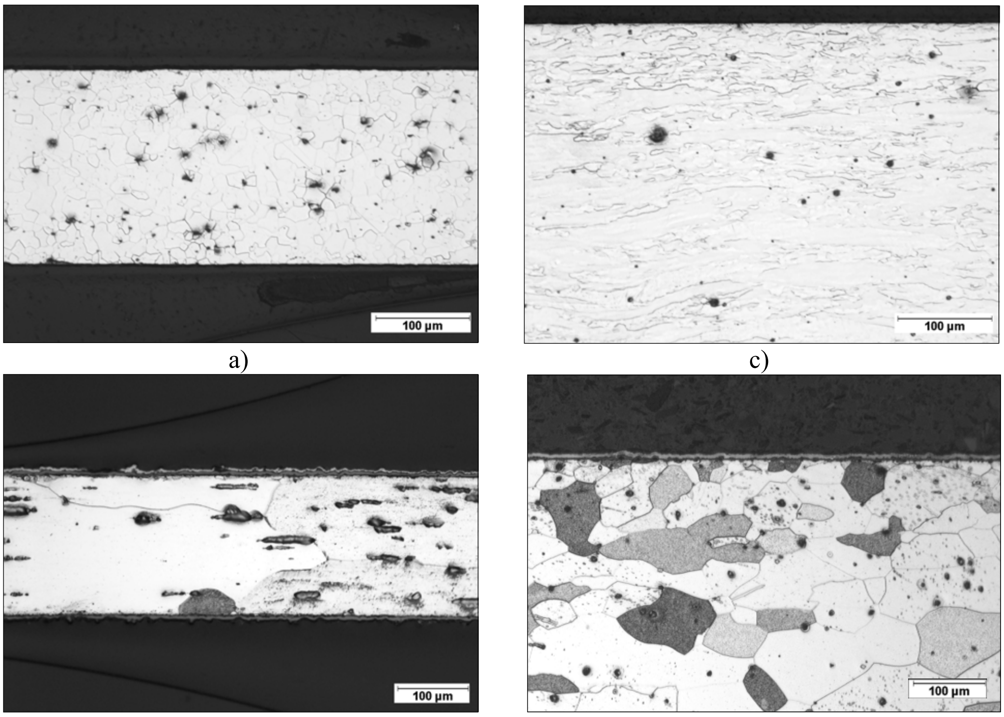

a) c)

b) d)

Figure 6.41: Microstructure of Steel Crofer B „as received“ and after 1000 h discontinues oxidation at 800°C in air; a) - thin specimen as received (0.2 mm $_{\text{JZN}}$), b) - thin specimen after 1000 h oxidation at 800°C in air (0.2 mm $_{\text{JZN}}$), c) - thick specimen as received (~ 3 mm $_{\text{JZF}}$), d) - thick specimen after 1000 h oxidation at 800°C in air (2 mm $_{\text{JZF}}$)

Figure 6.41 shows microstructures of steel Crofer B for plates with different initial thicknesses analysed “as received” and after 1000 h oxidation at 800°C. It is clearly visible that the 0.2 mm delivered plate (6.41 a) has a different microstructure from that with ~ 3 mm thickness (6.41 c). In both cases the materials were cold rolled and heat treated, resulting in a small and homogenous grain size for the components (6.41 a). However, thick components show insufficient metallurgical treatment showing in-homogeneity in the grain size (larger grains in the inner parts of the steel (6.41 c)). Smaller grain sizes for thin components may cause more rapid chromium diffusion via grain boundaries compared to thick components. However, it is necessary to take into account that the material re-crystallized during the oxidation process, so in the final stage of oxidation the grain size of the thin components is even larger than that for the thick one (figure 6.41 b and d).

As described in section 4.2 in most studied cases only one, thick plate of the material was available so the thin components were prepared by grinding the thick specimens to the required levels. In such cases there is no difference in grain size exists for the different specimens before oxidation because the specimens were prepared from the same initial plate. However, in such a case the thickness dependence of k_p was also observed (see e.g. section 6.1.2), thus the microstructure effect can not be the main explanation for the k_p-dependence on the specimen thickness.

Surface preparation

The data presented in the literature [Kofstad-1] clearly shows that surface preparation of the specimens may have an influence on oxidation. It is frequently concluded that polished specimens oxidised faster than ground ones. In the present studies all thick specimens were ground to 1200 grit surface finish using SiC grinding paper. For the delivered thin components the surface were left “as delivered” to keep the specimen thickness at the required level. The surface of the delivered plates seemed to be a bit smoother than those prepared in laboratory, however it was found that this effect could not be the main explanation for the k_p-dependence on the specimen thickness. This is especially obvious, when specimens of different thicknesses were prepared for one and the same plate. In that case all specimens experienced the same surface treatment and yet the thickness dependence of k_p was found.

6.1.4 Summary of specimen thickness effect during cyclic oxidation

Figures 6.42 and 6.43 summarise cyclic oxidation results for the studied steels taking thickness dependence into account. The results show, that the thickness dependence of the oxidation rate is for "shorter" oxidation times in fact quite similar for all studied steels, with exception of the high-Mn alloy HCH, which poses an "intrinsic" high growth rate. "Shorter" means in this context approximately 1000 h at 800°C and ~ 100 h at 900°C (figures 6.42 and 6.43 a). Major difference occurs after longer times of cyclic oxidation, especially at 900°C (figure 6.43 b). Then, enhanced oxidation as a result of cyclic induced oxide cracking become dominating. The tensile cracking (see section 6.1.3) becomes more pronounced in case of weak (i.e. thin) specimens and alloys. This has as a result, that thin specimens of the alloys with low amount of minor impurities (such as JS-3 and Crofer B) show a strong enhancement of the oxidation rate after long term cyclic oxidation, because of their lower creep strength compared to e.g. Crofer A (figure 6.43 b).

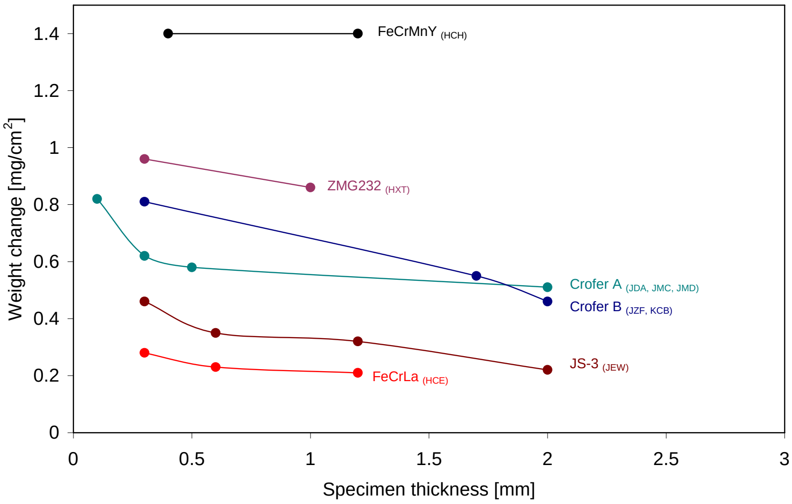

Figure 6.42: Summarised cyclic oxidation results for different steel as function of specimen thicknesses after 1008 h oxidation at 800°C in air.

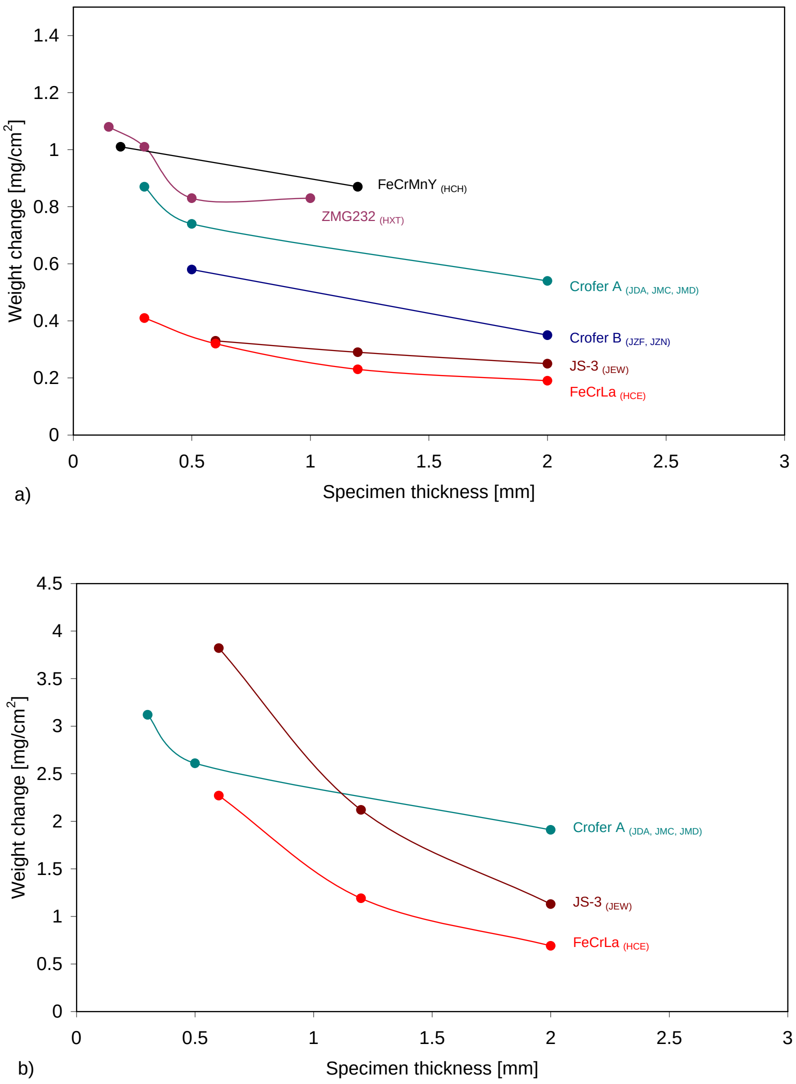

Figure 6.43: Summarised cyclic oxidation results for different steel as function of specimen thicknesses after oxidation at 900°C in air; a) 72 h, b) 1008 h

6.2 Mechanism of breakaway oxidation

The occurrence of the breakaway phenomenon strictly depends on the amount of chromium depleted at the scale/steel interface (ΔC) during the oxidation process (Figure 6.44):

$$\Delta C \sim \left(\frac{k_p}{D}\right)^{\frac{1}{2}} \qquad (6.2)$$

where: D is the diffusion coefficient of the scale forming element (Cr) in the alloy and k_p is the parabolic oxidation rate constant in cm^2s^{-1} [Kofstad-1].

If the ratio $\frac{k_p}{D}$ is small, the depletion profile of chromium will be flat as schematically shown in figure 6.44a [Quadakkers-9]. In such a case breakaway oxidation will occur when the chromium concentration will drop beneath a critical level in the whole specimen volume (breakaway type 1).

When a ratio $\frac{k_p}{D}$ is large, a steep slope in the depletion profile beneath the oxide scale will develop [Quadakkers-9, England-1] as is schematically shown in figure 6.44b. In such a case the steel is only heavily depleted in chromium beneath the scale/alloy interface, which can lead to the formation of the fast growing oxide, in spite of the fact that the total amount of chromium in the steel is still higher than the critical chromium content for occurrence of breakaway oxidation (breakaway type 2).

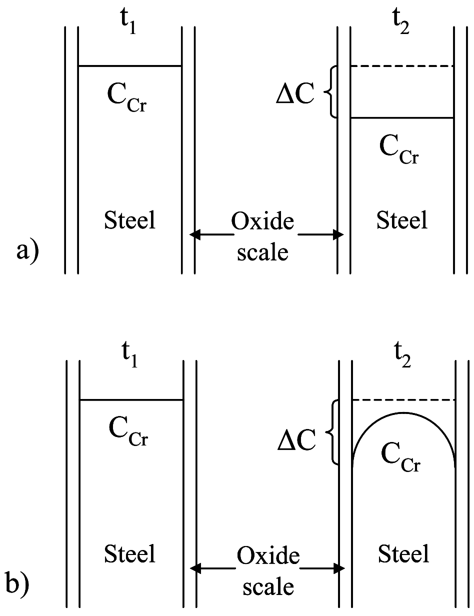

Figure 6.44: Schematic illustration of different type of Cr depletion profiles leading to breakaway oxidation: a) type 1 (k_p/D small), b) type 2 (k_p/D large)

A good example of both discussed behaviours can be found in figure 6.40. In the case of the dry air specimens the depletion profile of chromium is much flatter than in the specimen exposed to air + 7 % H_2O. The specimen exposed to air could finally lead to the breakaway phenomenon type 1 and to the breakaway phenomenon type 2 for the specimen exposed to air + 7 % H_2O.

It was found that for most studied cases breakaway type 1 occurs i.e. the slopes of the Cr-profiles are quite small and consequently can, with reasonable accuracy, be described as being flat (compare figure 6.52).

To get a more detailed insight into the effect of the catastrophic breakaway attack, the specimen was further exposed up to a final oxidation time of 900 h after visually observed breakaway. Figure 6.45 shows the weight change of a Crofer B sample (thickness: 0.2 mm) during breakaway oxidation at 900°C in air. The macroscopic image presented in figure 6.45 shows an advanced stage of catastrophic attack after oxidation.

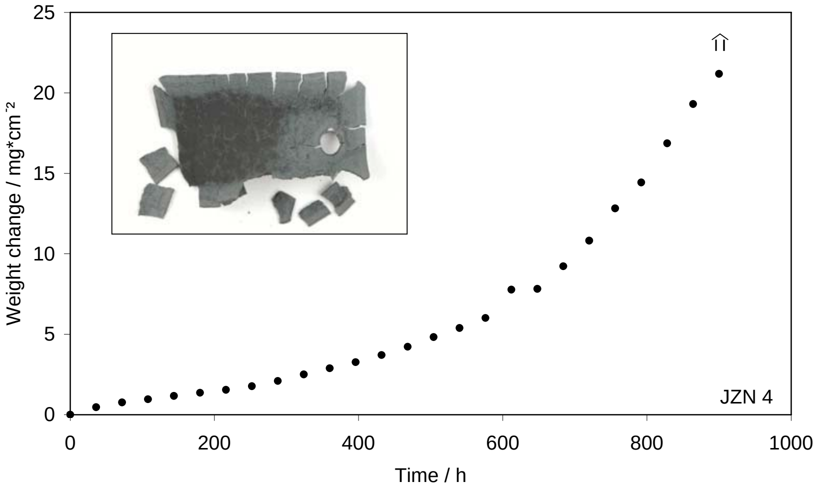

Figure 6.45: Mass change during cyclic oxidation of steel Crofer B at 900°C in air (JZN 4, specimen thickness 0.2 mm, breakaway).

Metallographic cross-sections (SEM images) presented in figure 6.46 show different stages of breakaway oxidation in various areas of the investigated specimens. A classic protective chromia scale is presented in picture 6.46 I, however in several specimen regions a large crack through the oxide scale was observed (6.46 II). It was also found in several places that iron oxide started to form in the area of the crack (6.46 III, IV). In the final stage (6.46 V) iron oxide grows inward and outward resulted in complete oxidation of the specimen.

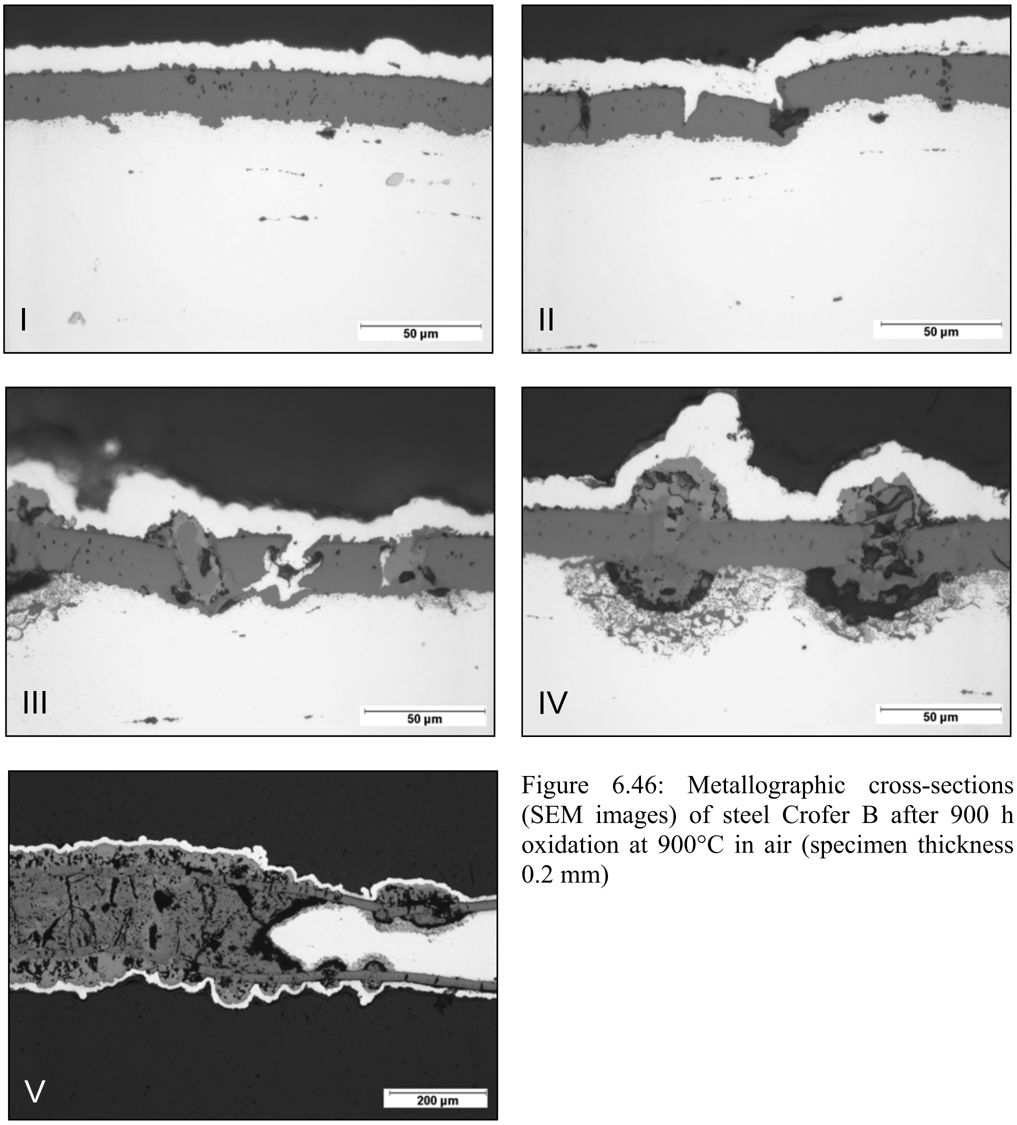

Figure 6.46: Metallographic cross-sections (SEM images) of steel Crofer B after 900 h oxidation at 900°C in air (specimen thickness 0.2 mm)

Detailed investigations of the area presented in figure 6.46 IV show that in the early stages of iron oxide formation chromium started to oxidise in the form of stringers embedded in the matrix of the steel (figure 6.47). Furthermore, a gap between the steel and the oxide was observed in the first stage of the catastrophic attack.

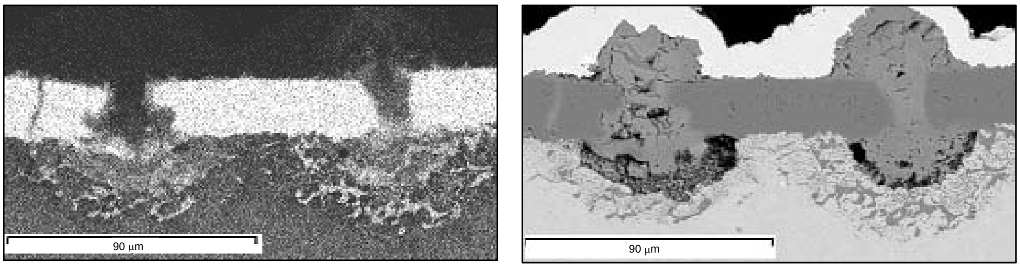

Cr

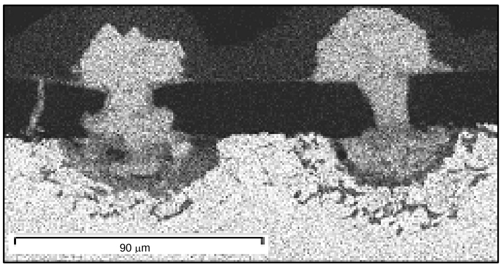

Fe

Figure 6.47: SEM element mapping of steel Crofer B after 900 h oxidation at 900°C in air (specimen thickness 0.2 mm)

Summarizing the results presented above, the mechanism of breakaway oxidation is proposed and schematically shown in figure 6.48. Dense at the beginning of oxidation oxide scale (6.48 a) is cracked due to oxide growth and/or thermally induced stresses. In the first oxidation stage the Mn and Cr reservoirs are high enough to re-heal the mentioned cracks (6.48 b). However, when the Cr (and also Mn) concentration reaches a level at which no more protective Cr-rich oxide can be formed, iron oxide starts to grow through the oxide scale cracks (6.48 c). In the later stages of catastrophic attack, the remaining chromium in the alloy oxidises in the form of stringers embedded in the material matrix and a large gap between steel and oxide scale formed (6.48 d). In the final stages of the breakaway oxidation, the whole specimen area is oxidised, however it is still possible to detect the Cr-rich oxide scale formed prior to breakaway oxidation.

Based on the considerations presented above it is possible to conclude that breakaway oxidation in such a case is caused more due to a mechanical mechanisms (crack formation) rather than due to a “chemical” one. However, it is necessary to take into account that the first reason for catastrophic attack is depletion of Cr and crack formation only accelerates the occurrence of breakaway oxidation.

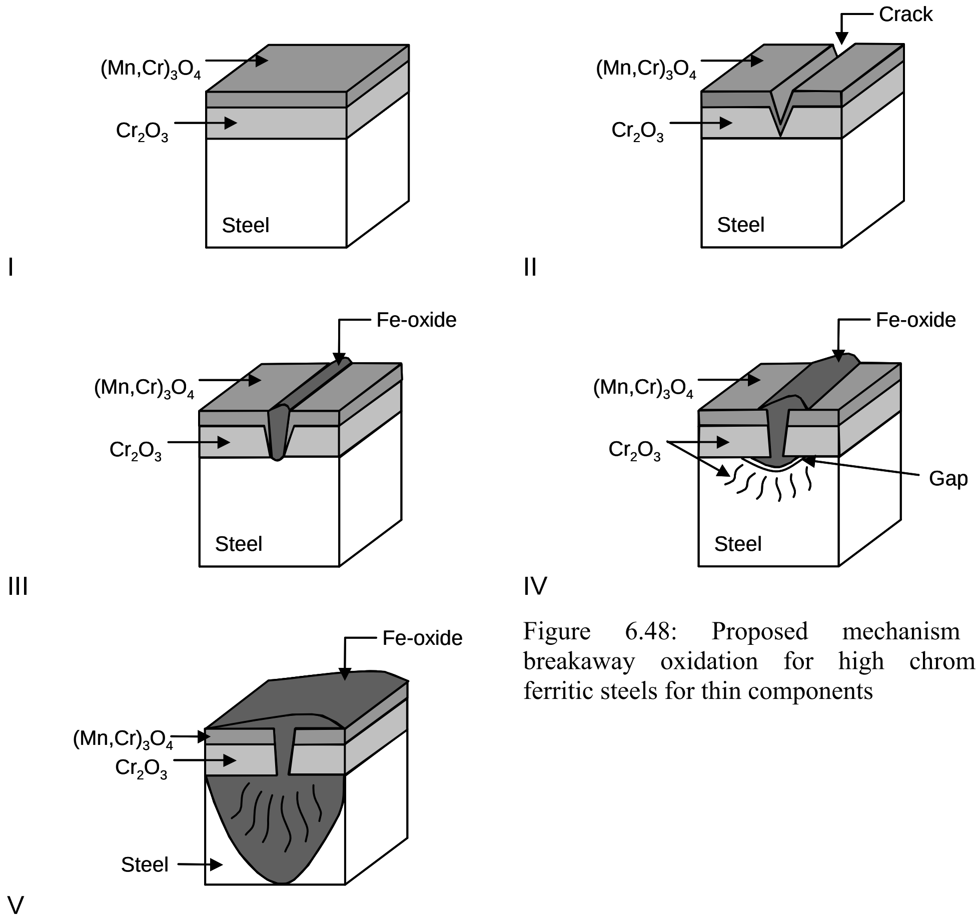

Figure 6.48: Proposed mechanism of breakaway oxidation for high chromium ferritic steels for thin components

The mechanism presented above is mainly valid for thin components where a thick oxide scales and the occurrence of stresses lead to crack formation. In case of thick components especially at lower temperatures (800°C) the chemical mechanism of the breakaway oxidation is expected rather than the mechanical one because the thinner oxide is less susceptible to crack formation during high temperature exposure.

Analysing chromium depletion profiles of the thinnest components it was found in several cases that after occurrence of breakaway oxidation the profile became more flat than in specimens after shorter oxidation times. Figure 6.49 shows chromium depletion profiles after different times of isothermal oxidation for specimens of Crofer A with 0.1 mm initial thickness. The relatively steep Cr depletion profile after 50 h of oxidation become flat when analysing specimens after 200 h and 250 h of oxidation, i.e. after occurrence of breakaway. The explanation of this fact could be that when breakaway oxidation occurs Fe becomes more rapidly oxidized than Cr resulting in equalization of the Cr concentration in the whole specimen volume.

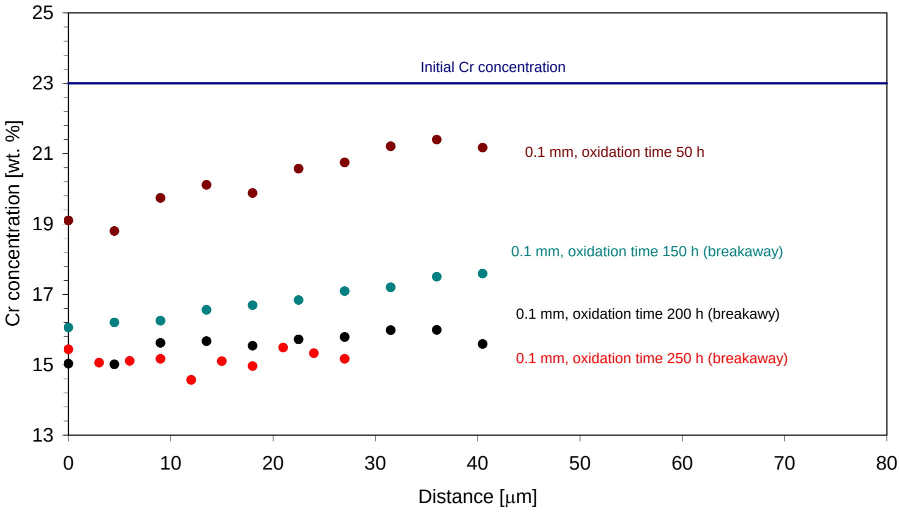

Figure 6.49: Measured Cr depletion profiles for specimens of steel Crofer A (batch JMB) during isothermal oxidation at 900°C in air.

It was found that during an oxidation of different samples from the same batch (repeated exposures for checking reproducibility) relatively high discrepancies in the weight change data were observed during prolonged exposures whereas in the earlier stages of oxidation the results show excellent reproducibility. A typical examples of such a behaviour are presented in figure 6.50. After about 400 h of exposure the weight change data starts to vary for different specimens. Taking into account the mechanism presented in figure 6.50, crack formation is a dominant process in such a case during prolonged exposure times. The crack formation is a statistical process, which depends on stress distribution, and therefore it is easy to understand that for different samples different weight changes are being observed. As the weight change is a direct measured for the consumption of scale forming elements, the data scatter after prolonged oxidation implies, that in determining occurrence of breakaway oxidation a “natural scatter” of the data points has to be taken into account.

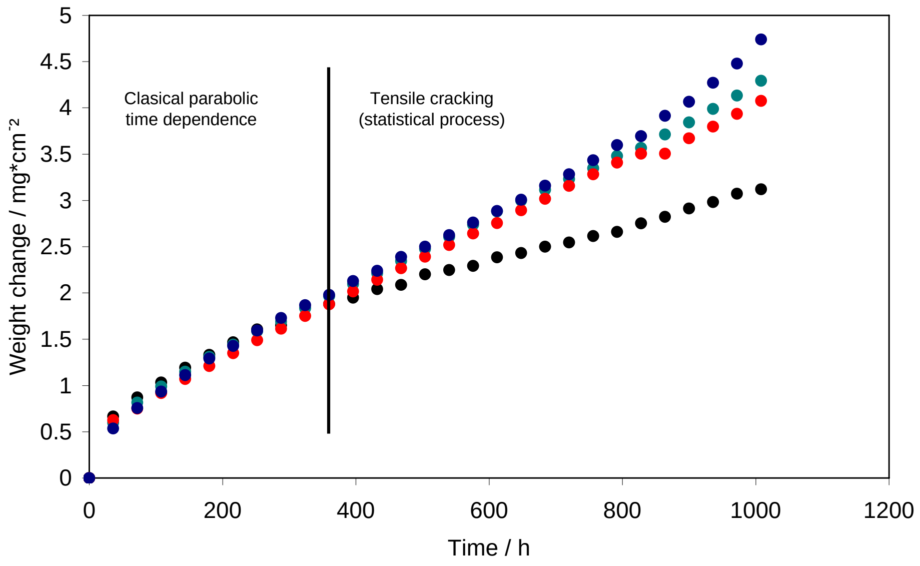

Figure 6.50: Mass change during cyclic oxidation of a 0.3 mm thick specimen (JMC) of Crofer A at 900°C in air showing scatter of oxidation rates after prolonged oxidation.

6.3 Lifetime prediction of chromia forming ferritic steels

As shown in paragraphs 5.1 and 6.1 depletion of chromium for Cr-rich ferritic steels leads in many cases to a breakaway oxidation phenomenon, which represents the lifetime limit of the mentioned steels. It is now proposed that the oxidation-limited life for chromia forming ferritic steels in the temperature range 800-900°C could be predicted by a similar approaches as those previously used for FeCrAl alloys (compare section 3.4.1) [Huczkowski-1, 2]. Therefore equations used in references [Quadakkers-8, 9, Gurrappa-1, Nicholls-1] were adjusted in such a way that they can be used for the investigated chromia forming ferritic steels.

In the model a flat specimen of thickness d (in cm) and infinite length and width was considered [Quadakkers-9]. The oxygen uptake (in $mg \cdot cm^2$) by the specimen surface A due to oxide scale growth is given by [Quadakkers 9, Gurrappa-1]:

$$\frac{\Delta m}{A} = k \cdot t^n \qquad (6.3)$$

in which t is the oxidation time in hours, k the oxidation rate constant and n the oxidation rate exponent [Gurrappa-1].

Assuming that the surface oxide consists completely of Cr_2O_3 (i.e. the Cr/O weight ratio is equal to 2.168), the amount of chromium $\frac{\Delta m(Cr)}{A}$ (in $mg \cdot cm^2$) in the scale is given by:

$$\frac{\Delta m(Cr)}{A} = 2.168 \cdot k \cdot t^n \tag{6.4}$$

The total amount of chromium $\Delta m(Cr)^{ox}$ (in $mg \cdot cm^2$) in the oxide scale on the surface of the specimen of infinite size is:

$$\Delta m(Cr)^{ox} = 2.168 \cdot A \cdot k \cdot t^n \tag{6.5}$$

Considering the volume of the specimen to be $\frac{1}{2} A \cdot d$ (in cm^3) the total amount of chromium (in mg) depleted from the alloy due to oxide formation after a certain time t is:

$$\Delta m(Cr)^{depl} = \frac{C_0 - C_t}{100} \cdot \rho \cdot \frac{1}{2} A \cdot d \tag{6.6}$$

in which ρ is the alloy density in $mg \cdot cm^3$, C_0 the initial alloy Cr content in wt-% and C_t the remaining Cr content at time t. As the amount of Cr depleted from the alloy will be equal to that tied up in the oxide, i.e. after a certain oxidation time, the following equation will be valid:

$$2.168 \cdot A \cdot k \cdot t^n = \frac{C_0 - C_t}{100} \cdot \rho \cdot \frac{1}{2} A \cdot d \tag{6.7}$$

Re-arranging the equation reveals the time, which is required to deplete the initial chromium content C_0 to a certain, i.e. lower chromium content in the alloy matrix after time t. If we define C_B as the critical Cr content at which breakaway oxidation starts, the time for the occurrence of this event is given by:

$$t_B = \left[2.3 \cdot 10^{-3} \cdot (C_0 - C_B) \cdot \frac{\rho \cdot d}{k} \right]^{\frac{1}{n}} \tag{6.8}$$

In the case of a rectangular specimen of length L, width b and thickness d (all values in cm) equation (6.8) will changes to:

$$t_B = \left[2.3 \cdot 10^{-3} \cdot (C_0 - C_B) \cdot \frac{\rho \cdot d}{k \cdot (1 + d/L + d/b)} \right]^{\frac{1}{n}} \tag{6.9}$$

in which the specimen thickness d in equation 6.8 is replaced by the factor:

$$\frac{d}{(1 + d/L + d/b)} \tag{6.10}$$

when considering the total surface area and volume of the specimen. It is of course also possible to make a similar calculation for different specimen shapes taking the correct volume to surface ratios of various types of specimen geometries such a bars or wires into account [Gurrappa-1, Nichols-1].

In the case of alloys which are prone to oxide spallation equation 6.8 can be changed in such a way that the spalling process is also taken into account. Assuming that this spallation starts after the oxide thickness reaches a critical thickness x^*, corresponding to a critical weight change Δm^*, the following expression was derived in reference [Quadakkers-9] for the time to breakaway for a flat specimen of infinite size (compare equation 6.8):

$$t_B = 2.3 \cdot 10^{-3} \cdot (C_0 - C_B) \cdot \rho \cdot d \cdot (k)^{-\frac{1}{n}} \cdot (\Delta m^*)^{\frac{1}{n} - 1} \tag{6.11}$$

It is necessary to take into account that for Crofer 22 APU type steels a double-layered oxide scales are usually formed. It is therefore necessary to assume that this information when calculating $\{Cr/O\}_{ratio}$ for the oxide scale formed. In such a case it is better to modify the equation 6.9 obtaining:

$$t_B = \left[0.005 \cdot \frac{1}{\{Cr/O\}_{ratio}} (C_0 - C_B) \cdot \frac{\rho \cdot d}{k \cdot (1 + d/L + d/b)} \right]^{\frac{1}{n}} \tag{6.12}$$

The boundary conditions for the $\{Cr/O\}_{ratio}$ in such a case are 2.168 if only Cr_2O_3 is formed and 1.626 if only Cr_2MnO_4 exists on the specimen surface. However, in most cases the value is between these two boundary values because both oxides are usually observed on the specimen surface. However, it is not easy to find an exact value of spinel thickness because it could be different for the different specimen thickness because of Mn depletion during the oxidation process (section 6.1.3). Therefore in most studied cases the value of $\{Cr/O\}_{ratio}$ was taken as for pure chromia scale (2.168), which could affect the calculation in such a way that the lifetime is slightly shorter than for the calculation where a spinel layer would be taken into account. From the practical point of view it is however better to underestimate the lifetime of the alloy to avoid overestimation (calculation of the longer lifetimes than experimental ones).

The approaches used in references [Quadakkers-8, 9, Gurrappa-1, Nicholls-1] to predict the time for the onset of breakaway can only be used if the depletion profiles of the scale forming elements in the alloy, here mainly Cr, are nearly ideally flat. Whether this is actually the case, will depend on the diffusion coefficient (D) of the scale forming element in the alloy and the growth rate of the oxide. Assuming classic parabolic oxidation, the scale thickness (x) and oxidation time (t) are related by:

$$x^2 = k_p \cdot t \qquad (6.13)$$

in which k_p is the parabolic oxidation rate constant. It is easy to derive from classical oxidation theory that the slope of the depletion profile in the alloy beneath the oxide layer depends on the ratio k_p / D [Kofstad-1]. If the ratio is large, as is the case in most chromia forming Ni - base alloys [England-1] and austenitic steels [Schütze-1] but also for ferritic steels at intermediate temperatures [Vossen-1], a steep slope of the depletion profile beneath the oxide scale will develop [Quadakkers-9, England-1]. If the ratio k_p / D is very small, the depletion profile is nearly ideally flat, as is generally the case in FeCrAl alloys when oxidized in the temperature range of approximately 1000–1300°C [Quadakkers-9].

Figure 6.51 shows mass change data of one of the studied ferritic steels (Crofer A) during oxidation at 800°C. The results show that the oxidation behaviour can in most studied cases, with reasonable accuracy, be described by a parabolic time dependence of the scaling rate. However, it is necessary to take into account that for exposures with observed scale tensile cracking (compare figure 6.50) it is difficult to derive a reliable time dependence of the scaling rate. Figure 6.52 presents measured Cr depletion profiles after various oxidation times for specimens of different initial thickness. The data shows, that the slopes of the Cr-profiles are quite small and consequently can, with reasonable accuracy, be described as being flat, as required for the modelling approach used in references [Quadakkers-8, 9, Gurrappa-1, Nicholls-1] for alumina forming ferritic steels.

Cr depletion profiles measured for the studies materials can be found in figures 10.1 – 10.12 in the Appendix.

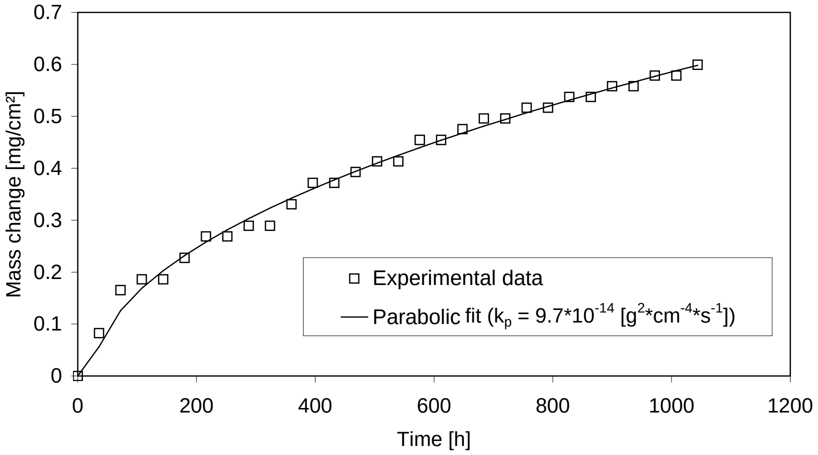

Figure 6.51: Mass change during cyclic oxidation of a 0.5 mm thick specimen (JMD 1) of Crofer A at 800°C in air showing a parabolic fit (eq. 6.13) of the experimental data.

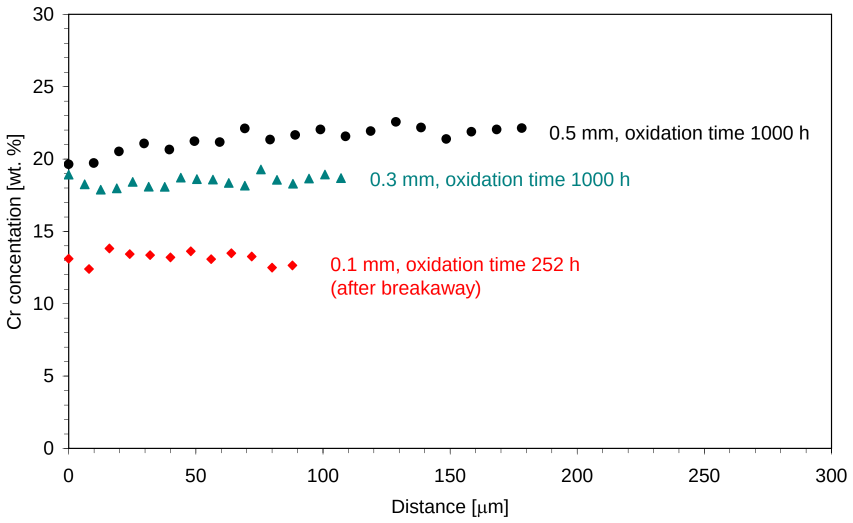

Figure 6.52: Measured Cr depletion profiles for specimens of Crofer A with different initial thickness after cyclic oxidation at 900°C in air.

Figure 6.53 shows a calculated lifetime diagram for Crofer A as a typical example of the lifetime calculation for chromia forming ferritic steels. The parameters used for the calculations are listed in the figure captions. Dashed lines (constant k_p values) were calculated taking into account kinetic data for thick specimens only (i.e. 2 mm). In the case of the solid lines show the thickness dependence of k_p is taken into account (compare figures 6.1 to 6.4). Based on EDX analyses, the Cr content at which breakaway occurs (figure 6.52) was near to 16 %. It is also in agreement with results for “low-Cr” steels (~ 16 wt. %). For such materials breakaway oxidation occurred at the first stage of oxidation if the temperature is high enough (900°C) even for thick (2 mm) specimens (compare section 5.1). Comparison of the calculated data with the available measured breakaway results (Figure 6.2) shows that by this approach the experimentally determined lifetimes during 900°C oxidation can be predicted with reasonable accuracy if the specimen thickness variation of k_p is taken into account.

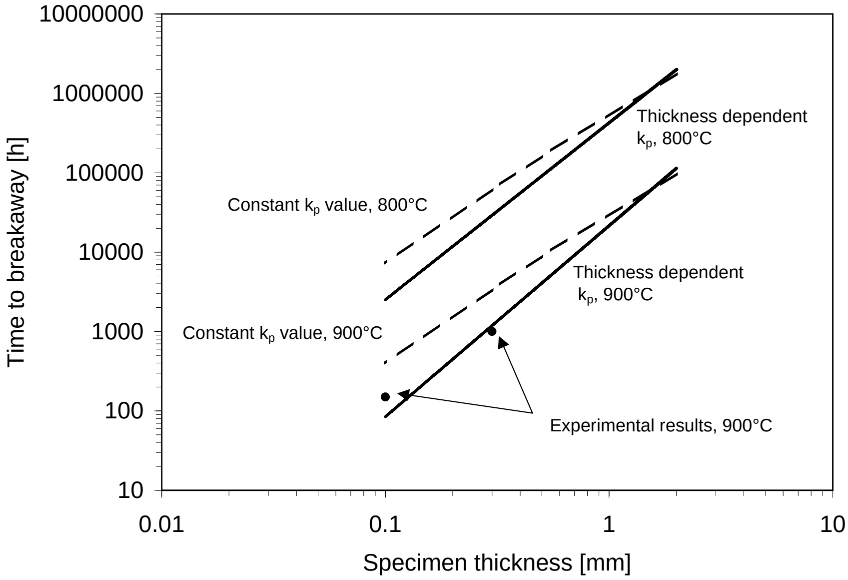

Figure 6.53: Calculated lifetimes for steel Crofer A at 800 and 900°C in air assuming a C_B value for Cr of 16 wt. % at both temperatures.

k_p-values used for the calculation of the life times for specimens with a various initial thickness [$g^2cm^{-4}s^{-1}$]:

800°C: k_p (2 mm) $= 6.49\cdot10^{-14}$
k_p (0.5 mm) $= 1.05\cdot10^{-13}$
k_p (0.3 mm) $= 1.12\cdot10^{-13}$
k_p (0.1 mm) $= 2.21\cdot10^{-13}$

900°C: k_p (2 mm) $= 1.00\cdot10^{-12}$
k_p (0.5 mm) $= 1.79\cdot10^{-12}$
k_p (0.3 mm) $= 2.49\cdot10^{-12}$
k_p (0.1 mm) $= 5.67\cdot10^{-12}$

Figures 6.54 and 6.55 show calculated lifetimes for various studied steels at 800°C and 900°C in air taking the thickness dependence of k_p into account and assuming a C_B value for Cr of 16 wt. %. At 800°C (figure 6.54) it is clearly visible that the model steel HCE shows the highest oxidation resistance and thus the longest lifetime. In case of steel HCH the decrease in lifetime of the thinner specimens is not as large as for the other steels. It is connected with the lower Mn depletion in the high-Mn HCH steel and thus hardly any thickness dependence was found for this steel (compare figure 6.29).

In the case of the 900°C calculation (figure 6.55) it was found that several steels, which for the thick components show high oxidation resistance (i.e. steel HCE and JS-3), they show rapid reduction of the lifetime for the thinnest components. This effect is caused by oxide growth and/or thermally induced stresses leading especially for thin specimens of weaker alloys to tensile cracking of the scale resulting in the creation of paths for access of molecular oxygen and thus enhanced scale growth rates (compare section 6.1.3). The effect is more pronounced for higher temperatures, i.e. 900°C, than for 800°C.

Presently available experimental breakaway data (marked with dots) show that the approach used for the experimentally determined lifetimes during 900°C oxidation can be used with reasonable accuracy for the studied ferritic steels if breakaway type 1 occurs (compare section 6.2). In case of breakaway type 2 it is possible to observe catastrophic oxidation faster than predicted. This is probably the case for the 0.6 mm specimen of the FeCrLa steel (batch HCE). It was found that the experimental depletion profile for this specimen showed a strong deviation from an ideal flat profile in contrary to a specimen from the same batch but with a thickness of 0.3 mm (figure 6.56).

At 800°C the experimentally determined lifetimes are not easy to obtain because of long oxidation times required. It is thus difficult to estimate, whether the assumptions made for 900°C are transferable to 800°C. Especially uncertain seems to be, whether the C_B-value derived at 900°C is transferable to lower temperatures.

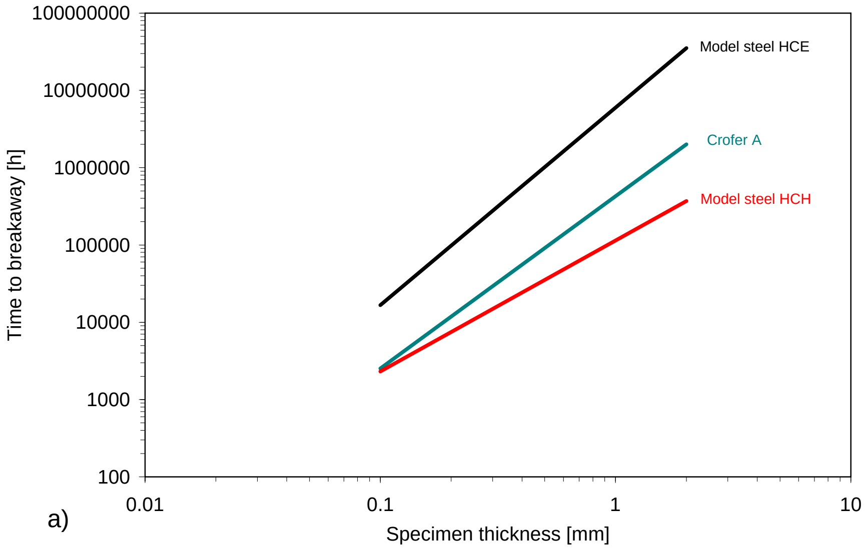

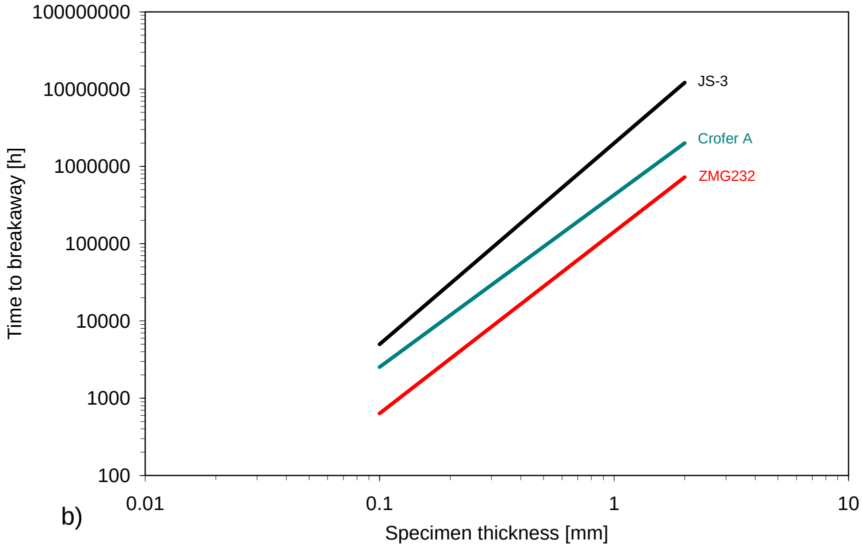

Figure 6.54: Calculated lifetimes for various studied steels at 800°C in air taking thickness dependence of k_p into account and assuming a C_B value for Cr of 16 wt. %.

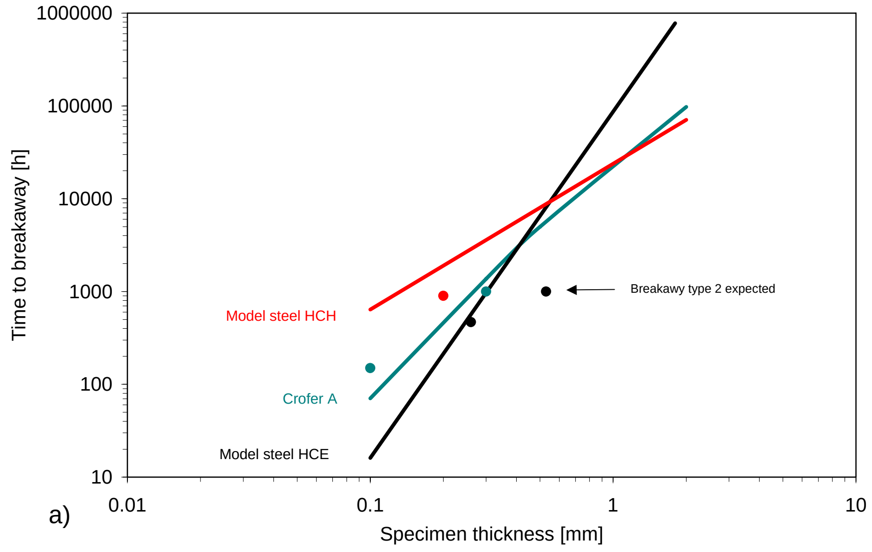

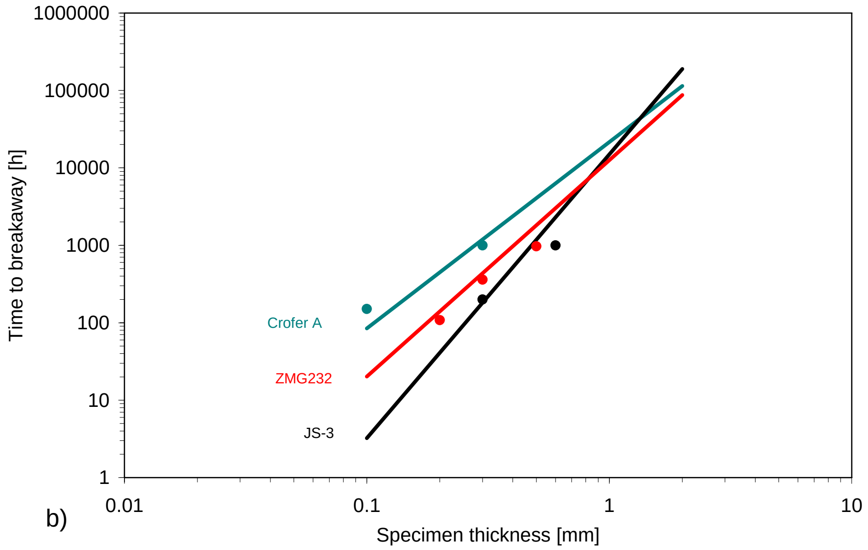

Figure 6.55: Calculated lifetimes for various studied steels at 900°C in air taking thickness dependence of k_p into account and assuming a C_B value for Cr of 16 wt. %. Dots indicate experimental breakaway points measured for studied materials.

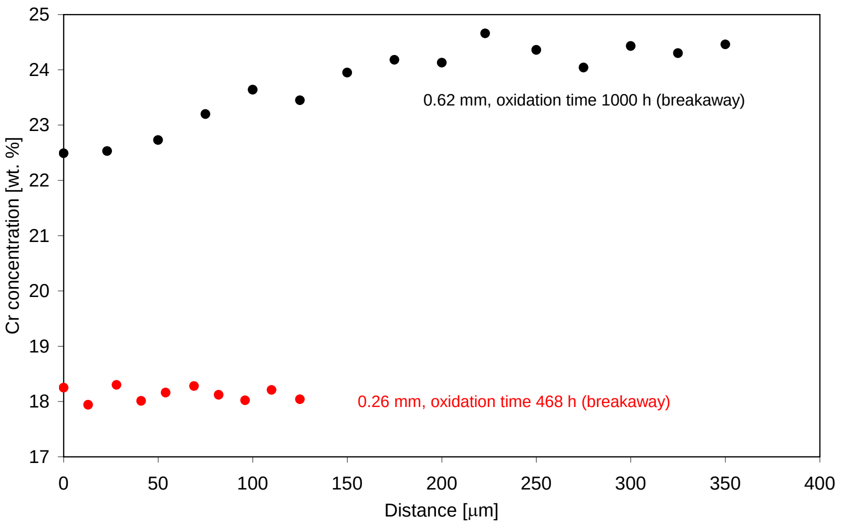

Figure 6.56: Measured Cr depletion profiles for specimens of model steel FeCrLa (batch HCE) with different initial thickness after cyclic oxidation at 900°C in air.

6.4 Summary of studies on oxidation limited life times

It is necessary to take into account that the lifetime of thin steel components (i.e. 0.1 mm) used as interconnectors for SOFC will be more shorter than the lifetime of thick components (i.e. 2.0 mm) of the same material because of the smaller reservoir of scale forming elements in thin components.

Besides, it has to be taken into account that, the oxidation rate k_p obtained for most of the studied materials increases with decreasing specimen thickness – thinner components of the same steel oxidise faster than thicker ones.

The k_p-dependence on specimen thickness is related to:

- Depletion of minor alloying elements (mainly Mn) – Mn suppresses the chromia growth for thick components by Cr/Mn-spinel formation. During oxidation of thin components (i.e. 0.1 mm) at 900°C the reservoir of Mn is insufficient to form a spinel phase even after relatively short oxidation times.

- The oxidation atmosphere, laboratory air, contains trace amounts of water vapour, which accelerate the growth of the chromia scale. After total depletion of Mn (see above) the growth rate of chromia is accelerated by the presence of water vapour in the air.

- Oxide growth and thermally induced stresses (in the later stages of oxidation) – during prolonged exposure of thinner components and thermally induced stresses lead to tensile cracking of the scale resulting in the creation of paths for access of molecular oxygen and thus enhanced scale growth rates

The breakaway oxidation phenomenon is in most cases caused by a mechanical mechanisms (crack formation) rather than only by “chemical” depletion of chromium. However, it is necessary to take into account that the first reason for catastrophic attack is depletion of Cr so crack formation only accelerates the to beginning of breakaway oxidation.

The oxidation lifetime for chromia forming ferritic steels in the temperature range 800-900°C can be predicted with reasonable accuracy by a similar approach as that previously used for FeCrAl alloys, if the mentioned factors affecting the scale growth rate are taken into account.

7. Electrical conductivity of the thermally grown, chromium rich oxide scales

As introduced in paragraph 3.5 the electrical conductivity of the interconnect is a crucial property for SOFC application whereby the conductivity of the chromium based oxide scale which forms during high temperature service has to be taken into account in the overall conductivity value. This section presents experimental data concerning the electrical conductivity of the surface oxide scales formed in the temperature range 600-800°C on selected high-chromium ferritic steels. The data will be correlated with oxide scale morphologies and compared with those obtained for two “pure chromia” forming materials.

Figure 7.1 shows weight change data for the studied materials after 1000 h of discontinuous exposure at 800°C in air. The oxide scales on the two ferritic steels and the Cr-base ODS alloy exhibited excellent adherence to the metallic substrate and no indications for scale spalling were found. On the contrary, the Cr-sample exhibited substantial scale spalling as confirmed by the metallographic cross-section in figure 7.2. Consequently, the specimen (“net”) weight change after 1000 h was substantially smaller than the total (“gross”) weight change corresponding to the oxide adhering to the substrate plus the spalled oxide (figure 7.1). A much smaller growth rate and far better scale adherence were found for the Cr-ODS-alloy, although, also for this materials scale damage as void formation was clearly found (figure 7.2).

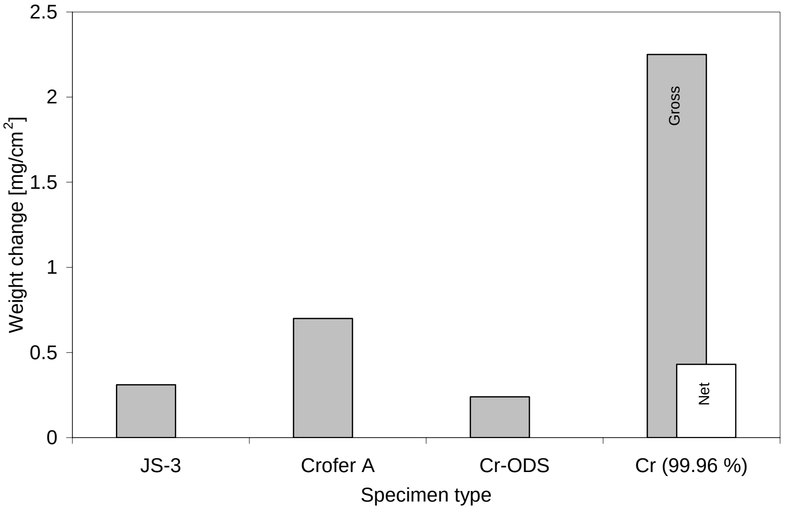

Figure 7.1: Weight change of the studied materials after 1000 h oxidation at 800°C in air. The measured weight change of the Cr specimen was affected by oxide spallation. The figure therefore shows a total (gross) weight change (including spalled oxide) and the specimen (net) weight change.

The latter effect was not observed in the scales on the two ferritic steels (figure 7.2) as already described in the previous sections. Both steels formed dense, compact oxide layers and the scale on steel JS-3 was, in agreement with the weight change data, only marginally thicker than that on the Cr-base ODS alloy. Both Cr-base materials exhibited sub-scale nitride formation, the effect being especially pronounced in case of the “pure-Cr”. Nitride formation was not observed in the two ferritic steels, which is, however, no proof that no nitrogen uptake occurred. Because the steels possess a much higher N-solubility than the Cr based materials, N-uptake may have occurred without the formation of metallographically visible nitride precipitates.

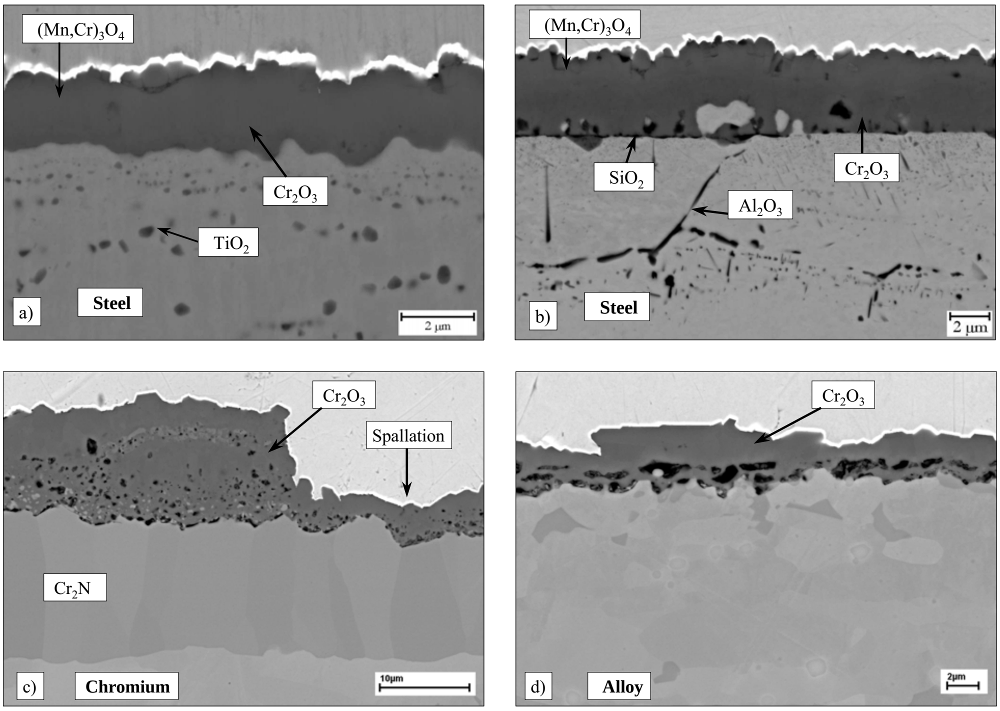

Figure 7.2: Metallographic cross-sections (SEM images) of the studied materials after 1000 h oxidation at 800°C in air.
a) Steel JS-3 [Piron-2]
b) Steel Crofer A [Piron-2]
c) Cr (99.96 %)
d) Cr-ODS alloy (Cr-5Fe-1Y_2O_3)

Figure 7.3 shows the temperature dependence of the electrical conductivity of the oxide scales on the studied materials compared with literature data for Cr_2O_3 [Holt-1, 2, Nagai-1] and recent results for Cr_2MnO_4 [Sakai-1]. To be able to compare the measured resistance results with the data published in literature for bulk oxides, the contact resistances (compare figure 3.17) were transferred into conductivity values thereby taking the metallographically measured oxide thicknesses into account. Strictly speaking, the surface scales formed on the various materials cannot be characterized by such a conductivity value, because the scales do not consist of a single oxide phase; they contain impurities and they grow in an oxygen partial pressure gradient. In figure 7.3 the estimated value is therefore termed “apparent conductivity”.

The conductivity data measured on at least two specimens of all studied materials showed excellent reproducibility for the two ferritic steels and the Cr-ODS-alloy, however substantial scatter was observed in case of the “pure-Cr”. Although during the 100 h pre-oxidation this material did not exhibit scale spallation, the metallographic cross section after 1000 h (figure

7.2) indicates, that already after relatively short oxidation times of a few hundred hours, significant scale damage due to pore and crack formation will prevail. These voids and gaps will substantially affect the conductivity measurements. The non-even distribution of the scale damage therefore explains the scatter in data obtained for the two “pure Cr” specimens.

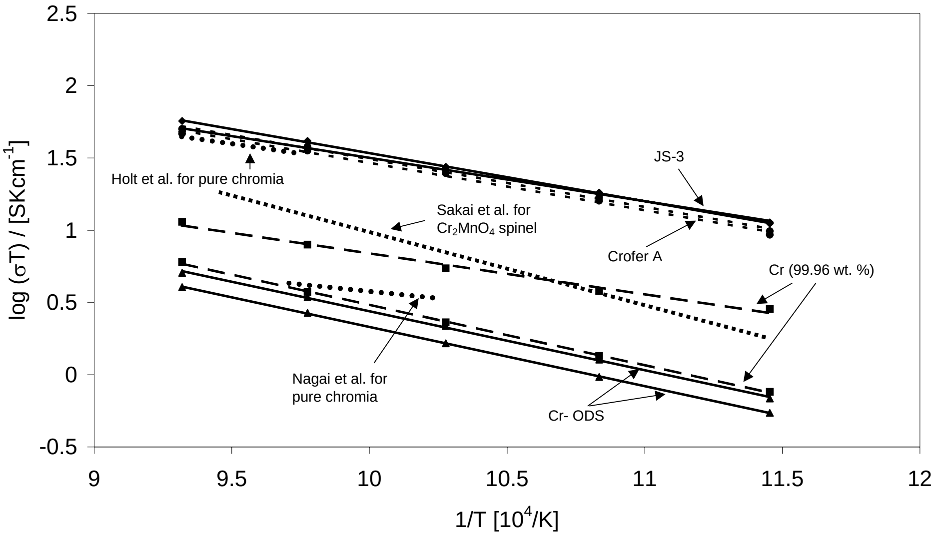

Figure 7.3: “Apparent electrical conductivity” (σ) of oxide scales, plotted as σT vs. reciprocal temperature, for investigated materials compared with literature data for Cr_2O_3 (Holt et al. [Holt-1, 2], Nagai et al. [Nagai-1]) and Cr_2MnO_4 (Sakai et al. [Sakai-1]).

The results in figure 7.3 clearly show higher conductivities for the oxides on the two ferritic steels than for those on the Cr-base materials. This is likely related to the in-scale voidage of the scales on the Cr-base materials in combination with a doping of the Cr_2O_3 scales formed on the two steel variants, e.g. by Ti and/or Fe and by the presence of the Cr/Mn-spinel phase [Huczkowski-3]. The minor additions of Si and Al in steel Crofer A apparently do not substantially affect the scale conductivity. Although the measured “apparent conductivities” can, for the reasons mentioned above, not in a straightforward way be compared with absolute values determined from bulk oxides, it is interesting to note, that the measured data are in a range, previously reported for bulk chromia by Holt at al. [Holt-1, 2] and Nagai at al. [Nagai-1] and recently for Cr_2MnO_4 by Sakai at al. [Sakai-1]. The latter authors observed a strong dependence of the spinel conductivity on Fe-additions.

7.1 Prediction of the electrical conductivity of thermally grown chromia

If for a certain steel an electrical conductivity of the oxide scale and oxidation kinetics are known in a certain temperature range it is possible to predict the electrical properties for a particular temperature.

As it was already mentioned in the literature review, equation 3.25 can be presented as follows:

$$ASR = \rho \cdot x \tag{7.1}$$

where: ASR is the area specific contact resistance of the oxide scale, ρ is the resistivity and x is the thickness of the oxide scale.

The resistivity (ρ) can be calculated from the formula:

$$\sigma T = f \exp\left(\frac{-E_{a_{el}}}{RT}\right) \tag{7.2}$$

taking into account that:

$$\rho = \frac{1}{\sigma} \tag{7.3}$$

where ρ is the electrical conductivity.

Re-arranging equation 7.2 yields for the resistivity:

$$\rho = T \cdot \frac{1}{f} \exp\left(\frac{-E_{a_{el}}}{RT}\right) \tag{7.4}$$

where f is a pre-exponential constant, $E_{a\,el}$ is the activation energy, R is the universal gas constant, and T the temperature.

The thickness of the oxide scale (x) can be calculated using equation:

$$x^2 = k_p \cdot t \tag{7.5}$$

where k_p is the oxidation rate constant (in $cm^2 s^{-1}$) and t is the oxidation time, knowing that:

$$k_p = k_p^o \exp\left(\frac{-E_{a_{ox}}}{RT}\right) \tag{7.6}$$

where k_p^o is a pre-exponential constant, $E_{a_{ox}}$ is the activation energy for oxidation, R is the universal gas constant, and T the temperature.

Comparing equation 7.5 and 7.6 the oxide scale thickness is given by:

$$x = \left(k_p^o\right)^{\frac{1}{2}} \cdot t^{\frac{1}{2}} \cdot \exp\left(\frac{-E_{a_{ox}}}{2RT}\right) \tag{7.7}$$

Finally it is possible to replace ρ and x in the equation 7.1 by formulas given in equations 7.4 and 7.7:

$$ASR = t^{\frac{1}{2}} \cdot \exp\left(\frac{-E_{a_{ox}} + 2 \cdot E_{a_{el}}}{2 \cdot RT}\right) \cdot \left(k_p^o\right)^{\frac{1}{2}} \cdot T \cdot \frac{1}{f} \tag{7.8}$$

The factors $E_{a_{el}}$, f, $E_{a_{ox}}$ and k_p^o can be calculated from equations 7.2 (electrical conductivity) and 7.6 (oxidation kinetics) using the slopes of the reciprocal curves:

- $\ln(\sigma T)$ vs. $1/T$ for electrical conductivity
- $\ln(k_p)$ vs. $1/T$ for oxidation kinetics

Figure 7.4 shows the predicted behaviour of the contact resistance for the steel Crofer A for various temperatures using conductivity and kinetics data from table 7.1 and parameters derived from equation 7.2 and 7.6 presented in table 7.2. The calculated curves show that the contact resistance increases with increasing temperature so the electrical conductivity after the same oxidation time will be higher if the steels is oxidised at lower temperatures. That means that the reduction of the fuel cell temperature should be beneficial from the viewpoint of electrical conductivity of the formed surface oxide scale. This conclusion is of course only valid, if the oxidation mechanisms do not change in the temperature range 600 – 900°C.

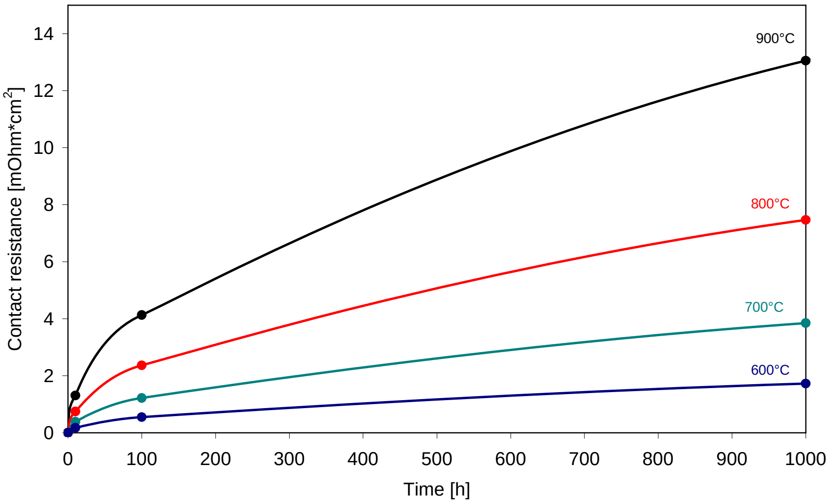

Figure 7.4: Calculated contact resistance of the thermally grown oxide scale on steel Crofer A for a various temperatures using equation 7.8

Temperature	Oxidation kinetics k_p [cm^2/h]	Conductivity [S/cm]
900°C	$1.27 \cdot 10^{-9}$	-
800°C	$7.43 \cdot 10^{-11}$	0.043
750°C	-	0.035
700°C	$1.08 \cdot 10^{-11}$	0.026
650°C	-	0.017
600°C	-	0.011

Table 7.1: Kinetics and electrical conductivity data used for the calculation in figure 7.4

$E_{a\,ox}$ [J/mol]	224187
k_p^o [cm^2/h]	9.56
$E_{a\,el}$ [J/mol]	63000
f [SK/cm]	57239.5

Table 7.2: Parameters derived from equation 7.2 and 7.6 used for the calculation presented in figure 7.4

7.2 The effect of contact paste on conductivity experiments

Based on the microstructural investigations after a number of conductivity tests, the question arose whether Pt paste can be considered as an inert material during the long term testing. Figures 7.5, 7.6 and 7.7 show oxide scale morphologies for specimens oxidised with and without Pt covers. The SEM images show that especially for steel JS-3 there is a clear difference in oxide scale morphology between the specimens covered with Pt compared with the non-covered specimens. This effect occurred independent of whether an electric voltage was applied or not. Therefore a number of conductivity tests with different types of contact pastes (Pt, Au) on specimens of JS-3 and Crofer 22 APU were carried out.

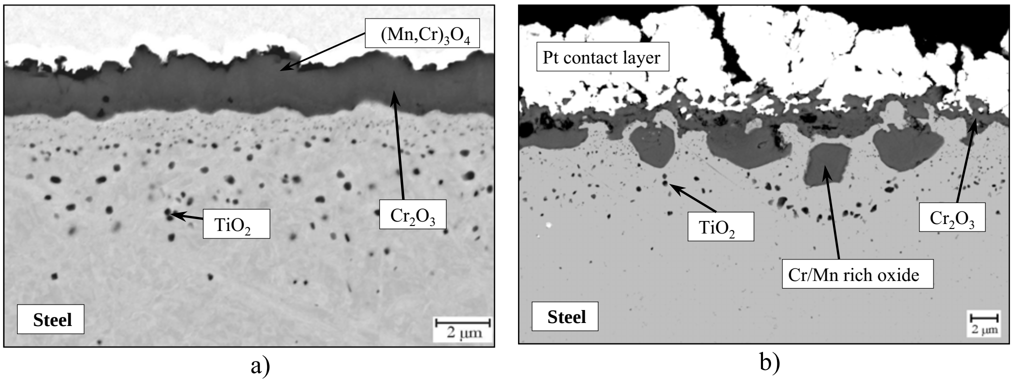

a) b)

Figure 7.5: Oxide scale morphology of steel JS-3 after oxidation at 800°C in air
a) 1000 h, normal discontinuous oxidation
b) 1350 h conductivity experiment (total oxidation time including preoxidation of 100 h) specimen covered with Pt-paste

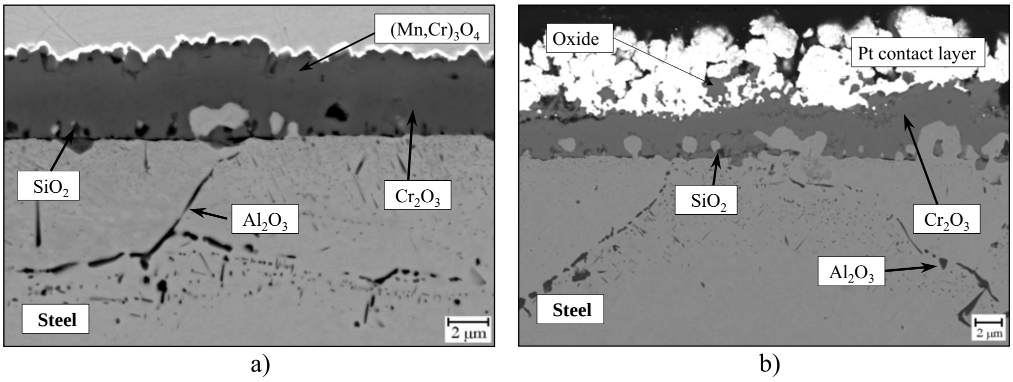

a) b)

Figure 7.6: Oxide scale morphology of steel Crofer A after oxidation at 800°C in air
a) 1000 h, normal discontinuous oxidation
b) 1350 h conductivity experiment (total oxidation time with preoxidation of 100 h); Specimens covered by Pt-paste

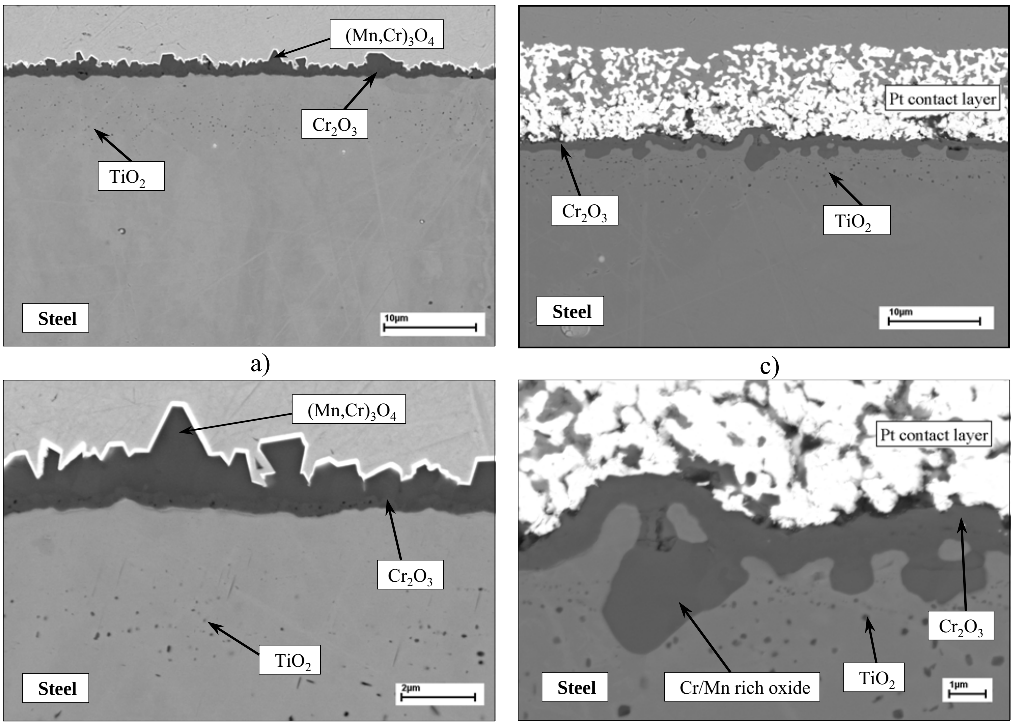

a) c)

b) d)

Figure 7.7: Oxide scale morphology of steel JS-3 after oxidation at 800°C in air (after 250 h preoxidation one side of the specimen covered by Pt paste); a), b) 750 h oxidation (250 h + 500 h), no Pt paste, c), d) 250 h oxidation + Pt paste cover + 500 h oxidation

Figure 7.8 clearly exhibits that there is a difference, although not "dramatic", in contact resistances measured on specimens covered with different contacting pastes. Specimens covered with the Au paste generally exhibited a higher contact resistance (lower electrical conductivity) than those covered with Pt paste. Figure 7.9 shows the oxide scale morphologies (metallographic cross-section) of the various samples after the conductivity tests. Generally the oxide scales on Au covered samples are thicker than those on Pt covered samples. This seems to be a likely explanation for the measured slightly higher contact resistance.

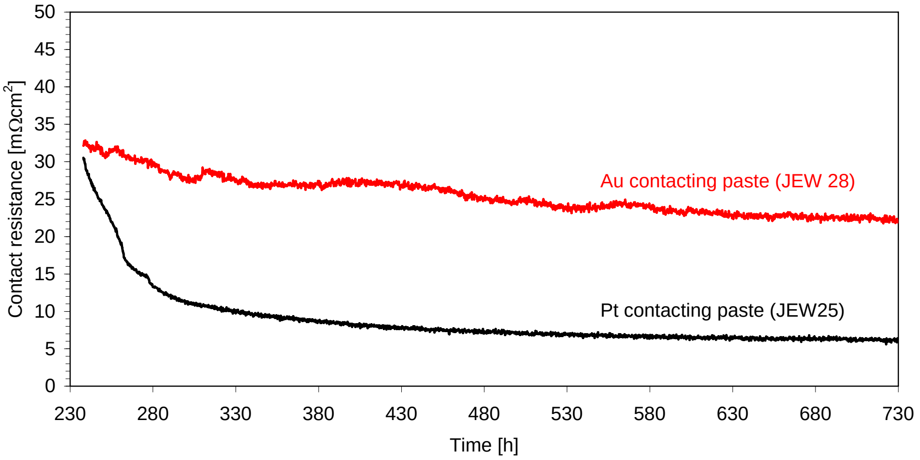

Figure 7.8: Contact resistance as a function of time of semi-commercial steel JS-3 covered with different contacting pastes at 800°C in air (test started after 250h pre-oxidation)

The "thinning" of the scale has as a result, that the conductivity data at the end of the long-term measurement relates to a relatively thin oxide scales which nearly exclusively consist of Cr_2O_3 because hardly any $(Cr,Mn)_3O_4$ remains. Figure 7.10 shows for the Crofer A that, in contrary to JS-3, only a minor difference exists between measured contact resistances using different contacting pastes. This might be related to the fact that for Crofer A the spinel phase is relatively thin (compare paragraph 5.3) and its destruction has only a limited influence on the overall conductivity value.

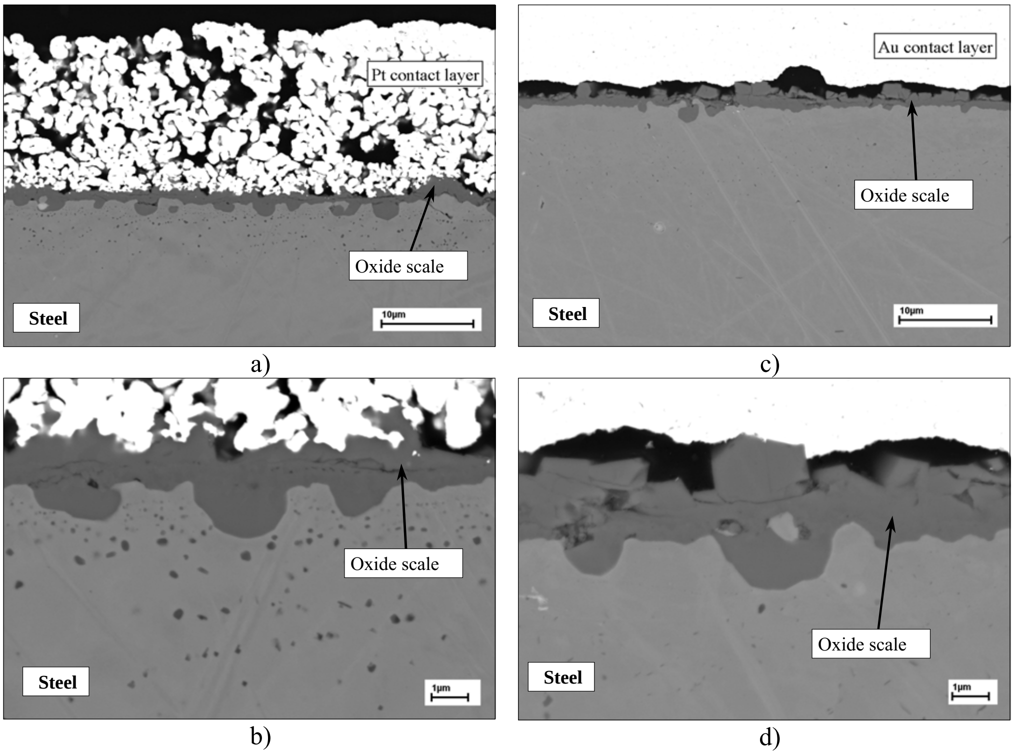

a) c)

b) d)

Figure 7.9: Oxide scale morphologies of JS-3 samples covered with different contacting pastes after 500 h electrical conductivity test at 800°C in air.
a), b) Pt contacting paste (JEW 25), c), d) Au contacting paste (JEW 28)

As far as known to the author, the “Pt effect” has not been described in the literature. Recent studies from Hultquist et al. [Hultquist-1, 2] indicated that the presence of Pt on a growing chromium based oxide changes the growth mechanism of the oxide scale, i.e. the presence of Pt promotes inward growth. The result from the present study indicates that part of the oxide scale reacts with the Pt paste during the high temperature test resulting in thinning of the scale during prolonged exposure. The metallographic and SEM investigations indicate that especially the spinel phase $(Cr,Mn)_3O_4$ is susceptible to reaction with the Pt paste. These observations indicate that the Pt effect is not solely related to a change of the transport processes in the scale.

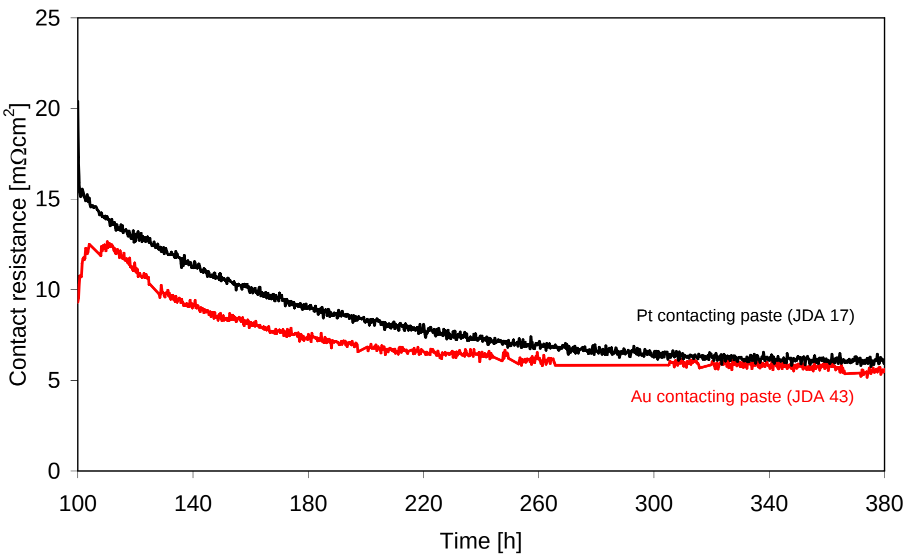

Figure 7.10: Contact resistance as function of time of steel Crofer A covered with different contacting pastes at 800°C in air (test started after 100 h pre-oxidation at 800°C)

To prove the finding presented in papers [Hultquist-1,2] two stage oxidation studies were performed. Figure 7.11 shows SNMS profiles for two specimens of steel JS-3 after two stage oxidation with ^{18}O tracer. In the first case (figure 7.11 a) after 5 h oxidation at 800°C in air the oxidising gas was changed to Ar-$^{18}O_2$ (20 h oxidation). For the second specimens a platinum layer was applied between the two steps of oxidation (compare section 4.5). The SNMS profiles for the specimens covered with platinum indicates that some of the Cr and Mn are incorporated into the platinum layer, which is also possible to be observed on the images in figures 7.5, 7.6, 7.7 and 7.9. Comparing the SNMS profile in figure 7.11 it is also clearly visible that the profiles of the oxygen tracer in platinum covered specimen varies from that observed on the specimen oxidised without platinum addition. It is probably connected with a change of oxide growth mechanism from outward to mixed (outward/inward) scale formation mechanisms.

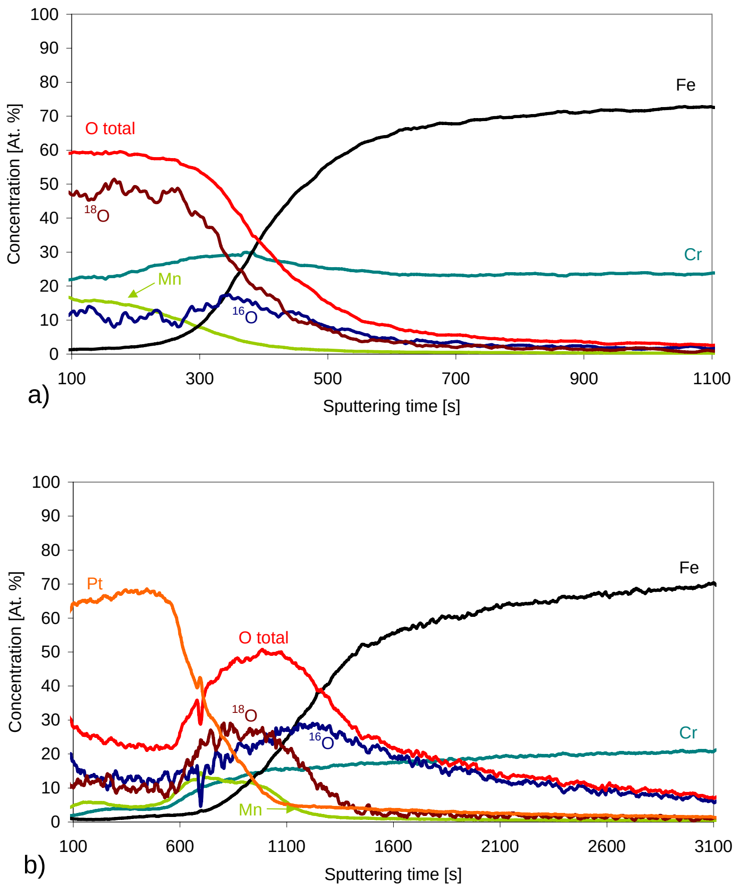

Figure 7.11: SNMS profiles of steel JS-3 after isothermal oxidation at 800°C in Ar-O_2. (two-stage oxidation using $^{18}O_2$ in the second oxidation step)

a) 5 h Ar-$^{16}O_2$, 20 h Ar-$^{18}O_2$
b) 5 h Ar-$^{16}O_2$, Pt-sputtering (compare section 4.5), 20 h Ar-$^{18}O_2$

7.3 Summary of the studies on electrical conductivity of the thermally grown, chromium rich oxide scales

Minor additions of Al and Si tend to increase the growth rate of the Cr-rich oxide scales on high-Cr ferritic steels. However, the electrical conductivity of the scales seems to be only marginally affected by these minor alloying additions, as long as no compact sub-surface layers (e.g. of silica) are formed.

The conductivities of the scales formed on the studied ferritic steels studied steels in the temperature range 600-800°C were higher than that of pure chromia formed on Cr-base materials.

This effect is probably related to a doping effect of the Cr_2O_3 scales in the case of Crofer 22 APU type interconnector steels.

The electrical conductivity of the Crofer 22 APU type steels seems to be sufficiently high for most envisaged SOFC applications.

Pt paste cannot be considered as an inert material during the long term electrical conductivity testing. It apparently modifies the morphology of the oxide scale, however no substantial change in the growth mechanism of the chromia scale is observed during the early stages of oxidation. The latter effect is less pronounced if Au-paste is being used.

8. Summary and conclusions

High-Cr ferritic steels seem to be promising candidates for interconnect materials for SOFCs. If one considers market available ferritic steels, those especially designed for SOFC show better properties at high temperatures than the other commercial materials. Especially the steel Crofer 22 APU seems to possess promising properties for SOFC interconnects because of its very good oxidation protection and excellent adhesion of the oxide scale to the metallic substrate when oxidised in the temperature range 800-900°C. It is however, necessary to point out that the exact composition of the steel is extremely important for its behaviour during high temperature service. In the case of Crofer 22 type steels (JS-3 / Crofer 22 APU) only a theoretically marginal addition of manufacturing related impurities (Si and Al) changes to a large extend the oxidation properties of the steel, i.e. they increase the growth rate of the chromia because of oxide scale cracking and thus access of oxygen to the metal surface. Detailed characterisation of steels JS-3/Crofer 22 APU after different kinds of oxidation tests show outward growth of the scale Cr-base scale likely governed by the formation of the external Cr/Mn spinel layer if oxidised at 800°C and 900°C in air. The top spinel layer of $(Cr,Mn)_3O_4$ is known to reduce the formation of volatile Cr species preventing poisoning of the cathode and the cathode/electrolyte interface in SOFC's.

One of the most important points in the case of ferritic steels for potential use as SOFC interconnects is the chromium reservoir in the steel. Ferritic high-Cr steels form chromia based scales during high temperature service. If a depletion of scale forming elements (mainly Cr) come to a critical level, protective scale formation will no longer be observed, a non protective Fe-rich oxide will be formed in the further stages of oxidation (breakaway oxidation). Due to the very high oxide growth rates accompanied by this event, the time at which breakaway oxidation occurs, represents the lifetime limit of the components. Therefore it is necessary to point out that steels with relatively low concentrations of chromium (e.g. 16 wt. %) are potentially less promising for SOFC use than the higher chromium steels (e.g. 22 wt. % of Cr).

SOFC market requirements (e.g. in the automotive industry) lead in many cases to the demand for a reduction of the fuel cell size and/or weight and thus of the interconnector thickness. Similar to the above presented discussion (chromium reservoir) also in the case of thin components (i.e. 0.1 mm) even with high chromium concentrations the depletion of the scale forming element leads to a fast breakaway phenomenon, and thus to a reduction of the component lifetime if compared with thick plates of the same material (i.e. 2 mm). It is important to note that the use of very thin components (i.e. 0.1 mm) for SOFC interconnectors can dramatically reduce the lifetime of the SOFC stack due to breakaway oxidation attack on the ferritic steel.

The breakaway oxidation phenomenon is in most cases caused by a mechanical mechanisms (crack formation) rather than only by “chemical” depletion of chromium. However, it is necessary to take into account that the first reason for catastrophic attack is depletion of Cr so the crack formation only accelerates the beginning of breakaway oxidation.

When oxidising specimens with different initial thicknesses it was found that the oxidation rates of the steels increase with decreasing specimen thickness, i.e. thinner components of the same steel oxidised faster than thicker ones. This effect is most probably caused by depletion of minor allying elements (manly Mn), which suppress the growth of chromia in thick components by Cr/Mn-spinel formation. During oxidation of thin components (i.e. 0.1 mm) at 900°C the reservoir of Mn is insufficient to form a spinel phase even after short oxidation times. This effect is accelerated by the presence of water vapour in the air, which additionally accelerates the formation of the chromia scale in thin components. Moreover, during prolonged exposure times it is necessary to take into account that for thin components growth and thermally induced stresses lead to tensile cracking of the scale resulting in the creation of paths for access of molecular oxygen and thus enhanced scale growth rates.

As explained above, for chromia forming ferritic steel components the oxidation-limited lifetime is primarily governed by the reservoir of the scale forming alloying elements rather than by their absolute concentration in the steel. The observed lifetime limits can be predicted with reasonable accuracy by a theoretical model, using oxide growth rate parameters, initial alloy Cr contents and critical Cr contents for protective chromia scale formation. Comparison of the calculated data with measured breakaway results shows that modelling allows prediction of the occurrence of breakaway oxidation with reasonable accuracy if the specimen thickness variation of k_p is taken into account.

The conductivities of the scales formed on the studied ferritic steels in the temperature range 600-800°C were higher than that of pure chromia formed on Cr-base materials. This effect is likely related to the doping effect of Cr_2O_3 scales in the case of Crofer 22 type interconnector steels. The electrical conductivity of the scales seems to be only marginally affected by minor alloying additions, as long as no compact sub-surface layers (e.g. of silica) are formed.

Pt paste cannot be considered as an inert material during long term electrical conductivity testing. It apparently modifies the morphology of the oxide scale, however no change in the growth mechanism of the chromia scale was observed during the early stages of oxidation. The on scale formation effect is less pronounced if Au-paste is used.

The electrical conductivities of the Crofer 22 type steels seem to be sufficiently high for most envisaged SOFC applications.

9. References

[Acres-1] – G.J.K. Acres, Recent advances in fuel cell technology and its applications, Journal of Power Sources 100, 2001, 60-66

[Ahmed-1] – O. Ahmed, D.J. Young, High Temperature Corrosion and Materials Chemistry II (Ed.: M.J. McNallan, E.J. Opila, T. Maruyama and T. Narita), 77-92, The Electrochemical Society, Pennington, NJ, 2000

[Badwal-1] – S.P.S. Badwal, R. Deller, K. Foger, Y. Ramprakash, J.P. Zhang, Interaction between chromia forming alloy interconnects and air electrode of solid oxide fuel cells, Solid State Ionic 99, 1997, 297-310

[Bandel-1] – G. Bandel, Besondere Erscheinungen bei der Zunderung hitzebeständiger Stähle und Legierungen, Arch. Eisenhütt Wes. 15, 1941/42, 271-284

[Batawi-1] – E. Batawi, K. Honegger, R. Diethelm, Factors Influencing the Degradation Performance of High Temperature Solid Oxide Fuel Cells Contacted with Metallic Bipolar Plates, Proceedings 6th IEA Workshop on Advanced SOFC, ENEA, 175-181, Rome, Italy, 1994

[Batawi-2] – E. Batawi, A. Plas, W. Straub, K. Honneger, R. Diethelm, New cost-effective ceramic oxide phases used as protective coatings for cgromium-based interconnects, Procedeeings 6th International Symposium Solid Oxide Fuel Cells (SOFC-VI) (Ed.: S.C. Singhal, M. Dokiya), 767-773, The Electrochemical Society, Pennington, NJ, 1999

[Baur-1] – E. Baur, H. Preis, Über brennstoff-ketten mit festleitern, Z Electrochem. 43, 1937, 727-732

[Birks-1] – N. Birks, G.H. Meier, Introduction to High Temperature Oxidation of Metals, Edward Arnold Ltd 1983

[Bongartz-1] – K. Bongartz, W.J. Quadakkers, P.J. Pfeifer, J.S. Becker, Mathematical modelling of oxide growth mechanisms measured by ^{18}O tracer experiments, Surface Sci. 292, 1993, 196-208

[Brady-1] – P.M. Brady, I.G. Wright, I.M. Anderson, V.K. Sikka, E.K. Ohriner, C. Walls, G. Westmoreland, M.L. Weaver, Ductilization of Cr via Oxide Dispersion, Proceedings of the 15th International Plansee Symposium (Ed.: G. Kneringer, P. Rodhammer, H. Wildner), 108-1-108-13, Plansee AG, Reutte, 2001

[Buchkremer-1] – H.-P. Buchkremer, U. Diekmann, L.G.J. de Haart, H. Kabs, U. Stimming, D. Stöver, Advances in the anode supported planar SOFC technology, Proceedings 5th International Symposium Solid Oxide Fuel Cells (SOFC-V) (Ed.: U. Stimming, S.C. Singhal, H. Tagawa, W. Lehnert), 160-170, The Electrochemical Society, Pennington, NJ, 1997

[Caplan-1] – D. Caplan, M. Cohen, High Temperature Oxidation of Some Iron-Chromium Alloys, Trans. Am. Inst. Min. metal. Engrs 194, 1952, 1057-1065

[Caplan-2] – D. Caplan, M. Cohen, High Temperature Oxidation of Chromium-Nickel Steels, Corrosion 15, 1959, 141-146

[Cappadonia-1] – M. Cappadonia, U. Stimming, K.V. Kordesch, J.C. Tambasco de Oliveira, Fuel Cells, Ullmann's Encyklopedia of Industrial Chemistry, Viley-VCH Verlag GmbH 2002

[Carrette-1] – L. Carrette, K.A. Friedrich, U. Stimming, Fuel Cells: Principles, Types, Fuels, and Applications, Chemphyschem 1, 2000, 162-193

[Chang-1] – S.Y. Chang, U. Krupp, H.-J. Christ, Formation and compensation of internal stresses during internal nitridation of nickel-base alloys , Materials Science and Engineering A 301, 2001, 196-206

[Chau-1] – K.T. Chau, Y.S. Wong, C.C Chan, An overview of energy sources for electric vehicles, Energy Conversion & Management 40, 1999, 1021-1039

[Chen-1] – X. Chen, P.Y. Hou, C.P. Jacobson, S.J. Visco, L.C. De Jonghe, Protective coating on stainless steel interconnect for SOFCs: oxidation kinetics and electrical properties, Solid State Ionics 176, 2005, 425-433

[Cotell-1] – C. Cotell, G. Yurek, R. Hussey, D. Mitchel, M. Graham, The Influence of Implanted Yttrium on the Mechanism of Growth of Cr_2O_3 on Cr, Journal Electrochemical Society 134, 1987, 1871-1872

[Crawford-1] – J.A. Crawford, R.W. Vest, Electrical Conductivity of Single-Crystal Cr_2O_3, Journal of Applied Physics, 35(8), 1964, 2413-2418

[Das-1] – D. Das, M. Miller, H. Nickel, K. Hilpert, Chromium Evaporation from SOFC Interconnector Alloys and Degradation Process by Chromium Transport, Proceedings 1st European Solid Oxide Fuel Cell Forum (Ed.: U. Bossel), Vol. 2, 703-713, Baden, Switzerland 1994

[Database] – Findit 1.2.0, ICSD Database, Februar 2003

[Decroix-1] – J. Decroix, R. Devin, R. Castro, L'oxydation á haute température d'aciers inoxydables au Cr et au Cr-Ni á I'air et en atmospheres pauvres en oxygéne, Mem. Scient. Revue Metall. 60(10), 1963, 665-675

[Dillon-1] – R. Dillon, S. Srinivasan, A.S. Arico, V. Antonucci, International activities in DMFC R&D: status of technologies, Journal of Power Sources 127, 2004, 112-126

[Ebbinghaus-1] – B.B. Ebbinghaus, Thermodynamics of Gas Phase Chromium Species: The Chromium Oxides, the Chromium Oxyhydroxides, and Volatility Calculations in Waste Incineration Processes, Comb. Flame 93, 1993, 119-137

[Edström-1] – J.O. Edström, Scaling of 18-8 Stainless Steel in Reheating Furnace Atmospheres, J. Iron. Steel Inst. 185, 1957, 450-466

[England-1] – D.M. England, A.V. Virkar, Oxidation Kinetics of Some Nickel-Based Superalloy Foils and Electronic Resistance of the Oxide Scale Formed in Air, Part I, Journal of The Electrochemical Society 146(9), 1999, 3196-3202

[England-2] – D.M. England, A.V. Virkar, Oxidation Kinetics of Some Nickel-Based Superalloy Foils in Humidified Hydrogen and Electronic Resistance of the Oxide Scale Formed, Part II, Journal of The Electrochemical Society 148(4), 2001, A330-A338

[Ertl-1] – S. Ertl, P. Huczkowski, T. Höfler, L. Singheiser, W.J. Quadakkers, to be published

[Evans-1] – H.E. Evans, Stress effects in high temperature oxidation of metals, International Materials Reviews 40 (1), 1-40, 1995

[Friedrich-1] – H.E. Friedrich, Challenges of Materials Technology for Low Consumption Vehicle Concepts, Advanced Engineering Materials, 5(3), 2003, 105-112

[Fujikawa-1] – H. Fujikawa, Y. Shida, K. Fujino, J. Murayama, High Temperature Oxidation Behaviour of Si-containing 11 % Cr Stainless Steels in Water Vapor Containing Atmosphere, Corrosion Engineering 31(3), 1982, 164-171

[Garcia-1] – M.J. Garcia-Vargas, L. Lelait, P. Stevens, J. Schefold, V. Kolarik, H. Fietzek, Influence of Humidity and Additive Elements on the Oxide Layer Composition and Properties of Chromia-Forming Alloys for SOFC Interconnects, Proceedings Sixth European Solid Oxide Fuel Cell Forum (Ed.: M. Mogensen), Vol. 3, 1662-1671, Luzerne, Switzerland 2004

[George-1] – Status of tubular SOFC field unit demonstrations, Journal of Power Sources 86, 2000, 134-139

[Ghosh-1] – D. Ghosh, E. Tang, M. Perry, D. Prediger, M. Pastula, R. Boersma, Status of SOFC development at Global Thermodynamics, Procedeeings 7th International Symposium Solid Oxide Fuel Cells (SOFC-VII) (Ed.: H. Yokokawa, S.C. Singhal), 101-110, The Electrochemical Society, Pennington, NJ, 2001

[Gil-1] – A. Gil, H.J. Penkalla, M. Hänsel, J. Norton, W. Köck, W.J. Quadakkers, The Oxidation Behaviour of Cr Based ODS Alloys in H_2/H_2O at 1000°C, IX Conf. On Electron Microscopy of Solids, 6-9 May 1996, Krakow-Zakopane. Poland, 441-446 (1996)

[Gindorf-1] – C. Gindorf, K. Hilpert, H. Nabielek, L. Singheiser, R. Ruckdäschel, G. Schiller, Chromium Release from Metallic Interconnects with and without Coatings, Proceedings Fourth European Solid Oxide Fuel Cell Forum (Ed.: J. McEvoy), Vol. 2, 845-854, Oberrohrdorf, Switzerland 2000

[Gindorf-2] – C. Gindorf, L. Singheiser, K. Hilpert, Chromium vaporisation from Fe, Cr base alloys used as interconnect in fuel cells, Steel Research 72, 2001, 528-533

[Glatz-1] – W. Glatz, G. Kunschert, M. Janousek, Powder-Metallurgical Processing and Properties of High Performance Metallic SOFC Interconnect Materials, Proceedings Sixth European Solid Oxide Fuel Cell Forum (Ed.: M. Mogensen), Vol. 3, 1612-1627, Luzerne, Switzerland 2004

[Graham-1] – M. Graham, R. Hussey, Analytical techniques in high temperature corrosion, Oxidation of Metals 44(1/2), 1995, 339-374

[Greiner-1] – H. Greiner, T. Grögler, W. Köck, R. Singer, Chromium based alloys for high temperature SOFC applications, Proceedings 4th International Symposium Solid Oxide Fuel Cells (SOFC-IV) (Ed.: M. Dokiya, O. Yamamoto, H. Tagawa, S.C. Singhal), 879-888, The Electrochemical Society, Pennington, NJ, 1995

[Grove-1] – W.R. Grove, On Voltaic Series and the Combination of Gases by Platinum, Philos. Meg. Ser. 3(14), 1839, 127-130

[Gurrappa-1] – I. Gurrappa, S. Weinbruch, D. Naumenko, W.J. Quadakkers, Factors governing breakaway oxidation of FeCrAl-based alloys, Materials and Corrosion 51, 2000, 224-235

[Günther-1] – C. Günter, H.-J. Beie, P. Greil, F. Richter, Parameters Infuencing the Longterm-Stability of the SOFC, Proceedings 2nd European Solid Oxide Fuel Cell Forum (Ed.: B. Thorstensen), Vol. 2, 491-501, Oberrohrdorf, Switzerland 1996

[Haanappel-1] – V.A.C. Haanappel, J. Mertens, D. Rutenbeck, C. Tropartz, W. Herzhof, D. Sebold, F. Tietz, Optimisation of processing and microstructural parameters of LSM cathodes to improve the electrochemical performance of anode-supported SOFCs, Journal of Power Sources 141, 2005, 216-226

[Hagel-1] – W.C. Hagel, A.U. Seybolt, Cation Diffusion in Cr_2O_3, Journal of the Electrochemical Society, 108(12), 1961, 1146-1152

[Haile-1] – S.M. Haile, Fuel cell materials and components, Acta Materialia 51, 2003, 5981-6000

[Hänsel-1] – M. Hänsel, W.J Quadakkers, L. Singheiser, H. Nickel, Korrosions- und Kommpatibitätsstudien an Cr-Basislegierungen für den metallischen Interkonnektor der Hochtemperaturbrennstoffzelle (SOFC), Report Forschungszentrum Jülich, Jülich FRG, Jül-3583, ISSN 0944-2952, 1998

[Hilpert-1] – K. Hilpert, D. Das, M. Miller, D.H. Peck, R. Weiß, Chromium Vapor Species over Solid Oxide Fuel Cell Interconnect Materials and Their Potential for Degradation Processes, J. Electrochem. Soc. 143, 1996, 3642-3647

[Hindam-1] – H.M. Hindam, W.W. Smeltzer, Growth and Microstructure of α-Al_2O_3 on β-NiAl, Journal of Electrochemical Society 127, 1980, 1630-1635

[Hojda-1] – R. Hojda, W. Heimann, W.J. Quadakkers, Production-capable materials concept for high-temperature fuel cells, ThyssenKrupp Techforum, July 2003, 20-23

[Holt-1] – A. Holt, P. Kofstad, Electrical conductivity and defect structure of Cr_2O_3. I. High temperatures (>~1000°C), Solid State Ionics 69, 1994, 127-136

[Holt-2] – A. Holt, P. Kofstad, Electrical conductivity and defect structure of Cr_2O_3. II. Reduced temperatures (<~1000°C), Solid State Ionics 69, 1994, 137-143

[Holt-3] – A. Holt, P. Kofstad, Elecrtical conductivity and defect structure of Mg-doped Cr_2O_3, Solid State Ionics 100, 1994, 201-209

[Holt-4] – A. Holt, P. Kofstad, Electrical conductivity of Cr_2O_3 doped with TiO_2, Solid State Ionics 117, 1994, 21-25

[Honnegger-1] – K. Honegger, A. Plas, R. Diethelm, W. Glatz, Evaluation of ferritic steel interconnects for SOFC stacks, Procedeeings 7th International Symposium Solid Oxide Fuel Cells (SOFC-VII) (Ed.: H. Yokokawa, S.C. Singhal), 803-810, The Electrochemical Society, Pennington, NJ, 2001

[Horita-1] – T. Horita, Y. Xiong, K. Yamaji, N. Sakai, H. Yokokawa, Stability of Fe-Cr Based Alloys in H_2-H_2O Atmosphere for SOFC Interconnector, Proceedings 5th European Solid Oxide Fuel Cell Forum (Ed.: J. Huijsmans), Vol. 1, 401-408, Luzerne, Switzerland 2002

[Horita-2] – T. Horita, Y. Xiong, K. Yamaji, N. Sakai, H. Yokokawa, Stability of Fe-Cr alloy interconnects under CH_4-H_2O atmosphere for SOFCs, Journal of Power Sources 118, 2003, 35-43

[Horita-3] – T. Horita, Y. Xiong, H. Kishimoto, K. Yamaji, N. Sakai, H. Yokokawa, Application of Fe-Cr alloys to solid oxide fuel cells for cost-reduction Oxidation behaviour of alloys in methane fuel, Journal of Power Sources 131, 2004, 293-298

[Huang-1] – K. Huang, P.Y. Hou, J.B. Goodenough, Characterisation of iron-based alloys interconnects for reduced temperature solid oxide fuel cells, Solid State Ionics 129, 2000, 237-250

[Huang-2] – K. Huang, P.Y. Hou, J.B. Goodenough, Reduced area specific resistance for iron-based metallic interconnects by surface oxide coatings, Materials Research Bulletin 36, 2001, 81-95

[Huczkowski-1] – P. Huczkowski, N. Christiansen, V. Shemet, J. Piron Abellan, L. Singheiser, W.J. Quadakkers, Oxidation limited life times of chromia forming ferritic steels, Materials and Corrosion 55 (11), 2004, 825-830

[Huczkowski-2] – P. Huczkowski, N. Christiansen, V. Shemet, J. Piron Abellan, L. Singheiser, W.J. Quadakkers, Oxidation Induced Lifetime Limits of Chromia Forming Ferritic Steels, Journal of fuel Cell Science and Technology 1, 2004, 30-34

[Huczkowski-3] – P. Huczkowski, N. Christiansen, V. Shemet, L. Singheiser, W.J. Quadakkers, Growth Rates and Electrical Conductivity of Oxide Scales on Ferritic Steels Proposed as Interconnect Materials for SOFCs, Proceedings Sixth European Solid Oxide Fuel Cell Forum (Ed.: M. Mogensen), Vol. 3, 1594-1601, Luzerne, Switzerland 2004

[Hultquist-1] – G. Hultquist, E. Hörnlund, Q. Dong, Platinum-induced oxidation of chromium in O_2 at 800 °C, Corrosion Science, 45 (12), 2003, 2697-2703

[Hultquist-2] – G. Hultquist, G.I. Sproule, S. Moisa, M.J. Graham, U. Södervall, Influence of Deuterium and Platinum on the Thermal Oxidation of GaAs, Journal of Electrochemical Society 150 (10), 2003, G617-G623

[Jiang-1] – R. Jiang, D. Chu, Comparative Studies of Methanol Crossover and Cell Performance for a DMFC, Journal of The Electrochemical Society 151(1), 2004, A69-A76

[Khanna-1] – A.S. Khanna, Introductin of High Temperature Oxidation and Corrosion, ASM International 2002

[Kofstad-1] – P. Kofstad, High Temperaure Corrosion, Elsevier Ltd 1988

[Kofstad-2] – P. Kofsatd, Nonstechiometry, Diffusion, and Electrical Conductivity in Binary Metal Oxides, John Wiley& Sons, Inc. 1972

[Kofstad-3] – P. Kofstad, R. Bredesen, High temperature corrosion in SOFC enviroments, Solid State Ionics 52, 1992, 69-75

[Köck-1] – W. Köck, H. Martinz, H. Greiner, M. Janousek, Development and processing of metallic Cr based materials for SOFC parts, Proceedings 4th International Symposium Solid Oxide Fuel Cells (SOFC-IV) (Ed.: M. Dokiya, O. Yamamoto, H. Tagawa, S.C. Singhal), 841-849, The Electrochemical Society, Pennington, NJ, 1995

[Krumpelt-1] – M. Krumpelt, J.Ralph, T. Cruse, J-M. Bae, Materials ofr Low Temperature SOFCs, Proceedings 5th European Solid Oxide Fuel Cell Forum (Ed.: J. Huijsmans), Vol. 1, 215-224, Luzerne, Switzerland 2002

[Kung-1] – S. Kung, T. Cal, T. Moris, E. Barringer, S. Elangovan, J. Hartvigsen, Proceedings 2000 Fuel Cell Seminar, p. 585, Portland, Oregon, 2000

[Lai-1] – G. Lai, High Temperature Corrosion of Engineering Alloys, ASM International, Materials Park, Ohio, USA, 1990

[Lamp-1] – P. Lamp, J. Tachtler, O. Finkenwirth, S. Mukerjee, S. Shaffer, Development of an Auxiliary Power Unit with Solid Oxide Fuel Cells for Automotive Applications, Fuel Cells, 3(3), 2003, 1-7

[Larminie-1] – J. Larminie, A. Dicks, Fuel Cell Systems Explained, John Wiley& Sons, Ltd 2000

[Larring-1] – Y. Larring, R. Haugsrud, T. Norby, HT Corrosion of a Cr-5 wt % Fe-1 wt % Y_2O_3 Alloy and Conductivity of the Oxide Scale, Effect of Water Vapor, J. Electrochem Soc. 150(8), 2003, B374-B379

[Larring-2] – Y. Larring, T. Norby, Spinel and Perovskite Functional Layers Between Plansee Metallic Interconnect (Cr-5 wt % Fe-1 wt % Y_2O_3) and Ceramic $(La_{0.85}Sr_{0.15})_{0.91}MnO_3$ Cathode Materials for Solid Oxide Fuel Cells, J. Electrochem Soc. 147, 2000, 3251-3256

[Liu-1] – Z. Liu, W. Gao, Y. He, Modeling of Oxidation Kinetics of Y-Doped Fe-Cr-Al Alloys, Oxidation of Metals 53 (3/4), 2000, 341-350

[Lu-1] – Y. Lu, L. Schaefer, A solid oxide fuel cell system fed with hydrogen sulphide and natural gas, Journal of Power Sources 135, 2004, 184-191

[Malkow-1] – T. Malkow, W.J Quadakkers, L. Singheiser, H. Nickel, Untersuchungen zum Langzeitverhalten von metallischen Interkonnektorwerkstoffen der Hochtemperatur-Brennstoffzelle (SOFC) im Hinblick auf die Kompatibilität mit kathodenseitigen Kontaktschichten, Report Forschungszentrum Jülich, Jülich FRG, Jül-3589, ISSN 0944-2952, 1998

[Malkow-2] – T. Malkow, U.v.d. Crone, A.M. Laptev, T. Koppitz, U. Breuer, W.J. Quadakkers, Thermal expansion characteristics and corrosion behaviour of ferritic steels for SOFC interconnects, Proceedings 5th International Symposium Solid Oxide Fuel Cells (SOFC-V) (Ed.: U. Stimming, S.C. Singhal, H. Tagawa, W. Lehnert), 1244-1252 The Electrochemical Society, Pennington, NJ, 1997

[Matsuzaki-1] – Y. Matsuzaki, I. Yasuda, Electrochemical properties of a SOFC cathode in contact with a chromium-containing alloy separator, Solid State Ionics 132, 2000, 271-278

[McCullough-1] – H.M. McCullough, M.G. Fontana, F.H. Beck, Trans. Am. Soc. Metals 43, 1951, 404.

[McEvoy-1] – A.J. McEvoy, Thin SOFC electrolytes and their interfaces – A near-term research strategy, Solid State Ionics 132, 2000, 159-165

[Menzies-1] – I.A. Menzies, D. Mortimer, NatureLond. 208, 1965, 1307.

[Minh-1] – N.Q. Minh, Solid oxide fuel cell technology – features and applications, Solid State Ionics 174, 2004, 271-277

[Minh-2] – N.Q. Minh, J. Am. Ceram. Soc. 176(3), 1993, 563-588

[Nagai-1] – H. Nagai, T. Fujikawa, K. Shoji, Electrical Conductivity of Cr_2O_3 Doped with La_2O_3, Y_2O_3 and NiO, Transactions of the Japan Institute of Metals 24(8), 1983, 581-588

[Nagai-2] – H. Nagai, K. Ohbayashi, J. Am. Ceram. Soc. 72, 1989, 400.

[Nagai-3] – H. Nagai, S. Ishikawa, N. Amano, K. Shoji, Electrical Conductivity of Sintered Cr_2O_3 Simultaneously Doped with NiO and Rare Earth Oxide at Low Oxygen Potential, N. Trans JIM 26(10), 1985, 753-762

[Naumenko-1] – D. Naumenko, private communication

[Nernst-1] – W. Nernst, Z Electrochem. 5, 1899, 41-43

[Nichols-1] – J.R. Nichols, R. Newton, M.J. Bennett, H.E. Evans, H. Al-Badairy, G. Tatlock, D. Naumenko, W.J. Quadakkers, G. Strehl, G. Borchardt, Development of a Life Prediction Model for the Chemical Failure of FeCrAl(RE) Alloys in Oxidising Environments, Life Time Modelling of High Temperature Corrosion Process, Number 34 (Ed.: M. Schütze, W.J. Quadakkers, J.R. Nichols), 83-106, Money Publishing, London, 2001

[Otsuka-1] – N. Otsuka, Y. Nishiyama, T. Kudo – Breakaway Oxidation of TP310S Stainless-Steel Foil Initiated by Cr Depletion of the Entire Specimen in a Simulated Flue-Gas Atmosphere, Oxidation of Metals 62 (1/2) 2004, 121-139

[Park-1] – J.H. Park, K. Natesan, Electronic Transport in Thermally Grown Cr_2O_3, Oxidation of Metals 33(1/2), 1990, 31-54

[Pfeifer-1] – P.-J. Pfeifer, H. Holzbrecher, W.J. Quadakkers, U. Breuer, W. Speier, Quantitative Analysis of Oxide Films on ODS-alloys using MCs^+-SIMS and e-beam SNMS, Fresenius J Anal Chem 346, 1993, 186-191

[Pint-1] – B.A. Pint, I.G. Wright, Long-term high temperature oxidation behaviour of ODS ferritics, Journal of Nuclear Materilas307-311, 2002, 763-768

[Piron-1] – J. Piron Abellan, V. Shemet, F. Tietz, L. Singheiser, W.J. Quadakkers, A. Gil. Ferritic steel interconnect for reduced temperature SWOFC, Proceedings 7th International Symposium Solid Oxide Fuel Cells (SOFC-VII) (Ed.: H. Yokokawa, S.C. Singhal), 811-819, The Electrochemical Society, Pennington, NJ, 2001

[Piron-2] – F.J. Piron Abellan, W.J. Quadakkers – Development of Ferritic Steels for Application as Interconnect Materials for Intermediate Temperature Solid Oxide Fuel Cells (SOFCs), Report Forschungszentrum Jülich, Jülich FRG, Jül-4170, ISSN 0944-2952, 2005

[Piron-3] – J. Piron Abellan, F. Tietz, V. Shemet, A. Gil, T. Ladwein, L. Singheiser, W.J. Quadakkers, Long Term Oxidation Behaviour and Compatibility with Contact Materials of Newly Developed Ferritic Interconnector Steels, Proceedings 5th European Solid Oxide Fuel Cell Forum (Ed.: J. Huijsmans), Vol. 1, 248-256, Luzerne, Switzerland 2002

[Quadakkers-1] – W.J. Quadakkers, J. Piron-Abellan, V. Shemet, L. Singheiser, Metallic interconnectors for solid oxide fuel cells – a review, Materials at High Temperatures 20(2), 2003, 115-127

[Quadakkers-2] – W.J. Quadakkers, D. Naumenko, E. Wessel, v. Kochubey, L. Singheiser, Growth Rates of Alumina Scales on Fe-Cr-Al Alloys, Oxidation of Metals 61(1/2), 2004, 17-37

[Quadakkers-3] – W.J. Quadakkers, L. Singheiser, Practical Aspects of the Reactive Element Effect, Material Science Forum 369-372, 2001, 77-92

[Quadakkers-4] – W.J. Quadakkers, H. Greiner, W. Köck, Metals and Alloys for High Temperature SOFC Application, Proceedings 1st European Solid Oxide Fuel Cell Forum (Ed.: U. Bossel), Vol. 2, 525-541, Baden, Switzerland 1994

[Quadakkers-5] – W.J. Quadakkers, German patent, DE 195 47 699 C2, 20.12, 1995

[Quadakkers-6] – W.J. Quadakkers, F. Baumanns, H. Nickel, German patent, DE 44 10 711, 7.9, 1995

[Quadakkers-7] – W.J. Quadakkers, T. Malkow, J. Piron Abellan, U. Flesch, V. Shemet, L. Singheiser, Suitability of Ferritic Steels for Application as Construction Materials for SOFC Interconnects, Proceedings Fourth European Solid Oxide Fuel Cell Forum (Ed.: J. McEvoy), Vol. 2, 827-836, Oberrohrdorf, Switzerland 2000

[Quadakkers-8] – W.J. Quadakkers, M.J. Bennett, Oxidation induced lifetime limits of thin walled, iron based, alumina forming, oxide dispersion strengthened alloy components, Materials Science and Technology 10, 1994, 126-131

[Quadakkers-9] – W.J. Quadakkers, K. Bongartz, The prediction of breakaway oxidation for alumina forming ODS alloys using Oxidation Diagrams, Werkstoffe und Korrosion 45, 1994, 232-241

[Quadakkers-10] – W.J. Quadakkers, J. Nicholls, D. Naumenko, J. Wilber, L. Singheiser, Factors Affecting Oxide Growth Rates and Lifetime of FeCrAl Alloys, Materials Aspects in Automotive Catalytic Converters (Ed.: H. Bode), 93-105, Wiley-VCH Verlag GmbH, Weinheim, Germany, 2002

[Rahmel-1] – A. Rahmel, J. Tobolski, Einfluss von Wasserdampf und Kohlendioxyd auf die Oxidation von Eisen in Sauerstoff bei hohen Temperaturen, J. Corros. Sci. 5, 1965, 333-346

[Sabioni-1] – A.C.S. Sabioni, A.M. Huntz, F. Millot, C. Monty, Self-diffusion in Cr_2O_3, II. Oxygen diffusion in single crystal, Philos. Mag. A66, 1992, 351-360

[Sakai-1] – N. Sakai, T. Horita, Y.P. Xiong, K. Yamaji, H. Kishimoto, M.E. Brito, H. Yokokawa, T. Maruyama, Structure and transport property of manganese - chromium - iron oxide as a main compound in oxide scales of alloy interconnects for SOFCs, Solid State Ionics 176 (7-8), 2005, 681-686

[Schütze-1] – M.Schütze, Protective Oxide Scales and Their Breakdown, Wiley, Chichester 1997

[Schütze-2] - M. Schütze, S. Ito, W. Przybilla, H. Echsler, C. Bruns, Test methods and data on the mechanical properties of protective oxide scales, Materials at High Tempertures 18, 2001, 39-50,

[Singhal-1] – S.C. Singhal, K. Kendall, High Temperature Solid Oxide Fuel Cells. Fundamentals, Design and Applications, Elsevier Ltd 2003

[Singhal-2] – S.C. Singhal, Advances in solid oxide fuel cell technology, Solid State Ionics 135, 2000, 305-313

[Singhal-3] – S.C. Singhal, Progress in tubular solid oxide fuel cell technology, Procedeeings 6th International Symposium Solid Oxide Fuel Cells (SOFC-VI) (Ed.: S.C. Singhal, M. Dokiya), 39-51, The Electrochemical Society, Pennington, NJ, 1999

[Singhal-4] – S.C. Singhal, Solid oxide fuel cells for stationary, mobile, and military application, Solid State Ionics 152-153, 2002, 405-410

[Skinner-1] – S.J. Skinner, J.A. Kilner, Oxygen ion conductors, Materials today, March 2003

[Smeltzer-1] – W.W. Smeltzer, The breakdown of the protective oxide film on transition metal alloys, Acta Met. 8, 1960, 268-270

[Song-1] – C. Song, Fuel processing for low-temperature and high-temperature fuel cells. Challenges, and opportunities for sustainable development in the 21st centaury, Catalysis Today 77, 2002, 17-49

[Stambouli-1] – A.B. Stambouli, E. Traversa, Solid oxide fuel cells (SOFCs): a review of an environmentally clean and efficient source of energy, Renewable and Sustainable Energy Reviews 6, 2002, 433-455

[Stambouli-2] – A.B. Stambouli, E.Traversa, Fuel cells, an alternative to standard sources of energy, Renewable and Sustainable Energy Reviews 6, 2002, 297-306

[Steele-1] – B.C.H. Steele, Materials for IT-SOFC stack, 35 years R&D: the inevitability of gradualness?, Solid State Ionics 134, 2000, 3-20

[Steinberger-1] – R. Steinberger-Wilckens, I.C. Vinke, L. Blum, L.G.J.(Bert) de Haart, J. Remmel, F. Tietz, W.J. Quadakkers, Progress in SOFC Stack Developmnet at Forschungszentrum Jülich, Proceedings Sixth European Solid Oxide Fuel Cell Forum (Ed.: M. Mogensen), Vol. 1, 11-19, Luzerne, Switzerland 2004

[Stöver-1] – D. Stöver, U. Diekmann, U. Flesch, H. Kabs, W.J. Quadakkers, F. Tietz, I. Vinke, Recent developments in anode supported thin film SOFC at Research Centre Jülich, Procedeeings 6th International Symposium Solid Oxide Fuel Cells (SOFC-VI) (Ed.: S.C. Singhal, M. Dokiya), 812-821, The Electrochemical Society, Pennington, NJ, 1999

[Su-1] – M.Y. Su, Diss. Abstr. Int., 48, 1988, 3049.

[Tietz-1] – F. Tietz, H.-P. Buchkremer, D. Stöver, Components manufacturing for solid oxide fuel cells, Solid State Ionics 152-153, 2002, 373-381

[Tietz-2] – F. Tietz, I. Arul Raj, W. Jungen, D. Stöver, High-temperature superconductor materials for contact layers in solid oxide fuel cells: I. Sintering behaviour and physical properties at operating temperatures, Acta materialia 49, 2001, 803-810

[Uehara-1] – T. Uehara, T. Ohno, A. Toji, Development of Ferritic Fe-Cr Alloy for SOFC Separator, Proceedings 5th European Solid Oxide Fuel Cell Forum (Ed.: J. Huijsmans), Vol. 1, 281-288, Luzerne, Switzerland 2002

[Vossen-1] – J.P.T. Vossen, P. Gavenda, K. Rahts, M. Röhrig, M. Schorr, M. Schütze, Limits of the oxidation resistance of several heat-resistant steels under isothermal and cyclic oxidation as well as under creep in air at 650°C, Materials at High Temperatures 14, 387-401, 1997

[Wagner-1] – C. Wagner, Beitrag zur Theorie des Anlaufvorgangs, Z. phys. Chem 21, 1933, 25-41

[Whittle-1] – D.P. Whittle, Ph.D. Thesis, University of Manchester, 1965

[Whittle-2] – D.P. Whittle, G.C. Wood, D.J. Evans, D.B. Scully, Concentration profiles in the underlying alloy during the oxidation of iron-chromium alloys, Acta Metallurgica, 15, 1967, 1747-1755

[Wilber-1] – J.P. Wilber, M.J. Bennett, J.R. Nichols, The Effect of Thermal Cycling on the Mechanical Failure of Alumina Scales formed on Commercial FeCrAl-RE Alloys, Proceedings of an EFC Workshop: Cyclic Oxidation of High Temperature Materials, Number 27 (Ed.: M. Schütze, W.J. Quadakkers), 133-147, IOM Communications Ltd, London, Great Britain, 1999

[Wood-1] – G.C. Wood, The oxidation of iron-chromium alloys and stainless steels at high temperatures, Corrosion Science, 2, 1962, 173-196

[Wood-2] – G.C. Wood, D.P. Whittle, On the mechanism of oxidation of iron-16.4 % chromium at high temperature, Corrosion Science, 4, 1964, 263-292

[Wood-3] – G.C. Wood, D.P. Whittle, The unusual scaling behaviour of iron-22.9 % chromium in air at 1100°C, Corrosion Science, 4, 1964, 293-313

[Wood-4] – G.C. Wood, D.P. Whittle, The mechanism of breakthrough of protective chromium oxide scales on Fe-Cr alloys, Corrosion Science, 7, 1967, 763-782

[Wright-1] – I.G. Wright, Metals Handbook, Vol. 13 Corrosion, 9th ed., ASM Metals Park. OH, 1987

[Yamamoto-1] – O. Yamamoto, Solid oxide fuel cells: fundamental aspects and prospects, Electochim. Acta 45, 2000, 2423-2435

[Yang-1] – Z. Yang, K.S. Weil, D.M. Paxton, J.W. Stevenson, Selection and Evaluation of Heat-Resistant Alloys for SOFC Interconnect Application, J. Electrochem Soc. 150(9), 2003, A1188-A1201

[Yang-2] – Z. Yang, J.S. Hardy, M.S. Walker, G. Xia, S.P. Simner, J.W. Stevenson, Structure and Conductivity of Thermally Grown Scales on Ferritic Fe-Cr-Mn Steel for SOFC Interconnect Applications, J. Electrochem Soc. 151(11), 2004, A1825-A1831

[Yearian-1] – H.J. Yearian, W.D. Derbyshire, J.F. Radavich, The Formation of Oxide Films On Chromium and 18 Cr-8 Ni Steels, Corrosion 13, 1957, 597t-607t

[Yearian-2] – H.J. Yearian, E.C. Randall, T.A. Longo, The Structure of Oxide Scales on Chromium Steels, Corrosion 12, 1956, 515t-525t

[Young-1] – D.J. Young, M.L. Burg, P.R. Munroe, Internal Precipitation of Al_2O_3 and Cr_2O_3 in Austenitic Alloys, Material Science Forum 461-464, 2004, 21-28

[Zahid-1] – M. Sahid, F. Tietz, D. Sebold, H.P. Buchkremer, Reactive Coatings against Chromium Evaporation in Solid Oxide Fuel Cells, Proceedings Sixth European Solid Oxide Fuel Cell Forum (Ed.: M. Mogensen), Vol. 2, 820-827, Luzerne, Switzerland 2004

[Zizelman-1] – J. Zizelman, J. Tachtler, Auxiliary Power Units with Solid Oxide Fuel Cell Technology for Independent Electric Power Supply in Passenger Cars, Proceedings 5th European Solid Oxide Fuel Cell Forum (Ed.: J. Huijsmans), Vol. 2, 1153-1164, Luzerne, Switzerland 2002

[Zhu-1] – W.Z. Zhu, S.C. Deevi, A review on the status of anode materials for solid oxide fuel cells, Materials Science and Engineering A362, 2003, 228-239

[Zhu-2] – W.Z. Zhu, S.C. Deevi, Opportunity of metallic interconnects for solid oxide fuel cells: a status on contact resistance, Materials Research Bulletin 38, 2003, 957-972

10. Appendix

Steel	Batch name	Composition (wt. %)								
		Fe	Cr	Mn	Ti	La	Si	Al	Ni	Y
JS-3	JEX	Bal.	23.3	0.4	0.047	0.089	0.009	0.005	-	-
JS-3	JEW	Bal.	22.9	0.4	0.046	0.087	≤0.01	≤0.01	<0.01	-
Crofer 22 APU (A)	JDA	Bal.	22.5	0.42	0.05	0.075	0.1	0.12	0.16	-
Crofer 22 APU (A)	JMB	Bal.	23.1	0.4	0.08	0.074	0.073	0.12	1)	-
Crofer 22 APU (A)	JMC	Bal.	22.6	0.4	0.072	0.07	0.056	0.12	1)	-
Crofer 22 APU (A)	JMD	Bal.	23.0	04.	0.076	0.077	0.067	0.12	1)	-
Crofer 22 APU (B)	JZF	Bal.	22.2	0.46	0.055	0.07	0.026	0.022	0.016	-
Crofer 22 APU (B)	JZN	Bal.	22.2	0.47	0.066	0.072	0.028	0.021	0.017	-
Crofer 22 APU (B)	KCB	Bal.	22.2	0.45	0.065	0.096	0.014	0.011	0.022	-
ZMG232	HXT	Bal.	22.1	0.48	-	<0.01	0.36	0.19	0.31	-
Alloy 446	HNK	Bal.	24.9	0.5	<0.005	<0.01	<0.01	-	-	-
1.4509	HLH	Bal.	18	0.38	0.12	-	0.7	0.03	0.12	-
1.4016	HMM	Bal.	16.3	0.19	<0.01	-	0.25	<0.02	0.2	-
1.4016-C3	HMP	Bal.	16.2	0.29	<0.01	-	0.41	<0.02	0.26	-
Model steel FeCrLa	HCE	Bal.	25.2	-	1)	0.42	-	1)	-	-
Model steel FeCrMnY	HCH	Bal.	25.4	1.55	-	-	-	-	-	0.17
Pure Cr	CSX	-	Bal.	-	-	-	-	-	-	-
Fe5Cr1Y_2O_3 (ODS)	DCU	4.9	Bal.	-	-	-	-	-	-	0.48
Fe5Cr1Y_2O_3 (ODS)	DCV	4.8	Bal.	-	-	-	-	-	-	0.49
Model steel (JS-3 base)	JLV	Bal.	23.3	0.38	0.049	0.06	0.12	≤0.01	-	-
Model steel (JS-3 base)	JLT	Bal.	23.4	0.36	0.048	0.11	≤0.01	0.14	-	-

1) Element not analysed

Table 10.1: Chemical composition of studied steels, part 1

Steel	Batch name	Composition (wt. %)					
		O	C	N	S	P	Others
JS-3	JEX	0.0016	0.007	0.0007	0.001	1)	
JS-3	JEW	0.0042	0.009	0.0009	< 0.001	1)	
Crofer 22 APU (A)	JDA	0.0046	0.008	0.0113	< 0.001	1)	
Crofer 22 APU (A)	JMB	0.0063	0.048	0.011	0.002	1)	
Crofer 22 APU (A)	JMC	0.0039	0.01	0.0108	0.001	1)	
Crofer 22 APU (A)	JMD	0.0049	0.015	0.0109	0.001	1)	
Crofer 22 APU (B)	JZF	0.0034	0.019	0.0073	< 0.001	< 0.01	
Crofer 22 APU (B)	JZN	0.0026	0.003	0.0068	< 0.001	< 0.01	
Crofer 22 APU (B)	KCB	0.0107	0.017	0.0023	0.002	< 0.01	
ZMG232	HXT	0.0013	0.017	0.0047	< 0.001	< 0.01	Zr: 0.13
Alloy 446	HNK	0.0056	0.039	0.1211	0.009	1)	
1.4509	HLH	0.0032	0.031	0.0137	0.002	1)	
1.4016	HMM	0.0075	0.054	0.0434	0.004	1)	
1.4016-C3	HMP	0.0129	0.072	0.0397	0.003	1)	
Model steel FeCrLa	HCE	0.0052	0.021	0.0057	0.001	1)	
Model steel FeCrMnY	HCH	0.0040	0.023	0.0012	0.003	1)	
Pure Cr	CSX						
Fe5Cr1Y_2O_3 (ODS)	DCU	0.3452	0.004	0.0044	< 0.001	1)	
Fe5Cr1Y_2O_3 (ODS)	DCV	0.3815	0.016	0.0152	< 0.001	1)	
Model steel (JS-3 base)	JLV	0.0163	0.017	0.0016	< 0.001	1)	
Model steel (JS-3 base)	JLT	0.0129	0.011	0.0014	0.001	1)	

1) Element not analysed

Table 10.2: Chemical composition of studied steels, part 2

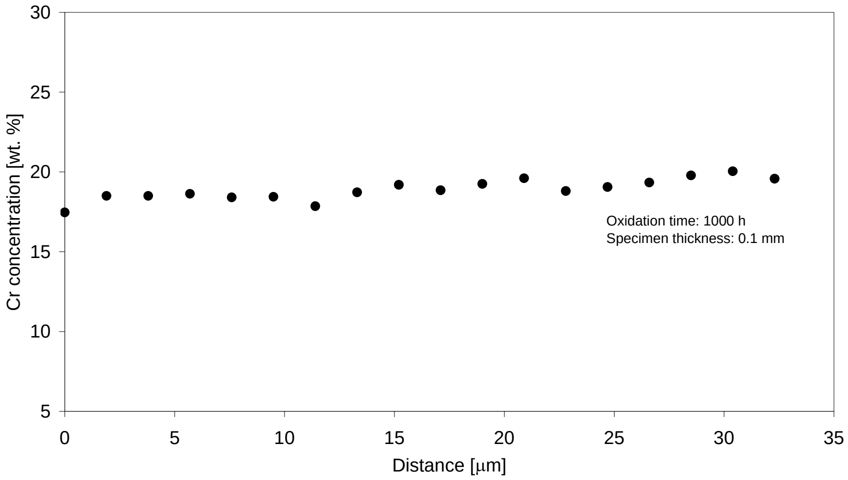

Figure 10.1: Measured Cr depletion profiles for specimens of steel Crofer A with different initial thickness after cyclic oxidation at 800°C in air.

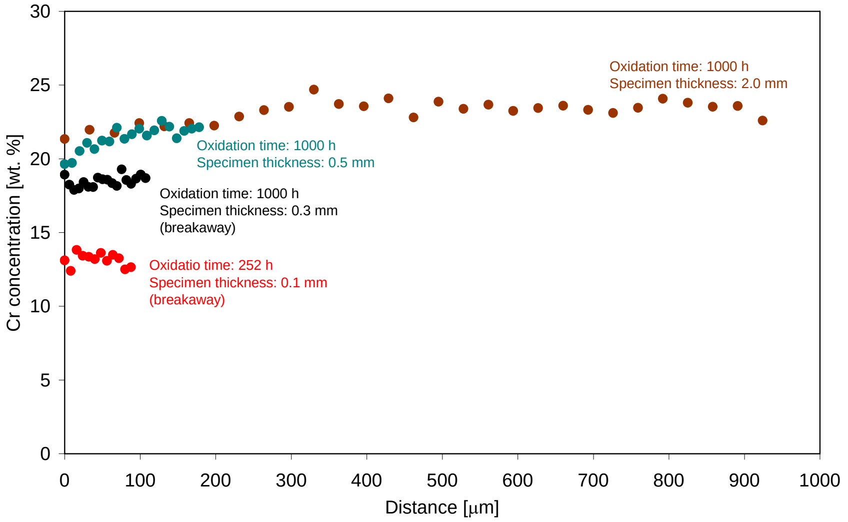

Figure 10.2: Measured Cr depletion profiles for specimens of steel Crofer A with different initial thickness after cyclic oxidation at 900°C in air.

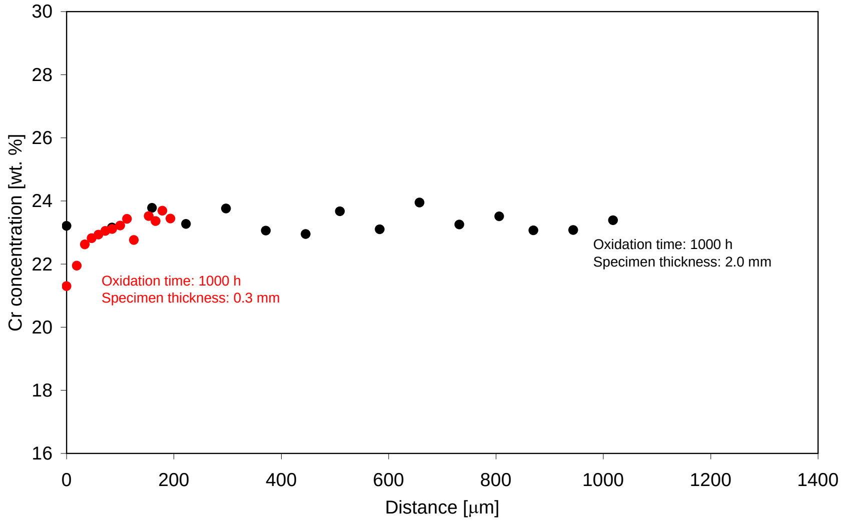

Figure 10.3: Measured Cr depletion profiles for specimens of steel JS-3 with different initial thickness after cyclic oxidation at 800°C in air.

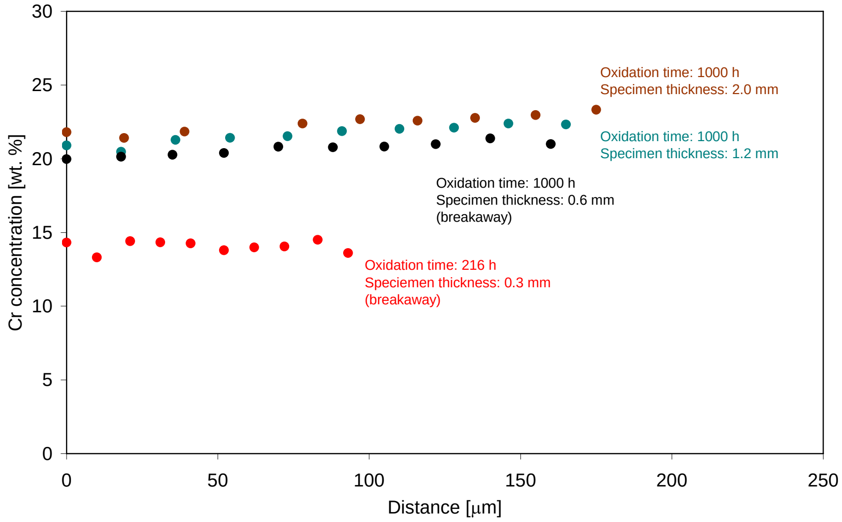

Figure 10.4: Measured Cr depletion profiles for specimens of steel JS-3 with different initial thickness after cyclic oxidation at 900°C in air.

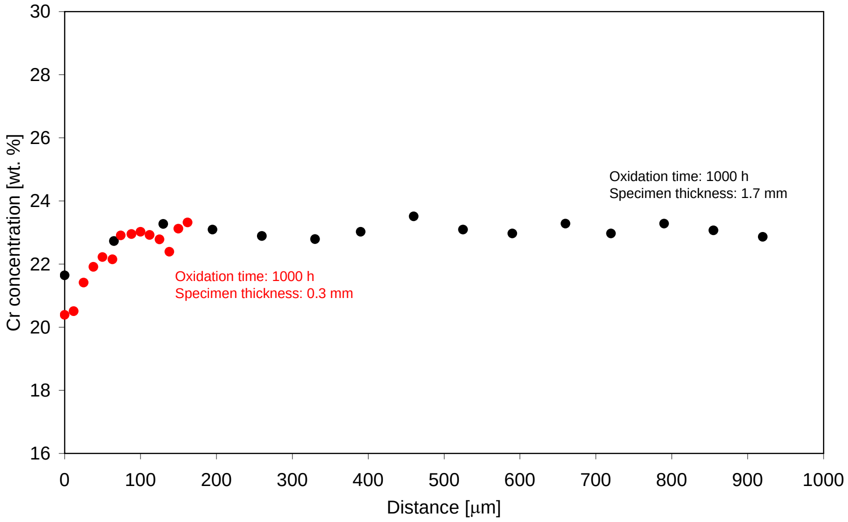

Figure 10.5: Measured Cr depletion profiles for specimens of steel Crofer B with different initial thickness after cyclic oxidation at 800°C in air.

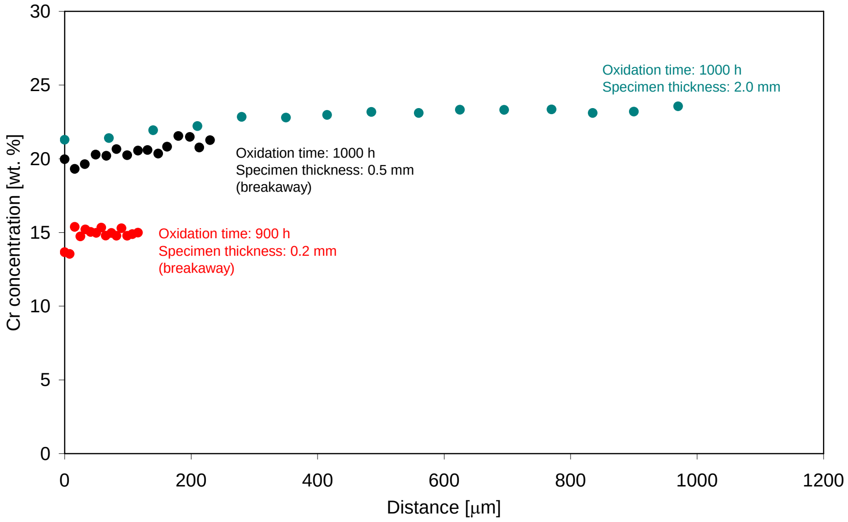

Figure 10.6: Measured Cr depletion profiles for specimens of steel Crofer B with different initial thickness after cyclic oxidation at 900°C in air.

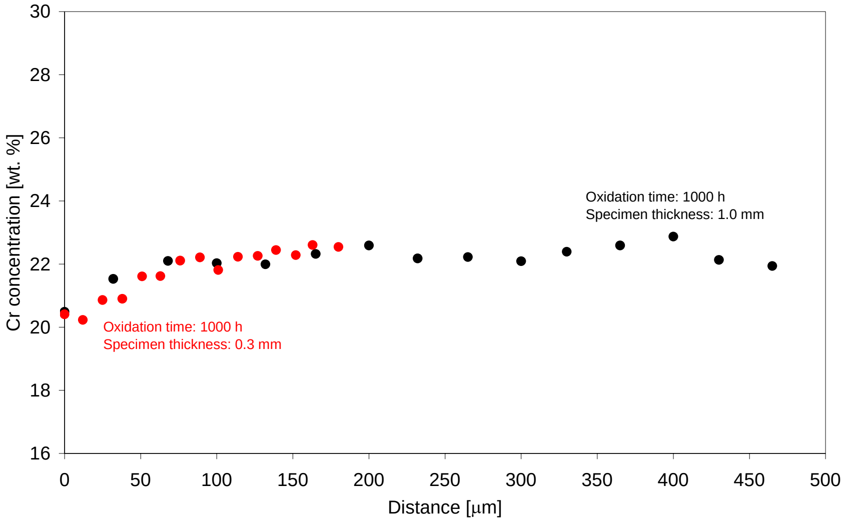

Figure 10.7: Measured Cr depletion profiles for specimens of steel ZMG232 with different initial thickness after cyclic oxidation at 800°C in air.

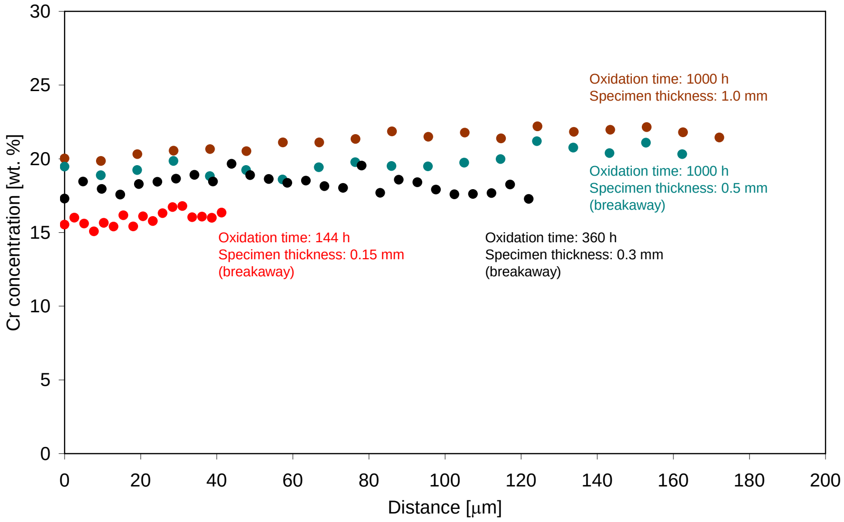

Figure 10.8: Measured Cr depletion profiles for specimens of steel ZMG232 with different initial thickness after cyclic oxidation at 900°C in air.

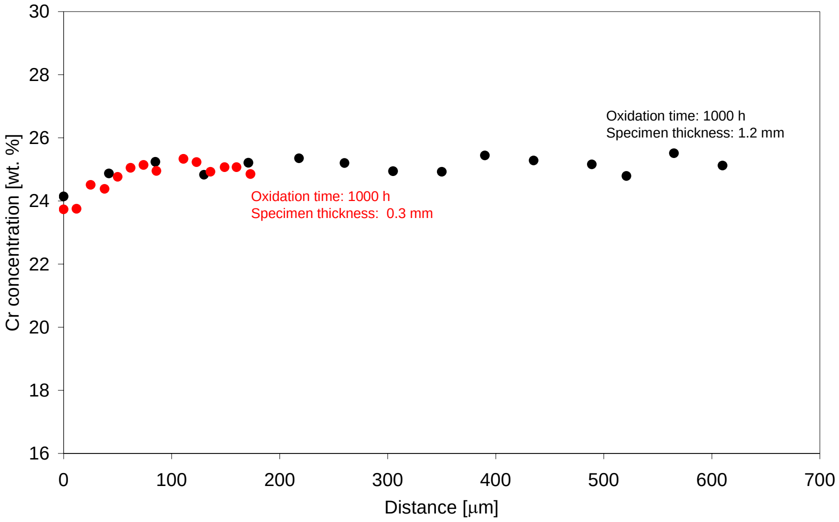

Figure 10.9: Measured Cr depletion profiles for specimens of model steel FeCrLa (batch HCE) with different initial thickness after cyclic oxidation at 800°C in air.

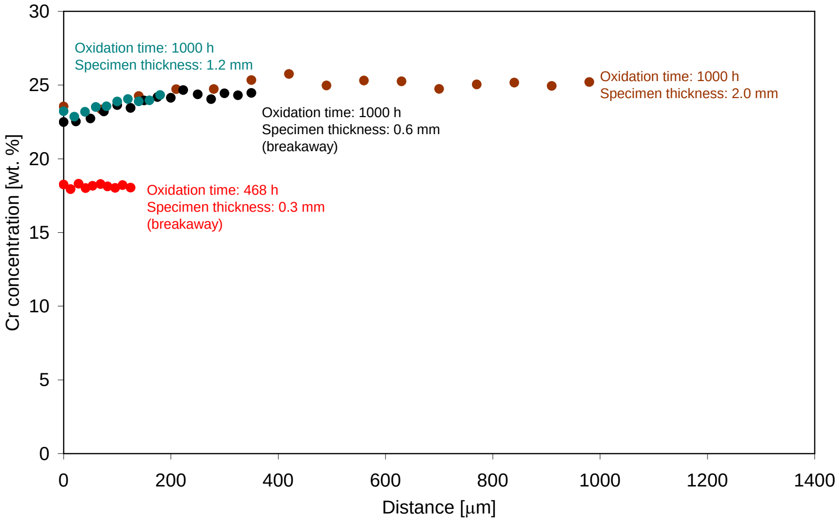

Figure 10.10: Measured Cr depletion profiles for specimens of model steel FeCrLa (batch HCE) with different initial thickness after cyclic oxidation at 900°C in air.

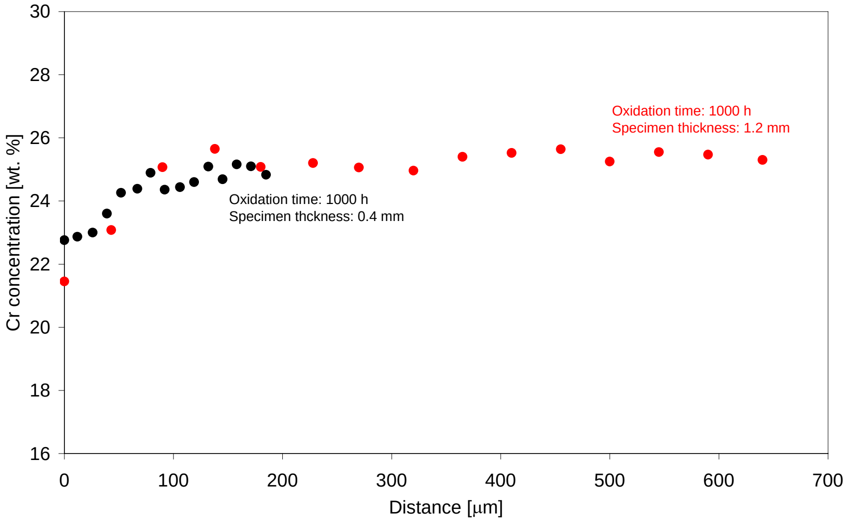

Figure 10.11: Measured Cr depletion profiles for specimens of model steel FeCrMnY (batch HCH) with different initial thickness after cyclic oxidation at 800°C in air.

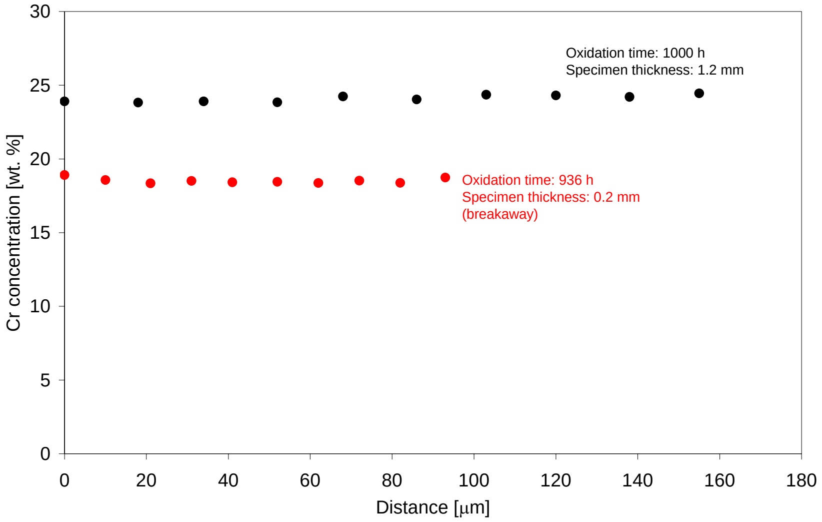

Figure 10.12: Measured Cr depletion profiles for specimens of model steel FeCrMnY (batch HCH) with different initial thickness after cyclic oxidation at 900°C in air.

Acknowledgements

The authors would like to thank all the people which have contributed to this work, especially our colleagues at the Institute of Energy Research, (IEF-2), Research Centre Jülich in which this work was carried out.

The authors are also grateful to:
Haldor Topsoe A/S and Topsoe Fuel Cell A/S for the financial support,
the Central Technology Division (ZAT), Research Centre Jülich,
and the Central Division of Analytical Chemistry (ZCH), Research Centre Jülich.

1. **Fusion Theory**
   Proceedings of the Seventh European Fusion Theory Conference
   edited by A. Rogister (1998); X, 306 pages
   ISBN: 978-3-89336-219-6

2. **Radioactive Waste Products 1997**
   Proceedings of the 3rd International Seminar on Radioactive Waste Products
   held in Würzburg (Germany) from 23 to 26 June 1997
   edited by R. Odoj, J. Baier, P. Brennecke et al. (1998), XXIV, 506 pages
   ISBN: 978-3-89336-225-7

3. **Energieforschung 1998**
   Vorlesungsmanuskripte des 4. Ferienkurs „Energieforschung“
   vom 20. bis 26. September 1998 im Congrescentrum Rolduc und
   im Forschungszentrum Jülich
   herausgegeben von J.-Fr. Hake, W. Kuckshinrichs, K. Kugeler u. a. (1998), 500 Seiten
   ISBN: 978-3-89336-226-4

4. **Materials for Advances Power Engineering 1998**
   Abstracts of the 6th Liège Conference
   edited by J. Lecomte-Beckers, F. Schubert, P. J. Ennis (1998), 184 pages
   ISBN: 978-3-89336-227-1

5. **Materials for Advances Power Engineering 1998**
   Proceedings of the 6th Liège Conference
   edited by J. Lecomte-Beckers, F. Schubert, P. J. Ennis (1998),
   Part I XXIV, 646, X pages; Part II XXIV, 567, X pages; Part III XXIV, 623, X pages
   ISBN: 978-3-89336-228-8

6. **Schule und Energie**
   1. Seminar Energiesparen, Solarenergie, Windenergie. Jülich, 03. und 04.06.1998
   herausgegeben von P. Mann, W. Welz, D. Brandt, B. Holz (1998), 112 Seiten
   ISBN: 978-3-89336-231-8

7. **Energieforschung**
   Vorlesungsmanuskripte des 3. Ferienkurses „Energieforschung“
   vom 22. bis 30. September 1997 im Forschungszentrum Jülich
   herausgegeben von J.-Fr. Hake, W. Kuckshinrichs, K. Kugeler u. a. (1997), 505 Seiten
   ISBN: 978-3-89336-211-0

8. **Liberalisierung des Energiemarktes**
   Vortragsmanuskripte des 5. Ferienkurs „Energieforschung“
   vom 27. September bis 1. Oktober 1999 im Congrescentrum Rolduc und
   im Forschungszentrum Jülich
   herausgegeben von J.-Fr. Hake, A. Kraft, K. Kugeler u. a. (1999), 350 Seiten
   ISBN: 978-3-89336-248-6

9. **Models and Criteria for Prediction of Deflagration-to-Detonation Transition (DDT) in Hydrogen-Air-Steam-Systems under Severe Accident Conditions**
   edited by R. Klein, W. Rehm (2000), 178 pages
   ISBN: 978-3-89336-258-5

10. **High Temperature Materials Chemistry**
    Abstracts of the 10th International IUPAC Conference, April 10 - 14 2000, Jülich
    edited by K. Hilpert, F. W. Froben, L. Singheiser (2000), 292 pages
    ISBN: 978-3-89336-259-2

11. **Investigation of the Effectiveness of Innovative Passive Safety Systems for Boiling Water Reactors**
    edited by E. F. Hicken, K. Verfondern (2000), X, 287 pages
    ISBN: 978-3-89336-263-9

12. **Zukunft unserer Energieversorgung**
    Vortragsmanuskripte des 6. Ferienkurs „Energieforschung“
    vom 18. September bis 22. September 2000 im Congrescentrum Rolduc und
    im Forschungszentrum Jülich
    herausgegeben von J.-Fr. Hake, S. Vögele, K. Kugeler u. a. (2000),
    IV, 298 Seiten
    ISBN: 978-3-89336-268-4

13. **Implementing Agreement 026**
    For a Programme of Research, Development and Demonstration on Advanced Fuel Cells: Fuel Cell Systems for Transportation. Annex X. Final Report 1997 - 1999
    edited by B. Höhlein; compiled by P. Biedermann (2000), 206 pages
    ISBN: 978-3-89336-275-2

14. **Vorgespannte Guß-Druckbehälter (VGD) als berstsichere Druckbehälter für innovative Anwendungen in der Kerntechnik**
    Prestressed Cast Iron Pressure Vessels as Burst-Proof Pressure Vessels for Innovative Nuclear Applications
    von W. Fröhling, D. Bounin, W. Steinwarz u. a. (2000) XIII, 223 Seiten
    ISBN: 978-3-89336-276-9

15. **High Temperature Materials Chemistry**
Proceedings of the 10th International IUPAC Conference
held from 10 to 14 April 2000 at the Forschungszentrum Jülich, Germany
Part I and II
edited by K. Hilpert, F. W. Froben, L. Singheiser (2000), xvi, 778, VII pages
ISBN: 978-3-89336-259-2

16. **Technische Auslegungskriterien und Kostendeterminanten von SOFC- und PEMFC-Systemen in ausgewählten Wohn- und Hotelobjekten**
von S. König (2001), XII, 194 Seiten
ISBN: 978-3-89336-284-4

17. **Systemvergleich: Einsatz von Brennstoffzellen in Straßenfahrzeugen**
von P. Biedermann, K. U. Birnbaum, Th. Grube u. a. (2001), 185 Seiten
ISBN: 978-3-89336-285-1

18. **Energie und Mobilität**
Vorlesungsmanuskripte des 7. Ferienkurs „Energieforschung“
vom 24. September bis 28. September 2001 im Congrescentrum Rolduc und im Forschungszentrum Jülich
herausgegeben von J.-Fr. Hake, J. Linßen, W. Pfaffenberger u. a. (2001), 205 Seiten
ISBN: 978-3-89336-291-2

19. **Brennstoffzellensysteme für mobile Anwendungen**
von P. Biedermann, K. U. Birnbaum, Th. Grube u. a. (2002)
PDF-Datei auf CD
ISBN: 978-3-89336-310-0

20. **Materials for Advances Power Engineering 2002**
Abstracts of the 7th Liège Conference
edited by J. Lecomte-Beckers, M. Carton, F. Schubert, P. J. Ennis (2002), c. 200 pages
ISBN: 978-3-89336-311-7

21. **Materials for Advanced Power Engineering 2002**
Proceedings of the 7th Liège Conference
Part I, II and III
edited by J. Lecomte-Beckers, M. Carton, F. Schubert, P. J. Ennis (2002), XXIV, 1814, XII pages
ISBN: 978-3-89336-312-4

22. **Erneuerbare Energien: Ein Weg zu einer Nachhaltigen Entwicklung?**
Vorlesungsmanuskripte des 8. Ferienkurs „Energieforschung“
vom 23. bis 27. September 2002 in der Jakob-Kaiser-Stiftung, Königswinter
herausgegeben von J.-Fr. Hake, R. Eich, W. Pfaffenberger u. a. (2002), IV, 230 Seiten
ISBN: 978-3-89336-313-1

23. **Einsparpotenziale bei der Energieversorgung von Wohngebäuden durch Informationstechnologien**
von A. Kraft (2002), XII, 213 Seiten
ISBN: 978-3-89336-315-5

24. **Energieforschung in Deutschland**
Aktueller Entwicklungsstand und Potentiale ausgewählter nichtnuklearer Energietechniken
herausgegeben von M. Sachse, S. Semke u. a. (2002), II, 158 Seiten, zahlreiche farb. Abb.
ISBN: 978-3-89336-317-9

25. **Lebensdaueranalysen von Kraftwerken der deutschen Elektrizitätswirtschaft**
von A. Nollen (2003), ca. 190 Seiten
ISBN: 978-3-89336-322-3

26. **Technical Session: Fuel Cell Systems of the World Renewable Energy Congress VII**
Proceedings
edited by D. Stolten and B. Emonts (2003), VI, 248 pages
ISBN: 978-3-89336-332-2

27. **Radioactive Waste Products 2002 (RADWAP 2002)**
Proceedings
edited by R. Odoj, J. Baier, P. Brennecke and K. Kühn (2003), VI, 420 pages
ISBN: 978-3-89336-335-3

28. **Methanol als Energieträger**
von B. Höhlein, T. Grube, P. Biedermann u. a. (2003), XI, 109 Seiten
ISBN: 978-3-89336-338-4

29. **Hochselektive Extraktionssysteme auf Basis der Dithiophosphinsäuren: Experimentelle und theoretische Untersuchungen zur Actinoiden(III)-Abtrennung**
von S. A. H. Nabet (2004), VI, 198 Seiten
ISBN: 978-3-89336-351-3

30. **Benchmarking-Methodik für Komponenten in Polymerelektrolyt-Brennstoffzellen**
von Matthias Gebert (2004), 194 Seiten
ISBN: 978-3-89336-355-1

31. **Katalytische und elektrochemische Eigenschaften von eisen- und kobalthaltigen Perowskiten als Kathoden für die oxidkeramische Brennstoffzelle (SOFC)**
von Andreas Mai (2004), 100 Seiten
ISBN: 978-3-89336-356-8

32. **Energy Systems Analysis for Political Decision-Making**
    edited by J.-Fr. Hake, W. Kuckshinrichs, R. Eich (2004), 180 pages
    ISBN: 978-3-89336-365-0

33. **Entwicklung neuer oxidischer Wärmedämmschichten für Anwendungen in stationären und Flug-Gasturbinen**
    von R. Vaßen (2004), 141 Seiten
    ISBN: 978-3-89336-367-4

34. **Neue Verfahren zur Analyse des Verformungs- und Schädigungsverhaltens von MCrAlY-Schichten im Wärmedämmschichtsystem**
    von P. Majerus (2004), 157 Seiten
    ISBN: 978-3-89336-372-8

35. **Einfluss der Oberflächenstrukturierung auf die optischen Eigenschaften der Dünnschichtsolarzellen auf der Basis von a-Si:H und µc-Si:H**
    von N. Senoussaoui (2004), 120 Seiten
    ISBN: 978-3-89336-378-0

36. **Entwicklung und Untersuchung von Katalysatorelementen für innovative Wasserstoff-Rekombinatoren**
    von I.M. Tragsdorf (2005), 119 Seiten
    ISBN: 978-3-89336-384-1

37. **Bruchmechanische Untersuchungen an Werkstoffen für Dampfkraftwerke mit Frischdampftemperaturen von 500 bis 650°C**
    von L. Mikulová (2005), 149 Seiten
    ISBN: 978-3-89336-391-9

38. **Untersuchungen der Strukturstabilität von Ni-(Fe)-Basislegierungen für Rotorwellen in Dampfturbinen mit Arbeitstemperaturen über 700 °C**
    von T. Seliga (2005), 106 Seiten
    ISBN: 978-3-89336-392-6

39. **IWV-3 Report 2005. Zukunft als Herausforderung**
    (2005), 115 Seiten
    ISBN: 978-3-89336-393-3

40. **Integrierter Photodetektor zur Längenmessung**
    von E. Bunte (2005), XI, 110 Seiten
    ISBN: 978-3-89336-397-1

41. **Microcrystalline Silicon Films and Solar Cells Investigated by Photoluminescence Spectroscopy**
    by T. Merdzhanova (2005), X, 137 pages
    ISBN: 978-3-89336-401-5

42. **IWV-3 Report 2005. Future as a challenge**
(2005), 115 pages
ISBN: 978-3-89336-405-3

43. **Electron Spin Resonance and Transient Photocurrent Measurements on Microcrystalline Silicon**
by T. Dylla (2005), X, 138 pages
ISBN: 978-3-89336-410-7

44. **Simulation und Analyse des dynamischen Verhaltens von Kraftwerken mit oxidkeramischer Brennstoffzelle (SOFC)**
von M. Finkenrath (2005), IV, 155 Seiten
ISBN: 978-3-89336-414-5

45. **The structure of magnetic field in the TEXTOR-DED**
by K.H. Finken, S.S. Abdullaev, M. Jakubowski, M. Lehnen, A. Nicolai, K.H. Spatschek (2005), 113 pages
ISBN: 978-3-89336-418-3

46. **Entwicklung und Modellierung eines Polymerelektrolyt-Brennstoffzellenstapels der 5 kW Klasse**
von T. Wüster (2005), 211 Seiten
ISBN: 978-3-89336-422-0

47. **Die Normal-Wasserstoffelektrode als Bezugselektrode in der Direkt-Methanol-Brennstoffzelle**
von M. Stähler (2006), VI, 96 Seiten
ISBN: 978-3-89336-428-2

48. **Stabilitäts- und Strukturmodifikationen in Katalysatordispersionen der Direktmethanolbrennstoffzelle**
von C. Schlumbohm (2006), II, 211 Seiten
ISBN: 978-3-89336-429-9

49. **Eduktvorbereitung und Gemischbildung in Reaktionsapparaten zur autothermen Reformierung von dieselähnlichen Kraftstoffen**
von Z. Porš (2006), XX, 182, XII Seiten
ISBN: 978-3-89336-432-9

50. **Spektroskopische Untersuchung der poloidalen Plasmarotation unter dem Einfluß statischer und dynamischer Ergodisierung am Tokamak TEXTOR**
von C. Busch (2006), IV, 81 Seiten
ISBN: 978-3-89336-433-6

51. **Entwicklung und Optimierung von Direktmethanol-Brennstoffzellstapeln**
von M. J. Müller (2006), 167 Seiten
ISBN: 978-3-89336-434-3

52. **Untersuchung des reaktiven Sputterprozesses zur Herstellung von aluminiumdotierten Zinkoxid-Schichten für Silizium-Dünnschichtsolarzellen**
von J. Hüpkes (2006), XIV, 170 Seiten
ISBN: 978-3-89336-435-0

53. **Materials for Advanced Power Engineering 2006**
Proceedings of the 8th Liège Conference
Part I, II and III
edited by J. Lecomte-Beckers, M. Carton, F. Schubert, P. J. Ennis (2006), Getr. Pag.
ISBN: 978-3-89336-436-7

54. **Verdampfung von Werkstoffen beim Betrieb von Hochtemperaturbrennstoffzellen (SOFC)**
von M. Stanislowski (2006), IV, 154 Seiten
ISBN: 978-3-89336-438-1

55. **Methanol as an Energy Carrier**
edited by P. Biedermann, Th. Grube, B. Höhlein (2006), XVII, 186 pages
ISBN: 978-3-89336-446-6

56. **Kraftstoffe und Antriebe für die Zukunft**
Vorlesungsmanuskripte des 1. Herbstseminars „Kraftstoffe und Antriebe für die Zukunft“ vom 9.-13. Oktober 2006 an der TU Berlin
herausgegeben von V. Schindler, C. Funk, J.-Fr. Hake, J. Linßen (2006), VIII, 221 Seiten
ISBN: 978-3-89336-452-7

57. **Plasma Deposition of Microcrystalline Silicon Solar Cells: Looking Beyond the Glass**
by M. N. van den Donker (2006), VI, 110 pages
ISBN: 978-3-89336-456-5

58. **Nuclear Energy for Hydrogen Production**
by K. Verfondern (2007), 186 pages
ISBN: 978-3-89336-468-8

59. **Kraft-Wärme-Kopplung mit Brennstoffzellen in Wohngebäuden im zukünftigen Energiesystem**
von C. H. Jungbluth (2007), XI, 197 Seiten
ISBN: 978-3-89336-469-5

60. **Finite Element Simulation of Stress Evolution in Thermal Barrier Coating Systems**
by P. Bednarz (2007), XIV, 121 pages
ISBN: 978-3-89336-471-8

61. **Modellierung der Prozesse in katalytischen Rekombinatoren**
von J. Böhm (2007), VI, 116 Seiten
ISBN: 978-3-89336-473-2

62. **Entwicklung einer Heliumstrahldiagnostik zur Messung der Elektronendichte und – temperatur mit hoher räumlicher und zeitlicher Auflösung**
von U. Kruezi (2007), IV, 151 Seiten
ISBN: 978-3-89336-476-3

63. **IEF-3 Report 2007. Von Grundlagen bis zum System**
(2007), 164 Seiten
ISBN: 978-3-89336-479-4

64. **Entwicklung eines Direkt-Methanol-Brennstoffzellensystems der Leistungklasse kleiner 5 kW**
von M. Nölke (2007), 194 Seiten
ISBN: 978-3-89336-481-7

65. **Effect of geometry and composition of Cr steels on oxide scale properties relevant for interconnector applications in Solid Oxide Fuel Cells (SOFCs)**
by P. Huczkowski, W.J. Quadakkers (2007), 159 pages
ISBN: 978-3-89336-484-8

In this book recently developed SOFC interconnect materials as well as other commonly used high-Cr commercial steels were investigated with respect to their oxidation behaviour in the temperature range required for SOFC application (700 °C – 900 °C). SOFC market requirements (e.g., in the automotive industry) lead in many cases to the demand for a reduction of the fuel cell size and/or weight and thus of the interconnector thickness. Therefore, the main emphasis was made to investigate changes in the oxidation behaviour in the case of thin components.

Author

Paweł Huczkowski studied at the Cracow University of Technology, Faculty of Chemical Engineering and Technology, Poland. Since May 2002 he has worked at the Research Centre Juelich, Institute of Energy Research, IEF-2: Microstructure and Properties of Materials in the group of Dr. Quadakkers (High Temperature Corrosion Group). The subject of his work is metallic materials for SOFC. The contents of this book have been submitted to the Technical University of Aachen (RWTH Aachen) in fulfilment of the requirements for a Doctor of Engineering degree.

Institute of Energy Research
IEF-2 Materials Microstructure and Characterization

The research topics of IEF-2 are focussed on the development and characterization of materials for efficient gas and steam power plants, for high temperature fuel cells and for future fusion reactor components subjected to high thermal loads. The scientific expertises of the institute cover microstructural investigations, surface analysis techniques and the physical, chemical, mechanical and corrosion behaviour of metallic high temperature materials and of ceramic materials used either as structural components or as elements of coating systems.

Forschungszentrum Jülich
in der Helmholtz-Gemeinschaft

Band / Volume 65
ISBN 978-3-89336-484-8

Energietechnik
Energy Technology